INVESTIGATION OF ENERGY DISSIPATION AND CAPTURE THROUGH FISSION MEASUREMENTS

A thesis submitted for the degree of

Doctor of Philosophy

by

Dongyun Jeung

The Australian National University

October, 2018

To my parents

Declaration

This thesis is an account of research undertaken between September 2013 and October 2018 at The Department of Nuclear Physics, Research School of Physics and Engineering, The Australian National University, Canberra, Australia.

The material presented in this thesis is, to the best of my knowledge, original and has not been submitted in whole or part for a degree in any university.

The author acknowledges that copyright of published works contained within this thesis resides with the copyright holders of those workers.

Dongyun Jeung
12 February 2019

Supervisors

Mahananda Dasgupta
Professor, Department of Nuclear Physics
Australian National University
Canberra, Australia

David Hinde
Professor, Department of Nuclear Physics
Australian National University
Canberra, Australia

Elizabeth Williams
Research Fellow, Autonomy, Agency and Assurance Institute
Honorary Senior Lecturer, Department of Nuclear Physics
Australian National University
Canberra, Australia

Advisor

Andrew Stuchbery
Professor, Department of Nuclear Physics
Australian National University
Canberra, Australia

Preface

This thesis describes the influence of the energy dissipative processes induced by transfer reactions on heavy ion fusion reactions, particularly at energies above the fusion barrier. All experiments were carried out using the 14UD tandem electrostatic accelerator of the Heavy Ion Accelerator Facility at the Australian National University in Canberra, Australia. All measurements documented in this work were made with the assistance of the nuclear reaction dynamics group and technical staff of the Department of Nuclear Physics.

The project was originally proposed by Prof. D.J. Hinde and Prof. M. Dasgupta. All measurements were carried out using the CUBE binary fission spectrometer, originally consisting of two multi-wire proportional counters (MWPCs) and the two Si surface barrier detectors. A third MWPC was added in the most recent measurements. The systems studied for this work included both 2-MWPC and 3-MWPC configurations. Analysis of the fission data was performed by the author using the customised program **dacube** originally written by Dr. E. Williams and adapted by the author, which was based on the existing C/C++ ROOT framework and its libraries. For extracting capture cross sections through the measurement of fission yields, coupled channels calculations and quasifission simulations (via **Quasisim**) were performed by the author. **Quasisim** is originally written by Dr. R. du Rietz. In addition, Time Dependent Hartree-Fock (TDHF) calculations, an optional part of **Quasisim** work, were performed by the author with assistance from Dr. K. Vo-Phuoc.

The following publications and conference proceedings are directly related to the work in this thesis:

1. *Dynamical approach to heavy ion-induced fission*
   D. Y. Jeung, E. Williams, D. J. Hinde, M. Dasgupta, R. du Rietz, M. Evers, C. J. Lin, D. H. Luong, C. Simenel and A. Wakhle, EPJ Web of Conf. **91**, 00005 (2015).

2. *Sub-barrier quasifission in heavy element formation reactions with deformed actinide target nuclei*
   D. J. Hinde, **D. Y. Jeung** , E. Prasad, A. Wakhle, M. Dasgupta, M. Evers, D. H. Luong, R. du Rietz, C. Simenel, E. C. Simpson, and E. Williams, Phys. Rev. C **97**, 024616 (2018).

3. *Fusion and quasifission studies for the* ^{40}Ca $+^{186}$ W,^{192} Os *reactions*
   E. Prasad, D. J. Hinde, E. Williams, M. Dasugupta, I. P. Carter, K. J. Cook, **D.**

Y. Jeung, D. H. Luong, C. S. Palshetkar, D. C. Rafferty, K. Ramachandran, C. Simenel, and A. Wakhle, Phys. Rev. C **96**, 034608 (2017).

4. *Nuclear structure dependence of fusion hindrance in heavy element synthesis*
J. Khuyagbaatar, H. M. David, D. J. Hinde, I. P. Carter, K. J. Cook, M. Dasgupta, Ch. E. Düllmann, **D. Y. Jeung**, B. Kindler, B. Lommel, D. H. Luong, E. Prasad, D. C. Rafferty, C. Sengupta, C. Simenel, E. C. Simpson, J. F. Smith, K. Vo-Phuoc, J. Walshe, A. Wakhle, E. Williams, and A. Yakushev, Phys. Rev. C **97**, 064618 (2018).

5. *Interplay of spherical closed shells and N/Z asymmetry in quasifission dynamics*
G. Mohanto, D. J. Hinde, K. Banerjee, M. Dasgupta, **D. Y. Jeung**, C. Simenel, E. C Simpson, A. Wakhle, E. Williams, I. P. Carter, K. J. Cook, D. H. Luong, C. S. Palshetkar, and D. C. Rafferty, Phys. Rec. C **97**, 054603 (2018).

6. *Capture cross sections for the synthesis of new heavy nuclei using radioactive beams*
A. Wakhle, K. Hammerton, Z. Kohley, D. J. Morrissey, K. Stiefel, J. Yurkon, J. Walshe, K. J. Cook, M. Dasgupta, D. J. Hinde, **D. Y. Jeung**, E. Prasad, D. C. Rafferty, C. Simenel, E. C. Simpson, K. Vo-Phuoc, J. King, W. Loveland, and R. Yanez, Phys. Rec. C **97**, 021602 (2018).

7. *Evidence for the Role of Proton Shell Closure in Quasifission Reactions from X-Ray Fluorescence of Mass-Identified Fragments*
M. Morjean, D. J. Hinde, C. Simenel, **D. Y. Jeung**, M. Airiau, K. J. Cook, M. Dasgupta, A. Drouart, D. Jacquet, S. Kalkal, C. S. Palshetkar, E. Prasad, and D. Rafferty, E. C. Simpson, L. Tassan-Got, K. Vo-Phuoc, and E. Williams, Phys. Rev. Lett. **119**, 222502 (2017).

Furthermore the author has contributed to the following publications, which have been or published:

8. *Fission cross sections as a probe of fusion dynamics at high angular momentum*
C. S. Palshetkar, D. J. Hinde, M. Dasgupta, E. Williams, K. Ramachandran, I. P. Carter, K. J. Cook, **D. Y. Jeung**, D. H. Luong, S. D. McNeil, D. C. Rafferty, and A. Wakhle, Phys. Rev. C **98**, 044603 (2018).

9. *Exploring Zeptosecond Quantum Equilibration Dynamics: From Deep-Inelastic to Fusion-Fission Outcomes in ^{58}Ni + ^{60}Ni Reactions*
E. Williams, K. Sekizawa, D. J. Hinde, C. Simenel, M. Dasgupta, I. P. Carter, K. J. Cook, **D. Y, Jeung**, S. D. McNeil, C. S. Palshetkar, D. C. Rafferty, K. Ramachandran, and A. Wakhle, Phys. Rev. Lett. **120**, 022501 (2018).

10. *Asymptotic and near-target direct breakup of ^{6}Li and ^{7}Li*
Sunil Kalkal, E. C. Simpson, D. H. Luong, K. J. Cook, M. Dasgupta, D. J. Hinde, I. P. Carter, **D. Y. Jeung**, G. Mohanto, C. S. Palshetkar, E. Prasad, D. C. Rafferty, C. Simenel, K. Vo-Phuoc, E. Williams, L. R. Gasques, P. R. S. Gomes, and R. Linares, Phys. Rev. C **93**, 044605 (2016).

11. *Observation of mass-asymmetric fission of mercury nuclei in heavy ion fusion*
E. Prasad, D. J. Hinde, K. Ramachandran, E. Williams, M. Dasgupta, I. P. Carter, K. J. Cook, **D. Y. Jeung**, D. H. Luong, S. McNeil, C. S. Palshetkar, D. C. Rafferty, C. Simenel, A. Wakhle, J. Khuyagbaatar, Ch. E. Düllmann, B. Lommel, and B. Kindler, Phys. Rev. C **91**, 064605 (2015).

12. *Reduced quasifission competition in fusion reactions forming neutron-rich heavy elements*
K. Hammerton, K. Z. Kohley, Z. D. J. Hinde, M. Dasgupta, A. Wakhle, E. Williams, V. E. Oberacker, A. S. Umar, I. P. Carter, K. J. Cook, J. Greene, **D. Y. Jeung**, D. H. Luong, S. D. McNeil, C. S. Palshetkar, D. C. Rafferty, C. Simenel, and K. Stiefel, Phys. Rev. C **91**, 041602 (2015).

The author also contributed to the following conference proceedings:

12. *Quasifission Dynamics in the Formation of Superheavy Elements*
D. J. Hinde, M. Dasgupta, **D. Y. Jeung**, G. Mohanto, E. Prasad, C. Simenel, E. Williams, I. P. Carter, K. J. Cook, Sunil Kalkal, D.C. Rafferty, E. C. Simpson, H. M. David, Ch. E. Düllmann and J. Khuyagbaatar, EPJ Web of Conf. **163**, 00023 (2017).

13. *Investigating fusion dynamics at high angular momentum via fission cross sections*
C. S. Palshetkar, D. J. Hinde, E. Williams, K. Ramachandran, M. Dasgupta, K. J. Cook, A. Wakhle, **D. Y. Jeung**, D. C. Rafferty, S. D. McNeil, I. P. Carter and D. H. Luong, EPJ Web of Conf. **163**, 00042 (2017).

14. *First Elastic Scattering Measurement of ^{8}Li on ^{209}Bi at the Australian National University*
C. Sengupta, I. P. Carter, K. J. Cook, E. C. Simpson, M. Dasgupta, D. J. Hinde, **D. Y. Jeung**, Sunil Kalkal, K. Vo-Phuoc, E. Prasad, D. Rafferty, C. Simenel and E. Williams, EPJ Web of Conf. **163**, 00052 (2017).

15. *Quasifission in heavy and superheavy element formation reactions*
D. J. Hinde, M. Dasgupta, **D. Y. Jeung**, G. Mohanto, E. Prasad, C. Simenel, J. Walshe, A. Wahkle, E. Williams, I. P. Carter, K. J. Cook, Sunil Kalkal, D. C. Rafferty, R. du Rietz, E. C. Simpson, H. M. David, Ch. E. Düllmann and J. Khuyagbaatar, EPJ Web Conf. **131**, 04004 (2016).

16. *Systematic study of quasifission characteristics and timescales in heavy element formation reactions*
    D. J. Hinde, E. Williams, G. Mohanto, C. Simenel, M. Dasgupta, A. Wakhle, I. P. Carter, K. J. Cook K, **D. Y. Jeung**, D. H. Luong, C. S. Palshetkar, E. Prasad, D. C. Rafferty, R. du Rietz and E. C. Simpson, EPJ Web of Conf. **117**, 08006 (2016).

17. *Exploring dissipative processes at high angular momentum in ^{58}Ni + ^{60}Ni reactions*
    E. Williams, D. J. Hinde, M. Dasgupta, I. P. Carter, K. J. Cook, **D. Y. Jeung**, D. H. Luong, S. D McNeil, C. S. Palshetkar, D. C. Rafferty, K. Ramachandran, C. Simenel, E. C Simpson E and A. Wakhle, EPJ Web of Conf. **117**, 08021 (2016).

18. *Nuclear structure effects in quasifission − understanding the formation of the heaviest elements*
    D. J. Hinde, E. Williams, G. Mohanto, C. Simenel, **D. Y. Jeung**, M. Dasgupta, E. Prasad, A. Wakhle, K. Vo-Phuoc, I. P. Carter, K. J. Cook, D. H. Luong, C. S. Palshetkar, D. C. Rafferty and E. C. Simpson, EPJ Web of Conf. **123**, 03005 (2016).

19. *Mass-asymmetric fission in the ^{40}Ca + ^{142}Nd reaction*
    E. Prasad, D. J. Hinde, E. Williams, M. Dasgupta, I. P. Carter, K. J. Cook, **D. Y. Jeung**, D. H. Luong, S. McNeil, C. S. Palshetkar, D. C. Rafferty, C. Simenel, A. Wakhle, K. Ramachandran, J. Khuyagbaatar, Ch. E. Düllmann, B. Lommel and B. Kindler, EPJ Web of Conf. **123**, 03006 (2016).

Acknowledgements

First and foremost I would like to express my deepest gratitude to my supervisors Nanda Dasgupta, David Hinde and Ellizabeth Williams for their great support, mentorship and encouragement. Nanda has an excellent ability to pick up my strengths and weaknesses, and well know how to deal with them. Her leadership, and sometimes her strictness have guided me in what I need to do and always in the right direction. There is no doubt about the dedication of David's unfailing assistance in the entirety of my work. Without his endless support and expertise, the fission analysis could not have been completed. The things I learned from Liz are countless; not just for academic study, but also computing skills, writing and editing skills, and logic and critical thinkings, as well as lots of tips to survive in the research field. These are valuable assets to me. As their leaderships have been in perfect harmony, I have developed into a research scientist.

I also give special thanks to the GSI members, especially Khuyabaatar Jadambaa, Helena David, and Joe Walshe (ANU) for contributing in developing an analysis code for the recent measurements in the early stages. Because of their work, I could easily adapt the code and apply to my data.

Finally, I would like to thank current and past members of the Nuclear Reaction Dynamics group and all the accelerator staff in the ANU. Without their team work, the goal of this project would not have been achieved. To my good friend Chandani Palshetka, thanks for being a mentor at the beginning of my PhD. To Boon and Kaitlin, seeing them since I was an undergraduate, and chasing your excellent work achievements, sometimes depressed me but also motivated me to work super hard. I am very grateful to the fission group members Lauren, Annette, and Kaushik, for reading draft chapters and giving me feedback.

Without the great support and encouragement of my family and friends over the past few years, I could not have reached this stage. Words cannot express how grateful I am to you. Especially to my dad, I can truly understand how hard you worked to achieve your academic career. I really respect you and hope you are proud of me.

Abstract

Fusion of atomic nuclei is a process in which two nuclei overcome their mutual Coulomb repulsion (barrier) and merge together to form a single nucleus. Fusion of light nuclei, such as hydrogen and helium, powers the stars, whilst fusion of heavy nuclei is used to form new heavy elements and isotopes in the laboratory. Although the concept of nuclear fusion has been known for almost a century, only the more recent development of precision experimental measurements and new theoretical ideas demonstrated how essential it is to consider quantum superposition effects.

It is now recognised that fusion cross sections at energies below and close to the barrier can only be understood if the colliding nuclei are considered to be in a coherent superposition of their internal states (e.g. vibrational, rotational states). The coupled channels model, which considers the coupling between the internal structure and the relative motion of the two colliding nuclei, has emerged as the most successful model of fusion. However, experimental measurements of fusion cross sections at energies above the barrier consistently fall below model predictions, the size of the deviation appearing to increase with increasing charge product of the colliding nuclei. These observations have led to a closer scrutiny of the way fusion is modelled.

Currently, the colliding nuclei are considered to remain in coherent superposition right until the separation inside the barrier where fusion is simulated by imposing a boundary condition such as the incoming wave boundary condition, or use of an imaginary potential. Thus the dissipation of kinetic energy that leads to fusion is not modelled explicitly. The question is whether energy dissipation starts even at larger separations, which can lead to some of the kinetic energy being lost well before separations at which fusion is simulated in the model. Such processes can potentially reduce fusion as the colliding nuclei will have less kinetic energy at the barrier. In this work, factors leading to the reduction of fusion in heavy ion collisions are explored, with a particular focus on the role energy dissipation plays in such reaction outcomes.

To probe energy dissipative processes, a series of experiments was conducted using the 14UD tandem accelerator and superconducting LINAC at the Heavy Ion Accelerator facility at the Australian National University. In these experiments, a range of projectiles bombarded fissile ^{232}Th targets at beam energies from below to above the capture barrier. Reaction outcomes were detected in coincidence using the CUBE binary fission spectrometer. A systematic study of transfer-fission, fusion-fission and quasifission was carried out through the analysis of each reaction's kinematic properties and mass-angle distributions.

Additionally, a new method for determining quasifission cross sections was developed and used to extract cross sections.

In this work, transfer-fission has been used as a proxy for energy dissipative processes since fission following transfer can only occur if the system formed following transfer has an excitation energy higher than the fission barrier (approximately 6 MeV). Transfer fission was found to increase relative to total fission as a function of charge product. For each reaction, the proportion decreased as a function of energy relative to the capture barrier energy. It is suggested that fusion is suppressed by transfer reactions as the charge product increases, and that self-consistent models of fusion need to properly take into account energy dissipation even outside the barrier in order to accurately predict fusion probabilities for heavy ion reactions.

Contents

List of Figures

List of Tables

Chapter 1

Introduction

1.1 Motivation and overview

The heaviest naturally occurring elements on Earth are Uranium (U), found in large quantities, and Plutonium (Pu), found in very small quantities. To create heavier elements, one must use nuclear reactors or particle accelerators. The creation of heavier elements has already provided great insights about the structure of atomic nuclei and their stability. Models have predicted the possibility of the existence of the superheavy elements (SHEs) associated with nuclear *magic numbers* $Z = 114$, 120, 126 or $N = 184$ [1, 2]. In 2016, the International Union of Pure and Applied Chemistry (IUPAC) announced the extension of the periodic table to include four new SHEs, $Z = 113$, 115, 117, and 118 [3]. These may not be the last elements to be added to the periodic table. The quest to extend the periodic table beyond Oganesson (Og, $Z = 118$) is a topic of great interest in nuclear physics because their synthesis provides us with extreme tests of our understanding of nuclear structure and reaction dynamics.

The formation of SHE ($Z \geq 104$) is very difficult to achieve since the cross sections in SHE synthesis are on the order of picobarns (10^{-12} barns) [4]. Not only it is an extremely challenging task to create these nuclei experimentally, it is also challenging to make a realistic model to describe fusion theoretically, to allow reliable predictions of the optimal reaction to use. Describing collisions of two nuclei, each of which is a complex quantum many body system in its own right, is difficult since their interaction involves many degrees of freedom. Reactions can proceed in many ways in heavy ion reactions. Two key outcomes are fusion and fission. Fusion means that the colliding nuclei merge into a compact single compound nucleus, which is essential for heavy element/SHE synthesis. In fission, the compound nucleus breaks into two fission fragments. In heavy ion reactions, fusion competes with various reaction processes, which makes it difficult to describe the fusion mechanism. Various models of fusion have developed, from macroscopic to microscopic. However, there is no comprehensive model describing all aspects of fusion. The work presented here examines dynamical processes involved in the reactions of heavy ion induced fusion through a series of measurements, with the aim of exploring the influence of energy dissipation on reaction outcomes.

In Section 1.2 and 1.3, the fundamental concept of fusion and how it is treated is presented. Section 1.4 illustrates discrepancies between experimental observations and calculations from the coupled channels model of fusion, which has been used with a lot of success to reproduce experimental data in many reactions, but also shows systematic failings. This motivates the work presented in this thesis; to investigate what has not been included in the coupled channels framework. To find clues, possible reaction channels seen in heavy ion fusion reactions are reviewed in Section 1.5.

1.2 Fusion

Nuclear fusion is commonly defined as the creation of a single compound nucleus (CN) at its equilibrium deformation following a collision of two nuclei. Effectively, fusion is thought of as an act of irreversible energy dissipation, converting the relative kinetic energy of the colliding nuclei into intrinsic excitation energy of the composite nucleus. The idea of irreversible energy dissipation can be well understood from Danish physicist Niels Bohr's illustration of the formation of a CN, shown in Fig. 1.1a [5]. Bohr illustrates that the formation of a CN is associated with sharing of energy. Once an incoming marble (representing a nucleon/projectile nucleus) rolls down into a dish (potential pocket), its kinetic energy is shared by other marbles through collisions. Their individual energies are not sufficient to overcome the potential energy barrier. Thus all marbles are trapped (fusion). In other words, if the energy of the projectile entering the heavy nucleus is

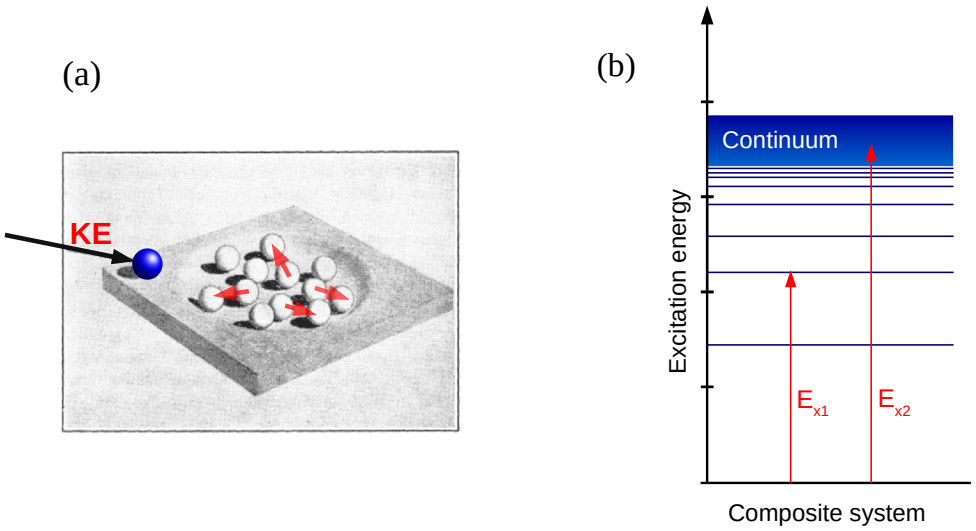

Figure 1.1: (a) The formation of the compound nucleus (CN) is represented as a sharing of the kinetic energy of an incoming marble with all other marbles [5]. In a fusion reaction, (b) the KE of the incoming projectile is converted into excitation energy of the composite system, occurring via energy dissipation. The high energy states form a continuum level density in the CN, which can be associated with irreversibility.

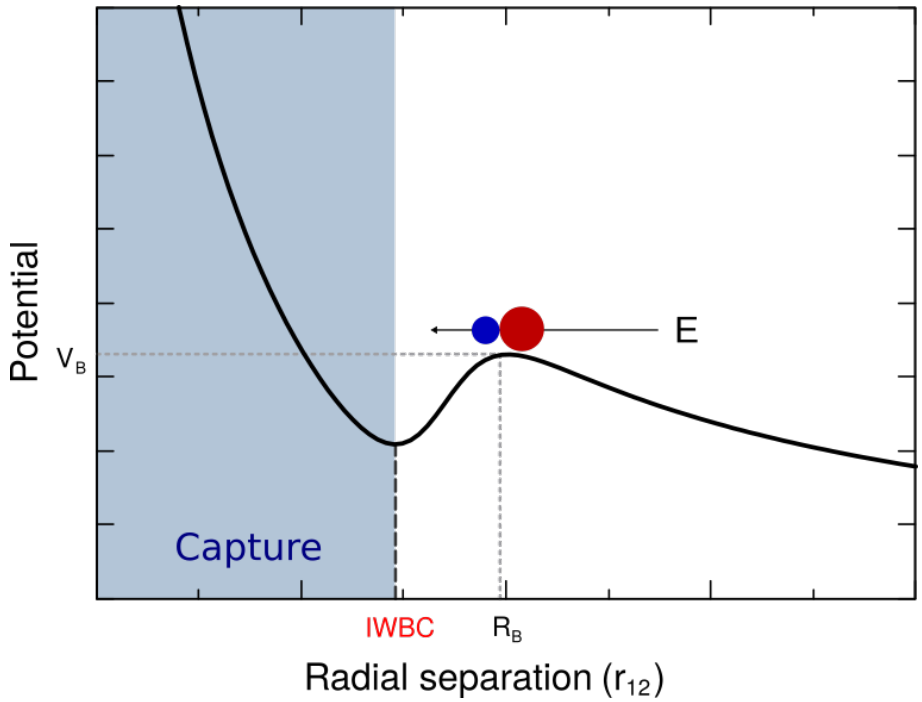

Figure 1.2: The coupled channels framework describes a fusion reaction in terms of the total interaction potential. The shaded area indicates the region of strong absorption (capture) taking place. In order to express the capture process, standard coupled channels models introduce an incoming wave boundary condition (IWBC) at the bottom of the potential pocket [6].

shared between many nucleons, thus converted into excitation energy of the composite nucleus as shown in Fig. 1.1b, the projectile cannot escape from the potential pocket. When captured inside the barrier, constituent nucleons of the projectile and of the target nucleus merge into a single CN, which loses memory of the entrance channel apart from the conserved quantities: energy, linear momentum and angular momentum. In collisions of two heavy nuclei, the initial configuration when the two nuclei touch is far from the equilibrium configuration of the CN. Thus fusion is conceptually divided into *capture* and subsequent shape evolution to the equilibrium deformation (*fusion*).

1.3 Modelling capture

Heavy ion reactions are commonly described by an interaction potential between the colliding nuclei along the direction of their relative motion (r_{12}), as shown in Fig. 1.2. The combination of Coulomb, centrifugal and nuclear potentials forms a barrier at a distance where the repulsive force is equal to the attractive force. Nuclear reactions are strongly dependent on this barrier, highlighting the importance of the energy of the incoming projectile. Capture takes place when the energy is higher than the barrier or, with lower probability, through quantum tunnelling at energies below the barrier.

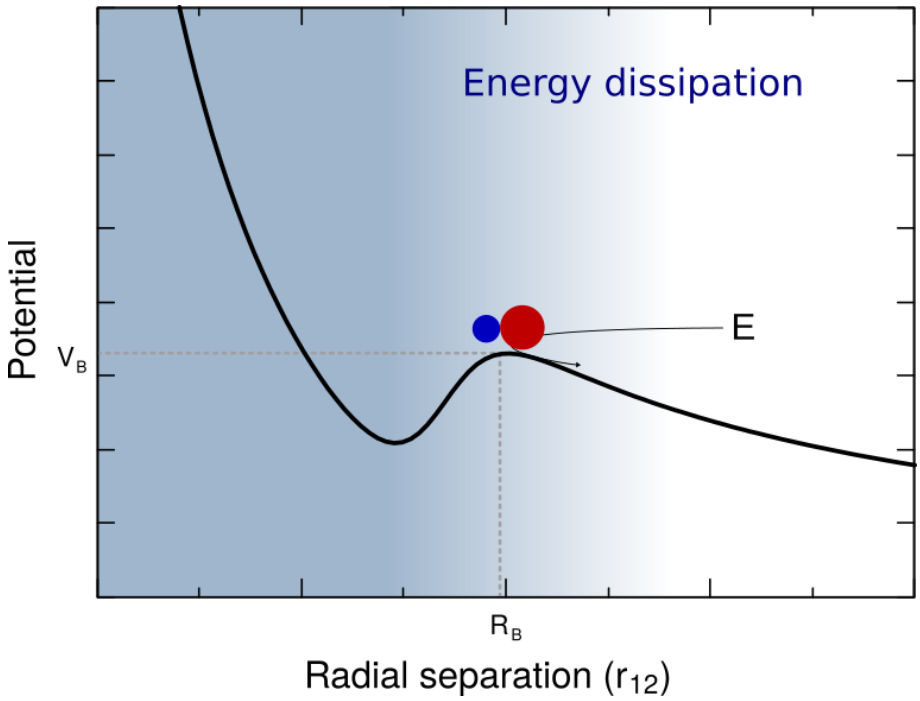

Figure 1.3: Dynamical approach to description of fusion reactions in terms of the total nuclear interaction potential. Various experimental observations support the idea that energy dissipative processes (shaded backgroud) occur at a large separation due to transfer reactions [7].

A successful quantum mechanical approach to nucleus-nucleus collisions is the coupled channels model, providing the most comprehensive explanation of elastic and inelastic scattering and transfer to discrete states [8]. This approach to modelling fusion (discussed in detail in Section 2.2) has been very successful in describing sub-barrier capture/fusion reactions, explaining the experimentally observed phenomenon of cross-section enhancement. In the coupled channels framework [8, 9], capture happens when separation of the colliding nuclei is less than the barrier radius, i.e. inside the potential pocket. Here the projectile is assumed to be completely absorbed into the target nucleus and thus a CN is formed. To make capture irreversible, the model uses a "mathematical trick" by applying an incoming wave boundary condition (IWBC) well inside the fusion barrier radius (R_B), irreversibly removing flux from the external (scattering) region. Therefore, Fig. 1.2 shows a colour-shaded region with a sharp cut-off at the IWBC radius, effectively describing irreversible energy loss well inside the barrier.

However, experiments have shown that dissipation of kinetic energy and angular momentum can occur at larger separations, outside the barrier. Direct evidence of this can be found from the observation of deep inelastic collisions (DICs), in which two nuclei overlap and exchange energy and nucleons [10, 11, 12], resulting in energy dissipation occurring even at energies near the fusion barrier. Recent ANU work [13, 14] shows evidence for energy dissipation at sub-barrier energies, which corresponds classically to separations larger

than the barrier. In Ref. [7], it was suggested that the contribution of DICs in heavy ion fusion reactions can lead to a coexistence between reversible (channel-coupling) and irreversible (thermalization) processes, resulting in a gradual transition occurring from a large radial separation, shown in Fig. 1.3 [7, 15], rather than a sharp transition shown in Fig. 1.2.

The absence of explicit irreversible energy dissipative processes in the coupled channels framework results in predictions that are inconsistent with observation in certain cases, in particular, for reactions at above-barrier energies. An example measured in ANU is discussed in the following section.

1.4 Suppression of fusion

The coupled channels (CC) approach has been a standard tool in analysing heavy ion reactions at energies near the fusion barrier, giving a comprehensive framework to calculate elastic and inelastic scattering, transfer reactions and fusion, and has been used successfully in reproduction of experimental data. This model explicitly considers the role of nuclear structure in collisions between nuclei in calculating fusion (capture) cross sections. ^{16}O reactions with Sm isotopes at near barrier energies are exemplary. In these, reactions of relatively light nuclei, capture is considered to be equivalent to fusion, since the projectile mass is expected to be absorbed by the target, resulting in a compact CN with unit probability following capture [16, 17, 18]. The enhancement of fusion cross sections in these reactions has been well understood in terms of the nuclear structure of the target nuclei. Despite its success at near-barrier energies, in several reactions there are inconsistencies between observations and model calculations, notably hindrance of fusion cross sections at deep sub-barrier energies [19, 20] and well above the barrier [15, 21]. In particular, this work is interested in the hindrance phenomenon at energies above the fusion barrier.

For the reaction ^{16}O + ^{208}Pb, CC calculations with a standard nuclear potential diffuseness (0.65 fm) overestimate fusion cross sections at energies above the fusion barrier, as shown in Fig. 1.4a [19, 22]. This reaction is not unique; in the systematic study of fusion suppression phenomena shown in Fig. 1.4b, suppression factors (S: ratio between experiments and model calculations) increase with an increase in the charge product (Z_1Z_2) [15]. This disagreement between the coupled channels calculations and measurements was suggested to be linked to the contribution of DICs, which are not included in the coupled channels framework [15]. In Ref. [15], it was suggested that an enhancement in DICs with increasing Z_1Z_2 may be responsible for the large suppression factor. If so, any observable outcomes resulting from the onset of dissipative processes would need to be taken into account in models describing the fusion process in heavy-ion reactions. Until the importance of dissipative processes in fusion is known, the quantitative role these processes play

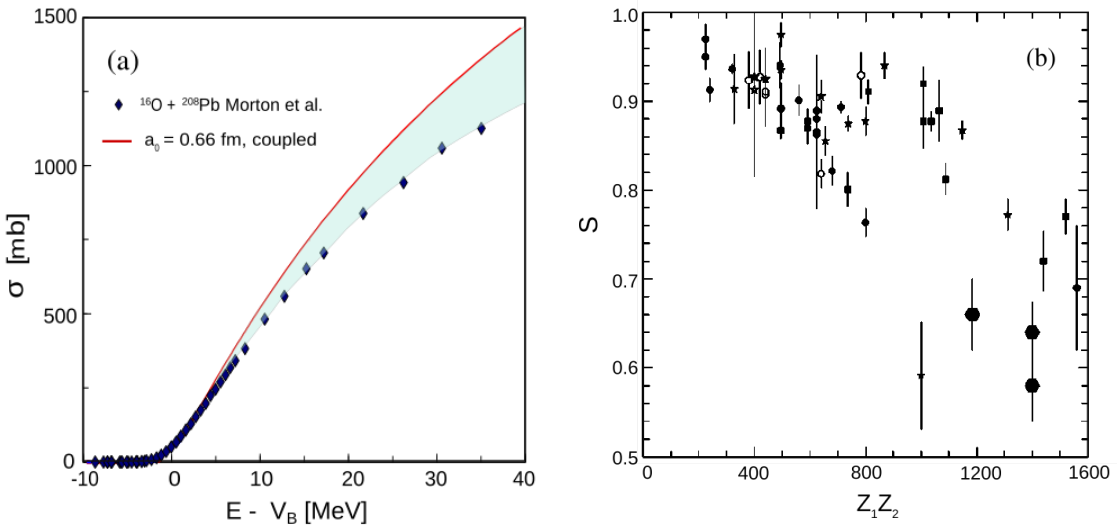

Figure 1.4: (a) A comparison of experimentally measured fusion cross sections (points) with coupled-channels calculations (red-line) for ^{16}O + ^{208}Pb [19]. Adapted from Ref. [19]. (b) Fusion suppression factors (S) with respect to model expectation as a function of the charge product (Z_1Z_2) for 46 different reactions at energies above their average fusion barriers. As Z_1Z_2 increases, fusion suppression increase [15]. Adapted from Ref. [15].

in reaction outcomes is not well understood.

The role of energy dissipation in quasi-elastic and deep inelastic processes has been studied at the Istituto Nazionale di Fisica Nucleare (INFN) in Italy by L. Corradi et. al. [23, 24]. The group compared the cross sections of multi-nucleon transfer channels with the results of the semi-classical code GRAZING [25] and found reasonable agreement. Within this semi-classical model, deep inelastic processes reduce the fusion cross sections as we observed experimentally at the ANU. However, channel couplings effects, important for near-barrier fusion, cannot be treated exactly in a semi-classical model.

In order to include energy dissipation explicitly into quantum models of fusion, it is crucial to understand dissipative mechanisms. One factor that is considered to be important in shaping the influence of the dissipation process on reaction outcomes is the density overlap of colliding nuclei; this influences the probabilities of nucleon-nucleon interactions that can result in conversion of kinetic energy and angular momentum of relative motion into thermal excitation energy, particularly of the heavy product.

One reaction mechanism that could result in energy dissipation is nucleon (or cluster) transfer. The heavy target-like nucleus may be excited by nucleon transfer to high excitation energy [26]. Transfer probabilities, in particular, are strongly affected by nuclear density overlap. Recent experiments [14] addressing this issue motivate this research project. Thus, the present work aims to expand on the investigation of the role of energy dissipation in heavy ion reactions by measuring the products of transfer reactions that lead to thermalization of the heavy reaction product, as well as measuring fusion cross

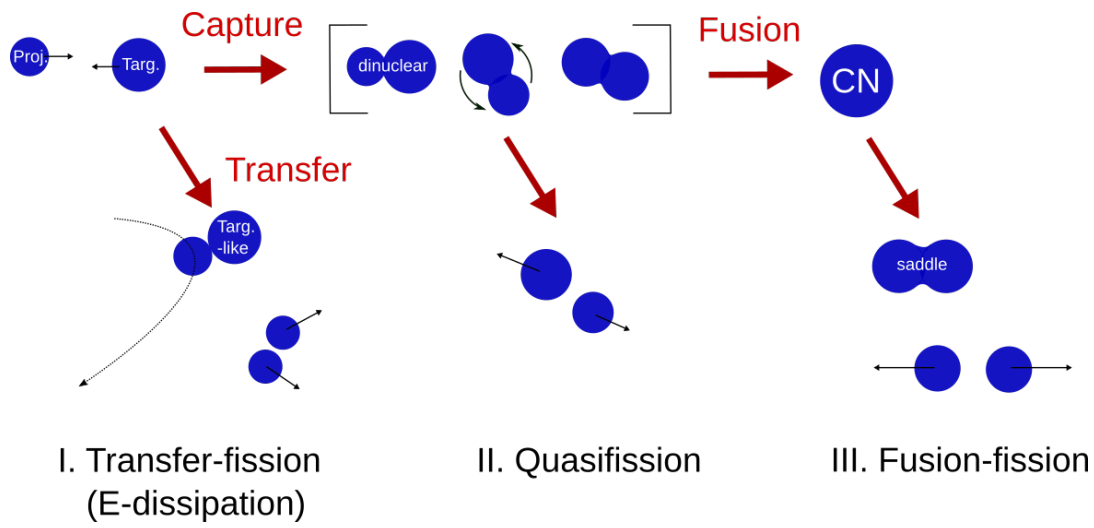

Figure 1.5: Schematic illustration of possible reaction channels seen in fusion reactions on actinide target. Fission can take place either before and after the capture reaction. Fission occurring prior to capture through transfer reactions is a signature of energy dissipation. After capture, QF can strongly compete with fission following fusion.

sections.

1.5 Outcomes of heavy-ion fusion reactions.

One way to study the two reaction outcomes of transfer and fusion in the same experiment is to exploit collisions in which both of these processes can lead to fission. Reactions with fissile targets (actinide nuclei) like Thorium (Th) and Uranium (U) are thus indicated, since the low fission barriers ($\sim$ 6 MeV [27, 28]) allow fission following both transfer and fusion. Fig. 1.5 shows the various processes that can lead to fission which can be observed in reactions on actinide target nuclei. Forming evaporation residues (ERs) following the compound nucleus (CN) formation is unfavourable decay mode. The first decay mode is fission of the target-like (heavy) nuclei after transfer reactions. Because of the low fission barrier, the exchange of nucleons between the colliding nuclei can result in excitation energies higher than the fission barrier. If this energy is shared amongst the nucleons of the heavy nucleus (thermalized), then fission can occur. Therefore, the observation of transfer-induced fission is a signature of the occurrence of energy dissipation. If the projectile is completely absorbed into the target nucleus, it forms a compact equilibrated compound nucleus (fusion).

Fission may occur after contact but before complete fusion, and is called quasifission (QF). It is a non-equilibrium dynamical process resulting in the rapid fission-like decay of the dinuclear system formed after capture of two colliding nuclei; the system fails to form a fully equilibrated CN. As the charge product of the reaction ($Z_1 Z_2$) increases, formation of a compact CN after capture is less likely due to an increase of the QF contribution

[29, 30, 31, 32]. The onset of QF [33] was predicted when $Z_1Z_2 > 1600$, but recent studies and observations including this work have found QF at Z_1Z_2 much less than 1600. Therefore, fusion suppression as a result of QF also needs to be taken into account in heavy element synthesis reactions. QF only results following capture, thus the sum of QF and fusion-fission is a good representation of the capture cross section, since the ER cross sections are negligible. Details of QF properties and methods for capture cross section determination depending on the presence of QF in reaction outcomes will be discussed in Chapter 2.

1.6 Aims

This thesis is aimed at understanding the fusion reaction mechanism and, in particular, the role of energy dissipation in heavy ion fusion reactions, by going beyond existing work through simultaneously measuring both the deep inelastic processes and capture cross-sections for the same systems. Measuring fission following transfer ensures that the kinetic energy has been dissipated into internal excitation (thermalisation) sufficient to overcome the $\sim$ 6 MeV fission barrier. The probabilities of transfer fission reactions are compared with capture reactions as a function of charge product. Since QF strongly competes with fusion with increasing charge product, investigation of the QF contribution is carried out as well due to the difficulty of fully separating QF from fission following fusion.

1.7 Outline of thesis

Chapter 2

This chapter gives an overview of the theoretical descriptions of heavy ion fusion reactions relevant to this work. In addition, the theoretical background for the capture cross section determination is described.

Chapter 3

This chapter describes the experimental methods used at the Heavy Ion Accelerator Facility at the Australian National University, from the beam production to the measurement of binary reaction products.

Chapter 4

The chapter details the procedure of reconstructing binary events using measured time of flight and position information. Fission event selection criteria are discussed. The kinematic properties of different types of fission events are illustrated.

Chapter 5

This chapter shows the features of fission following capture and transfer reactions and the contribution of transfer-fission as a function of $Z_1 Z_2$.

Chapter 6

In this chapter, the steps in determination of the total capture cross section are described. These are reaction-dependent, and are classified by the mass-angle correlations observed in mass-angle distributions.

Chapter 7

The quantitative suppression of capture by dissipative process is investigated through a comparison of experimental capture cross sections and coupled channels calculations. The chapter summarises the work presented in this thesis.

Chapter 2

Background Theory

Overview

Since the early 1990's, experimental techniques have been developed to allow precise ($\sim$ 1%) measurements of heavy ion capture cross sections. Driven by these advances, the coupled channels approach to model capture was refined in various ways to reduce the number of approximations that has been in use previously. However, to date, no models have been able to satisfactorily predict fusion cross sections for all reactions at energies both above and below the barrier, suggesting that a new understanding of capture and processes competing with capture is needed. In this chapter, two relevant existing models of capture will be presented. Additionally, theoretical inputs to the total capture cross section extraction will be outlined here.

Models of fusion

2.1 Single barrier penetration model

2.1.1 Nucleus-Nucleus Potential

The interaction between two colliding nuclei -the projectile and target- is usually described by an interaction potential, formed by the combination of a long-range repulsive Coulomb potential (V_{coul}), a short-range attractive nuclear potential (V_{nuc}), and a repulsive centrifugal potential (V_l) if there is relative angular momentum ($l\hbar$). The centrifugal potential represents the energy required to conserve angular momentum along the trajectory. These are shown in Fig. 2.1. The total internuclear potential is the sum of these potentials, expressed as a function of radial separation (r) between the centres of the two nuclei:

$$V_{tot}(r) = V_{nuc}(r) + V_{Coul}(r) + V_l(r) \tag{2.1}$$

The strong attractive force starts to act on the colliding nuclei when their surfaces are close to each other. The nuclear potential is typically assumed to take a Woods-Saxon form [34], which is characterised by the surface diffuseness parameter a_0, a potential depth

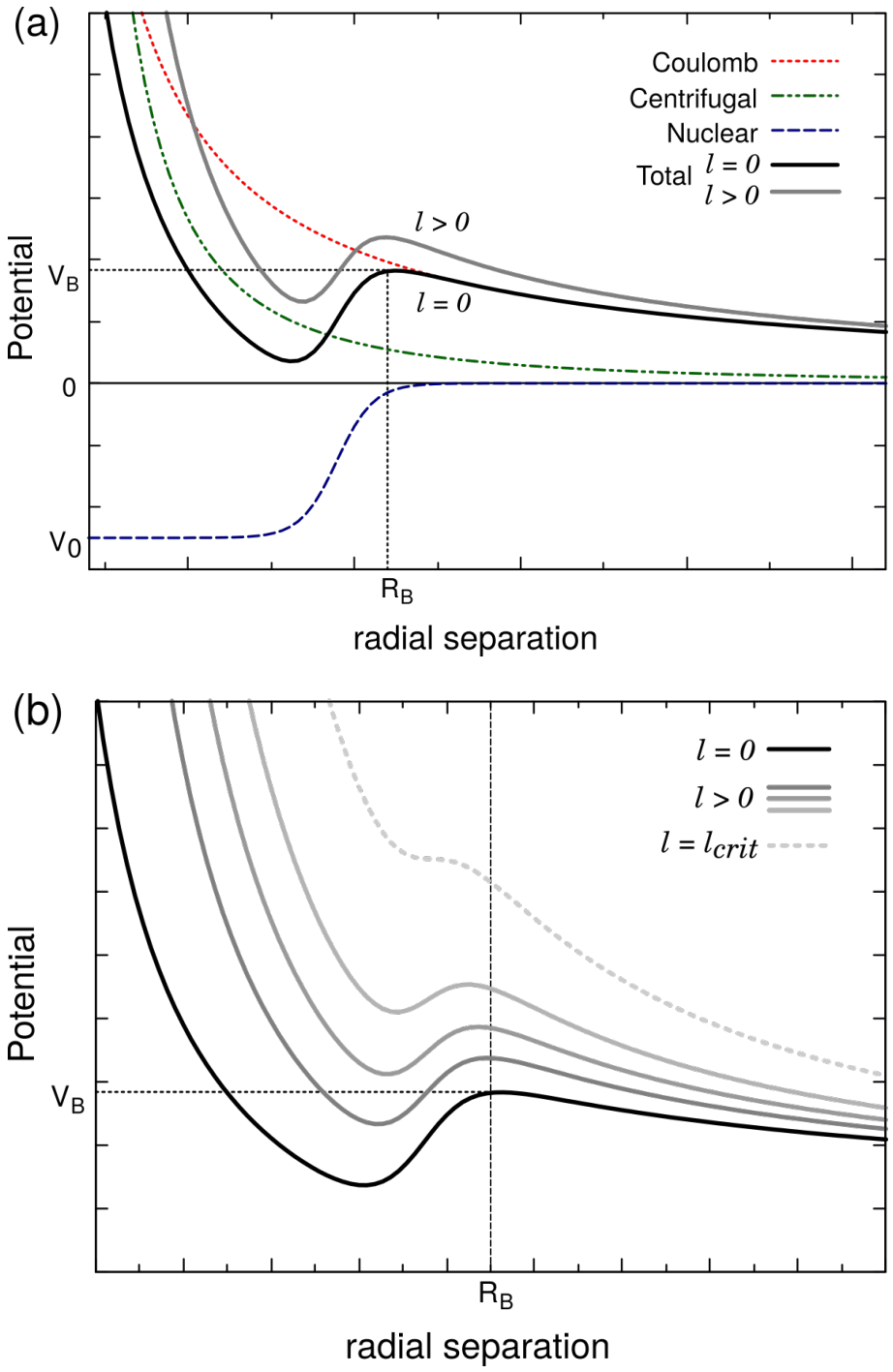

Figure 2.1: (a) Illustration of the total internuclear potential between the colliding nuclei as a function of the relative distance resulting from Coulomb repulsion (red dashed), short-range nuclear attraction (blue long dashed) and centrifugal repulsion (green double dot dashed) if $l > 0$. The Coulomb barrier is formed when the repulsive force is equal to the attractive force (a local peak showing up on the total potentials). R_B is the barrier radius. Panel (b) shows the variation of the total internuclear potential along l. As l increases, the barrier increases and the potential pocket becomes shallow and eventually vanishes at a critical angular momentum (l_{crit}).

V_0 , and the radius parameter r_0. It is given by:

$$V_{nuc}(r) = \frac{-V_0}{1 + \exp[(r - R_0)/a_0]} \tag{2.2}$$

R_0 can be related to the sum of the colliding nucleus radii, $R_0 = r_0(A_1^{1/3} + A_2^{1/3})$, and r_0 is thus expected to be ~ 1.2 fm [34, 35]. A typical diffuseness parameter $a_0 = 0.65$ fm is well accepted to reproduce elastic scattering [35]. However, a relatively higher a_0 is needed to fit heavy ion capture data [36, 37], which has helped to motivate this study.

The simplest expression for the Coulomb potential between two nuclei separated from each other ($r > R_0$) is given by:

$$V_{Coul}(r) = \frac{e^2}{4\pi\epsilon_0}\frac{Z_1 Z_2}{r} \tag{2.3}$$

where $Z_{1,2}$ are the nuclear charges of the colliding nuclei.

For non-head on collisions where the collision motion involves not only radial motion but also angular motion, the centrifugal potential is non-zero and is expressed as:

$$V_l(r) = \frac{l(l+1)\hbar^2}{2\mu r^2} \tag{2.4}$$

where $l\hbar$ is the orbital angular momentum and μ is the reduced mass, $\mu = \frac{A_1 A_2}{A_1 + A_2}$.

The sum of the three potentials forms a potential barrier - a local peak at a barrier radius R_B as shown in Fig. 2.1a. This is commonly known as the Coulomb (or capture) barrier (V_B): inside the barrier is a potential pocket where the projectile is considered to be irreversibly captured by the target. The height of the barrier varies depending on the angular momentum, as shown in Fig. 2.1b; as l increases, the barrier height increases and the potential pocket gets shallower, eventually vanishing at a critical value of l_{crit}.

2.1.2 Capture cross section

The yield of capture is expressed in terms of the cross section. The classical picture of the single barrier passing model is a simplistic way to approach a complex heavy ion fusion reaction and define the cross section. It neglects the dependence of the barrier radius on l, the effects of the intrinsic degrees of freedom of the two colliding nuclei, and the influence of competing reaction channels. The expression for the fusion cross section is:

$$\sigma(E) = \begin{cases} \pi R_B^2(1 - \frac{V_B}{E}) & for \quad E \geq V_B \\ 0 & for \quad E > V_B \end{cases} \tag{2.5}$$

where R_B is the radius of the $l = 0$ barrier and fusion is of course forbidden at energies below the barrier. It predicts that capture cross sections are inversely proportional to the

energy, with intercept V_B and slope πR_B^2.

This classical approach has shown success in describing capture/fusion cross sections measured with precision not better than 5%, and at energies above the barrier for the range $l < l_{crit}$ and some light projectile reactions [38, 39]. It is, however, not appropriate for reactions at energies near and below the barrier where the barrier penetration becomes an important pathway to fusion. To include this, it is necessary to treat the problem quantum mechanically. The quantum mechanical approach introduces a transmission coefficient, which represents the barrier penetration and reflection probability. The quantum mechanical definition for the cross section is given in angular momentum space as:

$$\sigma = \frac{\pi}{k^2} \sum_{l=0}^{\infty} (2l+1) T_l(E) \tag{2.6}$$

where k is a wave vector ($k = 2\pi/\lambda$, λ is the de Broglie wavelength), l is the angular momentum, and T_l is the transmission coefficient for a given l, which can be calculated using the parabolic barrier approximation or the Wentzel-Kramers-Brillouin (WKB) approximation [40, 41].

However, a range of heavy ion fusion experiments in the 1970s and 1980s found that measured fusion cross sections at near and sub-barrier energies were orders of magnitude larger than expected from quantum tunnelling using the single barrier penetration model. This enhancement of fusion below barrier revealed that the structure of the colliding nuclei plays an important role in fusion reactions [16, 17, 18]. The effect of nuclear structure of the colliding nuclei is taken into consideration in using the coupled channels method, as discussed below.

2.2 Coupled channels model

The most successful approach for describing heavy ion capture reactions based on quantum mechanics is the coupled channels (CC) method. This includes the coupling between the relative motion and the intrinsic degrees of freedom of the colliding nuclei, in particular static deformation, collective vibrations and nucleon transfer [6, 8, 42].

The colliding nuclei are described as being in a coherent superposition of intrinsic states, which typically include the ground state and low-lying collective states, vibration and rotation, as they approach the fusion barrier. The models do not explicitly account for the irreversible energy dissipation that occurs in capture. Instead, the CC equations are solved by imposing an incoming wave boundary condition (IWBC) which represents irreversible absorption inside the barrier radius [6]. CC models successfully reproduced the fusion enhancement observed at near-barrier energies. The CC approach led to the wide use of the barrier distribution concept, which is useful in understanding the fusion process [18].

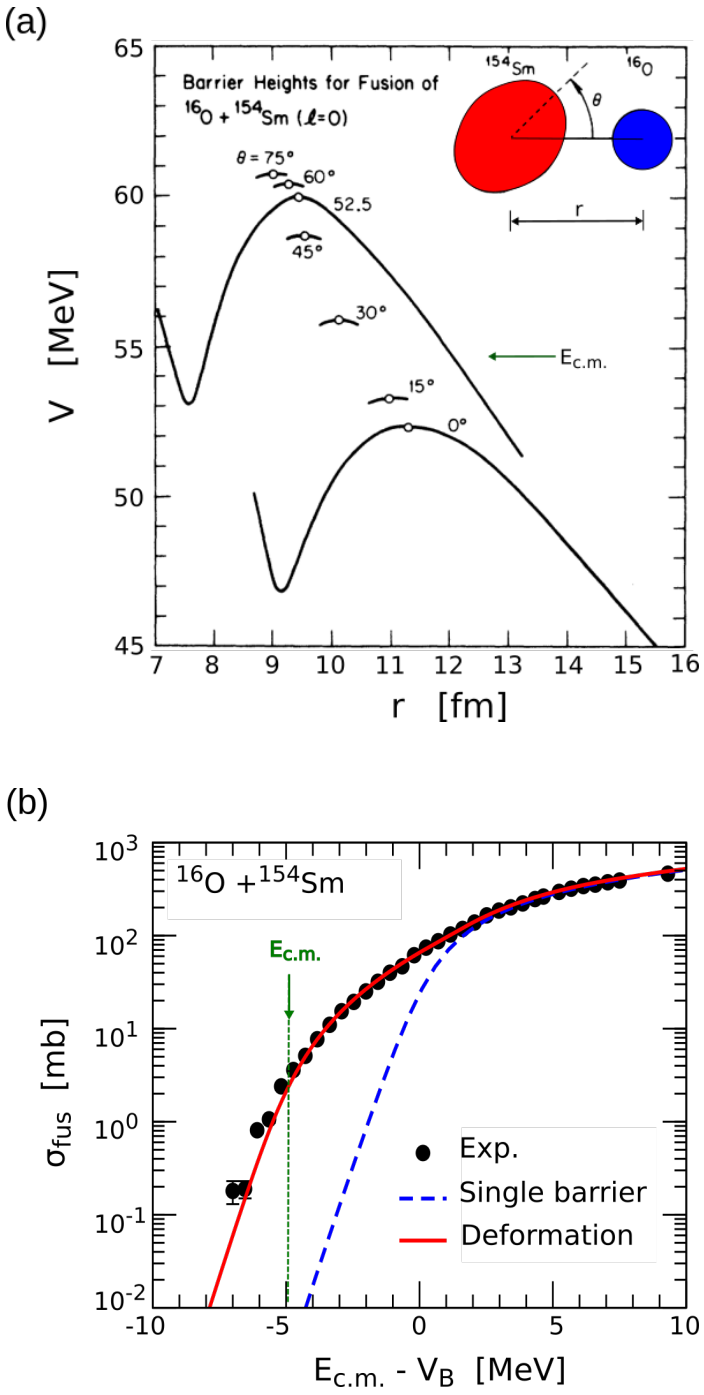

Figure 2.2: The reaction of ^{16}O on ^{154}Sm shows how nuclear structure plays an important role in fusion reactions. (a) The mutual orientation of the colliding nuclei results in a barrier distribution. Even though the incident beam energy is lower than the average barrier $V_B = 59$ MeV, it is higher than the barriers for the deformation-aligned (tip) collisions, resulting in an enhancement of fusion cross sections. Adapted from Ref. [43]. (b) Comparisons of measured fusion cross sections for ^{16}O + ^{154}Sm with calculations based on single barrier penetration (blue dashed line) and with deformation (red line) as a function of energy with respect to V_B. Adapted from Ref. [6].

The barrier distribution concept can be most easily understood by considering reactions with deformed nuclei. The reaction of ^{16}O (spherical projectile) + ^{154}Sm (well deformed target) is a well-known example demonstrating the effect of the different orientations of the ground state deformed nucleus relative to the projectile nucleus. This results in a distribution of barrier heights, as shown in Fig. 2.2a [18, 43, 44]. The radius of the barrier varies with the angle θ between the line joining the centres of the two nuclei and axis of symmetry of the deformed target. As θ increases from $\theta = 0°$ to 90° (decreasing distance) the barrier height increases; $\sim$ 59 MeV is the average Coulomb barrier for this reaction. Even if the incident energy ($E_{c.m.}$) is lower than the average barrier, passing over the lower barriers leads to capture, and in this reaction will subsequently lead to fusion, resulting in the enhancement of fusion cross sections, as shown in Fig. 2.2b.

Various sub-barrier reactions have been successfully described by the coupling effects of intrinsic degrees of freedom of the colliding nuclei, with observed fusion cross sections being reproduced with CC models [18, 44, 45]. However, there are some inconsistencies in the CC approach, indicating the possibility of missing physics in the model. CC calculations using a typical diffuseness parameter ($a_0 \sim 0.65$ fm) obtained from elastic scattering data overestimate fusion cross sections at energies both well-above the fusion barrier [46, 47] and at deep sub barrier energies [14, 48, 49]. This fusion hindrance has been tenatively linked to the absence of other energy dissipative processes in the CC framework exemplified by deep inelastic collisions. In this work, the contribution of energy dissipative process on capture at energies above the barrier is investigated.

Theoretical background to capture cross section measurements

Models of capture are tested by precise measurements of capture cross sections (σ_{cap}). In this work investigating reactions of a range of projectiles with ^{232}Th (fissile nucleus), the cross sections can be determined by the measured fission cross sections (σ_{fis}) following capture as the production of evaporation residues (ERs) is negligible for the systems studied in this work (i.e. $\sigma_{ER} \sim 0$). To obtain the total fission yield following capture, it would be ideal to measure fission cross sections over all angles. In practice, it is not possible to measure very close to the beam direction. Thus, angular distributions (i.e. $\frac{d\sigma}{d\Omega}$) are measured over a subset of solid angles (dΩ). One then uses theoretical $\frac{d\sigma}{d\Omega}$ distributions to extrapolate to angles close to the beam axis. The total cross section is then obtained by integrating the $\frac{d\sigma}{d\Omega}$ function obtained from the fit. In the following sections, model inputs needed to obtain capture cross section for two different scenarios are presented.

Note that if the reaction products dominantly result from fission following fusion (FF), then $\sigma_{cap} \simeq \sigma_{FF}$. If reaction outcomes include the products of QF, $\sigma_{cap} \simeq \sigma_{FF} + \sigma_{\mathrm{QF}}$, since

the full energy damping and evolution towards mass symmetry should not occur when the radial separation is smaller than that of the capture barrier.

2.3 Transition state model (TSM) for fusion-fission

A simple approach is applied to describe fission following a reaction in which a compact compound nucleus (CN) is formed. The decay of a CN by fission is usually described in terms of the transition state model (TSM) [50, 51]. In this approach, the highly deformed nucleus at the fission saddle-point configuration is considered to be a transition state between the equilibrium CN shape and the scission configuration.

According to the TSM, the angular distribution of fission fragments resulting from the fissioning system passing over the saddle configuration can be determined by three quantum numbers as shown in Fig. 2.3: J, the total angular momentum; K, the projection of J on the nuclear symmetry (fission) axis; and M, the projection on the space-fixed axis.

The model assumes that the fission fragments separate along the nuclear symmetry axis (= fission axis) and that the direction of this axis is unchanged as the system evolves from saddle to scission and separation. Although the composite system experiences dynamic changes in shape, the quantum numbers J and M are conserved in the entire fission process (neglecting particle evaporation) and K is taken to be determined at the saddle point. The fission angular distribution $W^J_{M,K}(\theta)$ is expressed as a function of the quantum numbers through $|D^J_{M,K}(\theta)|^2$, the symmetric-top wave functions, which depends on scattering angle θ with respect to the beam axis:

$$W^J_{M,L}(\theta) = [(2J+1)/2]|D^J_{M,K}(\theta)|^2 \ . \tag{2.7}$$

In this case, M is the projection of J on the beam axis (z).

For the simplest application of Eq. 2.7, it is assumed that $M = 0$, which is the case of the projectile and target nuclei have zero spins (true for all the reactions considered here) and no particle emission occurs before scission. A reduced equation for the fission angular distribution for the fission of spin zero nuclei including the contribution of all J leading to CN formation is given by Ref. [50]:

$$W(\theta) = \sum_{J=0}^{\infty}(2J+1)T_J \sum_{K=-J}^{J} \rho_J(K)|D^J_{0,K}(\theta)|^2 \tag{2.8}$$

where T_J is the transmission coefficient for fusion of partial wave J and $\rho_J(K)$ are the density of levels at the transition state with the assumption of a Gaussian K distribution

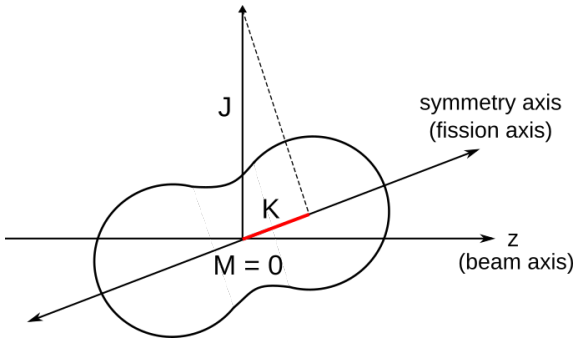

Figure 2.3: A schematic view of the angular momentum vectors at the saddle configuration for describing the fission angular distribution. In the TSM, the angular distribution of fission fragments splitting along the nuclear symmetry axis can be expressed as a function of two quantum numbers, which are the total angular momentum J and the projection of J onto the fission axis K at the saddle point if $M = 0$ (M is the projection of J on a space-fixed axis, here the beam axis).

given by

$$\rho_J(K) \propto \begin{cases} \frac{\exp(-K^2/2K_0^2)}{\sum_{K=-J}^{J} \exp(-K^2/2K_0^2)}, & \text{if } K \leq J. \\ 0, & K > J. \end{cases} \tag{2.9}$$

where K_0 is the variance of the K-distribution. The distribution of K, characterised by K_0^2, can be estimated from the properties of the fissioning system at the saddle-point, taken to be the transition state. Thus K_0^2 is given by:

$$K_0^2 = \frac{T\Im_{eff}}{\hbar^2} \tag{2.10}$$

where $\Im_{eff}$ is the effective moment of inertia and T is the temperature of the CN at the saddle point. These quantities are not necessarily well-known, so K_0 is treated as a fitting variable in this work.

This approach can be used to define the functional form for $W(\theta)$. Reproducing the experimental data taken over a restricted range in θ allows the extraction of the total fission cross section. Experimental fission angular distributions have been compared with calculations based on the TSM formalism, and successful fitting has been achieved for a range of measurements of heavy ion induced fission reactions [18, 52]. However, the assumption employed for the expression of the fission angular distribution in the TSM is that the direction of the projectile nucleus is '*forgotten*' [50]. In practice, this is true if the fissioning system evolves from a compact CN.

To determine cross sections for faster reactions following capture, that do not lead to CN formation but rather to QF (where a '*memory*' of the projectile mass and direction is often retained) [53], a different approach has been developed, which is presented below.

2.4 Dynamical approach for quasifission

After capture, a dinuclear nuclear system can evolve in shape to form a compact equilibrated compound nucleus (CN), or decay into fission-like (QF) events before forming a compact CN. The competition between the two processes has a complex dynamical nature. Quasifission becomes increasingly probable as the charge product of the colliding nuclei increases, and competes strongly with fusion, as discussed in Chapter 1. Experimentally, it is impossible to unambiguously separate event-by-event QF events from fission events following fusion because of their similar kinematic characteristics. Both reactions give binary reaction outcomes with full momentum transfer (FMT) and overlapping distributions. However, the angular distributions of fission fragments resulting from complete fusion generally differ from those of QF. Therefore, using the TSM for the angular distribution extrapolation may be no longer valid if the reaction products include QF yields, due to the violation of the fundamental assumption of the TSM, as discussed above. Currently, there are no reliable predictive models to describe QF angular distributions and thus an empirical approach is needed for systems in which the TSM is inappropriate to use because of the presence of QF products. For this, an empirical model called 'Quasisim' was used. Quasisim is a Monte Carlo calculation based on a phenomenological approach [30, 54]. The features of Quasisim, including how QF is modelled in terms of reaction timescales, are presented below.

2.4.1 Modelling quasifission: reaction timescales

Unlike the processes of fusion, in which the dinuclear system loses all memory of the reaction entrance channel, QF reactions can display a memory. Quasifission ($< 10^{-20}$ s) is faster than fusion-fission ($> 10^{-20}$ to 10^{-16} s) [54] and is therefore, strongly dependent on the entrance channel properties, such as Z_1Z_2 in the entrance channel, deformation alignment, nuclear structure, magicity, and the N/Z ratios of the colliding nuclei [55].

One method to gain information on reaction timescales is to investigate the correlation between fission fragment masses and their corresponding emission angles, known as the mass-angle distribution (MAD). The MAD directly reflects the dynamical evolution of the dinuclear system. The evolution of the dinuclear system with sticking time (t_s) is shown graphically in Fig. 2.4a. It illustrates that once an incoming projectile (blue) collides with a target nucleus (red) and sticks, the dinuclear system evolves while rotating. The longer the system sticks together, the larger the angle of rotation, and the more the masses of the constituents drift toward mass-symmetry, as shown in Fig. 2.4b. Eventually, after more than one rotation of the system, mass equilibrium is reached, resulting in a fission fragment mass distribution centred on symmetry, and the emission angle becomes uniformly distributed. Therefore, the presence of a correlation between masses of fragments and their emission angles in the MAD is a signature QF with a timescale less than one

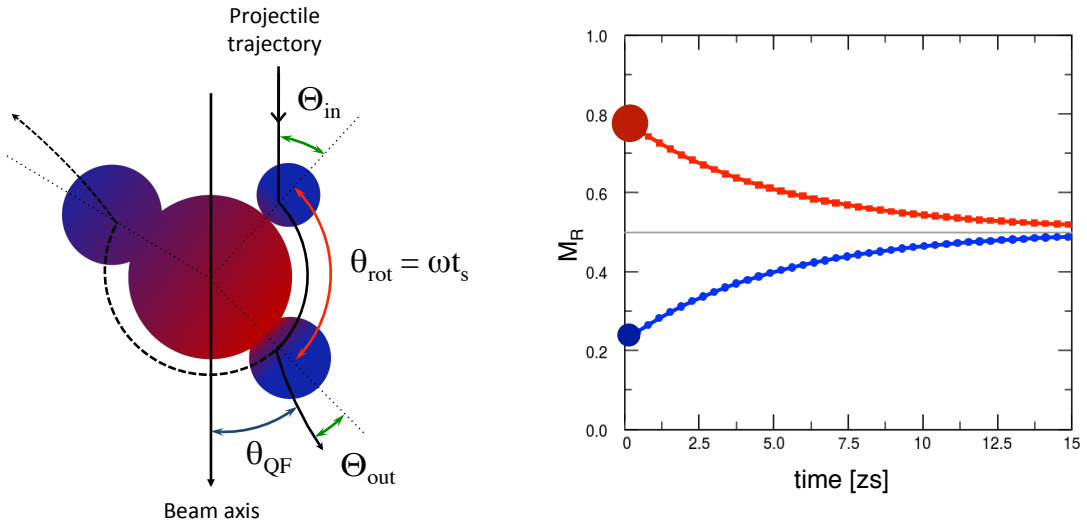

(a) Emission angle

(b) Mass drift

Figure 2.4: Schematic view of the evolution of the dinuclear system. (a) Three different evolution stages are shown, depending on sticking time (t_s) and rotation speed (ω). The observed emission angle (θ_{QF}) is determined by angles associated with the Coulomb trajectories for the incoming and outgoing nuclei (Θ_{in} and Θ_{out}) and the rotation angle (θ_{rot}). Adapted from Ref. [54]. (b) Schematic picture of the mass drift towards mass symmetry with time [30]. For projectiles heavier than oxygen, mass is generally transferred from the heavy to the light nucleus.

rotation time, and provides quantitative information on QF timescales. Fig. 2.5 shows schematically the trajectory of fission fragments on the MAD plot for a single angular momentum, along with sketches of the dinuclear system′s evolution in mass and rotation angle in the centre-of-mass frame over time.

The MAD is thus a good tool for investigating QF occurring with a time range between 10^{-21} and 10^{-20} s where the correlation between mass and angle of QF fragments is visually distinguishable from that of fusion-fission fragments. For longer QF times, the observed MAD may not show a correlation but an angular distribution still can show a difference from fusion-fission expectations calculated in the framework of the TSM [26].

2.4.2 Quasisim: mapping quasifission timescale

The simulation of QF populating the MAD is achieved through the Monte Carlos method, parameterizing the variables that influence the MAD. Below, the physical ingredients of the model and parameterizations used in this work are presented. Simulated MADs that describe the angular distributions of QF over the measured range allow extrapolation to angles closes to the beam direction. The adjustment of parameters and a detailed quantitative comparison between measured and calculated MAD will be given in Chapter 6.

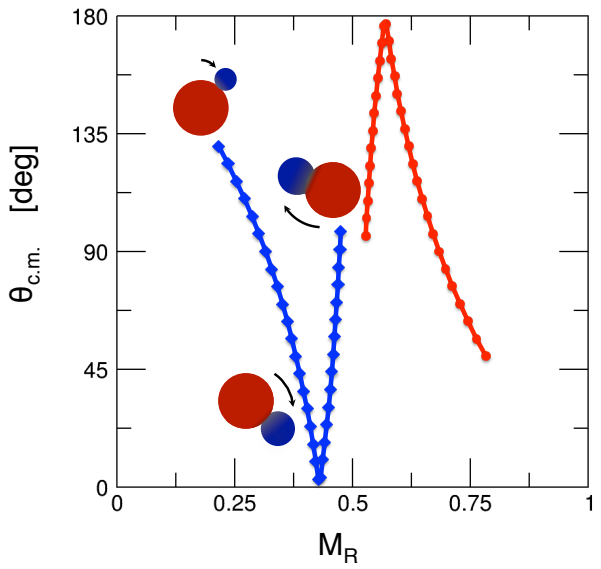

Figure 2.5: A trajectory of the dinuclear system evolving with time for a single angular momentum in a plot of mass ratio (M_R) *vs* scattering angle ($\theta_{c.m.}$). The longer the constituents stick together, the further the system approaches mass-symmetry ($M_R = 0.5$). The blue line is the trajectory of the projectile-like fragment and the red line is for the target-like fragment. Adapted from Ref. [54].

2.4.2.1 Determination of the emission angle in the centre of mass frame

The observed emission angle (θ_{QF}) of a projectile-like fission fragment, based on Ref. [30], is determined by these variables:

$$\theta_{QF}(t_s) = \pi - [\Theta_{in} + \theta_{rot}(t_s) + \Theta_{out}] \tag{2.11}$$

where $\theta_{rot}(t_s)$ is the rotation angle of the system while they stick together, and Θ_{in} and Θ_{out} are the angles associated with the classical Coulomb trajectories for the incoming and outgoing nuclei. Being a binary process, the target-like fragment is formed at the complementary angle ($\pi - \theta_{QF}$).

Details of angles related to Coulomb trajectory calculations are given in Appendix A. The rotation angle during the sticking time (t_s) between contact and scission is estimated from the relationship between the angular velocity ω and the sticking time t_s, $\theta_{rot} = \omega \times t_s$. Expressing the angular velocity in terms of J, the orbital angular momentum in the collision and $< I >$ the average moment of inertia during the sticking time, gives the rotation angle:

$$\theta_{rot}(t_s) = \frac{\sqrt{J(J+1)}\hbar}{< I >} t_s \ . \tag{2.12}$$

Each of the components in Eq. 2.12 is determined as detailed below in order to calculate the simulated MAD:

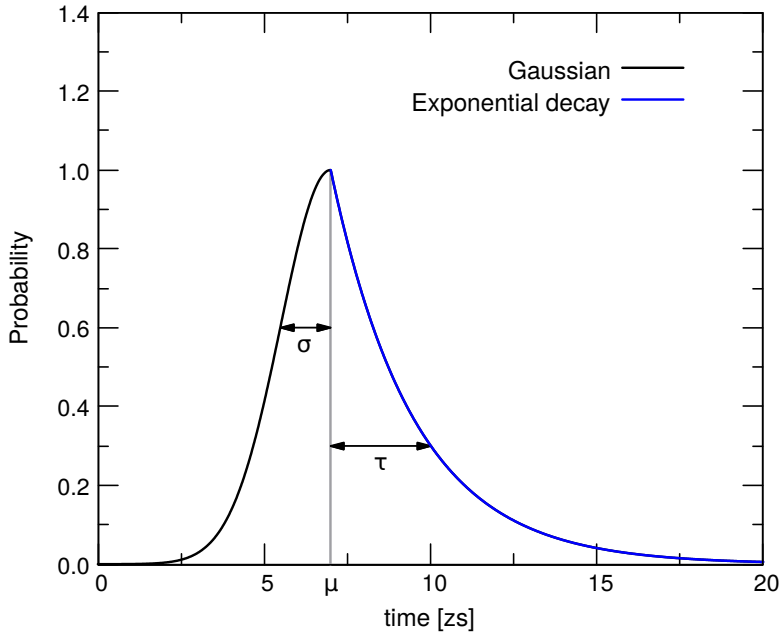

Figure 2.6: An empirical sticking time distribution used to simulate QF. It is assumed a half Gaussian function followed by an exponential fall and is parametrised with peak position (μ), width (σ) and decay time (τ).

1. Angular momentum distribution

   Angular momentum distributions were obtained through the capture partial wave cross sections σ_l calculated with a CC code such as CCFULL [6] or CCMOD [56]. These codes can provide the angular momentum distributions for each beam energy. In Quasisim, the angular momentum of each event is randomly chosen and weighted by the angular momentum distributions.

2. Sticking time distribution

   The sticking time is parameterized as a distribution rather than a single value. The assumed general form of the sticking time distribution is a half-Gaussian followed by an exponential decay [54], as shown in Fig. 2.6. This sticking time distribution is parameterized by the time of the peak (μ), the width of Gaussian distribution (σ) and decay time (τ).

3. Moment of inertia

   A constant moment of inertia (I) during the evolution state (rigid body) is assumed currently, though this could easily be changed. There are two ways used to estimate the average moment of inertia $< I >$. The first method is a direct estimation from the static shapes of the colliding nuclei. If the shapes of the initial nuclei are well known, $< I >$ can be estimated using geometrical relations [57]. In Appendix B, derivations of collisions based on geometry for (1) two spherical nuclei and (2) a

spherical projectile and deformed target are given.

Alternatively, $< I >$ can be calculated by using Time-Dependent Hartree-Fock (TDHF) calculations [58, 59], which provides the time-dependent moment of inertia ($I(t)$). The TDHF calculations take into account the shape evolution of the dinuclear system over the time. The average moment of inertia during the sticking phase is used for $< I >$.

2.4.2.2 Mass drift

While the dinuclear system is rotating, mass is transferred between the two constituents, and in QF it flows from the heavy nucleus to the light nucleus. Based on the work of Ref. [30], the masses of each constituent nucleus are assumed to evolve asymptotically to reach mass symmetry with time, as shown in Fig. 2.4b. The initial $M_R(0)$ is the ratio of projectile mass to the total mass. The mass flow between the two constituents can be defined in terms of the mass ratio M_R as follows:

$$M_R(t_s) = [M_R(0) - 0.5] \exp^{-t_s/t_m} + 0.5 \tag{2.13}$$

where t_m is the mass equilibrium time constant, determined to be 5.2×10^{-21} s by Ref. [30], and t_s is the sticking time. The mass ratio of the target-like nuclei is $(1 - M_R)$.

In the simulation, the final mass ratio is calculated when each event is randomly assigned a sticking time from the distribution. Once the system evolves at a particular sticking time t_s, the two constituent fragments are populated in the MAD according to $M_R(t_s)$ and $\theta_{c.m.}(t_s)$. To simulate fluctuations, the mass is selected within a Gaussian spread around the value of M_R calculated using Eq. 2.13 [54].

2.4.2.3 Specific conditions

In some systems, additional ingredients must be added to the simulation to account for localised physics phenomena. The following considerations are particularly relevant for this work.

1. Shell energy correction

   Once the nuclei are in contact, forming the dinuclear system, the system evolves in shape towards the minimum of the potential energy surface (PES) [60] before undergoing scission. For example, some events may be trapped in the shell closure region (e.g. ^{208}Pb) due to the presence of an energetically favourable pathway to scission. The simulation is designed to empirically take into account the effect of shell energy corrections in a simple way [59, 61]. A variable fraction can be centred around a selected M_R corresponding to the lead region by adjusting the shell fraction variable (input parameter).

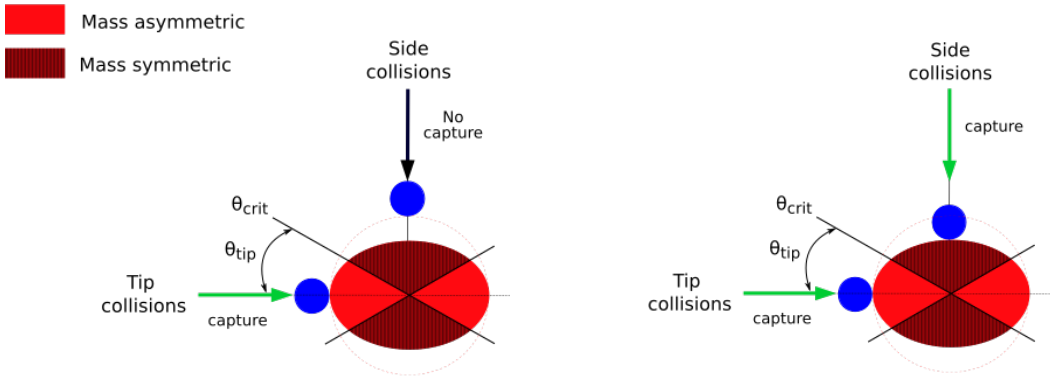

(a) E < V_B (b) E > V_B

Figure 2.7: Schematic illustration of a spherical projectile colliding with a deformed target. The angle between the touching point of the projectile and the deformation axis of the target nucleus is an important condition affecting the probability of both capture and QF. The type of collision, tip or side, is divided at a critical angle θ_{crit}. (a) At energies below the average barrier, only tip collisions can lead to capture. (b) However, all trajectories can lead to capture at energies above the barrier.

2. Influence of static deformation alignment

   The contact configuration between the projectile and deformed target nuclei is an important aspect of the QF process [61, 62] because it is associated with the probability of capture and with the lifetime of the dinuclear system, which is directly related to the mass equilibration of the QF fragments [63].

   As discussed in Section 2.2, different orientations of the deformed nucleus results in a distribution of barrier energies. The probability of capture at a given beam energy depends on this barrier distribution; the lowest barrier height is at $\theta = 0°$ whereas the highest barrier is at 90°. A simple graphical illustration is given in Fig. 2.7, showing tip (axial) and side (equatorial) collisions divided by a critical angle θ_{crit} [59, 63]; Fig. 2.7a is for reactions at energies below the barrier and Fig. 2.7b is for reactions at energies above the barrier.

   In reactions at $E < V_B$, only tip collisions undergo the capture process due to low barrier height and form an initially elongated dinuclear system. Therefore, the subsequent fission (fast QF) is expected to be asymmetrically distributed in mass and angular distributions. At $E > V_B$, all orientations lead to capture. A greater contribution of side collision results in symmetric distribution because more compact configurations are formed which empirically result in a longer mean lifetime of the system, and thus greater mass equilibration. A recent publication [59] discussed details of this concept for the ^{34}S + ^{232}Th system, which gave a standard picture to approach reactions on deformed nucleus.

Because of this correlation between capture and the subsequent QF, the three components of Eq. 2.12 are determined separately for tip and side collisions. This will be explained in details in Section 6.4.2, where the Quasisim code is used to extrapolate QF angular distributions to 0° and to 180°.

Chapter 3

Experimental Methods

Overview

To investigate energy dissipative processes affecting fusion reactions, a series of measurements was carried out at the ANU with projectiles ranging from ^{18}O to ^{48}Ca bombarding fissile target nuclei of ^{232}Th. A range of beam energies from $\sim$ 5% below to $\sim$ 20% above the fusion barrier was investigated. Precise measurements of reaction products were achieved using the CUBE binary fission spectrometer.

This chapter details methods of beam production and acceleration, the experimental setup, and the measurement of fission fragment time-of-flight and position, which are essential for reconstructing the fission events and identifying reaction outcomes.

3.1 Accelerators and Beam optics

All experiments in this work were carried out at the ANU Heavy Ion Accelerator Facility using the 14UD tandem accelerator and superconducting linear post accelerator (LINAC). A schematic view of the 14UD accelerator, including ion source and the beam focusing apparatus of relevance to this thesis, is shown in Fig. 3.1. The 14UD is a National Electrostatics Corporation Pelletron accelerator, which uses a potential difference (maintained by three rotating chains of charged pellets) to accelerate a beam of charged particles up to the desired energy [64, 65]. Since the 14UD is only capable of maintaining terminal voltage up to 15 MV [65], experiments requiring even higher beam energies use the LINAC. The LINAC consists of 12 Split Loop Resonators (SLRs) housed in 4 cryostats [66], and is introduced after the 14UD accelerator. Unlike the 14UD, the LINAC (schematic view in Fig. 3.2) uses resonant radio frequency cavities to accelerate charged particles passing through the superconducting resonators.

For all experiments the accelerator was operated by members of the Nuclear Reaction Dynamics Group, including the author. The author also contributed to running many other experiments during the Ph.D course work from 2013 to 2018 and mastered operating both 14UD accelerator and LINAC[1], including tuning the beam, changing ion source

[1]The author participated in two LINAC runs in 2013 and 2016.

cathode samples (beam species) and beam energies.

Most of the beam optics components and diagnostic elements were controlled through a computer interface using custom software based on EPICS[2]. The methods for obtaining the desired beam characteristics are described below. Accelerator operation can be divided into three stages: beam production, acceleration, and transportation.

3.1.1 Beam production

The tandem accelerator operation requires the production of negative ions. This is done using a SNICS (Source of Negative Ions by Caesium (Cs) Sputtering) ion source, consisting of the cathode, ioniser and a Cs oven [67].

The negative ions are produced by sputtering a water-cooled cathode containing a sample of the required beam species with ionised Cs. Cs vapour is introduced from the Cs oven and fills the ion source chamber. Some Cs is ionised when making contact with the surface of the hot ioniser and produces positively charged Cs ions (Cs^+). These Cs ions accelerate towards the cathode, which is operated at a negative bias of -5 kV, and thus collide with the sample material pressed into the cathode, knocking out atoms or ions of this sample material. Some Cs vapour condenses on the surface of the cooled cathode, forming a thin layer of neutral Cs atoms. The atoms of the sputtered sample material can gain an electron as they pass through the neutral Cs layer on the surface of the sample. Only singly charged negative ions exist stably. These negative ions are then repelled from the cathode. Finally, they are extracted by the positively biased extractor electrode [68, 69]. The extracted ions are pre-accelerated in a potential of 150 kV and travel towards the mass selection magnet.

Depending on the electron affinity of the beam species, negative ions are extracted in the form of either atomic ions or molecular ions. In the case of a source material having a low electron affinity, such as Calcium (Ca) and Magnesium (Mg), low pressure ammonia gas (NH_3) is introduced at the front of the cathode to make a negative hydride ion. The recipe for beam preparation of various species is given in Ref. [70].

The production of negative ions is dependent on the supply of Cs^+ sputter ions, the neutral Cs film on the sample, and the focus of Cs sputter ions onto the sample. Therefore, to ensure that the desired beam current is produced, the accelerator operator controls the temperature of the Cs oven, the current of the ioniser, and the position of the cathode sample.

3.1.2 Beam transportation and acceleration

Once the beam is produced in the ion source, it starts a journey of acceleration and navigation through various beam optical and diagnostic components. These components

[2]Experimental Physics and Industrial Control System (https://epics.anl.gov/)

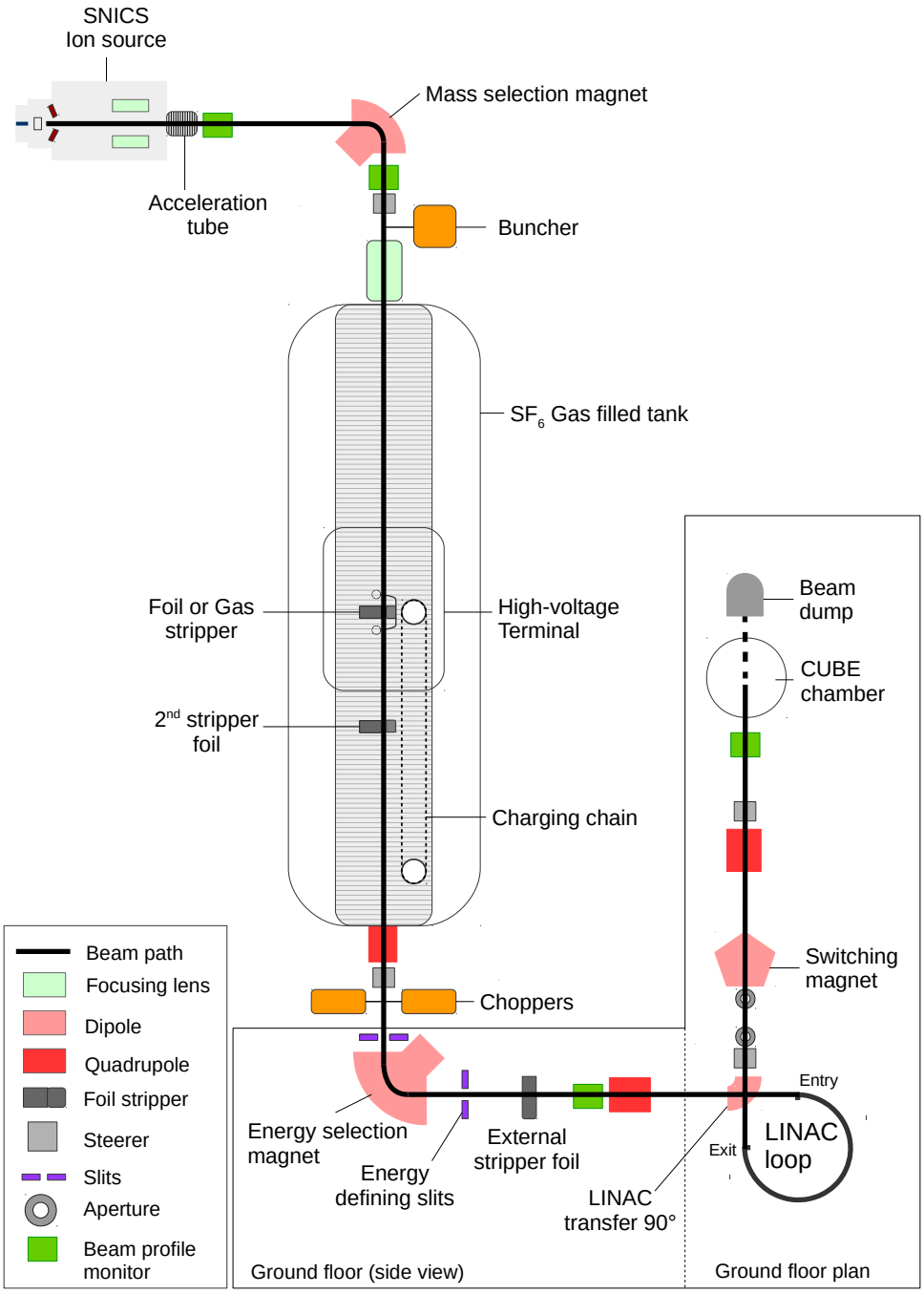

Figure 3.1: Schematic illustration of the 14UD tandem accelerator. The mass and energy of the beam are selected as it passes through the mass selection magnet and energy selection magnet, respectively. A pulsed beam is generated using the buncher and choppers. The beam is guided through various focusing and steering elements. When further acceleration through the LINAC is required, the beam is guided to the LINAC loop; otherwise, it is directly transported to the CUBE chamber by the LINAC transfer 90° dipole magnet where the measurement of reaction products takes place.

are used to guide the beam to the desired destination and to focus the beam in order to maintain intensity along the beam path. The optical elements consist of focusing elements including double focusing dipole and quadrupole magnets, as well as steering elements such as beamline switching magnets and steerers. The shape and position of the beam are monitored through beam profile monitors (BPM) and the current or intensity of the beam is measured with Faraday cups. Among all the beam transport elements, the dipole magnets located at the top and bottom of the 14UD tank, and the dipole achromats located in the LINAC loop are the key components, selecting the beam mass and energy.

After the negative ion beam exits the SNICS source and pre-acceleration tube, ions enter the mass selection magnet. Initially, the negative ion beam includes sample source ions, molecular ions and ions of contamination materials from the ion source. In most cases, impurities are filtered out, allowing the desired mass of the beam to exit the mass selection magnet by setting the magnetic field to select a particular ion mass. According to the Lorentz force law, a charged particle (q) moving perpendicular to a constant magnetic field travels in a circular path of radius ρ. The force is expressed as:

$$F = q\vec{v} \times B = \frac{mv^2}{\rho} \tag{3.1}$$

where B is the magnetic field, v is the velocity of the charged ion, and m is the mass of the ion. The fundamental quantity that determines the characteristics of the beam is known as the magnetic rigidity[3] ($B\rho$). Rearranging Eq. 3.1 and re-expressing in terms of energy (E) provides the expression for magnetic rigidity:

$$B\rho = \frac{\sqrt{2mE}}{q} \tag{3.2}$$

Since E and q are the same for all ions entering the mass selection magnet, a given magnetic field uniquely selects a single mass. The mass-selected beam then enters the acceleration tube located in the 14UD tank, which is filled with sulphur hexafluoride (SF_6) gas to prevent electrostatic discharges (sparks). There are two stages of acceleration in the 14UD. In the first stage, the negative ions are accelerated towards the positively charged high voltage terminal located in the middle of the tank. The ions pass through either a thin Carbon (C) stripper foil or a gas-filled stripper canal. At this point, the charge of the beam is changed through stripping of a number of electrons; namely, it becomes a positive ion beam with a distribution of charge stages [71, 72]. This positive ion beam undergoes a second stage of acceleration because it is now repelled by the positive terminal voltage.

[3]The magnetic rigidity is an important factor for obtaining the desired beam but is also a very useful property for tuning the beam, because one can scale magnets along the beam path based on the rigidity of different beam species and energies relative to a previous beam choice.

For a given charge state q, the energy of the beam (in MeV) is given by:

$$E_{beam} = V_T(1 + q) + E_{pre} \tag{3.3}$$

where V_T is the terminal voltage in units of MV and E_{pre} is determined by pre-acceleration volts, which was 150 kV for the experiments reported here. If additional energy is required, a second C foil stripper, located one third of the way between the terminal and the bottom of the 14UD tank is used for the production of beams with higher charge states, allowing higher energies. For acceleration by the LINAC, an external foil located after the energy selection magnet can be used to give an even higher charge state, and thus an even higher energy gain.

The accelerated positively charged ion beam leaves the tank and enters the energy selection magnet. This is a 90° bending magnet which bends the beam into the horizontal plane, and selects the desired beam energy in accordance with the magnetic rigidity given in Eq. 3.2. Only a specific charge state of the beam is selected. Precise energy definition is achieved by setting a nuclear magnetic resonance (NMR) frequency that determines the strength of the magnetic field and thus selects the correct beam rigidity [73]. The accuracy of the energy determination has been demonstrated by repeating measurements of the magnet constant (magnet calibration measurement), giving the calibration results with variations of less than ±0.05% [73]. That is, an absolute beam energy, in general, can be considered as having an uncertainty of less than ±0.05% of the beam energy.

After energy selection occurs, the beam can either be sent directly to the target area, or for further acceleration using the LINAC. The latter choice was made for beams of ^{40}Ca and ^{48}Ca in this thesis. Since the LINAC operation and the measurements with the CUBE detector system required a pulsed beam, pulsed beam generation is described first, followed by the description of the superconducting LINAC.

3.1.3 Pulsed beam production

Initial tuning of the beam into the CUBE detector chamber (where all experiments in this thesis took place) was with a DC beam, which also can be used for some measurements. However, it is advantageous to use a pulsed beam formed passing through a buncher and choppers in the measurement of fission, as the time structure can be used for the velocity reconstruction and is also essential to operation of the LINAC. The buncher is located in between the mass selection magnet and the focusing lens on the top of the 14UD tank. It can operate in two ways: via a single-frequency mode or a three-frequency mode with bunching efficiencies of $\sim$ 25% and $\sim$ 50% respectively [74]. The principal frequency is the $1/16^{\text{th}}$ sub-harmonic of the LINAC frequency of 150 MHz. Two orthogonal choppers, operating at 1/2 and $1/16^{\text{th}}$ sub-harmonics and located at the bottom of the 14UD tank, cut the tails off the bunched beam and clean up the beam profile. As a

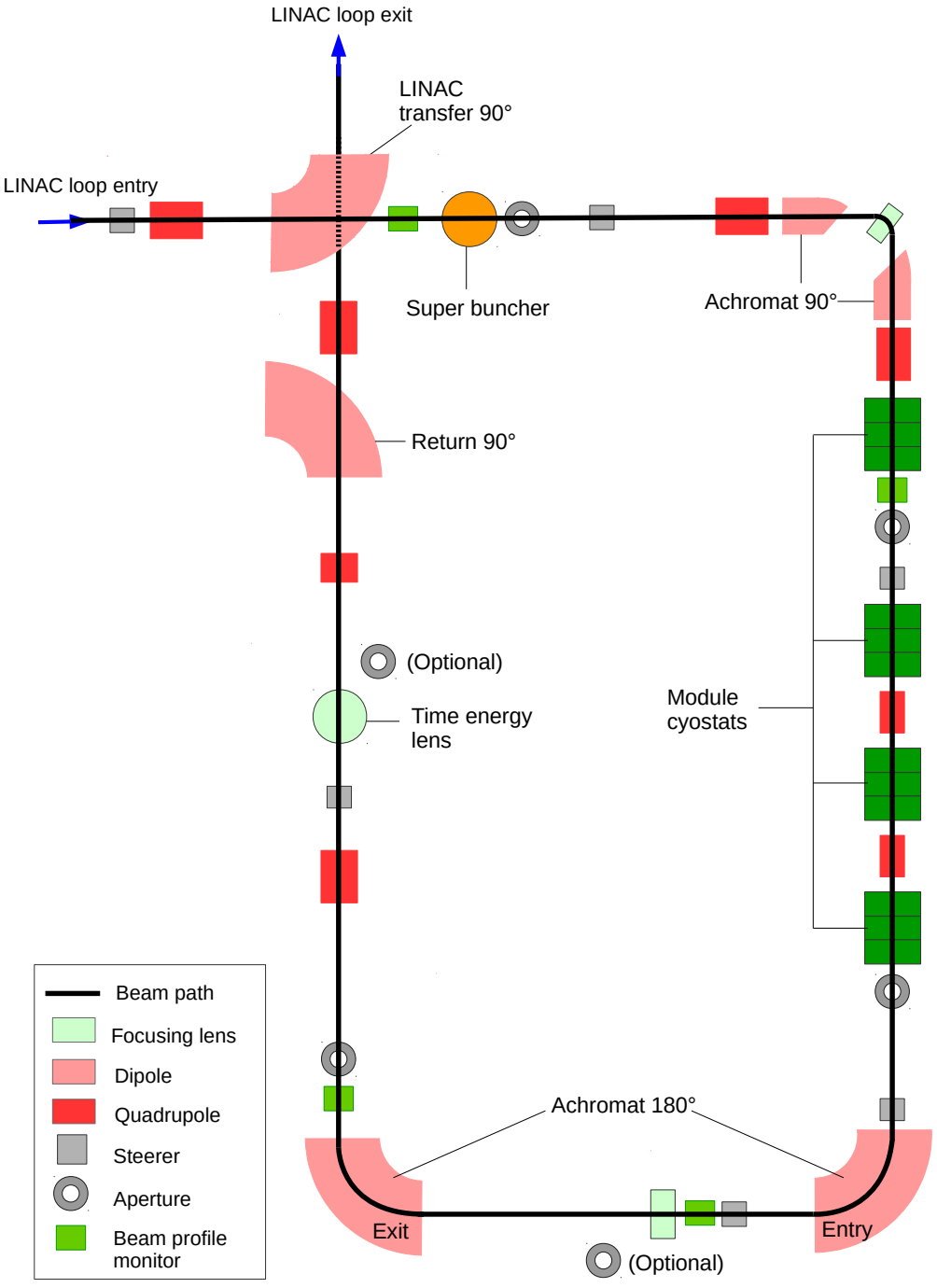

Figure 3.2: Schematic illustration of the superconducting LINAC loop. The charged particles are accelerated when they pass through resonating fields inside the resonator cavities. The energy of the beam is determined by the magnetic field of the 180° achromat entry, dipole, calibrated with respect to the field of the energy selection magnet in the 14UD. Finally, focusing elements guide the beam back to the target area.

result, a pulsed beam with a typical width of 1 - 1.5 ns FWHM and pulse separation of 106.6 ns is generated. Because of the high frequency of the LINAC resonators, in cases when the LINAC is used, the beam profile is compressed to 50 - 100 ps FWHM [74] via the superconducting buncher (super buncher) located soon after the beam enters the LINAC loop. Finally, the beam can be rebunched again after exiting the resonators using the time-energy lens located in the end of the LINAC loop. The resulting pulsed beam, consisting of projectile nuclei of the required energy, react with target nuclei mounted on a multi-target ladder placed in the centre of the CUBE chamber, which operates under vacuum at a pressure of around 2×10^{-5} Torr when the fission detectors (with 0.25 m^2 of 0.9 μm thick plastic window) are filled with 4 Torr of operating gas.

3.1.4 The superconducting LINAC

The accelerated beam with a selected charge state q is directed through the superconducting LINAC booster shown in Fig. 3.2, consisting of a superconducting buncher made up of a $\beta = 0.1$ Quarter Wave Resonator ($\beta = v/c$), 12 Split Loop Resonators (SLRs) housed in 4 separate cryostats, and optical elements [74, 75, 76]. In general, experiments using the LINAC are carried out in descending order of energy. Therefore, initially all resonators are set up to achieve the maximum acceleration required by setting the optimal phase and amplitude [74, 77]. The energy gain or loss introduced by the SLR is calculated by the equation [74]:

$$\Delta E = qE_{acc}L_{SLR}\cos(\Delta\Psi_{acc})T_{\beta} \tag{3.4}$$

where q is the charge state of the ion beam, E_{acc} is an average accelerating field, L_{SLR} is the active length of the SLR, $\Delta\Psi_{acc}$ is the resonator field phase deviation from 0°, and T_{β} is the transit time factor. The details of each terms are described in Ref. [74].

Like the energy selection magnet in the 14UD loop, the 180° achromat entry 90° magnet dipole is used to define and set the energy of the LINAC beam. This is calibrated using the known beam energy from the 14UD before acceleration by the LINAC. Once the energy-selected beam passes through the achromat entry, various beam optical elements guide the beam to the exit of the LINAC loop and transport it to the target area.

The LINAC resonators in the ANU can achieved an acceleration field of 3.5 MV/m [75]. During the experiments that the author participated in, the average energy gain per resonator was around 10 MeV for the $^{64}Ni^{20+}$ beam, the heaviest beam species used, which allowed access to accelerated Ni ions of energies up to 382 MeV. In comparison, the maximum energy for ^{64}Ni using the 14UD accelerator was 269 MeV.

3.2 Experimental setup

Two types of detectors, multi-wire proportional counters (MWPCs) and Si monitor detectors, are housed in the CUBE chamber to detect reaction products as shown in Fig. 3.3. Fission fragments are detected with the CUBE detector system, consisting of either two or three large area MWPCs. Fig. 3.3a shows a typical arrangement of MWPCs for the two-detector configuration. The front and back detector were mounted at $\theta_{cube} = 45°$ and 90° scattering angles with respect to the beam axis and 180.0 mm from the target for each experiment. Recent experiments, including reactions of ^{48}Ca with ^{232}Th for this thesis, were carried out with a three-detector configuration; an additional MWPC was mounted at $\theta_{cube} = 135°$, called here "the small back detector". Fig. 3.3b shows the configuration of the two back detectors. The MWPCs are arranged to cover a wide range of angles to detect fission fragments. As a result, measurements with high statistical accuracy can be achieved. The choice of detector configurations for each measurement are listed in Table 3.1. The target ladder was in the centre of the chamber, oriented with the normal at 60° with respect to beam axis to minimise the energy loss of reaction products in the targets. Apart from MWPCs, two Si surface barrier detectors (called monitors), are also mounted symmetrically around the beam axis at angles of $\theta_m = 22.5°$ or 30° (out of the page) in the forward hemisphere to detect elastically scattered particles. They are used to tune the pulsed beam and for absolute cross section determination.

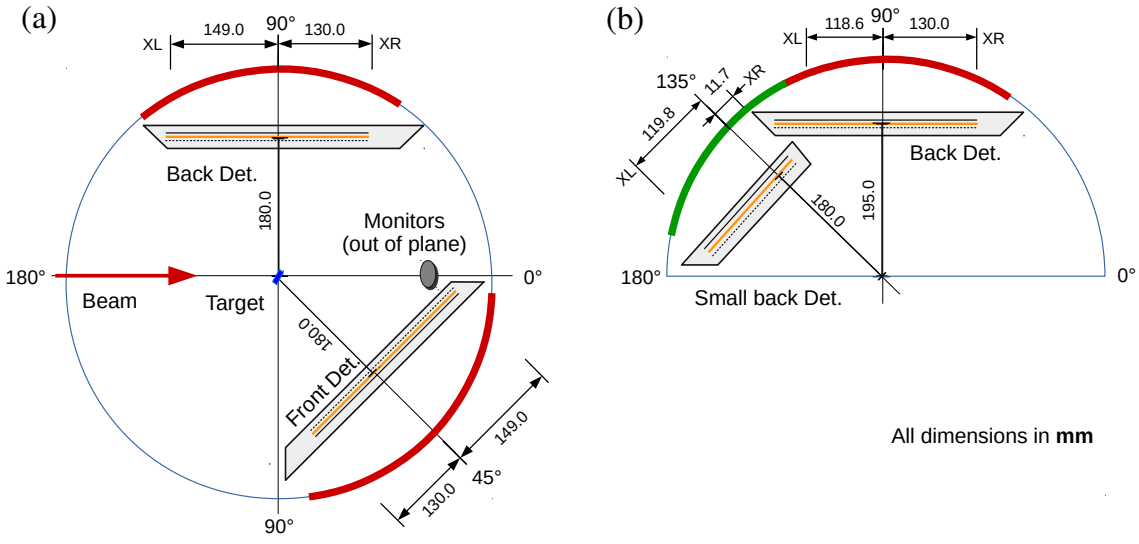

Figure 3.3: (a) The 2-MWPC configuration. (b) Configuration of back detectors when using 3 MWPCs. 30.4 mm of the left side of the back detector (XL) is blocked by the small back detector. The details of detector arrangements used for measurements are listed in Table 3.1.

Table 3.1: Detector configuration options and angular coverage.

Detectors	**Option**	**XL | XR Length [mm]**	**Angular Coverage**
Back	A	130 | 149	50° - 125°
	B	149 | 130	55° - 130°
Small back	C	119.8 | 11.7	117.5° - 168.5°
Front	All cases	149 | 130	5° - 80°

3.2.1 Detector system

In order to reconstruct the fission events using the kinematical coincidence method [26], the information of time-of-flight (ToF) and positions of the fission fragments are required. In addition, energy loss information can be useful to identify singles events, in particular, separating elastic events from products of reactions with light impurities in sub-barrier elastic scattering nomarlisation measurements. The following subsections describe the required information was extracted from the CUBE detectors, as well as the yields of Rutherford scattering from the monitors, which were used for the solid angle normalisation to measure the absolute cross sections.

3.2.1.1 CUBE detectors

The nuclear reaction dynamics group has designed and developed a binary fission spectrometer called CUBE, consisting of two standard MWPCs have a large active area (279.0 mm × 357.0 mm) and an additional MWPC, approximately half the size of the standard one, which was made in 2015[4]. Fig. 3.4 shows the composition of each MWPC. A cathode centre foil (CF) is sandwiched in between X and Y orthogonal grids of anode wires. The region between the electrodes is filled with propane gas supplied to maintain a typical 4 Torr gas pressure. The position grids are made of 20 μm tungsten (W) wires coated with gold (Au) with uniform spacing of 1 mm. One end of each wire is connected to one tap of a delay chip, which are connected to form a delay line. The CF was made by coating a thin Au layer ($\sim$ 40 $\mu g\,cm^{-2}$) on both sides of a 0.9 μm thick polyethylene terephthalate (Mylar) foil through evaporation. It is segmented into 4 (or 2 in case of the small back detector) separate parts (quadrants), using an evaporation mask, to reduce the capacitance and thus increase the pulse height of the timing signals from the CF.

[4]The author participated in the manufacture of MWPCs and adapting the analysis code 'dacube' for the 3-MWPC setup.

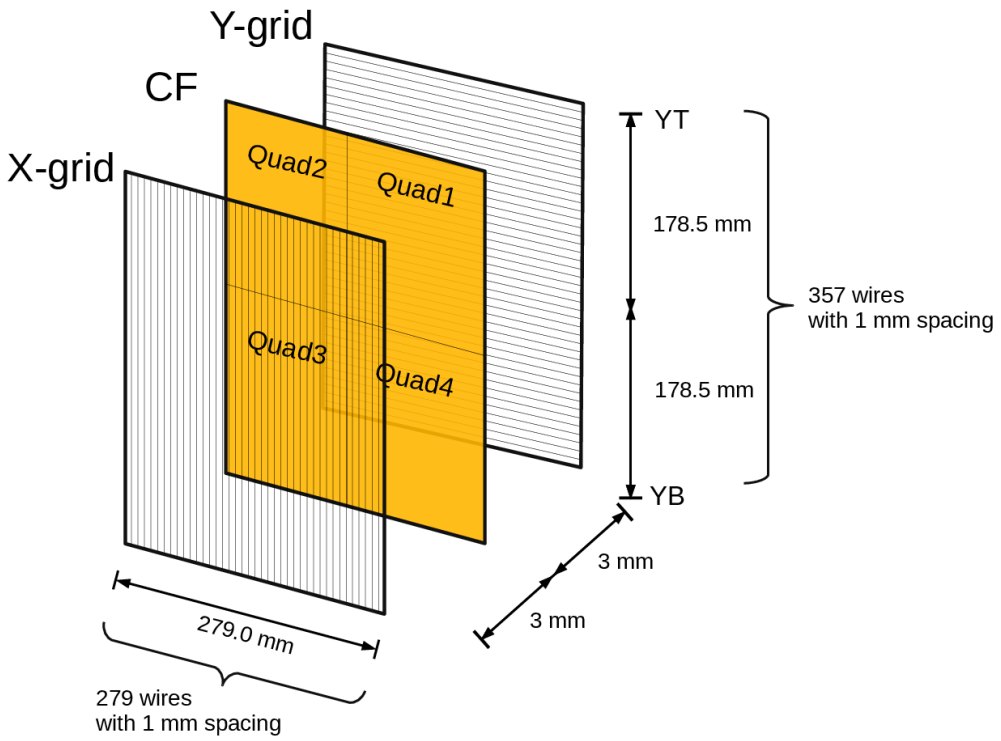

Figure 3.4: The composition of the standard MWPC (279.0 mm × 357.0 mm) consisting of position grids and the centre foil (CF) which is divided into quadrants. The small back detector is approximately half the size (131.5 mm × 357.0 mm) with a CF divided into two sectors.

Collection of position signals

The wire grids in each MWPC allow position to be determined for each detected particle. Once a fission fragment passes the grid, electrons from ionisation are accelerated to the closest anode wire and through charge multiplication around the wire generate a signal pulse that propagates through to the opposite ends of the delay line. The time difference of the delayed readouts from opposite ends, for each X- and Y-plane, gives the position coordinate (X, Y) on the active area of the detector with a resolution of FWHM $\sim$ 1 mm, which is similar to the beam spot size [78, 79]. The position calibration is detailed in Section 4.2.1.

Collection of timing and energy loss signals

The centre foil (CF) provides the timing information (t), which will be processed into the time-of-flight (ToF) of a particle, and also an energy loss (ΔE) signal. The collected charge resulting from interaction with gas molecules after the particle passes through the grid (98% transparency), is proportional to the energy loss of the heavy charged particle. The size of the energy loss signal is expected to be according to the Bethe-Bloch (stopping

power) equation [78]:

$$\frac{dE}{dx} \propto \frac{Z_s \rho_s}{A_s} Z_p^2 f\left(\frac{E_p}{A_p}\right) \tag{3.5}$$

where s indicates the stopping material, having atomic weight A, atomic number Z, the density ρ, and p indicates an incident charged particle colliding with energy E and mean charge state Z_p.

The signal amplification around the position wires is not uniform, resulting in a reduction in energy loss resolution compared with that of the (already poor) resolution coming from the small primary ionisation energy loss. In the work presented here, the information of ΔE was not used in the fission analysis directly. However, this information can be useful in identifying some clusters of events after kinematic reconstruction. Especially, it can easily make use of identifying elastically scattered particles from the unprocessed data, which is helpful for determining measured velocities, as discussed in Chapter 4.

3.2.1.2 Monitors (Si-detectors)

Elastically scattered particles are detected by ion-implanted silicon beam monitor detectors, whose signals are generated by charge carriers that are created via the ionisation process inside the detector volume [79]. Yields of Rutherford scattering were used to normalise the beam and to extract the absolute cross sections of fission fragments measured in the CUBE detectors. The setup employs two monitors placed symmetrically about the beam axis because the sum of yields from two monitors is essentially independent of small beam spot movements, and thus accounts for small changes in the beam spot position. Details of the extraction of the absolute cross sections will be described in Chapter 6.

3.2.2 Signal processing and Data acquisition system

3.2.2.1 Signal processing

The electronics arrangement for the reactions studied in this thesis slightly varied depending on the time when the measurements were carried out. Fig. 3.5 is one example, showing the arrangements used in the measurements of ^{48}Ca bombarding ^{232}Th performed in November - December 2016. The signals for each MWPC and monitor were collected as an event when trigger conditions were satisfied. The selected trigger condition depended on the aim of the run. For fission experiments, events from the CUBE detectors were collected in coincidence trigger mode; namely, events were only recorded when events in the front MWPC were coincident with the back or small back MWPC. The coincidence trigger with the back MWPCs avoided a high count rate caused by elastically scattered particles in the front counter. For elastic calibration runs, performed at $\sim$ 80% of the Coulomb barrier, events were collected with back detector singles triggers because the measurement

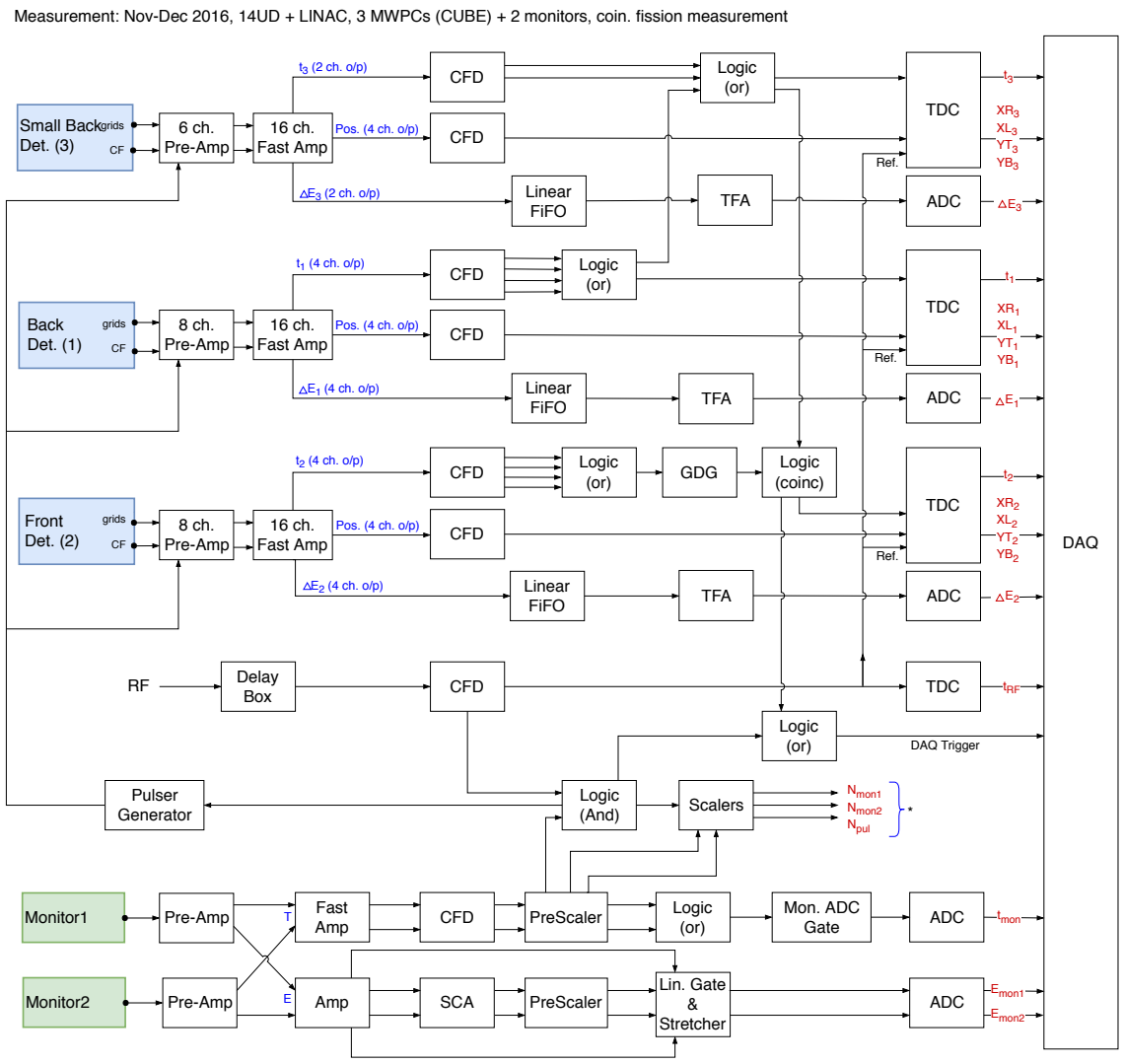

Figure 3.5: Schematic diagram of the electronics setup used for the fission measurement with CUBE and monitor detectors. The abbreviations used are as follows: Pre-Amp = pre-amplifier, Amp = amplifier, CFD = constant fraction discriminator, Linear FIFO = linear fan in and out, GDG = Gate and delay generator. The blue terms indicate signal branches. The red terms are the final output signals collected. *Scalers are recorded in the logbook during the measurements.

is to determine the solid angle of the back detectors. The prescaled monitors were always an element in the trigger.

Electronic pulses, which were triggered by one of the monitors, were sent to each MWPC pre-amplifier and also sent to a scaler in order to estimate the overall dead time of the data acquisition (DAQ) system and of whatever multi-parameter gates were applied in the fission analysis.

The DAQ employed SILENA analogue-to-digital (ADC) converters and a CAEN time-to-digital converter TDC to collect list-mode data, in which coincident data from each channel of the ADC/TDC modules were grouped into a single event. For fission mea-

surements done before 2015, position and timing signals were obtained using Time to Amplitude Converters (TAC). After that, position and timing signals were obtained using a TDC.

3.2.2.2 Data collection and post-processing

Signals from the DAQ were collected using the in-house data collection program (DCP) developed by G. S. Foote. All subsequent offline data processing and analysis were achieved in ROOT, an object oriented data analysis framework developed by CERN [80]. A DCP data file containing list-mode data collected during the experiment should be formatted into a hierarchical structure ($Tree \supseteq Branch \supseteq Leaf$) for the analysis based on the ROOT framework. A raw ROOT data file contains a '$CubeTree$' with branches, which are detectors, namely '$CUBE$' and '$monitors$', and a single signal like RF. Each branch contains leaves, which correspond to signals that belong to each branch such as position, t and $\triangle E$ for '$CUBE$', and energies for '$monitors$'.

The DCP to ROOT format conversions were done with a script originally written by M. L Brown, or a conversion package code developed by N. Withers and E. Williams. The former script required editing depending on the experimental definition, providing specific interface and channel numbers of ADC or TDC modules. The later package can read the DCP configuration information in the raw data file directly and can filter out damaged/unregistered events in the DCP file. For recent data, with position and timing signals collected via a TDC, an additional script written by the author was used to rearrange the ROOT tree structure after the DCP to ROOT conversion, to interface with the analysis code.

3.3 List of measurements

Table 3.2 contains details of systems studied in this thesis, showing reactions for a range of projectiles colliding with ^{232}Th targets, as well as calibration runs used for solid angle normalisation. Each table provides information on backing materials that support the target, and the range of energies with respect to the capture barrier. The systematic description of W. J. Świątecki et al. expresses the capture barrier as [81]:

$$V_B = 0.85247z + 0.001361z^2 - 0.00000223z^3 \tag{3.6}$$

where z is the Coulomb parameter given by:

$$z = \frac{(Z_1 Z_2)}{A_1^{1/3} + A_2^{1/3}} \tag{3.7}$$

Reactions studied in this work are categorised into 'Light systems' and 'Heavy systems'.

Details of the system classification is given in Chapter 5. It will be shown the different categories exhibit different features; namely a significant contribution of QF was seen in the heavy systems compared to the light systems. For this reason, two different methods, were used to derive the total capture cross sections. This will be discussed in Chapter 6.

Table 3.2: Details of reactions on ^{232}Th targets and calibration measurements. Target and backing thicknesses and the number of MWPCs used for the measurement and their configuration options are given. The range of energies with respect to the capture barriers (V_B), the compound nucleus (CN), the charge products of the reaction (Z_1Z_2), and the system category are indicated. Detector configuration (A, B, C) are given in Table 3.1.

Exp. dataset	**Acc.**	**Proj.**	**Targ.**	**Targ. thickness [μg/cm^2]**	**Backing**	**Backing thickness [μg/cm^2]**	**Det. No.**	**Det. Conf.**	**CN**	Z_1Z_2	**E/V$_B$ range**	**V$_B$ [MeV]**	**Calib.**	**Category**
SICO		^{18}O		279	Al	30	2	B	^{250}Cf	720	0.93 - 1.15	78.0	a	Light
SICO	14UD	^{30}Si		279	Al	30	2	B	^{262}Rf	1260	0.94 - 1.08	135.7	a	system
SSITHU		^{34}S	^{232}Th	58	C	10	2	B	^{266}Sg	1440	0.87 - 1.07	154.8	b	
CAGEX	14UD	^{40}Ca		58	C	15	2	A	^{272}Ds	1800	0.93 - 1.02	193.8	b	Heavy
CA40X	+	^{40}Ca		279	Al	30	2	B	^{272}Ds	1800	1.05 - 1.15	193.8	b	system
GSI3	LINAC	^{48}Ca		115	Al	57	3	A, C	^{280}Ds	1800	0.98 - 1.18	189.1	c	
Calib. a	14UD	^{30}Si	^{208}Pb	56	C	12	2	B	^{238}Cm	1148	0.70	125.8		
Calib. b		^{34}S	^{197}Au	250	self-support		2	B	^{231}Am	1264	0.60	139.4		
Calib. c	14UD + LINAC	^{58}Ni	^{197}Au	180	self-support		3	A, C	^{255}Bh	2212	0.84 - 0.86	239.0		

Chapter 4

Analysis of Coincident Fission Fragments

Overview

The ultimate goal of the fission analysis in this thesis is to understand the fusion reaction mechanism from observed reaction outcomes. When observing binary reaction outcomes, the kinematic properties of each event holds important information about the properties of the reaction in question. This chapter focuses on the procedure of reconstructing events and reviews event selection criteria using the analysis code 'dacube'. It is explained how the raw parameters are processed, and how each binary event is reconstructed. Fig. 4.1 illustrates the sequence of steps, starting with the conversion of raw signals to physical quantities through calibration and transformation, and then the derivation of velocities and mass ratios of fission fragments. Lastly, it summarises how desired fission events are selected from other coincident events.

4.1 Analysis code: 'dacube'

The reaction dynamics group in the ANU has developed a fission analysis program aimed at performing kinematic reconstructions of binary reaction outcomes, and aiding the analysis and interpretation of these outcomes. 'dacube'[1] is the most recent version, developed from the code 'daGUI' written by R. du Rietz, which was used until 2013. 'dacube' was initially written by E. Williams and continuously enhanced by the code users including the author. The author developed the code to accommodate the third detector and the cross section determination. The 'dacube' package is a collection of C/C++ codes, using ROOT 5.34 libraries developed by CERN, and allows for event reconstruction, event selection, and absolute cross section evaluation. Details of the code structure and how the parameters are processed are illustrated in Appendix D. There are three input files re-

[1] 'dacube' is a far more bug free package compared to 'daGUI' and runs more flexibly in the ROOT platform. It has more functional tools such as the measurement of absolute cross sections and a comparison with predicted kinematical quantities.

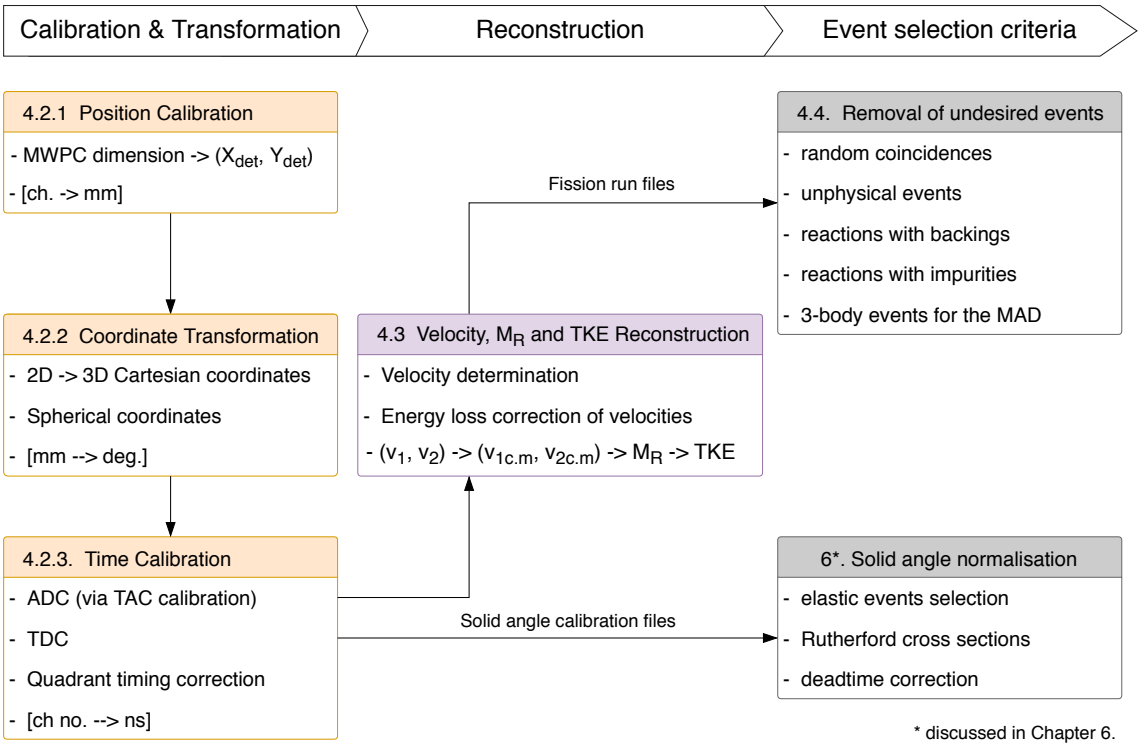

Figure 4.1: A flow chart of the binary events reconstruction procedure. The thesis section where each procedure is described is given in the heading of each box.

quired to run the code: a ROOT-formatted raw data file, a detector file and a sorting file. The detector file contains physical parameters relevant to calibration and transformation such as the geometrical position and dimensions of the MWPCs, and some calibration parameters for time and position. The sorting file contains experiment and reaction system information such as the beam species and energy, target information, beam type[2], and beam timing parameters (T_0, δT_2, and δT_3), which are key parameters used in the velocity reconstruction.

4.2 Calibration & Transformation

Velocity vectors of the coincident fission fragments are derived using the raw position and timing information extracted from each MWPC. Firstly, the raw signals of position and Time of Flight (ToF) in channels are transformed into physical units of mm and ns through calibration and transformation, as described below.

[2]Depending on the beam type, pulsed (AC) or continuous (DC), the reconstruction method differ. The AC-type uses the kinematic coincidence method as described in Ref. [26] whilst the DC-type uses the time difference method [82].

4.2.1 Position calibration

The position signals of the particles from the MWPC grid planes were obtained, as discussed in Section 3.2.1, by measuring the propagation time of signals at each end of the delay line connected to the MWPC grid wires. The time difference of the arrival of propagated signals at the opposite ends gives the position information in channels with respect to the detector edges, $\mathrm{X}_{det} = t_{XL} - t_{XR}$ and $\mathrm{Y}_{det} = t_{YT} - t_{YB}$. This position information is then turned into a physical position in mm after position calibration. Since the MWPC readouts result in good position resolution and linearity, the position calibration is achieved by matching the illuminated full active area (for data recorded in singles) to the known dimensions of the MWPC. As an example, Fig. 4.2a shows the full active area of the back detector after position calibration. Labels XL, XR, YT, and YB correspond to the edges of the MWPC.

4.2.2 Transformation

Firstly, the position in the individual 2D detector coordinate systems are transformed into the 3D reference frame using the known positions of the detectors in space relative to the target frame centre, (X_{det}, Y_{det}) $\rightarrow$ (x, y, z) where the z-axis corresponds to the beam axis. Positions in the 3D Cartesian coordinate system are then transformed into spherical coordinates, in which the particle positions are expressed in terms of scattering angles θ and azimuthal angle ϕ and a distance r from the origin where the reaction takes place. The transformation calculations are based on the Walton 1967 and Arfken 1985 derivation [83]. Fig. 4.2b shows the full active area of the detectors. The transformation must be accurately carried out since the kinematics of the fission fragments are reconstructed based on the transformed angles, as discussed in Section 4.3. The accuracy of the transformation is confirmed by comparing measured angles between heavy elastically scattered beam particles and the coincident target recoils (folding angles) with their calculated values.

4.2.3 Time calibration

The objective is to determine the flight time from the target (ToF_i) to detector 'i'. The time recorded (t_i) in channels is converted through the calibration ns/ch$_i$, and a time offset T_i for each detector.

$$\begin{aligned} ToF_1(\mathrm{ns}) &= t_1(\mathrm{ch}) \times (\mathrm{ns/ch})_1 + T_1(\mathrm{ns}) \\ ToF_2(\mathrm{ns}) &= t_2(\mathrm{ch}) \times (\mathrm{ns/ch})_2 + T_2(\mathrm{ns}) \\ ToF_3(\mathrm{ns}) &= t_3(\mathrm{ch}) \times (\mathrm{ns/ch})_3 + T_3(\mathrm{ns}) \end{aligned} \tag{4.1}$$

The time calibration is achieved by determining the calibration coefficient that trans-

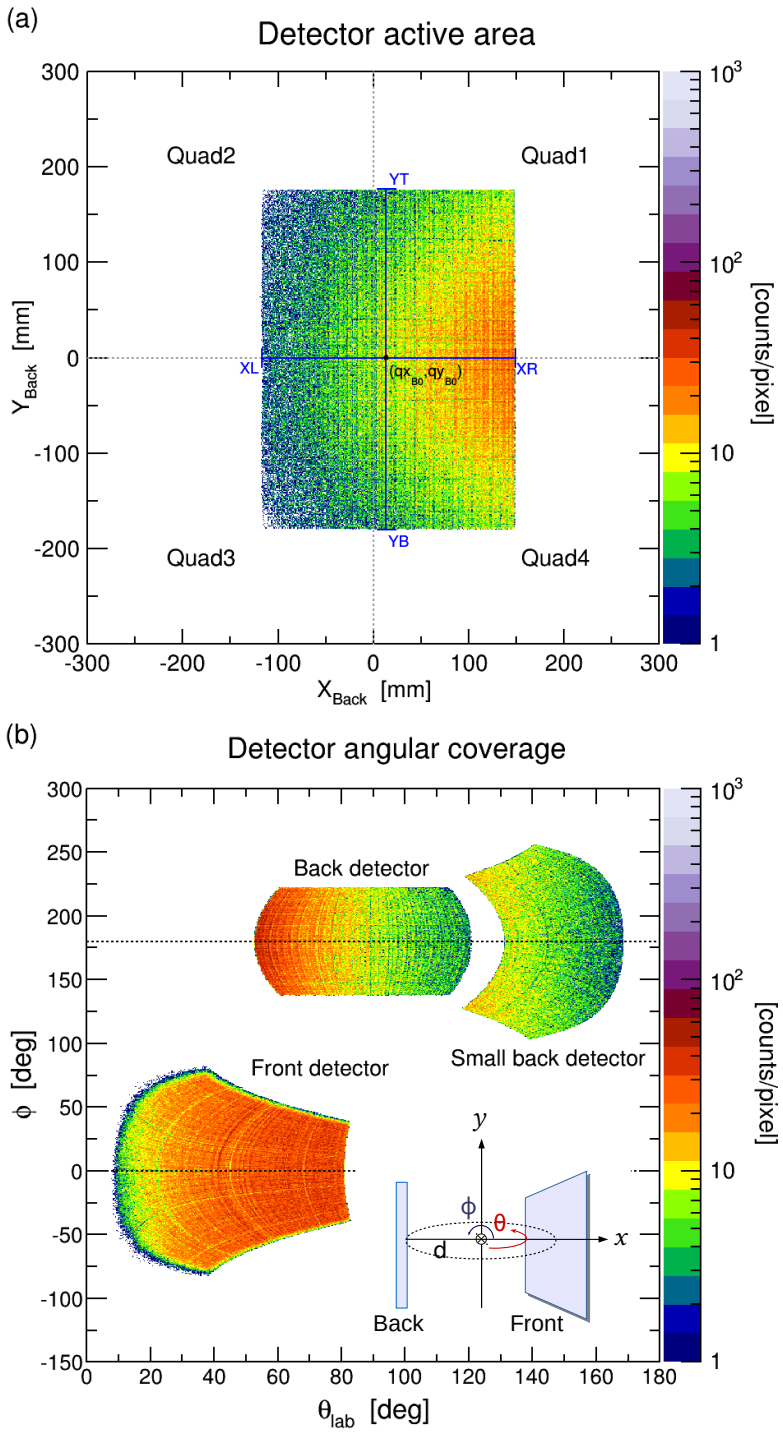

Figure 4.2: Scatter plots of particle positions: (a) The full active area of a MWPC in Cartesian coordinates in units of mm with respect to the closest point on the detector to the target. The quadrants, achieved by segmenting the centre foil are shown by full lines, and its central point (qx_0, qy_0) by dotted lines. (b) The full active area of the MWPCs in the spherical polar coordinate system, in units of degrees. The detector location is defined by distance (d) of their normal to the target, giving azimuthal angle (ϕ) and polar angle (θ) relative to the beam axis.

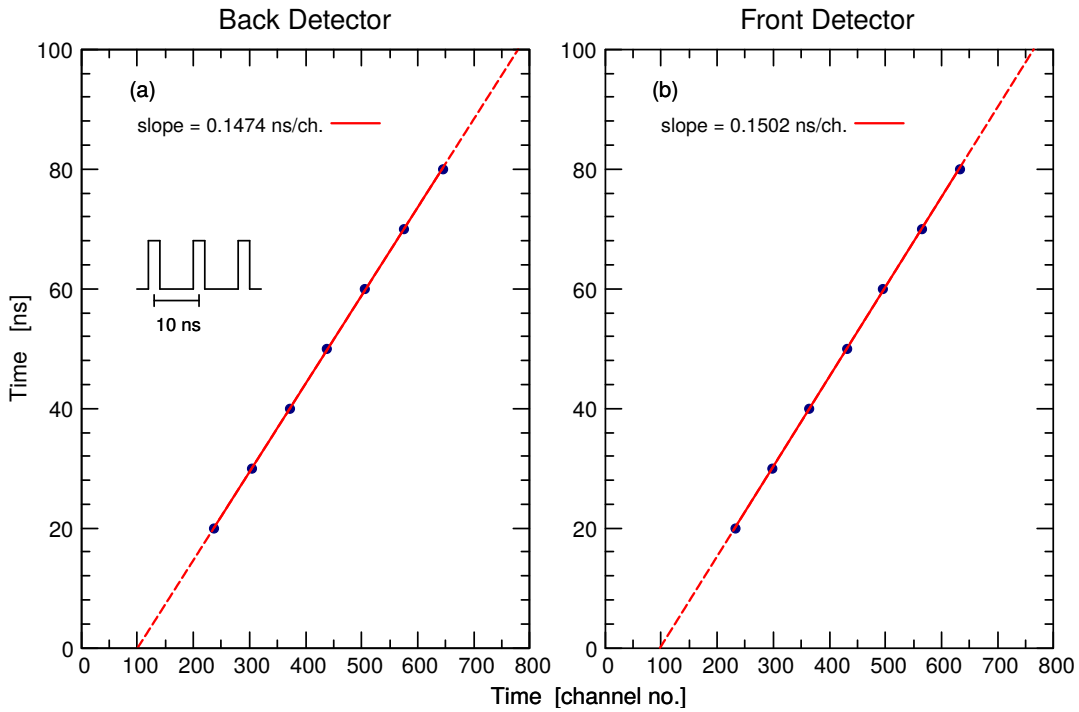

Figure 4.3: An example of the time calibrations for the back and front detector in panels (a) and (b) respectively, showing a nearly perfect linearity. Their slopes are the calibration coefficients.

forms the raw output in channel numbers to a time in nanoseconds. For datasets collected using CAEN V1190B TDCs, recorded time signals (in channels) are directly calibrated using the conversion coefficient given by CAEN, 0.097656 ns/ch [84]. The time calibration of the CAEN TDC was checked at the ANU and measured values agreed within 1 part in 20000. Datasets collected via the TAC and registered with ADCs are calibrated as described below.

TAC calibration:

A TAC calibration must be performed when time signals are collected using a TAC and ADC. Using an Ortec 462 time calibrator, which was set to generate pulses with a separation of multiples of 10 ns, the TAC calibration of each MWPC was accomplished. The separation between two pulse peaks displayed in a time spectrum (taking the centroid of the pulse peak) in channel numbers corresponds to 10 ns; this relationship is shown in Fig. 4.3. The slopes in Fig. 4.3a and Fig. 4.3b are time calibration factors that determine the relationship between channel number and time difference for each MWPC.

4.2.4 Timing signal corrections

The centre foil (CF) is segmented into four quadrants for the front and back MWPCs, and only two 'quadrants' of the same size for the small back counter. Timing signals from

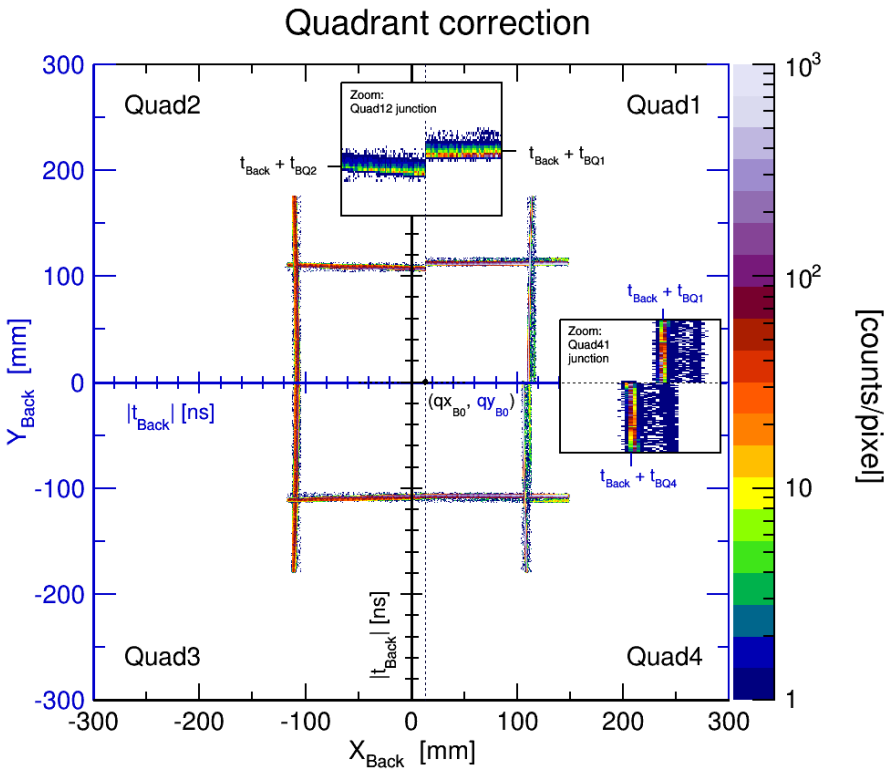

Figure 4.4: A scatter plot of timing signals from the four quadrants *vs* positions in the back detector. Two types of axises are superimposed in this figure to show a relation of timing signals to arriving at each quadrants: blue axes shows time *vs* Y-position and black axes show X-position *vs* time. t_{Back} is the average flight time of elastic particles and $t_{BQ1,2,3,4}$ are correction parameters. See text for full description.

each quadrant are processed through separate pre-amplifiers, fast amplifiers and constant fraction discriminators (see Fig. 3.5). Subsequently, an 'OR' of the first timing logic signals from the different quadrants is taken (Quad 1 || Quad 2 || Quad 3 || Quad 4) and sent to the TAC or TDC. Slightly different lengths of the cables or other differences in the analogue processing time of the quadrant time signals results in timing offsets between quadrants. Therefore, 'dacube' is designed to correct small differences in the analogue electronic timing for the 4 or 2 quadrants, using the observed time distribution of elastic events in neighbouring quadrants.

In order to demonstrate the signature of differences in quadrant time response, Fig. 4.4 was generated by giving an artificial offset value to quadrant 1 (Quad 1) in the back detector calibration file. Here, the calibrated time (t_{Back}) is plotted against the calibrated position of X or Y of elastically scattered particles. Ideally, there should be no discontinuity in t_{Back} (and also t_{Front}) across a quadrant boundary. But as seen in Fig. 4.4, timing signals are offset compared to signals from neighbour quadrants. Times from the different quadrants are aligned by adding offsets to each quadrant, resulting in a smooth transition at all quadrant junctions.

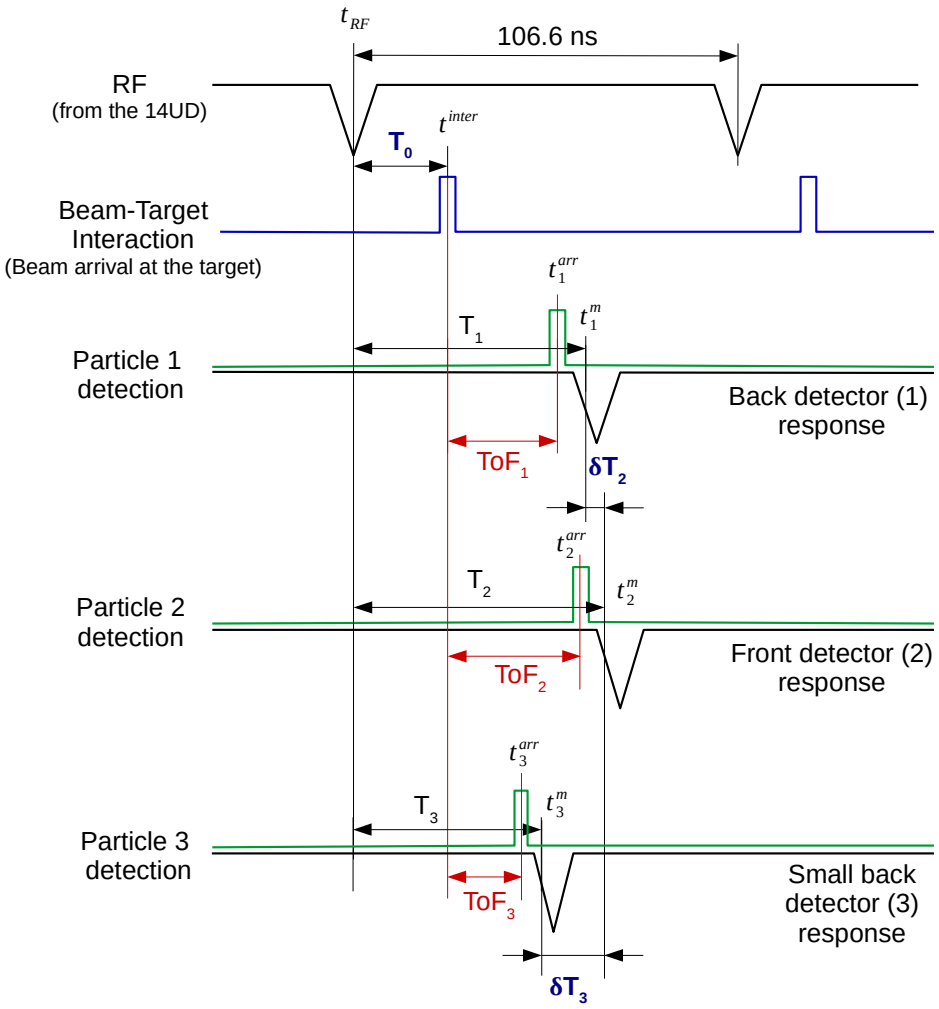

Figure 4.5: Illustration of the time-of-flight (ToF) measurement. Recorded time information (T_i) is a time difference of a measurement time (t_i^m) and the RF reference time (t_{RF}), where i refers to each MWPC. However, the true meaning of ToF of the particle is the time taken from the interaction point (target) to the detector ($t_i^{arr} - t^{inter}$). The exact flight time is corrected by introducing three arbitrary parameters, T_0, δT_2, and δT_3. T_0 is the offset between the RF and the arrival of the beam pulse at the target, and δT_2 and δT_3 are a time difference of the front and back, and front and small back detectors.

In addition, the position of the quadrant boundaries can be optimised. The centre of the CF (qx_0, qy_0) is the point where all four quadrants meet as shown in Fig. 4.2a. This central point is tunable such that in the case of a small mismatch occurring (for example, during construction of the foil) between the real central point and the design value (-12, 0) in mm (which is the centre of the detector frame), it can be corrected by adjusting the quadrant centre point a few mm away from this value.

4.2.5 Time-of-Flight (ToF) of fission fragments

Fig. 4.5 shows the time structure related to defining Time-of-flight (ToF). ToF is defined as the time taken from the interaction time (t^{inter}) to the arrival time (t_i^{arr}) at the centre foil in the detector, where i refers to each MWPC. Having obtained a single flight time (in ns) for each detector, relative to the RF pulse, the timing offsets (T_i) between the RF pulse and the arrival of the beam at the target must be determined. This offset varies from one beam energy or nuclide to another, depending on the flight time from the beam choppers to the target. For each detector, from one beam to another the offsets T_i change by the same amount. To simplify the data analysis, the offsets can be written as the sum of an offset related to the beam arrival time (T_0) and a constant offset ($\delta\mathrm{T}_i$) for each detector resulting from the electronics units processing the time signals. Thus,

$$\begin{aligned} T_1 &= T_0 + \delta T_1 \\ T_2 &= T_0 + \delta T_2 \\ T_3 &= T_0 + \delta T_3 \end{aligned} \tag{4.2}$$

In practice, the time offset $\delta\mathrm{T}_1$ is set to zero, thus T_0 is set for each beam to give the correct value of T_1. Then $\delta\mathrm{T}_2$ and $\delta\mathrm{T}_3$ are the relative time shifts between detectors 2 and 3 and detector 1 respectively, which do not change from one beam tune to another, unless the electronics or cables are changed. The determination of T_0, $\delta\mathrm{T}_2$ and $\delta\mathrm{T}_3$ are described in Section 4.3.4.

4.3 Reconstruction of reaction kinematics

The analysis software 'dacube', supports two methods for the kinematic reconstruction of fission events, depending on the type of the beam. These are the time difference method [82, 85], and the absolute time of flight method [26, 30]. The former method is applied to DC beam datasets and determines the masses of fission fragments assuming binary events following full momentum transfer (FMT) to the fissioning system, using the conservation of linear momentum (p). The latter method is applied to pulsed beam datasets, and is the framework for this study. This method was necessary as both FMT-fission and transfer-fission are expected [26], thus FMT-fission cannot be assumed. Coincident pairs of fission fragments are characterised in terms of their velocity vector components. The following sections describe the details of the kinematic coincidence method and how the parameters are derived. In addition, details of energy corrected velocities and how the measured velocities are accurately determined for each reaction are discussed.

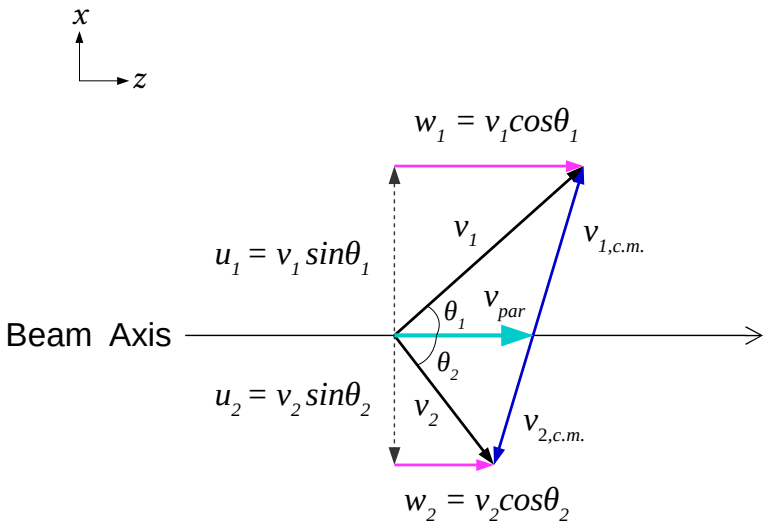

(a) Fissioning system in the plane including the beam axis.

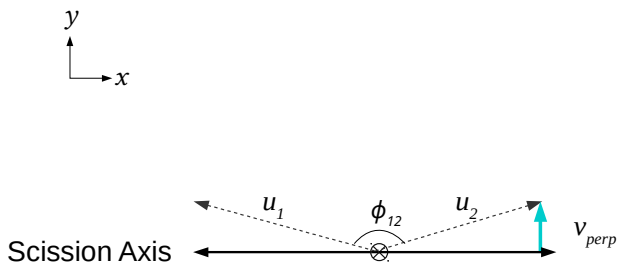

(b) Fissioning system perpendicular to the beam axis.

Figure 4.6: Diagram of the binary fission velocity components, adapted from Ref. [26]. (a) The relationship between velocities of the fission fragments in the centre-of-mass ($v_{i,c.m.}$) and laboratory frame (v_i) provides the parallel velocity component of the fissioning nucleus along the beam axis (v_{par}). (b) The perpendicular component (v_{perp}) appears when fission particles are kicked out of the reaction plane.

4.3.1 Velocity reconstruction

Fig. 4.6 shows the decompositions of velocity vectors of the binary fragments in a coordinate system in which the interaction point of the beam with the target is the origin. Fig. 4.6a shows vectors in the plane containing the beam axis whereas Fig. 4.6b shows components perpendicular to the beam axis. The velocity vectors of the fragment pair both originate from the reaction point, with folding angles $\theta_{12} = \theta_1 + \theta_2$ in the reaction plane and $\phi_{12} = \phi_1 + \phi_2$ perpendicular to it. For true binary reactions, $\phi_{12} = 180°$. In fission, neutron evaporation before or after scission causes small perturbations away from 180°. The velocity of the binary fragment i in the laboratory frame is decomposed into

components parallel and perpendicular to the beam axis, given by:

$$w_i = v_{||,i} = v_i \cos\theta_i \tag{4.3}$$

$$u_i = v_{\perp,i} = v_i \sin\theta_i \,, \tag{4.4}$$

where the perpendicular components (u_i) can only be positive while the parallel components (w_i) can be either positive or negative depending on the scattering angles.

In the centre-of-mass frame, fission fragments are always emitted back to back (ignoring small perturbations from neutron evaporation) and thus, the sum of the linear momentum is always 0 ($\sum \vec{p}_i = 0$). There is variation in the magnitude of the fragment velocities in the centre-of-mass frame depending on the binary fragment masses and total kinetic energies, but the requirement that the fragment velocities are co-axial results in the following relationship between u_i and w_i.

$$\frac{u_1}{w_1 - v_{par}} = -\frac{u_2}{w_2 - v_{par}} \tag{4.5}$$

where v_{par} is the (parallel) velocity of the nucleus undergoing fission.

Rearranging Eq. 4.5 in terms of measured velocities and scattering angles gives [26]:

$$v_{par} = \frac{v_1 v_2 \sin(\theta_1 + \theta_2)}{v_1 \sin\theta_1 + v_2 \sin\theta_2} \,. \tag{4.6}$$

The perpendicular component v_{perp} is defined by the azimuthal folding angle ϕ_{12} and decomposed vectors u_i as shown in Fig. 4.6b. It is determined from the measured velocities as follows [26]:

$$v_{perp} = \frac{u_1 u_2 \sin\phi_{12}}{\sqrt{u_1^2 + u_2^2 - 2u_1 u_2 \cos\phi_{12}}} \,. \tag{4.7}$$

It is expected to be centred around zero for FMT-fission.

4.3.2 Mass ratio (M_R)

M_R is defined as the fraction of the total mass carried by one of fragment relative to the summed mass of both fragments. Its complementary fragment mass ratio is $(1 - M_R)$. M_R can be derived in two ways; both methods are based on linear momentum conservation. The first is from conservation of momentum in the the plane perpendicular to the beam:

$$m_1 u_1 = m_2 u_2 \;; \tag{4.8}$$

rearranging this equation gives:

$$M_R = \frac{A_2}{A_1 + A_2} = \frac{u_1}{u_1 + u_2} \,. \tag{4.9}$$

However, when θ_i is close to the beam axis u_i can be very small, and the evaporation of light particles that perturbs the fission fragment velocity vectors resulting in a significant spread in u_i, and poor definition of M_R.

The method used in this work avoids this effect. The conservation of linear momentum is applied to the reaction in the centre-of-mass frame using either the measured v_{par} or the expectation that $v_{par} = v_{c.m.}$:

$$A_1 v_{1c.m.} = A_2 v_{2c.m.} \tag{4.10}$$

Rearranging this equation gives:

$$M_R = \frac{A_2}{A_1 + A_2} = \frac{v_{1c.m.}}{v_{1c.m.} + v_{2c.m.}} \tag{4.11}$$

where $v_{c.m.}$ are obtained from v_{lab} by subtracting v_{par}.

The total kinetic energy (TKE) of the fission fragments, assuming the sum of their individual masses is the compound nucleus mass is given by:

$$< TKE >= \sum_{i=1}^{2} \frac{1}{2} m_i \, v_{i,c.m.}^2 \ . \tag{4.12}$$

This corresponds to the pre-neutron emission TKE for first-chance fission.

4.3.3 Energy loss correction

Both beam particles and fission fragments experience energy loss as they pass through the target (and backing) material. Therefore, 'dacube' was designed to account for these energy losses and derive the original velocities. It is assumed that the reaction takes place in the mid-point of the target layer.

The thickness and material of the target (A_{targ}, Z_{targ}), backing ($A_{backing}$, $Z_{backing}$), target angle and the beam energy are given in the input file for each run. The first energy correction is applied to the beam particles, namely the projectile (A_{proj}, Z_{proj}). The second correction is applied to the fission fragments. Initially, the masses and energies of the fission fragments are derived from the measured velocities. The energy loss in the target + backing requires information on both A, Z of the fragment. Fragment charges are estimated from the N/Z of the fissioning system. The code corrects the energies of the fission fragments then re-determines velocities through an iterative process. This correction uses the following steps:

(1) From the measured direction of the fragments and the target angle, it evaluates the thickness of target and backing material traversed, assuming interaction in the centre of the target layer;

(2) It calculates the energy loss in the target and backing using their stopping powers[3] [86], and the energy of an outgoing fission fragments calculated using m_i and v_i. The summation of this outgoing energy and the energy losses gives the new corrected energy of the outgoing fission particles;

(3) With this new corrected energy, velocities and masses are re-evaluated and the energy loss is re-estimated. The fragment energies are iteratively corrected through repeating step (2) until the corrected energy loss converges within 10 keV, or until 10 iterations have passed.

This method works very well for the thin targets ($<\sim$ 100 μg/cm^2) used in the measurements.

4.3.4 Determination of beam interaction time

The evaluation of fission fragment velocities is achieved through the determination of the optimum values of the time calibration parameters, including the effects of energy loss correction (T_0, δT_2, δT_3) to obtain the ToF, and hence the individual fragment velocities v_i. Therefore, the timing parameters are optimised until the binary FMT-fission events satisfy the following conditions:

I. $< v_{par} > = v_{CN} = v_{c.m.}$
The deduced average v_{par} ($< v_{par} >$) should be the mean velocity of the fissioning nuclei in the laboratory reference frame (v_{CN}). For the reactions and beam energies studied in this work, when fission results from complete fusion this should correspond to $v_{c.m.}$, the calculated centre of mass velocity. The expectation $< v_{par} > = v_{CN} = v_{c.m.}$ are used interchangeably. Using the conservation of linear momentum, v_{CN} (in units of cm/ns) is deduced from the reaction information as follows:

$$v_{CN} = 0.982 \frac{A_{proj}}{A_{proj} + A_{targ}} \sqrt{\frac{2E_{beam}\,(\mathrm{MeV})}{A_{proj}}} \tag{4.13}$$

where A_{proj} and A_{targ} are the mass numbers of the projectile and target nuclei and E_{beam} is the energy of the beam in the lab frame in MeV. The coefficient 0.982 is a constant factor for converting the atomic mass unit (u) to MeV/c^2.

II. $v_{perp} = 0$
Measured values are expected to form a distribution centred around $v_{perp} = 0$. Although fission fragments may have a small perpendicular velocity component due

[3] 'dacube' uses the J. F. Ziegler et al. (1985) for stopping power calculations. The current code is designed to calculate only for a single element. Therefore, for a compound target, the corrected target thickness which corresponds to the same energy loss in the single element must be given in the input file.

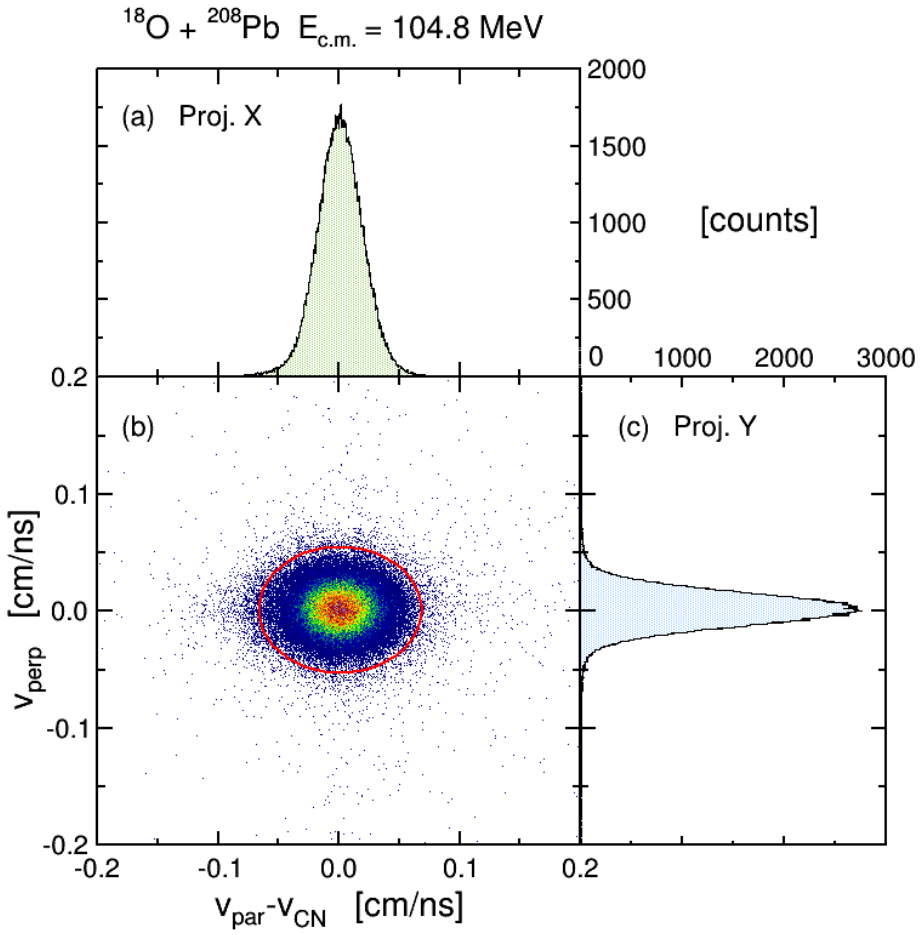

Figure 4.7: (b) Experimentally determined velocity components of the fissioning nuclei for ^{18}O + ^{208}Pb at $E_{c.m.}$ = 104.8 MeV, for fission events only. In reactions with Pb and lighter target, fission essentially results from the FMT reactions. The red elliptical gate selects FMT events for generation of the MAD. Panels (a) and (c) are projections onto the x-axis and y-axis of a scatter plot (a). T_0 is tuned until the FMT-fission events are centred at $v_{par} - v_{CN} = 0$.

to light particle emission both before and after scission, this does not compromise deriving the mass ratio (M_R) of the fission fragments.

Fig. 4.7b shows the distribution of ($v_{par} - v_{CN}$) *vs* v_{perp} for ^{18}O + ^{208}Pb at $E_{c.m.}$ = 104.8 MeV. All fission events are expected to originate from FMT fusion reactions. Therefore, the FMT-fission events should be distributed in the centre of Fig. 4.7b when (T_0, δT_2, δT_3) are optimised.

The parameters δT_2, δT_3 are determined using reactions[4] where mass-symmetric fusion-fission outcomes are expected, such as ^{18}O + ^{208}Pb, as shown in Fig. 4.8. They are adjusted until the mass ratio distribution (the projection of the MAD onto M_R) is symmetric about $M_R = 0.5$ at all angles as well as maintaining $< v_{par} > = v_{c.m.}$. As discussed in Section 4.2.5, once δT_2, δT_3 are fixed, only T_0 is adjusted for each beam species and

[4]In general, reactions on Pb, Au, and W targets are good candidates.

energy of the beam.

Although the description focuses on fission outcomes, elastic outcomes can also be used for the verification of velocity vector reconstruction since elastically scattered events follow the same kinematic reconstruction principle. This means the elastic events are also expected to be distributed in the centre of velocity vector plot. The width of the distribution for elastic scattering events arises from angular scattering in the target (which can be very significant for low energy recoils at angles approaching $\theta_{lab} = 90°$), elastic scattering at different depths in the target and the experimental time resolution. These effects are generally larger for elastic-recoil coincidence measurements than for fission-fission coincidences.

4.4 Fission event selection criteria

With successful setup of the timing calibration constants the velocities of binary events will be well reconstructed. The next step is satisfying the fission event selection criteria. Reconstructed binary events includes fission events, elastic scattering events, reactions with impurities in the target and backing, and coincidences where one fission fragment may be detected in coincidence with a projectile-like or target-like particle. To select out the desired fission events, a series of gates have been placed on the derived quantities. Although the spectra of individual reactions have slightly different characteristics depending on the reaction system and energy, Fig. 4.9a and Fig. 4.9b show the most common gates used to select fission events and remove other coincident events. The following sections illustrate how fission events differ from other coincident events in their kinematic features.

4.4.1 Separation of fission events from elastic scattering

Elastic scattering events are the dominant outcome. Since the velocity of the fissioning compound nucleus and that of the centre-of-mass are the same, the deduced velocities (v_{par} and v_{perp}) of elastically scattered particles and FMT-fission should be the same. A comparison of the masses best distinguishes fission from elastic scattering, thus they will be separated in spectra related to M_R and to a larger extent in TKE. As shown in Fig. 4.9a, a range of mass ratio values distinguishes fission (and quasifission) events from the elastically scattered events, which show two high intensity regions near the mass ratios corresponding to the projectile and target.

4.4.2 Reduction of contaminant events

Events from interactions with the target material are distinguished from those with other elements in the target, such as the backing material or impurities, by comparing v_{par} with the expected v_{CN}, as shown in Fig. 4.9a. Since v_{CN} is calculated for the desired reaction,

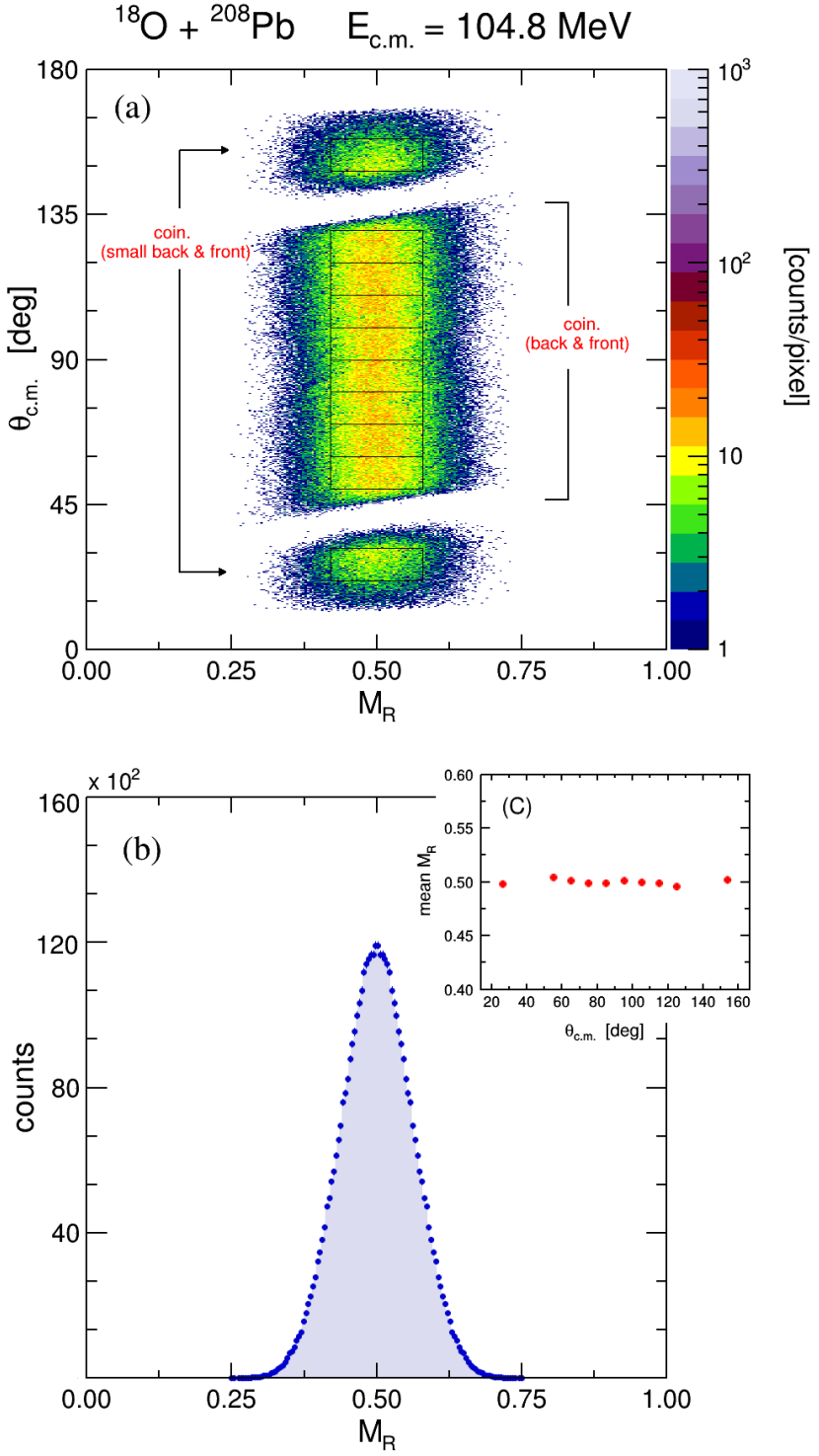

Figure 4.8: The ^{18}O on ^{208}Pb system is a good choice for determine the δT_2 and δT_3 parameters. (a) Shows the mass-angle distribution. It is tuned until (b) the observed M_R distribution becomes symmetric. To confirm that δT_i is optimised precisely, (c) a plot of the mean $\theta_{c.m.}$ *vs* M_R is useful, generated by applying gates centred on $M_R = 0.5$ for various angle bins in the MAD (black boxes in (a)). In particular, this system has no mass-angle correction (a signature of no significant QF), and mean values are consistent with $M_R = 0.5$ within calibration and statistical uncertainties.

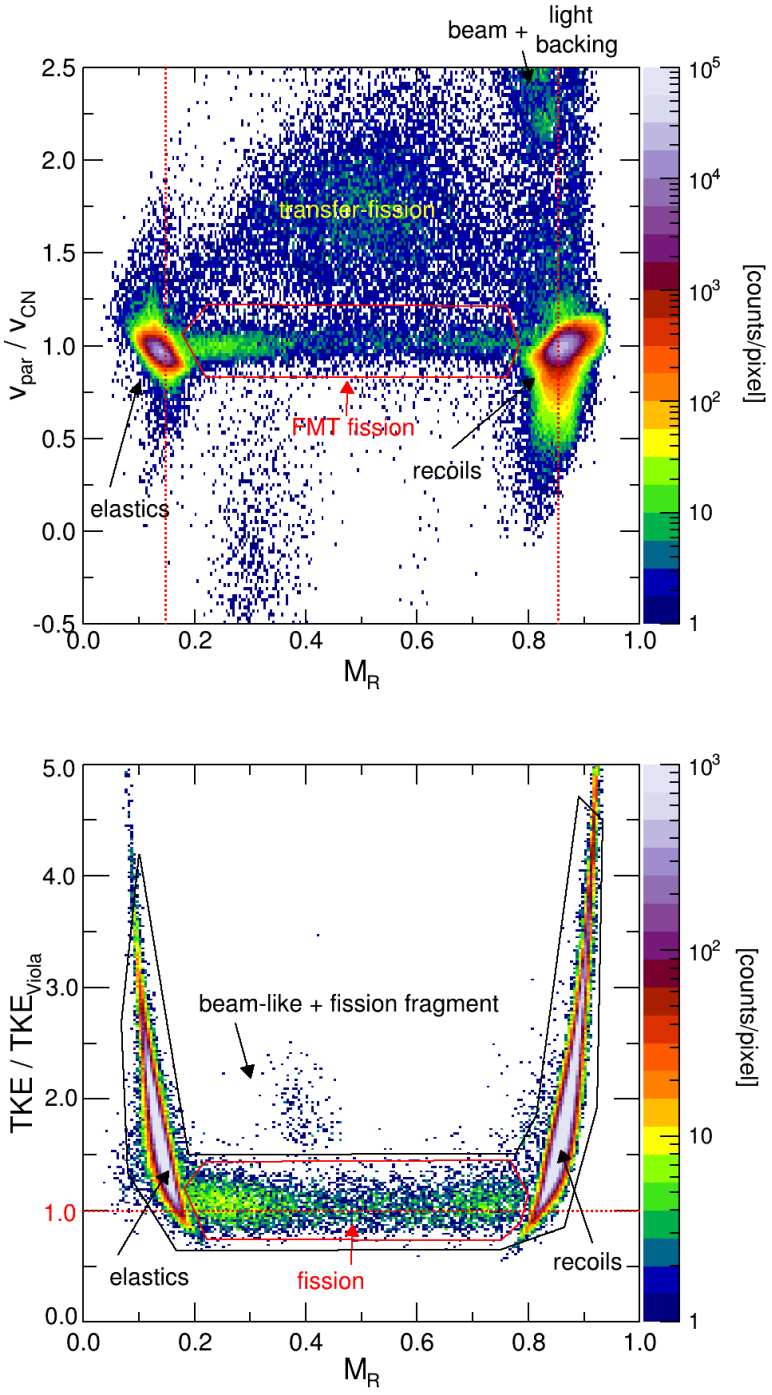

Figure 4.9: The most common figures showing distinguishing features for different reaction outcomes for ^{40}Ca + ^{232}Th at $E_{c.m.}$ = 193.1 MeV. Details of their features are discussed in the text. (a) Scatter plot of deduced M_R *vs* the ratio of v_{par} to the expected v_{CN}. Fission events populate the region between elastic scattering products. (b) Scatter plot of deduced M_R *vs* relative total kinetic energy (See text) after applying a FMT-boundary gate (e.g. Fig. 4.7). The black solid line shows the gate used to generate the MAD for FMT events, which normally includes the elastic scattering in order to observe the evolution of the fission fragments masses in MADs. The red polygon shows the gate used for the determination of the capture cross section.

binary events from those systems are grouped in the wrong place. Note that M_R is only correct for binary events when T_0 is optimised.

A comparison of the TKE of fission events with their expected values allows additional separation of fission events from random coincidence events and also can be used to check that the FMT-fission events are properly reconstructed. Fig. 4.9b shows a scatter plot of M_R against the experimentally determined TKE divided by the most probable TKE release for fission, defined by the Viola systematics [87]. TKE_{Viola} comes from a fit to light-ion induced fission kinetic energies. This represents fission where the projectile kinetic energy is fully damped (dissipated). According to Ref. [87], the average TKE (in MeV) is given approximately by

$$TKE_{Viola} = 0.1189\,\frac{Z_{CN}^2}{A_{CN}^{1/3}} + 7.3\,(\mathrm{MeV})\,. \tag{4.14}$$

For fission with a wide range of mass-split, this can easily be extended to derive a TKE dependent on the mass-split [85], where the 7.3 MeV has been absorbed into the term dependent on M_R .

$$TKE_{Viola}(M_R) = \frac{0.789(1-M_R)\,Z_{CN}^2}{[M_R^{1/3} + (1-M_R)^{1/3}]\,A_{CN}^{1/3}}\,. \tag{4.15}$$

By dividing the experimental TKE (M_R) by the Viola prediction ($\mathrm{TKE}/\mathrm{TKE}_{Viola}$ = RTKE) the fully damped events should lie close to the value RTKE = 1.

After applying a gate on FMT events (as shown in Fig. 4.7), three groups of events can be identified in Fig. 4.9b: (1) those corresponding to fission events (2) elastic scattering, and (3) non-fission coincidence events, originating from detection of one fission fragment in coincidence with a beam-like particle.

The fission events indeed lie along RTKE $\sim$ 1 throughout the fission M_R region, indicating that these events show essentially full energy dissipation. The two high intensity regions on either side of the fission events represent elastic and quaiselastic scattering events. Their distributions in TKE are elongated because the scattered particles are significantly faster than fission fragments, resulting in poorer energy resolution. Additionally, the very large number of elastic events results in the distribution appearing to be very wide. Events arising from fast particles, mainly projectile-like nuclei, in coincidence with a fission fragment, lie above the fission events. To reject those events, it is essential to apply a gate like the black polygon or the red polygon on the scattered plot of M_R *vs* RTKE depending on the final purpose of the dataset.

Once genuine coincident fission events were investigated, interested reactions outcomes were selected by applying appropriate gates. Chapter 5 describes investigation of the competition between fission following capture, and fission following transfer.

Chapter 5

Characterizing Fission following Capture and Transfer reactions

Overview

In this chapter, a systematic study of the ratio of full momentum transfer (FMT) fission (following capture) to transfer-fission has been investigated making use of each reaction's different kinematic properties. The dependence on charge product (Z_1Z_2) and beam energy are investigated. The relative yields of FMT-fission events and transfer-fission events as a function of Z_1Z_2 provides information to understand the influence of energy dissipation and its dependence on the density overlap of the colliding nuclei.

5.1 Classification of fission

5.1.1 Identification of FMT-fission and transfer-fission

^{232}Th is a heavy nucleus, and highly fissile, with a low fission barrier ($\sim$ 6 MeV) [27, 28]. This means fission can happen via two experimentally distinct pathways: fission following a transfer reaction, and fission following full momentum transfer (FMT). FMT-fission occurs when the momentum of the projectile has been completely transferred to the composite system after capture. In contrast, transfer-induced fission occurs from a target-like nucleus formed following nucleon transfer between the colliding nuclei resulting in an excitation energy higher than the fission barrier. The observation of the latter events is clear evidence of energy dissipation taking place in peripheral reactions. These two fission decay modes are distinguished using their kinematic properties, as described below.

5.1.1.1 Kinematical features

The kinematical properties of the reactions can be used to distinguish transfer-fission and FMT-fission. The outcomes of transfer-fission consist of two fission fragments with one projectile like nucleus (a 3-body system), whereas only a pair of fission fragments (a 2-body system) are observed for FMT-fission. Although the current detector system is

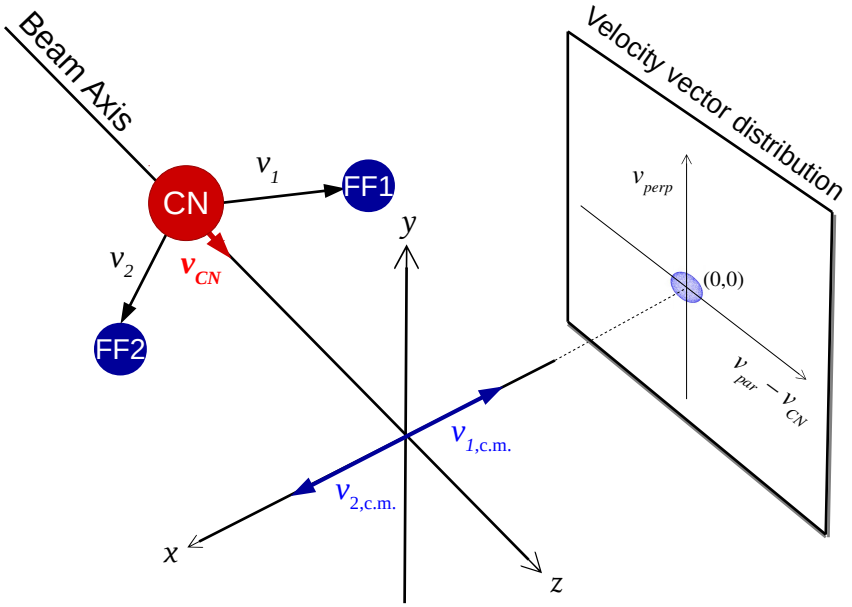

(a) Full momentum transfer fission.

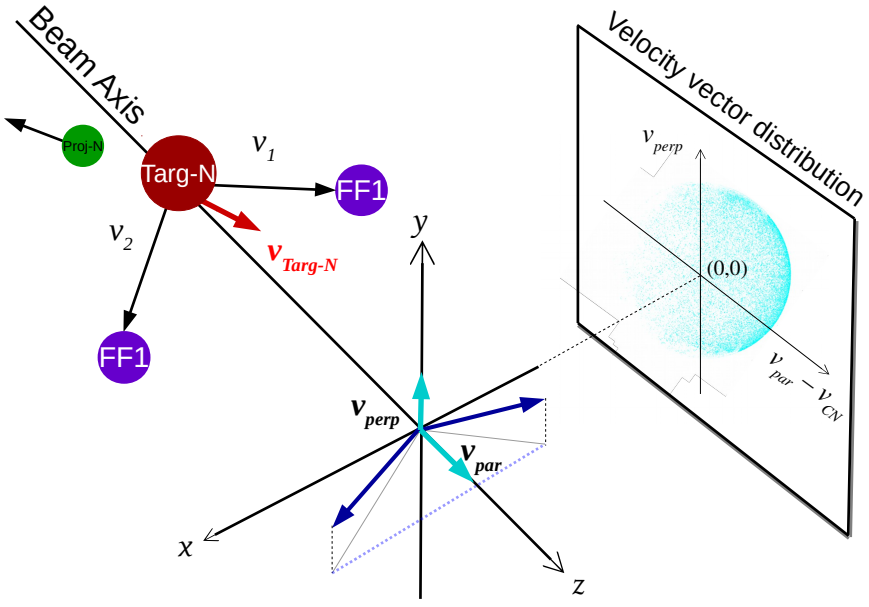

(b) Fission following a transfer reaction.

Figure 5.1: Kinematics of the two types of fission, transfer-fission and FMT-fssion (a) The FMT-fission events are co-planar with the beam axis and fragments travel back-to-back in the centre-of-mass frame. Velocities are tightly grouped in the centre of the velocity distribution (b) Unlike FMT-fission, a majority of transfer-induced fragments have a large perpendicular velocity component and can have larger or smaller parallel velocities depending on the beam energy and the mass of the projectile.

designed to detect a pair of fission fragments in coincidence, fission events reconstructed under the kinematic coincidence method distinguish the two different fission modes. They are distinguishable and separable to a large extent in the experimentally deduced source velocity vector distributions, (v_{par} - v_{CN}) *vs* v_{perp}.

Fig. 5.1 shows diagrams of the velocity vector components of the fissioning nucleus for the two processes. In the case of FMT-fission (Fig. 5.1a), fission fragments originating from the fused system travel back-to-back in the centre-of-mass frame (i.e. $\sum \vec{p} = 0$). Therefore, FMT-fission events are expected to travel with $< v_{par} > \; = v_{CN}$ and $v_{perp} = 0$, as discussed in Section 4.3.4. However, experimentally measured velocity vectors of FMT-fission events deviate slightly from the expectation due to the emission of light particles during collisions. Thus, these events are tightly populated in the centre of the source velocity distribution at (v_{par} - v_{CN}) = 0, $v_{perp} = 0$. In contrast, source vectors of transfer-fission events (Fig. 5.1b) lie on the surface of a set of spheres whose radii are determined by the momentum of the outgoing projectile-like nucleus. The projection onto the (v_{par} - v_{CN}, v_{perp}) plane results in most transfer-fission events being separated from the FMT-fission component.

5.1.1.2 Characteristics of FMT-fission and transfer-fission distributions

In practice, FMT-fission and transfer-fission events are separated using the source velocity distribution (v_{par} - v_{CN} *vs* v_{perp}), generated *after* applying a polygon gate on M_R between elastic and recoil peaks in a scatter plot such as Fig. 4.9b. Fig. 5.2 shows scatter plots of measured velocity components of fissioning nuclei for ^{232}Th reactions at $E/V_B \sim 1$ for each of the reactions measured in this thesis.

FMT-fission events form a tight distribution (events inside red gates) at the centre, around zero $(0, 0)$. The emission of light particles (mainly n, but also p and α particles) from the nuclei either before or after scission perturbs the fission fragment velocity vectors. It is insignificant, however, because the momenta of the emitted particles are small compared to those of the fission fragments [26].

Transfer-fission events show a much more diffuse distribution, but are constrained by kinematical limits that depend on the momentum of the recoiling projectile-like nucleus. For transfer reactions resulting in loss of mass from the lighter projectile nucleus (stripping), these limits force the events to be bounded inside of radius $v_{c.m.}$ at $(0, 0)$. But observed events are slightly offset from the expected limits, which is seen in all systems. These are two possible explanations for this. The first is transfer reactions resulting in a heavier projectile-like nucleus (pickup). Generally this is much weaker than the stripping process because of the increase in Coulomb energy if the projectile-like nucleus has higher charge. Optimum Q-values that account for the change in Coulomb energy following transfer are given in Table 5.1, and show that they are generally more negative for the

Table 5.1: The optimum Q-values for neutron (n), proton (p), and deuteron (d), and alpha particle (α) transfer reactions for the reactions studied in this work.

System	Optimum Q-value [MeV]											
	pick-up						stripping					
	n	***p***	***d***	***2n***	***2p***	***α***	***n***	***p***	***d***	***2n***	***2p***	***α***
^{18}O + ^{232}Th	-2.48	-9.00	-8.12	0.01	-11.09	-4.50	-3.26	-1.22	-1.89	-1.21	1.99	8.37
^{30}Si + ^{232}Th	0.15	-8.57	-6.35	4.23	-13.51	-3.99	-5.82	0.07	-4.15	-8.11	4.75	1.65
^{34}S + ^{232}Th	0.55	-9.16	-6.30	5.32	-14.15	-4.05	-6.63	2.36	-2.53	-9.08	7.65	3.70
^{40}Ca + ^{232}Th	1.92	-13.88	-8.05	8.29	-23.04	-5.01	-10.85	4.34	-3.51	-17.95	12.23	3.44
^{48}Ca + ^{232}Th	-1.29	-5.19	-4.85	-0.06	-5.80	-2.15	-5.16	-3.30	-6.43	-6.25	-2.47	-4.22

pick-up channels.

The second can arise from sequential fission from a heavy-target nucleus formed after a very asymmetric quasifission (QF) event. This reason is mainly relevant to Ca projectile reactions. Very asymmetric QF events may result in a projectile-like nucleus, which is heavier than the initial projectile (i.e. has more momentum), and if the complementary target-like nucleus undergoes fission (secondary fission), then this event can be outside the circle. Note that this type of fission also forms a 3-body since two fission fragments are produced (from the heavy target-like nucleus) as well as the projectile-like nucleus. According to Ref. [30], the fraction of sequential fission is insignificant. Therefore, in this work the 3-body system will be mainly referred to transfer-fission.

Unlike FMT-fission events, transfer-fission events show variations in source velocity distributions depending on beam energy and the mass of the projectile. Firstly, the size of a transfer-fission boundary is dependent on the mass of the projectile. As projectile mass increases, a larger momentum can be transferred to the target, leading to a larger recoil velocity of the fissioning nucleus.

Secondly, transfer-fission event distributions are skewed, unlike FMT-fission events in which the emission is isotropic. The distributions of transfer-fission events shown in Fig. 5.2 are reactions where the projectile-like nucleus travels backwards after a transfer reaction due to low beam energy, and consequently the target-like nucleus (fissioning nucleus) travel forward. In other words, the grazing angle is close to 180° for reactions at near or below the barrier. As a result, the parallel velocity (v_{par}) is greater than the centre-of-mass velocity ($v_{c.m.}$), which is equivalent to the expected v_{CN}. As beam energy increases, the grazing angle, and the projectile travels more forwards, and thus the target-like nucleus moves more backwards, resulting in $v_{par} < v_{c.m.}$ (e.g. Fig. 5.5 at $E/V_B = 1.191$).

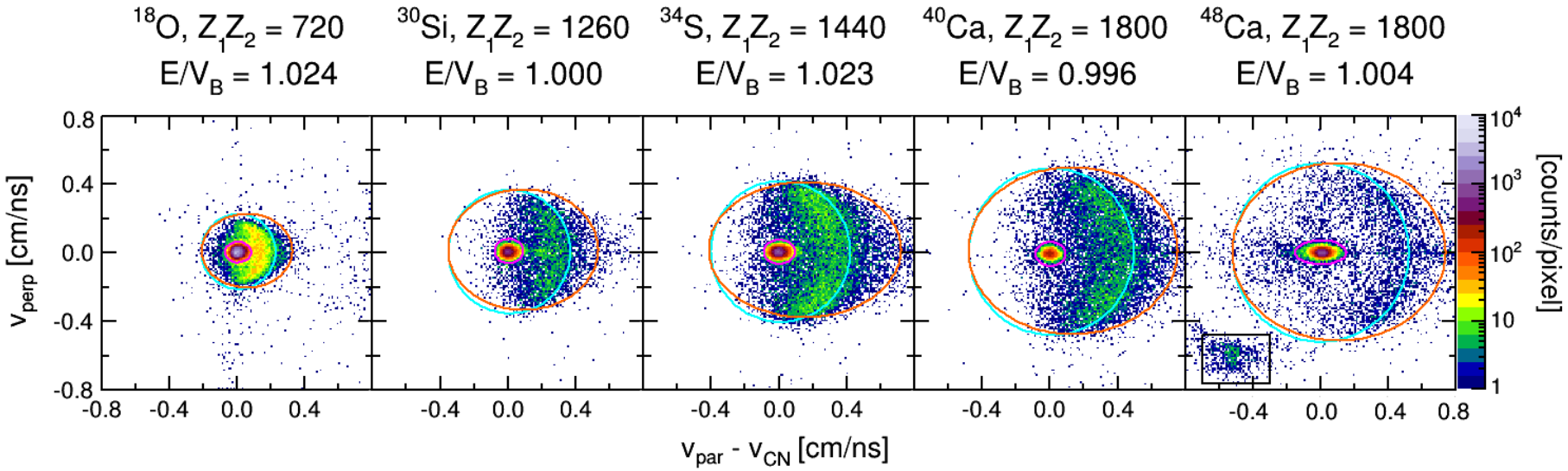

Figure 5.2: Experimentally determined velocity vector components of the fissioning nuclei for ^{18}O, ^{30}Si, ^{34}S, ^{40}Ca, and ^{48}Ca + ^{232}Th systems (labelled with Z_1Z_2) at the near-barrier energies (E/V_B) indicated. The small pink elliptical gate is the gate separating FMT-fission events and is applied to generate the FMT MAD. Transfer-fission events should be generally constrained inside a circle of radius v_{CN} (cyan circle). As discussed in the text, there are mechanisms that can results in events outside this limit (orange ellipse), and these are seen increasingly for heavier projectiles. The events inside a rectangle for the ^{48}Ca reaction are spontaneous fission events of ^{248}Cm, placed on the same target ladder.

5.1.2 Identification of fusion-fission and quasifission

5.1.2.1 Mass-angle distributions

With increasing Z_1Z_2, the FMT-fission of the composite system splits into two pathways since complete fusion has to face a strong competing process, QF [30, 31]. Experimentally, it is difficult to separate QF from fusion-fission since QF exhibits similar characteristics as fusion-fission, such as full energy dissipation and considerable transfer of mass between the two constituents. However, there are methods to identify the presence of QF in fusion reactions. Here we used mass-angle distributions (MADs) and their projected mass-ratio (M_R) distributions. The MAD is only valid for FMT-fission events since calculation of M_R and $\theta_{c.m.}$ relies on two-body kinematics, thus requiring elimination of transfer fission events by gating around the FMT-fission boundary (see Fig. 5.2). In this section, since interpreting MAD features is important for fast QF identification, a brief introduction of the MAD is given below. In the next chapter (Section 6.3.3), details are given on how fission fragments are displayed in MADs, in particular the mirroring process is explained in detail.

Typically, MADs display fission events together with elastic scattering events to visualize the evolution of the dinuclear system and include other possible reaction channels, such as quasi-elastics (close to elastic scattering), fast QF, and deep inelastic reactions. For reactions with the lighter projectiles like ^{18}O in this work, elastically scattered particles are absent since detector electronics thresholds were able to reject elastic events, whilst accepting all fission events.

The MAD displays a single fission event as a pair of detected fragments by mirroring the coincidence events about $M_R = 0.5$ and $\theta_{c.m.} = 90°$ [55]; one fragment is at (M_R, $\theta_{c.m.}$) and its complementary fragment is at ($1-M_R$, $180° - \theta_{c.m.}$). The scale of counts given by the colour scheme is directly proportional to $d^2\sigma/d\theta dM_R$ due to the constant acceptance in the azimuthal angle $\Delta\phi$, discussed in Section 6.3.3, except at the forward and backward detector edges. MADs of ^{48}Ca + ^{232}Th are displayed without elastics, and the colour scheme directly represents $d^2\sigma/d\theta dM_R$. Because the ^{48}Ca + ^{232}Th data were measured using a 3-MWPC configuration, a wider angular range is covered.

The following figures show all the systems examined in this work, at all energies measured. Each figure shows the source velocity distributions in the top panels and experimental FMT MADs in the bottom panels.

(a)

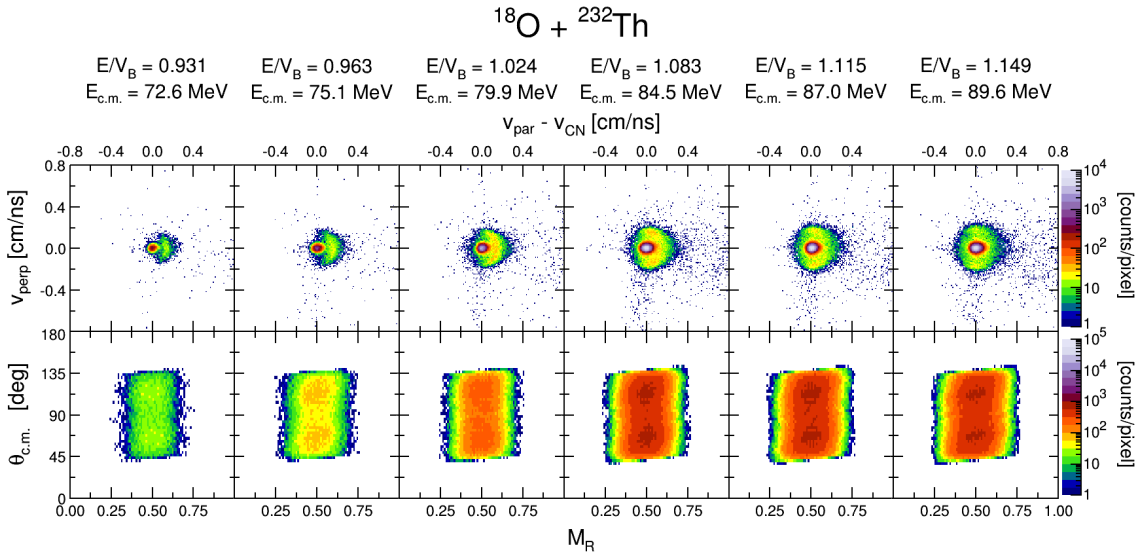

(b)

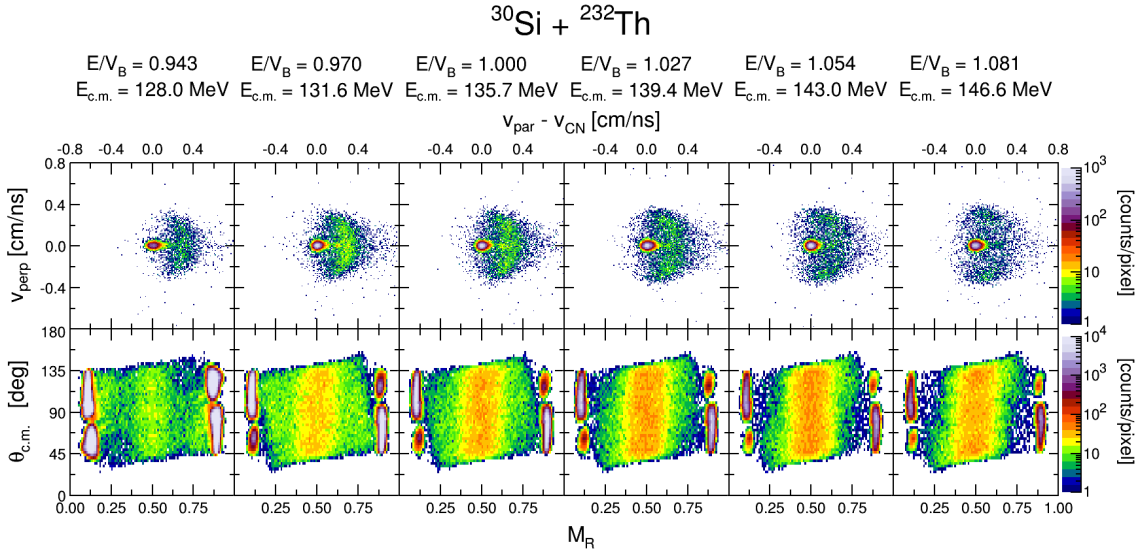

Figure 5.3: (a) For ^{18}O + ^{232}Th reactions and (b) for ^{30}Si + ^{232}Th reactions, the upper panels show experimentally deduced velocity components of fission fragments $v_{par} - v_{CN}$ and v_{perp}. The lower panels show experimental MAD of FMT events. The centre-of-mass energy is given for each measurement, and the energy with respect to the capture barrier [81] denoted by E/V_B.

(a)

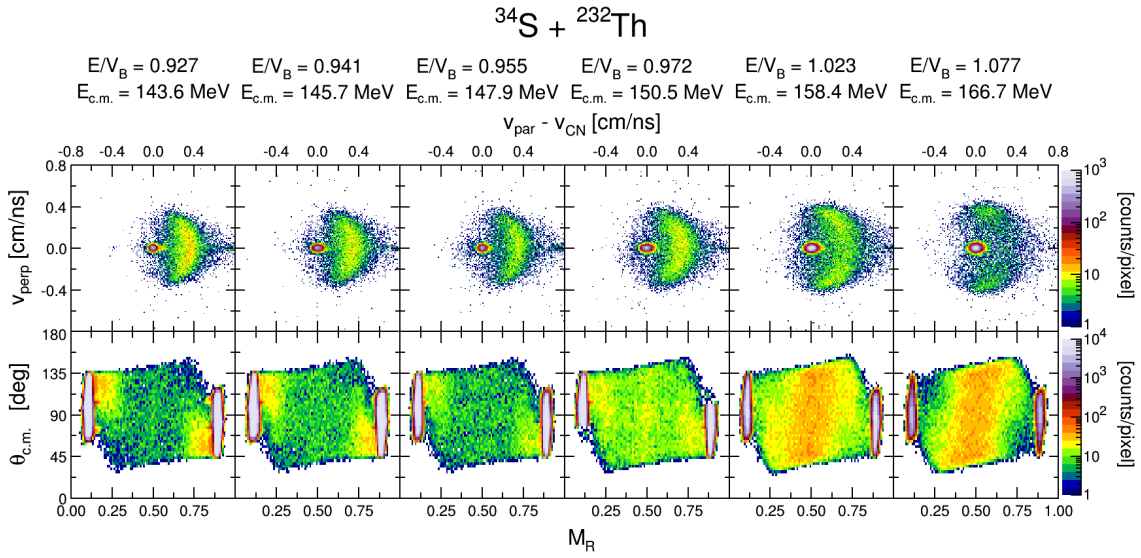

(b)

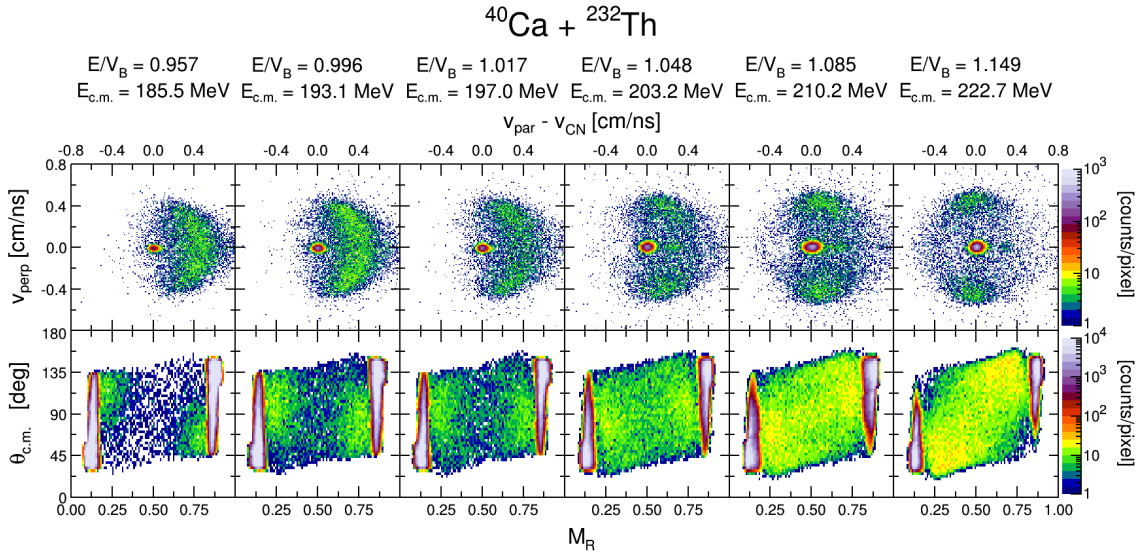

Figure 5.4: (a) For ^{34}S + ^{232}Th reactions and (b) for ^{40}Ca + ^{232}Th reactions, the upper panels show experimentally deduced velocity components of fission fragments $v_{par} - v_{CN}$ and v_{perp}. The lower panels show experimental MAD of FMT events. The centre-of-mass energy is given for each measurement, and the energy with respect to the capture barrier [81] denoted by E/V_B. In case of the ^{34}S + ^{232}Th reactions, elastically scattered events are not visible at the forward angles since the energy signal for the recoiling target nucleus at backward angles is below the detector threshold.

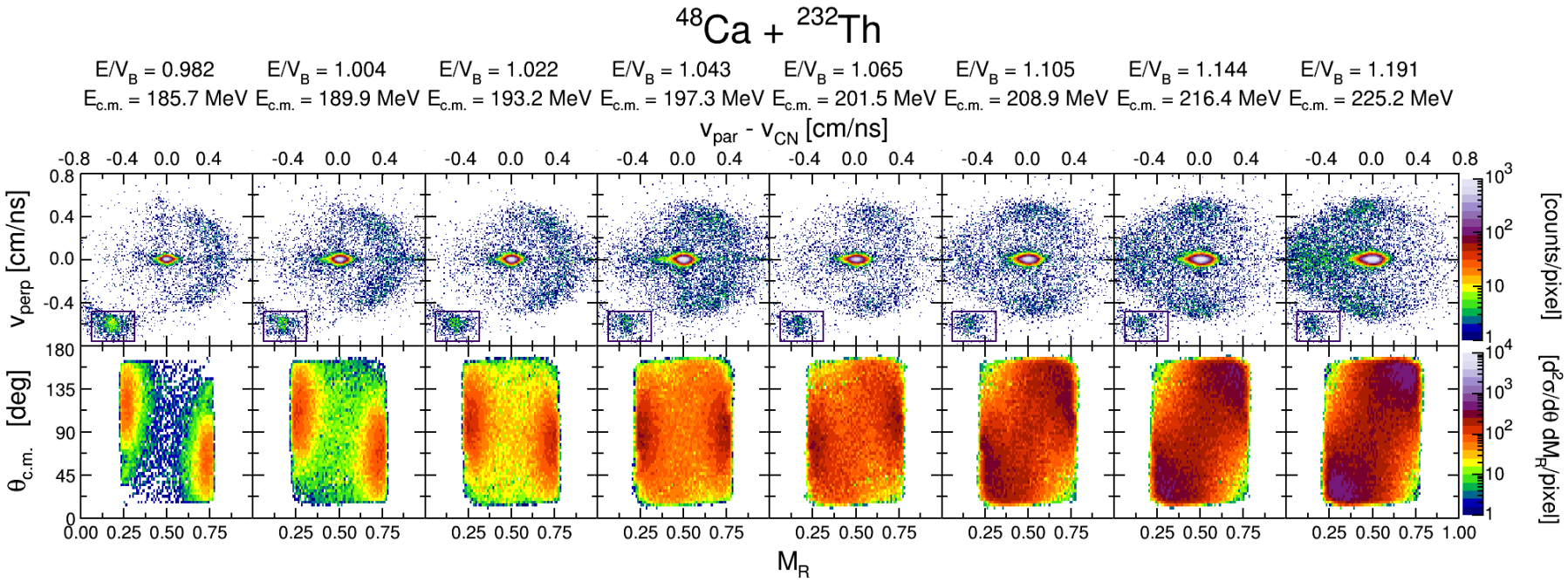

Figure 5.5: For the ^{48}Ca + ^{232}Th reaction, the top panels show experimentally deduced velocity components of fission fragments $v_{par} - v_{CN}$ and v_{perp}. Events inside the rectangle box are spontaneous fission of ^{248}Cm, which had been placed on the same target latter. The lower panels shows experimental MAD scatter plots without elastics at energies from below to well-above the fusion barrier for ^{48}Ca + ^{232}Th.

5.1.2.2 Classification of reactions depending on the observation of a mass-angle correlation

Having presented all the FMT-fission MADs in Figs. 5.3, 5.4, and 5.5, a description of their features is given here. Depending on the lifetime of a dinuclear system while rotating, a correlation between fission fragment masses and their corresponding emission angles is observed in MADs. The fast QF process shows a strong mass-angle correlation since a short contact time allows only a small amount of mass exchange and small rotation angle. As the contact time gets longer, more mass exchange occurs between the two constituents and eventually, the system reaches mass equilibrium. Once the dinuclear system undergoes more than one revolution, the masses of fission fragments are no longer correlated with emission angle, resulting a symmetric mass distribution, peaked at $M_R = 0.5$.

In this work, we classify the systems as *light* or *heavy* systems, depending on the presence of fast QF. This is required in order to determine the capture cross sections, as discussed in Chapter 6. The presence of fast QF in the FMT-fission events was confirmed by observation of a mass-angle correlation in the MADs, showing asymmetry about 90° of the yield for a given mass ratio other than $M_R = 0.5$. ^{18}O + ^{232}Th and ^{30}Si + ^{232}Th are classified as light systems. ^{34}S + ^{232}Th , ^{40}Ca + ^{232}Th and ^{48}Ca + ^{232}Th are classified as heavy systems.

In general, there is a strong mass-angle correlation seen in the heavier system (Fig. 5.4 and Fig. 5.5) compared to the lighter system (Fig. 5.3). MADs of ^{18}O + ^{232}Th reactions show symmetric mass-distributions peaked at $M_R = 0.5$ and symmetric angular distributions around $\theta_{c.m.} = 90°$. As Z_1Z_2 increases, the MADs show asymmetric distributions, a clear experimental signature of fast QF products. Table 5.2 summarises the features of the MADs for each system.

Table 5.2: Summary of quasifission (QF) observations from MADs and M_R distributions for the systems studied.

Figure	**System**	Z_1Z_2	**Presence of QF**	**General features**
Fig. 5.3a	^{18}O + ^{232}Th	720	Fusion-fission characteristics dominant	- No mass-angle correlations. - Symmetric mass distribution, centred at $M_R = 0.5$. - Narrow width of M_R-distribution.
Fig. 5.3b	^{30}Si + ^{232}Th	1260	Onset of QF Energy dependent	- Weak mass-angle correlations. - Broad width of mass distributions compared to ^{18}O + ^{232}Th system.
Fig. 5.4a Fig. 6.10b	^{34}S + ^{232}Th	1440	QF dominant Energy dependent	- Strong mass-angle correlations. - Energy dependent with strong mass asymmetric components at $E < V_B$. - Fission components centred on mass symmetry with an increase of energy.
Fig. 5.4b Fig. 6.11b	^{40}Ca + ^{232}Th	1800	QF dominant All beam energies	- Strong mass-angle correlations. - Strong mass-asymmetric components for all energies. - Fission fragments are uniformly distributed over a range of M_R as energy increases.
Fig. 5.5 Fig. 6.15	^{48}Ca + ^{232}Th	1800		

5.2 Detector angular coverage

The fragment detection efficiency varies depending on the folding angles, θ_{12} and ϕ_{12} of a pair of fission fragments, these angles being between their velocity vectors. The geometry of the CUBE detector system was carefully configured in view of the geometrical efficiency to detect fission fragments, considering their angular correlation in the laboratory frame when travelling towards each of the MWPCs. The arrangement of MWPCs was set up originally to detect FMT-fission events, based on expected folding angles, but not for transfer-fission events. Therefore, the detection efficiency of transfer-fission events must be examined in this work.

Through a direct comparison between FMT-fission (capture) and transfer-fission yields, the influence of energy dissipation on fusion reactions with an increase in the density overlap of the colliding nuclei is investigated in this work. Before extracting the number of both events from the source velocity distributions by applying gates shown Fig. 5.2, a careful selection of the detector angular coverage is required in the analysis to avoid missing transfer-fission events and also FMT-fission events. Some fission fragments may have folding angles that extend beyond the CUBE detector geometry, meaning that only one of the fragments is detected. To ensure that we had adequate solid angle coverage for both events, the efficiency of detecting both fission fragments was tested with the method given below.

5.2.1 Folding angles of fission fragments

A framework for checking that the coincidence detection efficiency is essentially 100% for both FMT-fission and transfer-fission is to look at the position distribution (in angle) in the front detector, θ *vs* ϕ, after gating on a certain angular range in the back detector. Then one determines whether fission fragments are clustered well-inside the front detector boundary (the polygon shown in Fig. 5.6b corresponds to the edges of the front detector). If the fission fragments lie up to the edge of the front detector, there is a high chance to miss the detection of some fission fragments. For example, in the ^{18}O + ^{232}Th reaction at $E_{c.m.}$ = 89.6 MeV, selecting the angular coverage in the back detector to be $90^\circ < \theta_{lab} < 110^\circ$ and $150^\circ < \phi_{lab} < 210^\circ$ (indicated by the red rectangle in Fig. 5.6a). The complementary fission fragments of FMT-fission and transfer-fission events observed in the front detector are shown in Fig. 5.6b and 5.6c, respectively. Fission events following the FMT reactions are tightly grouped, while fission events following transfer reactions spread further from the centre of the front detector ($\phi_{Front} = 0^\circ$).

Before describing the details of finding optimal angular ranges, given in the following section, the velocity vectors of fission fragments and their geometrical relations with respect to the MWPC arrangement need to be understood. The arrangement of back and front MWPCs had already been set to take into account the most efficient range of

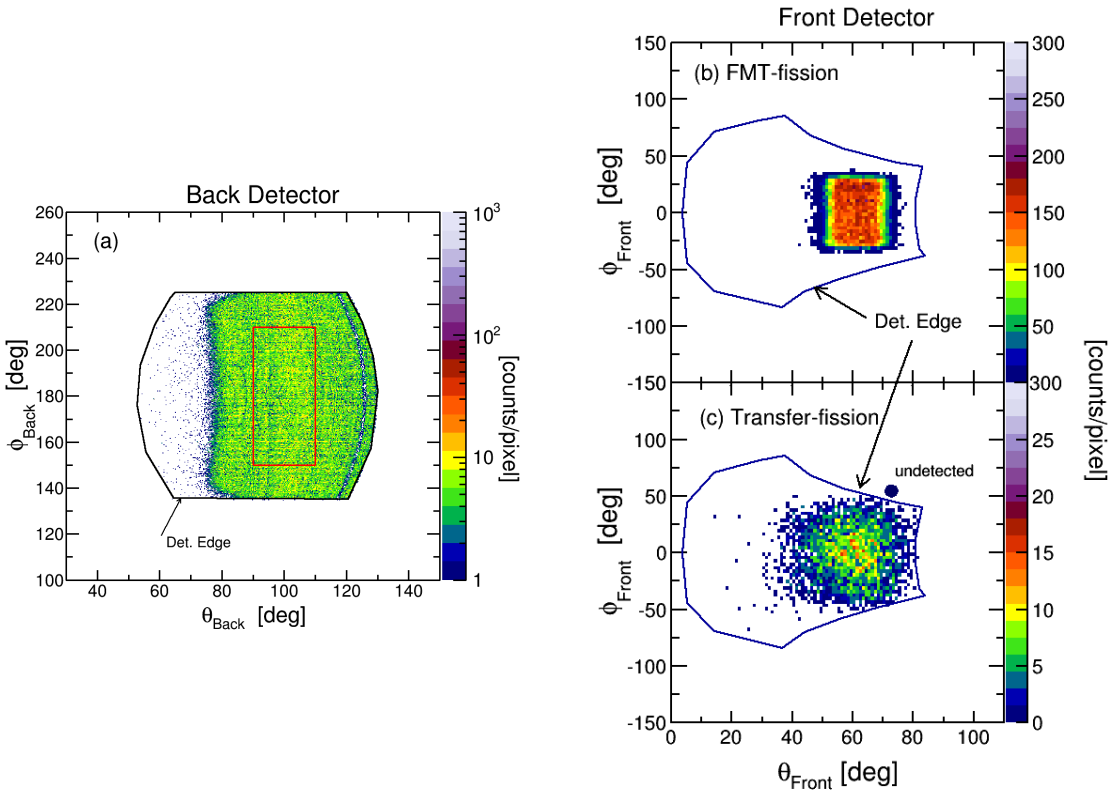

Figure 5.6: Position distributions in angle for the ^{18}O + ^{232}Th reaction at $E_{c.m.}$ = 89.6 MeV. (a) Fission fragments detected in the back detector. The red rectangle is a gate testing whether their complementary fission fragments are well-inside the front detector edges or not. (b) FMT-fission events are tightly grouped inside the front detector. However, (c) transfer-fission events spread out and some of events are close to the front detector edge. This shows that there is a higher possibility to miss transfer-fission events detections compared to FMT-fission events. Note that these figures were generated with different bin sizes.

scattering angles θ. Depending on the mass and beam energy of the projectile nucleus, the position distributions of the FMT-fission events detected in the front and back detectors (in the lab frame) were different, as shown in Fig. 5.7a. The folding angle θ_{12} depends on the centre of mass velocity ($v_{c.m.}$), which can be calculated by Eq. 4.13. For transfer-fission events the prediction of correlation angles is more difficult, and depends strongly on the beam energy. The angular range that gives full efficiency for transfer-fission events has been determined empirically through the detection efficiency test described in the following section.

Except at the very top and bottom of the back detector edges, back-to-back fission fragments (FMT-events) having $\phi_{12} = 180°$ can be detected by both MWPCs. However, fission fragments resulting from transfer reactions have ϕ_{12} larger or smaller than 180° depending on the momentum transferred from the projectile-like nucleus to the target-like nucleus. As the projectile becomes heavier, more momentum is transferred to the target-like nucleus, leading to larger recoil velocities. Consequently, some ϕ_{12} may go beyond

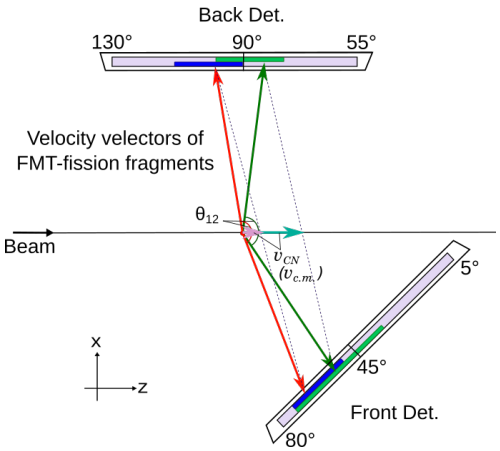

(a) View in-beam direction

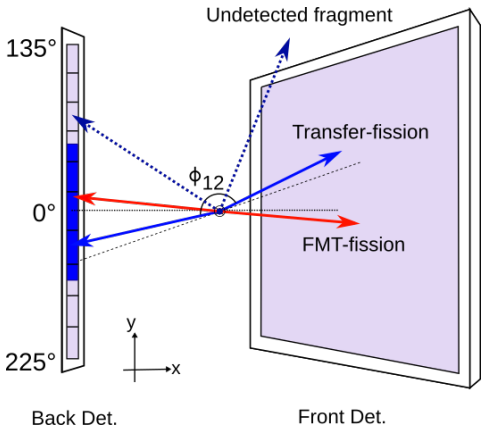

(b) Top view

Figure 5.7: Schematic view of folding angles, θ_{12} and ϕ_{12} of a pair of fission fragments. (a) A pair of green vectors is a case for a large expected compound nucleus v_{CN} (e.g. ^{40}Ca + ^{232}Th) whereas that of red vectors is a case for a small v_{CN} (e.g. ^{18}O + ^{232}Th). Once a gate (indicated by the green or blue box) is applied to the back detector, the complementary fission fragments were found inside the green (or blue) box in the front detector. (b) There is a higher chance of undetected fission fragment pairs for transfer-induced fission due to the probability of large perpendicular velocity component compared to FMT-fission.

the CUBE detectors' geometry, meaning that detection of both fragments fails as shown in Fig. 5.7b. Therefore, a careful selection of an optimal ϕ range is required especially for fission following transfer reactions.

If the event detection efficiency for FMT and transfer-fission is different, the yields cannot be compared. Therefore, the following section describes the tests used to determine the appropriate ranges to compare the two types of events.

5.2.1.1 Detection efficiency test

A systematic investigation was carried out by comparing the ratios of transfer-fission to FMT-fission yields for uniform cuts in ϕ with an interval of $\Delta\phi$ for a fixed θ_{lab} range, or vice versa for checking θ_{lab} coverage. Here the ϕ angular coverage determination is explained. The same procedure was also carried out for θ_{lab} coverage.

For example, the ϕ angular coverage with a fixed θ range in the back detector was divided into intervals of 10°. The ratio of the number of transfer-fission to FMT-fission events in each of sliced gates were compared, as shown in Fig. 5.8. If there is no efficiency drop as ϕ varies, the ratio should be constant. As the gate gets close to the bottom or top of the back detector edges, the detection efficiency drops and thus the ratio falls. In general, applying a rectangle gate ($\Delta\theta \times \Delta\phi$) in the centre of the back detector (centred at $\phi = 180°$) results in both types of events being detected with full efficiency for most of reactions.

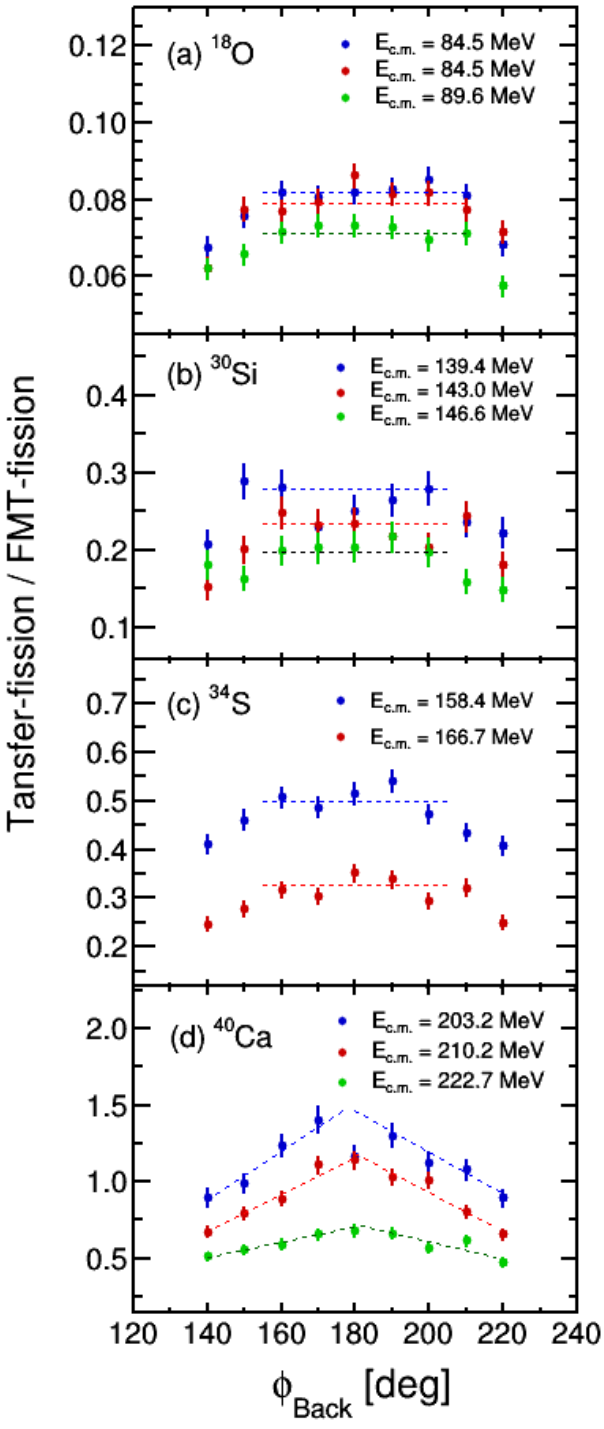

Figure 5.8: Ratio of transfer-fission to FMT-fission events at $E > V_B$ as a function of the mid point of an interval of with $\Delta\phi = 10°$. The range of θ for all systems is given in Table 5.3. Dashed lines refer to relatively constant ratio ranges. (a) Is for ^{18}O + ^{232}Th, (b) for ^{30}Si + ^{232}Th, and (c) for ^{34}S + ^{232}Th. (d) Unlike the above three systems, ratio shows no constant region for ^{40}Ca + ^{232}Th. This is why ^{40}Ca + ^{232}Th system required a different way of extracting the number of events. The details are described in Section 5.2.1.2.

Table 5.3: Selected angular ranges allowing full-efficiency comparison of FMT-fission and transfer-fission yields.

System	E_{beam} range	θ^{lab}_{Back} range	$\Delta\theta$	ϕ^{lab}_{Back} range	$\Delta\phi$
$^{18}O + ^{232}Th$	$E < V_B$	90° - 110°	20	145° - 215°	70
	$E > V_B$			150° - 210°	60
$^{30}Si + ^{232}Th$	$E < V_B$			145° - 215°	70
	$E > V_B$			150° - 205°	55
$^{34}S + ^{232}Th$	$E < V_B$	85° - 120°	35	150° - 210°	60
	$E > V_B$			155° - 205°	50
	v_{perp} range				
$^{40}Ca + ^{232}Th$	$v_{perp} > 0$	75° - 105°	30	135° - 165°	30
	$v_{perp} < 0$			195° - 225°	30

Although the ratios are slightly fluctuating in the angular range close to 180° due to poor statistics (each gate contains only ∼ 6% of the total fission events seen in the full active area), the ratios can be regarded as constant for $^{18}O + ^{232}Th$, $^{30}Si + ^{232}Th$, and $^{34}S + ^{232}Th$ within the ϕ ranges given in Table 5.3. The ratios for $^{40}Ca + ^{232}Th$ measurements are falling from $\phi_{Back} = 180°$, unlike the reactions with the lighter projectiles. This indicates that even for a gate in the middle of the detector, some transfer-fission events are undetected. To resolve this problem, a different approach is required to extract the number of transfer-fission events, as described below.

5.2.1.2 Detection efficiency test for $^{40}Ca + ^{232}Th$

For $^{40}Ca + ^{232}Th$, the central gate in ϕ_{Back} does not provide full efficiency for transfer-fission due to the large recoil velocity of the fissioning nucleus, resulting in source of the coincident fission fragments passing outside the front detector. Therefore to determine the yield, fission fragments following transfer reactions were divided into two groups, those having a positive perpendicular velocity group and those with a negative perpendicular velocity. The complementary fission fragments of each group can be captured in different ϕ ranges. For example, Fig. 5.9a and Fig. 5.9b show the events in the negative velocity group are well inside the front detector active area if the ϕ range indicated with the orange box is selected. A case where some transfer-fission events will be undetected is shown in Fig. 5.9c and Fig. 5.9d. This shows that events in the positive group are well inside the front detector boundary if the ϕ_{Back} range (blue box) is close to the top of the back

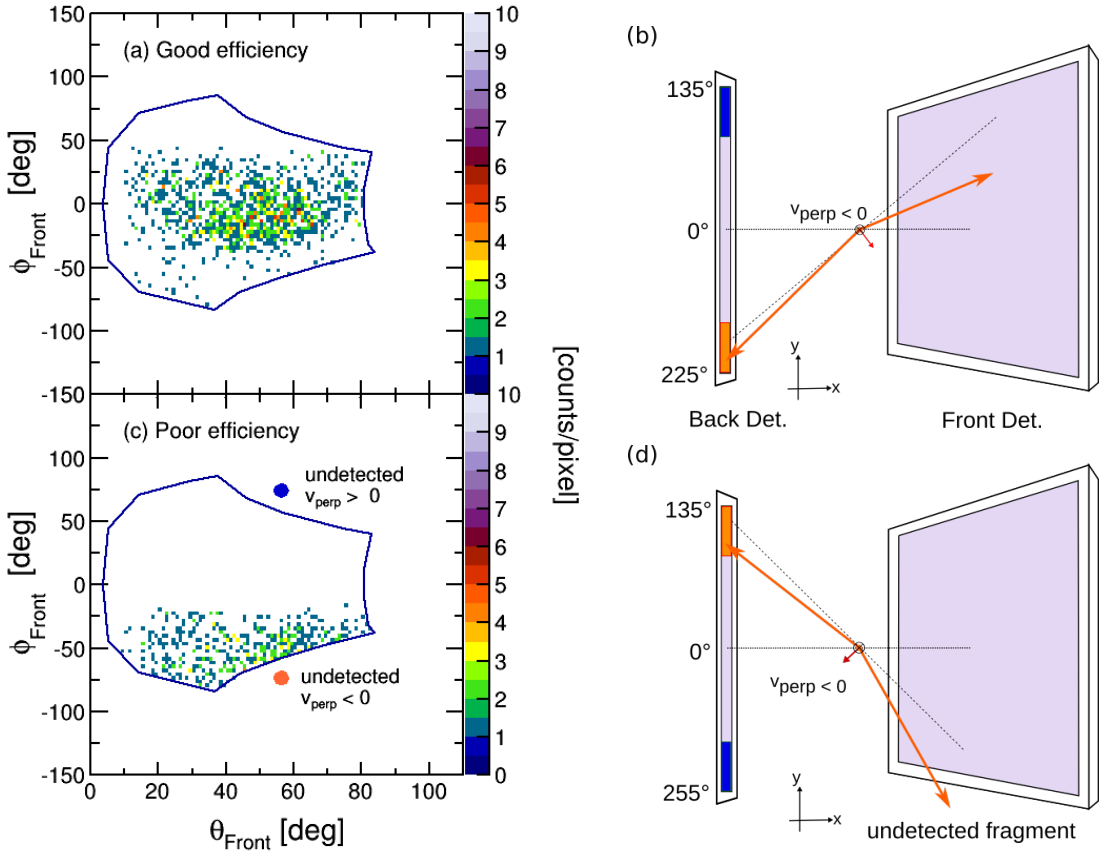

Figure 5.9: Determination of detection efficiency of transfer-fission fragments for ^{40}Ca + ^{232}Th. Fission is divided into two groups depending on the perpendicular velocities, positive or negative. Orange boxes are the ϕ ranges for the events in the negative group and blue boxes for the events in the positive group. Panels (a) and (b) show the case of events lying well inside the front detector boundary whereas panels (c) and (d) shows the case where the efficiency drops due to events lying close to and outside the edge of the detector.

detector, however some events might be undetected if the ϕ_{Back} range is in the opposite end of the back detector. Therefore, the number of transfer-fission events were extracted from the two separate group with different ranges of ϕ angular coverage given in Table 5.3. Unlike transfer-fission, fission following FMT are nearly constant over the ϕ range and thus the average of counts from the two ranges were taken to plot Fig. 5.10. The next section discusses the results of comparison yields of transfer-fission and FMT-fission for all systems.

5.3 Systematics of transfer-fission probabilities

The numbers of FMT-fission and transfer-fission events were extracted from the measured velocity vector scatter plots as described in Section 5.2.

The total fission events (N_{Tot}) are the sum of the FMT-fission (N_{FMT}) and transfer-fission events (N_{TF}). Fig. 5.10a shows the ratio of N_{FMT} to N_{Tot} as a function of the beam energy normalised by the barrier. The errors of the ratios were obtained from the error propagation of the statistical errors. The results provided for ^{19}F + ^{232}Th [62, 63] had been extracted from the difference between total fission and FMT-fission cross sections.

This work is interested in beam energies above the capture barriers. Fusion reactions are governed by quantum tunnelling at energies below the barrier, resulting a significant suppression of fusion, whereas it is known that transfer reactions extend much further below the barrier. Thus the increasing fraction of transfer-fission below-barrier is expected. Consequently, the ratio increases rapidly as energy decreases. Above-barrier, the fraction of N_{FMT}/N_{Tot} appears to be approaching a saturation value. However, that value depends strongly on Z_1Z_2, varying from 10% transfer-fission for ^{18}O + ^{232}Th to $>$ 40% transfer-fission for ^{40}Ca + ^{232}Th.

An increase in Z_1Z_2 is equivalent to an increase of the density overlap of the colliding nuclei at the barrier. A large density overlap, indicating more interaction between the two nuclei, appears to result in an increase of the transfer reaction probability relative to capture. The enhancement in transfer-fission for collisions between larger nuclei, associated with larger density overlap, may be happening at the expense of the capture cross section. To address this question in a quantitative way, FMT-fission cross sections must be determined, as discussed in the following chapter.

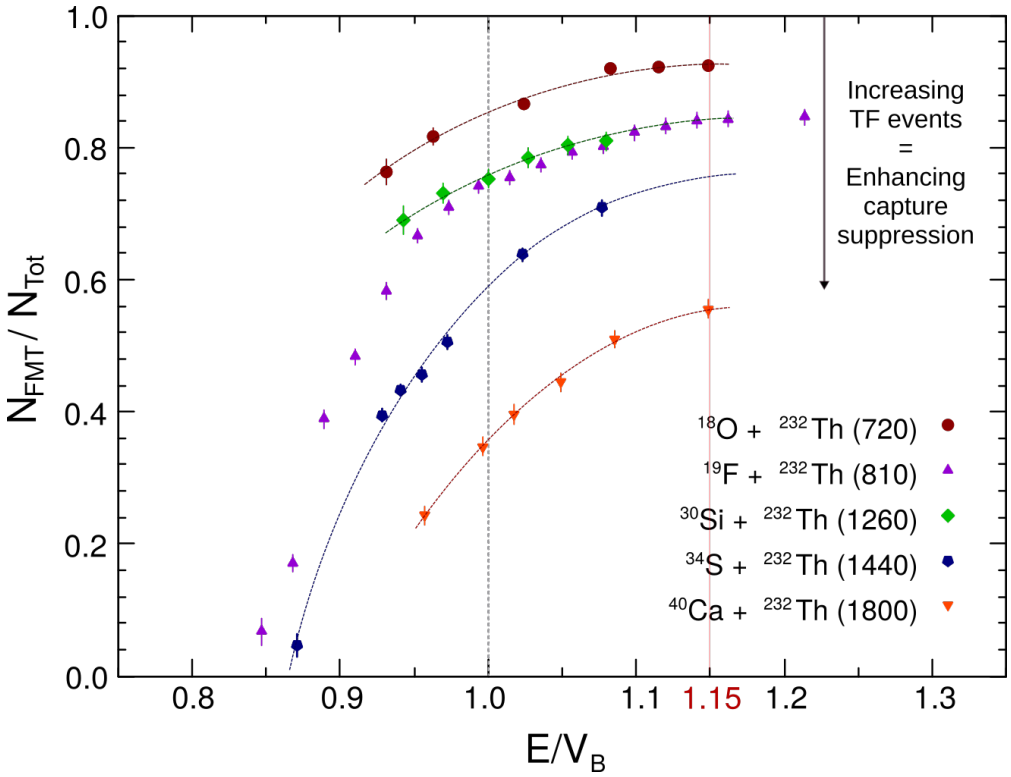

Figure 5.10: The ratio of FMT-fission (N_{FMT}) to the total fission (N_{Tot}) as a function of energy normalised to the capture barriers. The numbers inside the brackets are the product of the charges of the colliding nuclei (Z_1Z_2). As Z_1Z_2 increases, the transfer-fission events increase and consequently enhance the suppression of capture. The curve lines guide the eye to estimate N_{FMT}/N_{Tot} at $E/V_B \simeq 1.15$. These estimated ratios for all systems will be discussed in Chapter 7.3.

Cross Section Determination

Overview

To quantify fusion suppression, it is necessary to extract the capture cross sections and compare them with expectations from a model without energy dissipation mechanisms outside the capture barrier radius (the coupled channels model). This chapter describes how absolute cross sections of fission-like processes following capture (full momentum transfer fission) are determined. It describes two methods which are used for extrapolation to 0° and 180° in order to integrate over the full angular range to get the total capture cross sections. One uses a model of fusion-fission angular distributions, fitting experimental data with calculations, and the other is via an empirical model of quasifission called 'Quasisim', which calculates a MAD based on an empirical sticking time distribution matched to the experimental MAD.

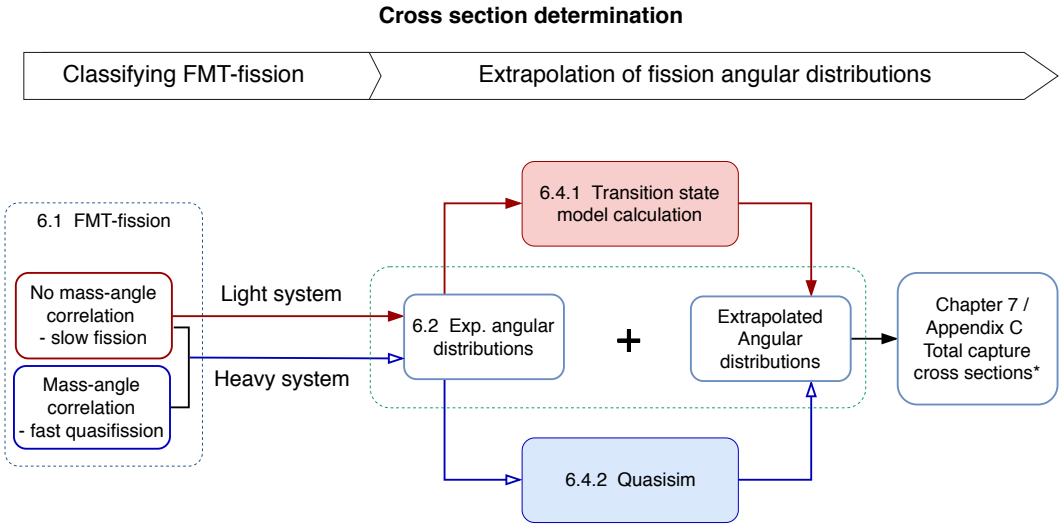

Figure 6.1: Flow chart of capture cross section determination depending on the category of the system, light or heavy, classified by whether there is a mass-angle correlation or not. An interpretation of the total capture cross sections for all systems is discussed in Chapter 7 and their values are given in Appendix C.

6.1 Classifying FMT-fission reactions

The term **fusion** is used to describe the merging of two colliding nuclei to form a new compound nucleus (CN), at its (compact) equilibrium deformation. The presence of quasi-fission (QF) for collisions with higher Z_1Z_2 requires a change in terminology. QF is associated with passage inside the entrance-channel potential barrier, but not formation of a compact CN. The term **capture** is used to describe the sum of QF and true fusion, since fission following fusion can be difficult to separate from QF. Both correspond to collisions overcoming the entrance-channel (capture) barrier. For the reactions studied in this work, using an actinide target nucleus, FMT-fission is the predominant decay mode following fusion (at all beam energies), meaning that $\sigma_{ER} \sim 0$. Therefore, the total FMT-fission cross section (σ_{fis}) can be regarded as the capture cross section (σ_{cap}).

Experimental capture cross sections were obtained through the sequence of steps shown in Fig. 6.1. Depending on the proportion and characteristics of the QF contribution, the method of extrapolation of the fission angular distributions outside the measured angular range was different, as described in Section 2.2. Therefore, the systems studied in this work are categorised into two groups: light and heavy systems, as discussed in Section 5.1.2.

To determine the capture cross sections, the transfer-fission events must first be removed. As described in Section 5.1.1, this was achieved by applying a gate on the source velocity distributions to select FMT-fission events, by applying the pink elliptical gate centred on (v_{par} - v_{CN}, v_{perp}) = (0, 0) shown in Fig. 5.2.

6.2 Determination of the differential cross section

Before describing the extrapolation of the angular distribution beyond the angular range covered experimentally in Section 6.4, the extraction of the fission angular distributions (differential cross sections) is described below.

The number of particles striking the detector at a given angle θ (θ is the *lab* frame angle and applies to all subsequent equations in this section) and beam energy E is given by Ref. [88]:

$$N(\theta, E) = I_p \, N_t \, \frac{d\sigma}{d\Omega}(\theta, E) \; d\Omega \tag{6.1}$$

where I_p is the number of projectile particles passing through the target, N_t is the number of target nuclei per unit area (nuclei/cm^2), $\frac{d\sigma}{d\Omega}$ is the differential cross section in units of mb/sr, and $d\Omega$ is the solid angle in steradians (sr).

Unlike the solid angle of the monitor Ω_{mon}, the solid angle of the CUBE detectors Ω_{cube} can be defined for a given choice of angle bin due to the CUBE detectors' position

sensitivity and large angular coverage. Thus it can be expressed as:

$$d\Omega_{cube} = \iint \sin\theta \, d\theta \, d\phi \tag{6.2}$$

$$\simeq \sin\theta_c \, \Delta\theta \, \Delta\phi \tag{6.3}$$

where θ_c stands for a mid-angle of a bin width of $\Delta\theta$. By generating angle bins in the transformed (θ, ϕ) representation of the detector coverage, rather than (x, y), bins of fixed $\Delta\theta$ and $\Delta\phi$ can be defined.

In fission measurements, reaction products detected by the CUBE detectors and monitors can be written as:

$$N^{fis}_{cube}(\theta_c, E) = I_p \, N_t \, \frac{d\sigma_{fis}}{d\Omega_{cube}}(\theta_c, E) \; \sin\theta_c \, \Delta\theta \, \Delta\phi \tag{6.4}$$

$$N^{el}_{mon}(\theta_m, E) = I_p \, N_t \, \frac{d\sigma_{el}}{d\Omega_{mon}}(\theta_m, E) \; d\Omega_{mon} \tag{6.5}$$

where θ_m represents the monitor angle. The CUBE detectors may detect elastically scattered particles and fission fragments (denoted as *fis*). The monitor detectors are mounted at a forward angle such that they always see elastic scattering (denoted as *el*) following the Rutherford scattering formula at any energy.

By taking the ratio of particles observed in the CUBE detectors to the monitor detectors (Eq. 6.4/Eq. 6.5), the number of interacting particles (I_p and N_t) cancel out. Rearranging the ratio gives the fission differential cross section as:

$$\frac{d\sigma_{fis}}{d\Omega_{cube}}(\theta_c, E) = \frac{N^{fis}_{cube}}{N^{el}_{mon}} \, \frac{d\sigma_{el}}{d\Omega_{mon}}(\theta_m, E) \, \frac{d\Omega_{mon}}{\sin\theta_c \, \Delta\theta \, \Delta\phi} \, . \tag{6.6}$$

Since the MAD is typically plotted as $\frac{d\sigma_{fis}}{d\theta_{cube}}$ from the relationship between $\frac{d\sigma}{d\Omega}$ and $\frac{d\sigma}{d\theta}$, Eq. 6.6 is multiplied by $2\pi \sin\theta_c$ and gives:

$$\frac{d\sigma_{fis}}{d\theta_{cube}}(\theta_c, E) = \frac{N^{fis}_{cube}}{N^{el}_{mon}} \, \frac{d\sigma_{el}}{d\Omega_{mon}}(\theta_m, E) \, \underbrace{\frac{2\pi \, d\Omega_{mon}}{\Delta\theta \, \Delta\phi}}_{S(\theta)} \tag{6.7}$$

where the last term of Eq. 6.7 is defined as the normalisation constant per bin $S(\theta)$. This solid angle ratio $S(\theta)$ is determined by a measurement of Rutherford scattering (calibration measurement, *cal*) in the CUBE and monitor detectors at sub-barrier energy ($E \leq 0.8 V_B$). By replacing the term fis by el, rearranging Eq. 6.7 gives:

$$S(\theta) = \frac{N^{el,cal}_{mon}}{N^{el,cal}_{cube}} \left(\frac{d\sigma^{cal}_{el}}{d\Omega_{cube}}(\theta_c, E) \right) \Big/ \left(\frac{d\sigma^{cal}_{el}}{d\Omega_{mon}} \right) 2\pi \, \sin\theta_c \, . \tag{6.8}$$

In order to extract the fission differential cross section by substituting Eq. 6.8 into

Eq. 6.7, the widths of the bins $\Delta\theta$ and $\Delta\phi$ must be the same as used for the fission measurements.

6.3 Cross section code

This section describes the determination of each of components of Eq. 6.7 in practice. It also explains how the differential cross sections are determined in the centre-of-mass ($c.m.$) frame.

6.3.1 Requirements and Considerations

The terms in Eq. 6.7 and Eq. 6.8 are evaluated as described below.

(1) Define the angle bin width ($\Delta\theta$).
The bin width is defined depending on statistics and the detector configuration. Typically, 5° has been used since fusion-fission angular distributions do not vary rapidly with angle [89]. This angular width was used for light reactions. For heavy reactions, the angular distributions can vary more rapidly with angle and the solid angle normalisation changes rapidly with angle between the two backward angle detectors, so a 3° bin width was used.

(2) Determine the elastic yields from the two monitor detectors (N_{mon}).
Two monitors were used, at scattering angles θ_m =22.5° (or 30°) on either side of the beam, to take into account variation of scattering angle due to possible movement of the beam spot. The use of the sum of the elastic yields from these monitors compensates for small changes in the beam spot position or entry angle [89].

(3) Correct for dead-time in recording the signals of the detected particles (N_{mon} and N_{cube}).
During data collection, there will be dead time in the data acquisition system. The number of events recorded for the monitors or the CUBE detectors are corrected using a dead time correction factor. This is the ratio of the known number of pulses (recorded via a scaler counter) to the number of recorded signals in the monitors, or time and position for the MWPCs. For the latter signals were generated by a pulser which was triggered by one of monitors. (see Fig. 3.5 for the electronic setup of the detector system).

(4) Determine the normalisation factors, $S(\theta_{lab})$.
$S(\theta_{lab})$ per angle bin is determined using the information obtained from the calibration run. In cases where the 3-detector configuration was used, the elastic scattering measurements for the calibration runs were recorded in singles for back and small

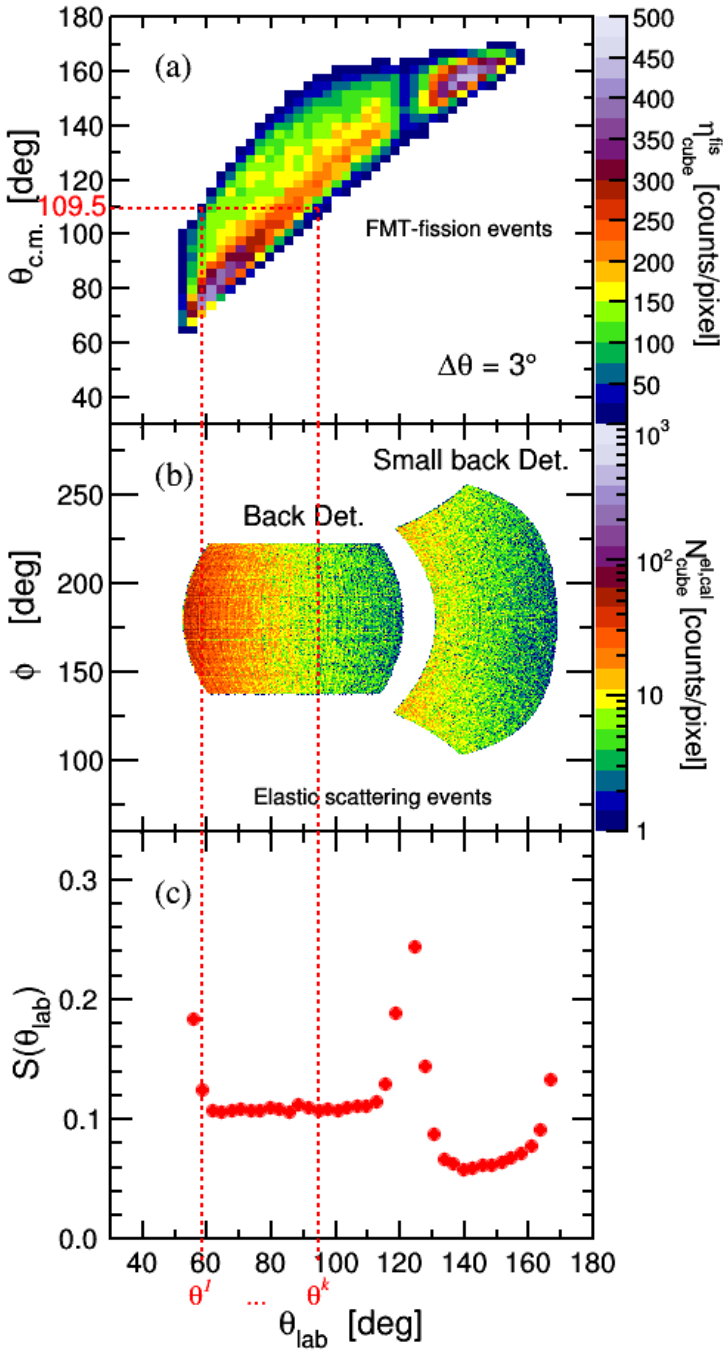

Figure 6.2: (a) Scatter plot of θ_{lab} *vs* $\theta_{c.m.}$, generated with only FMT-fission events for ^{48}Ca + ^{232}Th at $E_{c.m.}$ = 216.4 MeV. The efficiency corrected yield (η^{fis}_{cube}) is given by the colour scheme. (b) The active area of the back and small back detector in spherical coordinates from the calibration run of elastic scattering of ^{58}Ni from ^{197}Au. Most of the θ_{lab} angular coverage in the back detector has a constant $\Delta\phi$, except for the forward and backward edges of the detector. In contrast, $\Delta\phi$ varies with θ_{lab} for the small back detector. The measurement of elastic scattering provides the solid angle normalisation coefficients ($S(\theta_{lab})$) as shown in (c). This shows clearly the fact that the $S(\theta_{lab})$ are inversely proportional to $\Delta\phi$.

back detectors separately. Since the two calibration runs were measured with different conditions such as beam current and time, the events detected in the small back detector were scaled with respect to the back detector (by using the sum of monitor elastic counts). The (θ, ϕ) coverage of the backward angle detectors is shown in Fig. 6.2b, and $S(\theta_{lab})$ is shown in Fig. 6.2c. The calibration measurements used for this work are listed in Table 3.2.

6.3.2 Frame transformation

Eq. 6.7 is in the laboratory frame since the detector solid angles are only constants in the laboratory frame. Since we know for each event the value of θ at which it was measured in the *lab* frame, for each event we can generate the associated cross section by setting $N^{fis}_{cube} = 1$, using the appropriate value of $S(\theta_{lab})$ at the θ_{lab} where the event was observed. We also have knowledge of the kinematics of each event, and so can evaluate the angle in the centre-of-mass ($c.m.$) frame. The cross section associated with this single event is then assigned to the $\theta_{c.m.}$ bin as appropriate.

Many *lab* angles (1 to k^{th}) angle bin can populate a single bin in $\theta_{c.m.}$ for reactions where there is a wide range of mass-splits, as shown in Fig 6.2a. Each single event at θ^k_{lab} is normalised by the normalisation factor corresponding to the k^{th} bin ($S(\theta^k_{lab})$). The sum of individual solid angle normalised event (cross sections) gives the total differential cross section at $\theta_{c.m.}$. In other words, by making the $\theta_{c.m.}$ assignment event-by-event and populating bins in $\theta_{c.m.}$, the transformation of solid angle from the *lab* frame to the $c.m.$ is automatically taken into account. Angles in the $c.m.$ frame from 90° to 160° (or 135° for the 2-MWPC configuration) have essentially full coverage in θ_{lab}, when $S(\theta_{lab})$ is taken into account. This is seen in Fig. 6.2a.

6.3.3 Mass-angle distributions and angular distributions

Fig. 6.3 shows the MAD ($d^2\sigma_{fis}/d\theta_{c.m.}\, dM_R$) for cross section-normalised fission data for ^{48}Ca + ^{232}Th at $E_{c.m.}$ = 216.4 MeV. Pairs of fission fragments were detected in coincidence in (1) the (back-front) detector pair or (2) (small back-front) detector pair.

Plotting mass ratios and angles of the fragments observed in the back detectors gives the MAD shown in Fig. 6.3a. However, the complementary fragment with M'_R= (1 - M_R) and $\theta'_{c.m.}$ = (180° - $\theta_{c.m.}$) was also observed in the front detector. This fragment can also be plotted in the MAD (black squares). Without any restriction, this would lead to excess yield where the same (M_R, $\theta_{c.m.}$) in both (back-front) and (front-back) coincidences, indicated by white circles in Fig. 6.3a. To eliminate this issue, a "mirror line" is defined (avoiding regions of no angular coverage) beyond which events are rejected before plotting the fragment detected in the front detector. An example of a satisfactory mirror line (all such lines should pass through a central point at (0.5, 90°)) is shown in Fig. 6.3a. The

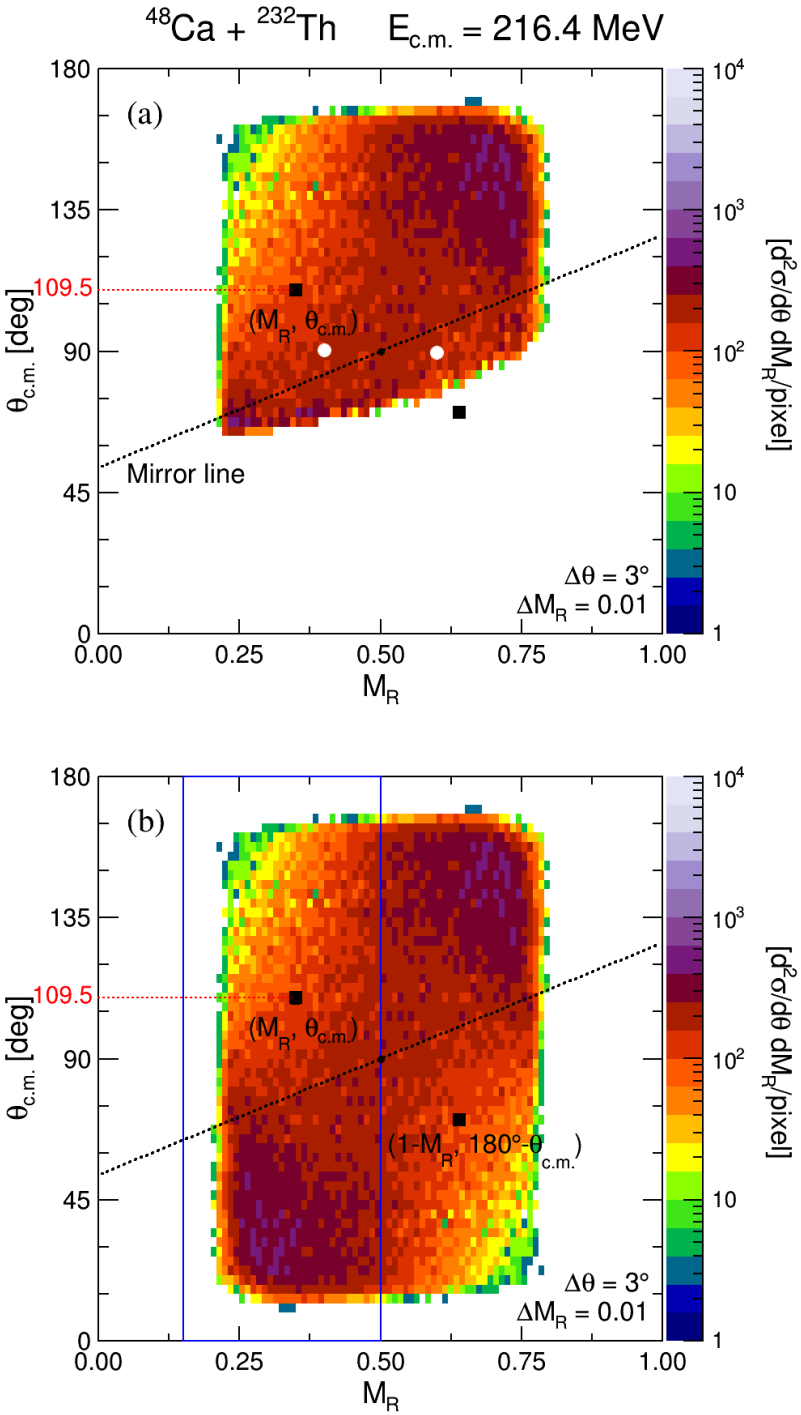

Figure 6.3: Generation of full mass-angle distributions (MAD). (a) This MAD was plotted showing the fission fragments (M_R, $\theta_{c.m.}$) observed in the back detectors. The projection onto the y-axis provides the angular distribution for all masses. Where masses are independent of angles over 90° to 180°, this angular distribution is suitable for light systems (^{18}O + ^{232}Th and ^{30}Si + ^{232}Th). The dotted-line is a mirror line across which fission fragments are reflected to produce the mirrored MAD shown in (b) (see text). The complementary fission fragment is definition observed at (1 - M_R, 180° - $\theta_{c.m.}$). The blue rectangle is the gate to generate angular distributions over 0° to 180° range (e.g. Fig. 6.4).

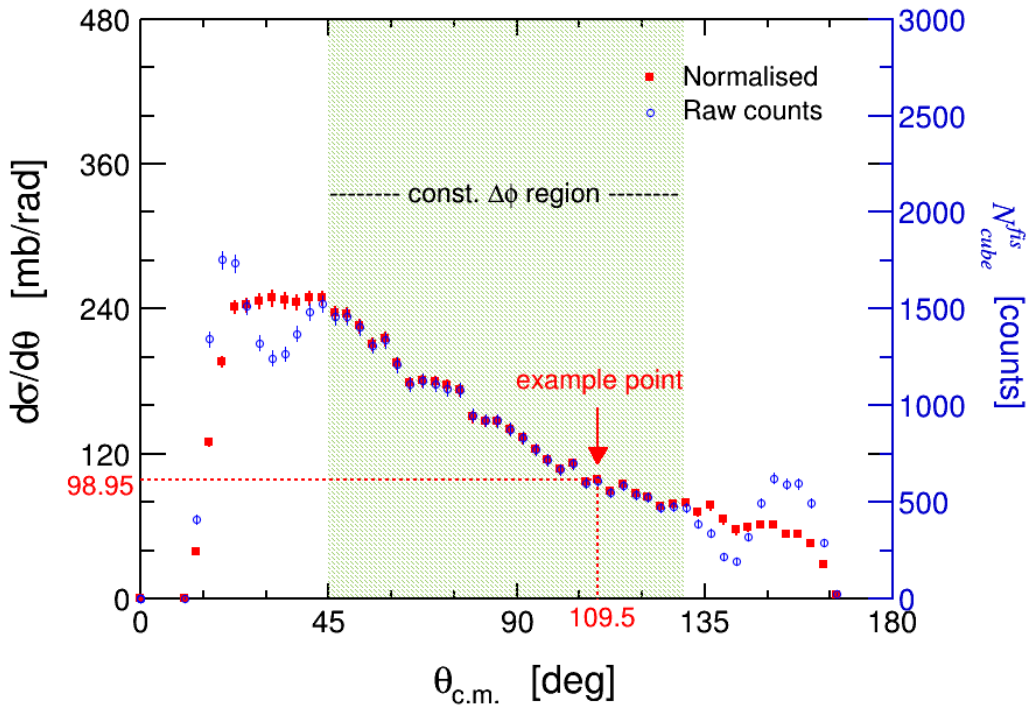

Figure 6.4: Fission angular distribution for $M_R < 0.5$. An example point is a data point demonstrated for the frame transformation given in Section 6.3.2. The differential cross section (red square) is proportional to the number of fission events (blue hollow) in the constant $\Delta\phi$ region.

full MAD using a fiducial (mirror) line shown in Fig. 6.3a.

Projection of the MAD onto the y-axis provides angular distributions. When obtained from the mirrored MAD, the mass range should be restricted to $M_R < 0.5$ (or $M_R > 0.5$). This method is applied in generating angular distribution for heavy systems where fast QF is significant, since emission angles are strongly correlated with masses of the fragments. However, for light system fission angular distributions were generated considering all mass ratios, but only over the angular range $\theta_{c.m.} > 90°$.

6.3.4 Experimentally determined differential cross sections

S(θ_{lab}) is inversely proportional to the CUBE bin width $\Delta\theta$ and to the ϕ coverage $\Delta\phi$ at angle θ_{lab}. It results in the yields of fission events converted from non-constant $\Delta\phi$ ranges being corrected by the solid angle factor. Fig. 6.4 shows the effect of this correction. In the constant $\Delta\phi$ (green-shaded region), the number of fission events in counts is proportional to the differential cross sections $\left(\frac{d\sigma_{fis}}{d\theta_{c.m.}}\right)$, but not in the region covered by the small back detector and edges of the back detector, which are in non-constant $\Delta\phi$ ranges. The red points show how the raw counts (blue) are corrected by the normalisation procedure resulting in a smooth dependence of cross section on angle.

The experimental uncertainties come from the total number of raw counts N_j for a

given bin in $\theta_{c.m.}$. Another contribution comes from the solid angle normalisation measurement, added in quadrature. The statistics for the elastic normalisation measurement is always much higher than a fission measurement, so the raw fission counts provides the main contribution to the experimental uncertainty.

6.4 Extrapolation

The measured differential cross sections were calculated from Eq. 6.7 for the angles covered by the CUBE detectors. Therefore, to obtain the total capture cross sections σ_{cap} from the fission differential cross sections, it is necessary to extrapolate to regions beyond the detector's angular coverage. This procedure is presented in this section. There are two methods to achieve this, depending on the characteristics of the QF component in the fission products: one for light systems (Method 1) and one for heavy systems (Method 2). Method 1 fits the differential cross section $\left(\frac{d\sigma}{d\Omega}\right)$ of all fissions. Method 2 uses the differential cross section of fission fragments $\left(\frac{d\sigma}{d\theta}\right)$ for mass ratio $M_R \leq 0.5$.

6.4.1 Method 1: Using the transition state model

The decay of the compound nucleus by fission is generally described by the transition state model (TSM), and its angular distribution is expressed in terms of angular momentum quantum numbers. Eq. 2.8 given in Section 2.3 is an expression for the fission angular distribution when the target and projectile spins are zero, and with the assumption of a Gaussian K-distribution. The K-distribution is characterised by its variance K_0^2, which is usually assumed to be independent of J. The extrapolation of measured fission angular distributions was achieved by adjusting the value of K_0 for a calculated J distribution until a minimum χ^2 fit to the experimental angular distributions was achieved.

The corresponding results for the ^{18}O + ^{232}Th and ^{30}Si + ^{232}Th reactions at different energies are shown in Fig. 6.5. The curves in both figures are fits to the data using the TSM. There are small distortions in the measured fission angular distribution for ^{18}O + ^{232}Th, centred at $\theta_{c.m.} = 110°$. These may be caused by (1) non-linear responses from the detector (2) any difference between non-linearities determined from the calibration and those applicable during the fission measurements[1]. These resulted in re-distribution of events within the angular range measured, but no loss of fission events. This was demonstrated by simultaneous measurements for ^{18}O + ^{208}Pb, where the extracted fission cross sections agreed with measurements taken at a different time without this non-linear behaviour. The detector's x-grid and delay line were replaced after this measurement

[1] In one beamtime, which normally takes a few days up to several weeks, a series of fission measurement with a range of energies are carried out, and a single elastic scattering measurement for calibration is typically performed. We do not expect any geometrical changes in detectors and electronics during the beamtime.

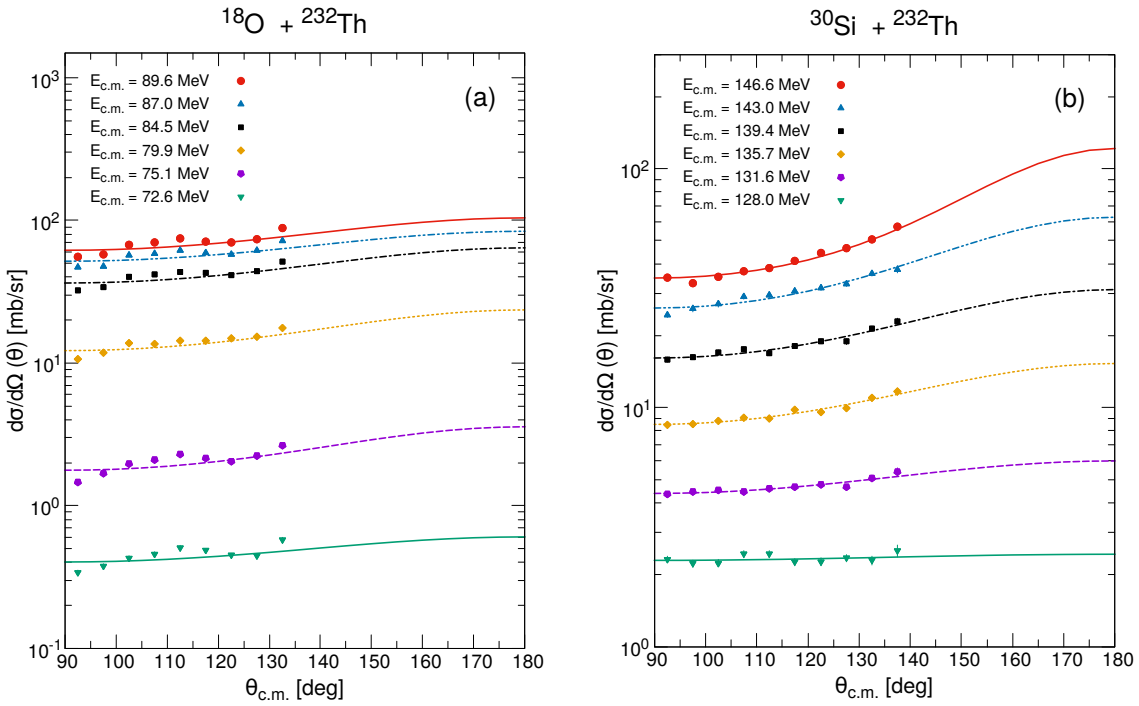

Figure 6.5: (a) Shows the fission fragment angular distribution for ^{18}O + ^{232}Th and (b) for ^{30}Si + ^{232}Th at different energies as a function of the scattering angle in the center-of-mass frame. The lines are the results of the TSM calculations fit to the experimental distribution and thus extrapolations to 180°.

which resolved the problem.

The total capture cross sections for ^{18}O + ^{232}Th and ^{30}Si + ^{232}Th reactions were obtained by integrating the fitted angular distributions $\left(\frac{d\sigma_{fis}}{d\Omega}\right)$, multiplied by $2\pi \sin\theta_{c.m.}$, over all angles from 90° to 180°. The total capture cross sections are presented as a function of the beam energy in Fig. 7.2 in the following chapter, and their values are given in Appendix C.

6.4.2 Method 2: Using Quasisim

Following the ideas of Ref. [30], a simulation of QF mass and angular distributions has been developed at ANU [54]. The principles are described in Section 2.4.2. The computer code Quasisim calculates the angle of observation and the mass-split of a QF event based on the impact parameter, sticking time and mass evolution function. Through the simulation of many QF events, using the Monte Carlo approach, a MAD and its mass and angle projections are built up for a given set of assumptions.

The key variable determining the angle of emission from a given fission event is the rotation angle of the system between contact and scission ($\theta_{rot}(t_s)$). In simplest terms, this is defined by the angular velocity and sticking time (t_s). In turn, the angular velocity is determined by the angular momentum divided by the moment of inertia.

6.4.2.1 Inputs

To take into account the effect of static deformation alignment on capture angular momentum distributions and QF characteristics in the calculation of MADs using Quasisim, input parameters were prepared for tip and side collision separately and the resulting MADs were summed.

(1) Angular momentum distribution

For a measurement at a given beam energy, a distribution of angular momenta will be involved. This is determined by a model of capture. For the reactions measured here, involving ^{232}Th target nuclei, the static deformation of ^{232}Th must be taken into account [59, 63, 82, 90]. Following previous work, a simplified approach to the effect of deformation on QF characteristics has been taken, dividing collisions into those with the tip of the prolate ^{232}Th, and those with the side as described below. Thus separate angular momentum distributions must be generated for each.

This was achieved using a semi-classical model of capture implemented in the code CCMOD [56]. The capture barriers derived from Eq. 3.6 [81], given in Table 3.2, were used for coupled channels calculations. Here the static deformation of ^{232}Th is treated classically, but other aspects of the collisions are treated quantum mechanically. As well as the deformation, the octupole vibrational state in the target, and quadrupole and octupole states in the projectile nuclei have been included in the calculation of the angular momentum distributions.

A critical angle θ_{crit} was defined between the line joining the centres of the two colliding nuclei, and the deformation axis of the ^{232}Th (see Fig. 2.7). Below this angle, the collisions were defined as tip collisions, with a certain set of characterises defining QF sticking time and mass evolution. Above this angle, different characteristics were taken, such that the experimental MAD could best be described. Angular momentum distributions calculated by CCMOD for ^{34}S + ^{232}Th and ^{40}Ca + ^{232}Th are shown in Fig. 6.6, for critical angles taken to be $\theta_{crit} = 25°$ for ^{34}S [63], and assumed to be 30° for ^{40}Ca [63]. Those for tip collisions are shown by red-dashed lines, and for side collisions by blue-dashed-dotted lines. The weighting of Quasisim calculations of MADs for tip and side collisions followed those from the CCMOD calculations.

For the purpose of extrapolating the angular distributions, uncertainties in the capture angular momenta can be compensated by changing the assumed sticking time distributions. Matching the measured angular distribution is the goal here, to obtain a reliable extrapolation, and thus capture cross sections. Thus questions about the exact angular momentum distributions and moments of inertia could be neglected.

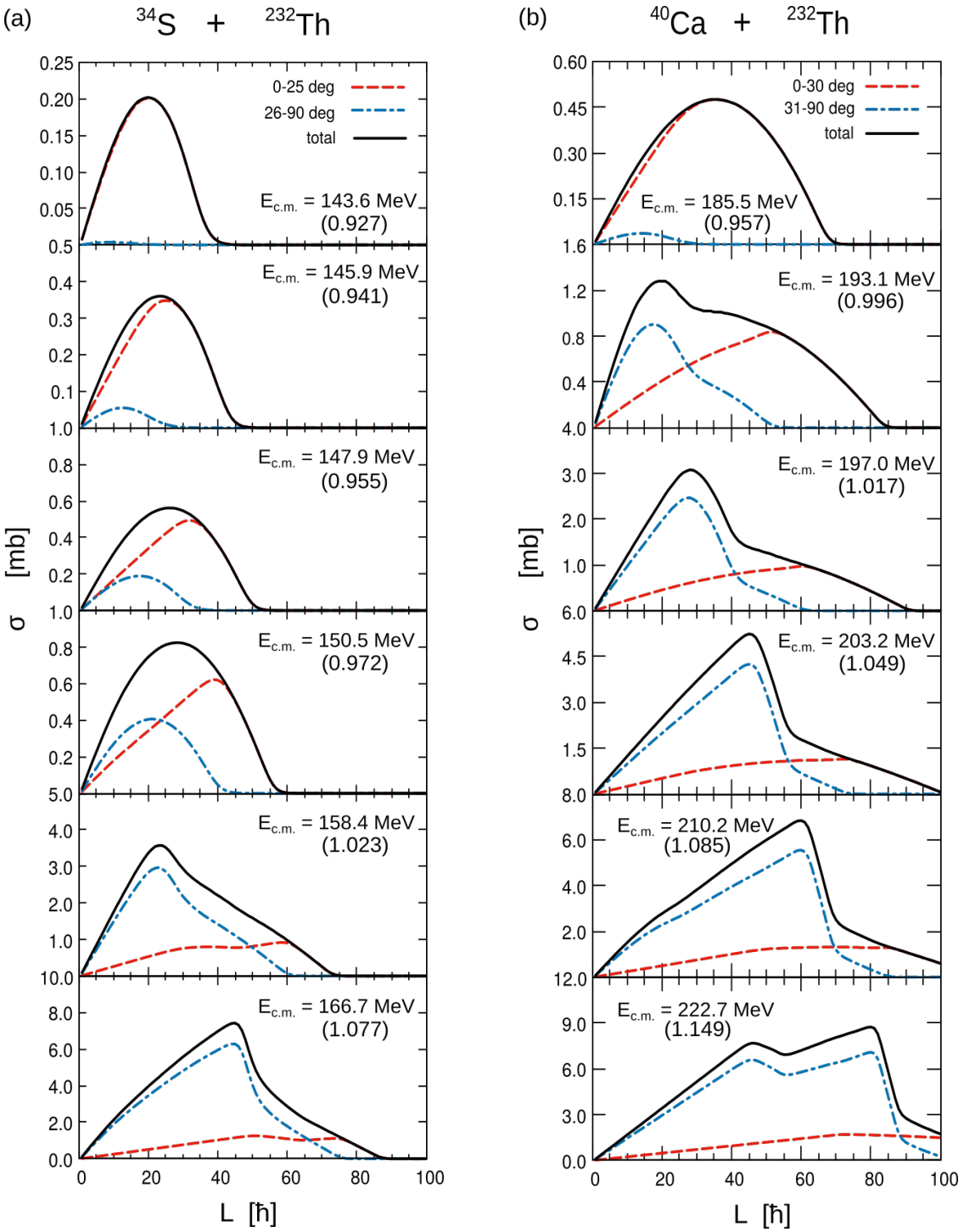

Figure 6.6: Angular momentum distributions for ^{34}S + ^{232}Th and ^{40}Ca + ^{232}Th. (a) For the ^{34}S + ^{232}Th system, the critical angle is taken as 25° [63]. (b) For the ^{40}Ca + ^{232}Th system, the critical angle is taken to be 30°. The red-dashed line distribution is for tip collisions, the blue dot-dashed line is for side collisions, and the black solid line is the total distribution, the sum of two distributions. The centre-of-mass energy is given in each panel and the ratio of the beam energy to the capture barrier (E/V_B) is given inside the bracket.

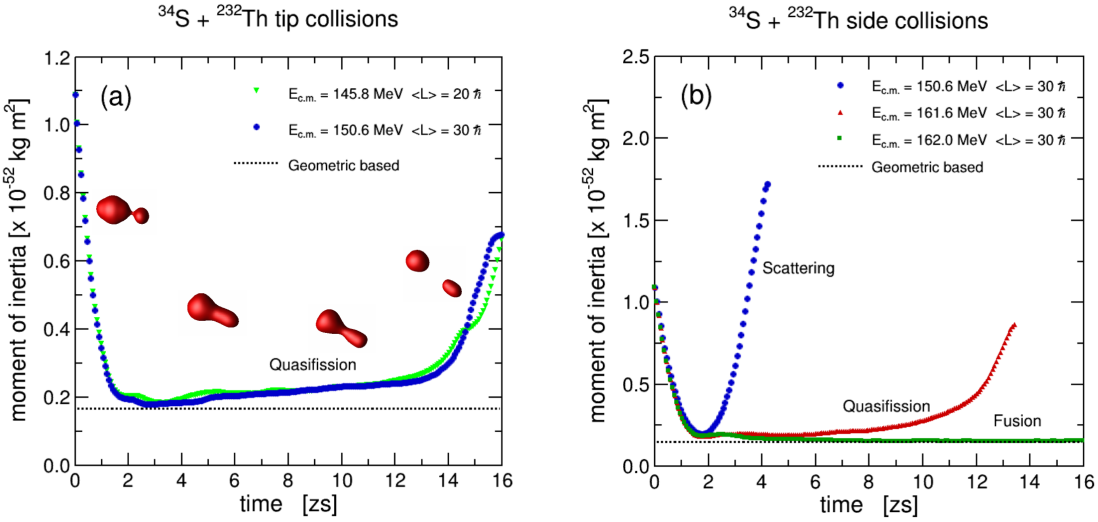

Figure 6.7: TDHF calculations of the moment of inertia perpendicular to the scission axis as a function of the time, performed for different centre-of-mass energies and angular momenta for ^{34}S + ^{232}Th, where the average barrier of this system is 154.8 MeV [81]. (a) Tip collisions can lead to QF at energies below the average barrier. Images are snapshots of a dinclear evolution for the reaction at $E_{c.m.}$ = 150.6 MeV with the average angular momentum of 30 $\hbar$. (b) Different outcomes are observed in side collisions depending on the centre-of-mass energy $E_{c.m.}$.

(2) Moment of inertia

There are largely two methods used to estimate the average moment of inertia $< I >$, as discussed in Section 2.4.2. A direct estimation of $< I >$ from the static shapes of the two colliding nuclei was applied to the ^{40}Ca + ^{232}Th system, using the formula given in Appendix B.

$< I >$ obtained from TDHF calculations[2] was used for the ^{34}S + ^{232}Th system in the work presented here. The TDHF calculations provided time-dependent moments of inertia $I(t)$ for various angular momenta and centre-of-mass energies $E_{c.m.}$ in order to sample collisions leading to both QF and fusion. Fig. 6.7 shows $< I >$ of geometrical-based calculations (I_{geo}) and $I(t)$ from TDHF calculations (I_{TDHF}) for ^{34}S + ^{232}Th as a function of time. This shows three features; (1) $I_{geo} \leq I_{TDHF}$ for QF; (2) at $E < V_B$, tip collisions can lead to capture and then to QF, and (3) side collisions can contribute to fusion at $E > V_B$. The second and third features together with [14, 63] support the strong effect of deformation alignment on fusion reactions where an elongated shape is formed via tip collisions; this leads to mass asymmetric QF at $E < V_B$. As the collision energy increases, reactions are likely to result in near-symmetric mass splits and eventually

[2]The author "experimented" with TDHF calculations [91] for ^{34}S + ^{232}Th and ^{54}Cr + ^{238}U reactions to help to understand the dynamics of fusion reactions. It allowed the testing of some entrance channel effects on QF and sticking time, and on the dinuclear system evolution. However, it was not significant for this project, so details of the TDHF calculations were omitted.

above-barrier reactions resulting in fusion. In contrast, where a compact shape is formed via side collisions, with a very long sticking time, this should eventually result in fusion-fission with a mass distribution peaked at $M_R = 0.5$. This perspective is important for parametrising sticking time distributions, as discussed in the following section.

Within the measured energy ranges, TDHF calculations of $I(t)$ for collisions resulting in QF are not very different, and the impact on reproducing the experimental MAD is negligible. Therefore, an average value of $< I >$ for the collisions was used in Quasisim. In general, I_{geo} is $\leq I_{TDHF}$. As a result of testing for the ^{34}S + ^{232}Th reaction, the use of two different values of $< I >$ produced the same MAD if the sticking time distribution was scaled appropriately, meaning that there is no change in the total capture cross section calculation.

(3) Sticking time distribution

The form chosen for the sticking time distribution to reproduce the experimental MADs is a half-Gaussian followed by an exponential decay, parametrised by the peak sticking time (μ), the width of the half Gaussian distribution (σ) and the decay time (τ) [54]. Sticking time distributions were systematically parametrised based on two fundamental observed characteristics: (1) that the QF timescale of tip collisions is faster than that of side collisions, $t_{tip} < t_{side}$ and (2) that fast QF leads to asymmetric mass distributions whereas slow QF leads to mass symmetric distributions. This is associated with the effect of the contact configuration (deformation alignment) on the reaction dynamics, related to the shape evolution of the dinuclear system over the potential energy surface (PES). This results in a beam energy dependent outcome. At $E < V_B$, elongated configurations (tip collisions) break apart soon after capture, leading to a mass asymmetric distribution. In contrast, at $E > V_B$ (where side collisions are dominant), the more compact configuration results in longer sticking times and mass distributions closer to symmetry. Simplistically, the fast QF process contributes an asymmetric mass distribution whereas the slow QF process contributes a symmetric mass distribution. The I_{TDHF} calculation shown in Fig. 6.7b for a side collision shows a shorter QF timescale than the tip collision. However, the I_{TDHF} shown was calculated for a particular energy that resulted in a relatively fast QF outcome. Other (higher) energies resulted in fusion (as shown).

Depending on beam energy and reaction, one or more sticking time distributions were used; by default tip and side collisions have their own distribution. If needed, tip and side collisions can also be split into two components, $fast$ and $slow$. The reason for this is that within a fixed ratio of tip to side collisions, mass-asymmetric (symmetric) tip (side) collisions cannot reproduce the experiments [63]. Owing to this, by defining $fast$ and $slow$ process for both tip and side collisions, deficiencies in the mass-asymmetric/symmetric yields can be compensated. Fig. 6.8 is a graphical illustration showing the composition

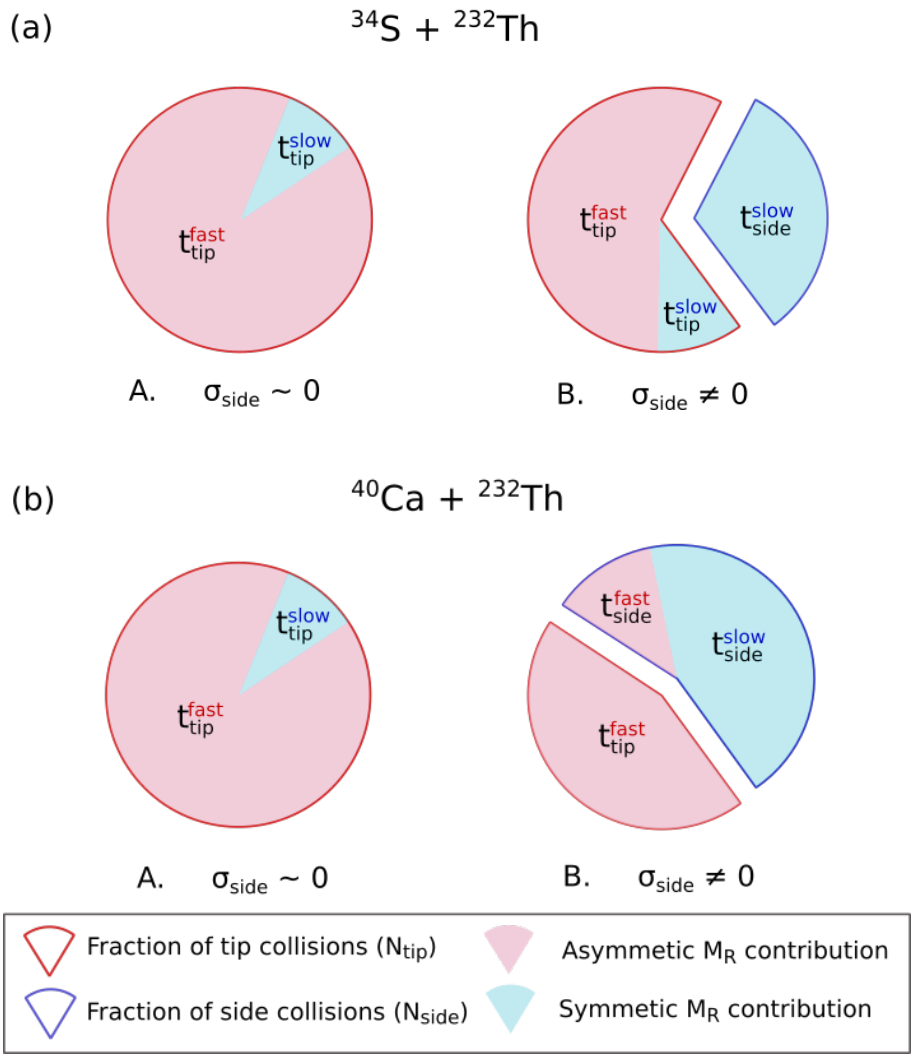

Figure 6.8: Illustration of portions of mass-asymmetric and symmetric contribution in tip and side collisions (a) for $^{34}S + ^{232}Th$ and (b) for $^{40}Ca + ^{232}Th$. Only the lowest beam energy reactions in which side collisions are not expected to contribute (as shown in Fig. 6.6) follows type A, otherwise higher beam energies follow type B.

of sticking time distribution components adopted depending on the beam energy (which determines the different probabilities of side/tip collisions) and reaction.

Fig. 6.9a and Fig. 6.9b shows sticking time distributions required to fit the experimental MAD for $^{34}S + ^{232}Th$ and $^{40}Ca + ^{232}Th$ respectively. The red lines are for tip, and the blue lines for side collisions. In practice, the width σ and decay time τ values in the simulations sensitively affected reproduction of experimental MADs in the angular range covered by the detector. There were no significant variations in the peak sticking time μ in simulations where the experimental MADs were reproduced. Note that the terms *fast* and *slow* were assigned depending on the relative timescales of reactions resulting in asymmetric mass splits.

For $^{34}S + ^{232}Th$ reactions, sticking time distributions were parametrised from the

lowest beam energy to the highest energy. At the lowest beam energy, side collisions are not expected to contribute to the reaction in accordance with the angular momentum distributions, as shown in Fig. 6.6a. The experimental MAD (Fig. 6.10a) shows there are some mass-symmetric components in this reaction. The reaction must have some slow QF contribution which can lead to mass-symmetric components. Therefore, the sticking time distribution of tip collisions was split into two components. The ratio of fast to slow components was fixed to 3:1. The parameters of the two sticking time distributions were taken as initial parameters. On a basis on these, parameters were adjusted for higher beam energies. The mean time of the three distributions followed the order $t_{tip}^{fast} < t_{tip}^{slow} < t_{side}^{slow}$.

For ^{40}Ca + ^{232}Th reactions, parametrising is more difficult compared to the ^{34}S + ^{232}Th case, since the majority of reactions were measured at energies above the barrier, resulting in broad M_R-distributions and ambiguous mass-symmetric/asymmetric components as shown in Fig. 6.11b. According to the angular momentum distributions shown in Fig. 6.6b, tip and side collisions are comparable except at the lowest and highest energies. There was no way to experimentally determine the portion of asymmetric and symmetric contributions originating from tip and side collisions; the lowest energy obviously resulted from tip collisions but it was not clear for the rest of the energies. Therefore, parametrisation of the sticking time distributions was systematically approached. Unlike the ^{34}S + ^{232}Th reaction, for the ^{40}Ca + ^{232}Th reaction the sticking time distribution of side collisions is composed of both fast and slow process. The order of the mean time of the three sticking time distributions followed $t_{tip}^{fast} < t_{side}^{fast} < t_{side}^{slow}$. The approach of parametrising the sticking time distributions at the lowest beam energy was the same as for ^{34}S + ^{232}Th but the highest energy reactions were analysed in the order of descending energy since the contribution of tip collision is far lower than that of side collisions. Parameters of each of the sticking time distributions were adjusted iteratively by changing the portion of fast and slow component contribution in order to match the both simulated angular and mass distributions to those of experiment. The proportion of fast and slow process for side collisions was found a ratio of 3 to 7 for the two highest energies and 2 to 8 for two intermediate energies.

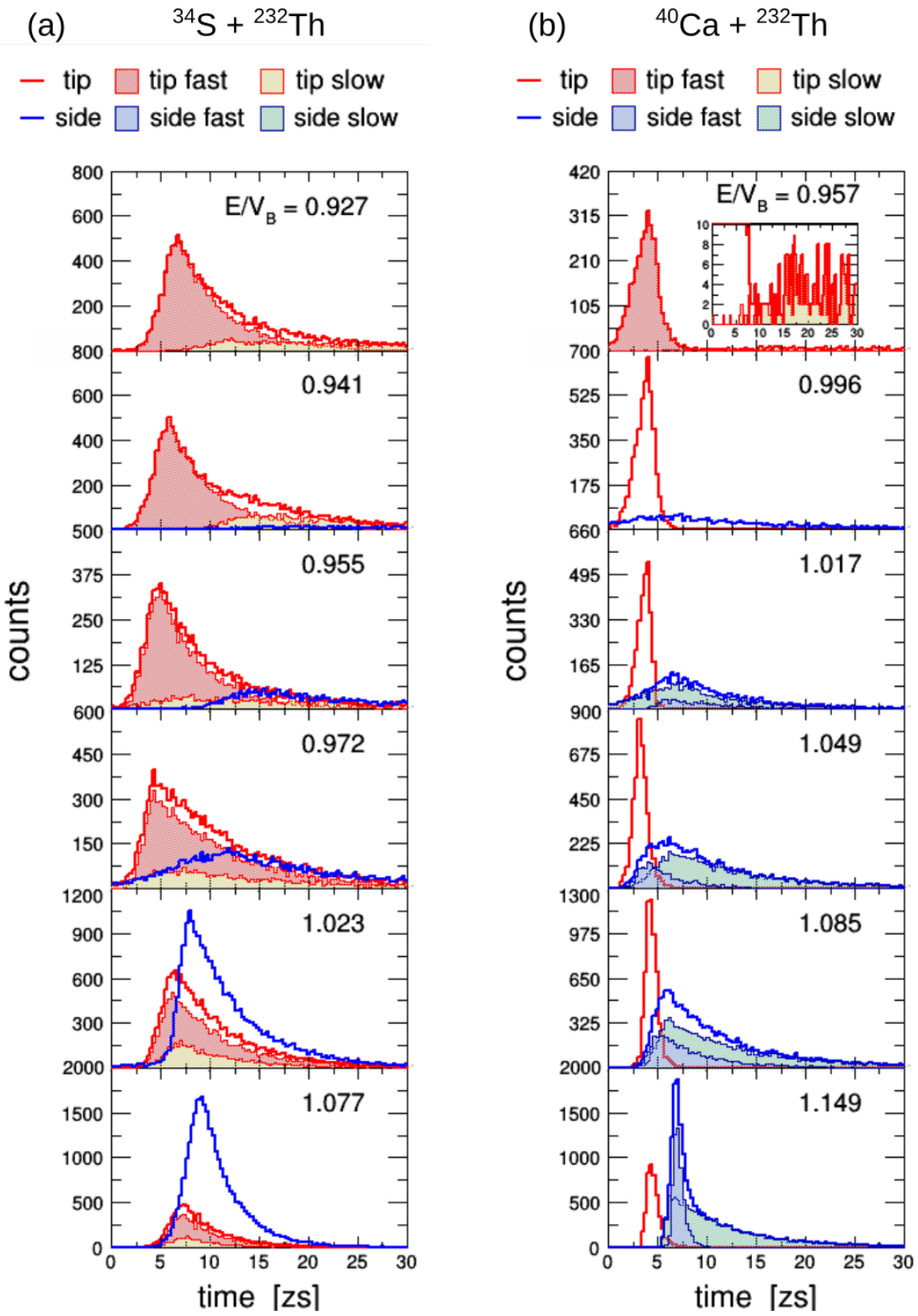

Figure 6.9: Sticking time distributions (a) for ^{34}S + ^{232}Th reactions and (b) for ^{40}Ca + ^{232}Th reactions. The red line is the time distribution used for the tip collisions whereas the blue line for the side collisions. Unlike the ^{34}S + ^{232}Th system, the time distributions of ^{40}Ca + ^{232}Th are specifically divided into fast and slow components for each of tip and side collisions. See text for more explanation.

6.4.2.2 Results of simulations

Comparisons of experimental data and simulated data are shown Fig. 6.10 and Fig. 6.11 for ^{34}S + ^{232}Th and ^{40}Ca + ^{232}Th respectively. The top row of panels in (a) are measured MADs, with simulated MADs for the bottom row. The upper panels in (b) are comparisons between measured angular distributions of the projectile-like fission fragments (blue points) and simulations (red points). The lower panels show comparisons between measured mass ratio distributions (blue points) and simulation (red points). Panels (c) show the respective ratios of the experimental distributions to the simulated distributions, without error bars from statistics.

The simulation followed an iterative process until good agreement was acheived between the experimental data and the simulated data in the region of the experimental angular coverage with the full detection efficiency. This resulted in the ratios of measured data and simulated data being close to 1. There were statistical fluctuations within 5% - 10%. Overall the simulated MADs successfully reproduced the experimental MADs. For ^{40}Ca + ^{232}Th, as beam energy increases, the simulated data are higher than the measured data at backward angles from 100° to 135°, since the simulations were focused on matching the experimental data at more forward angles. This deviation may because of some correlations not yet taken into account in Quasisim. This issue will be investigated in more detail through dedicated measurements in future. For the purpose of extrapolation of the angular distribution, the simulation was scaled by a factor to match the experimental data.

Fig. 6.12 and Fig. 6.13 show the final fission angular distributions for the ^{34}S and ^{40}Ca reactions (for $M_R < 0.5$), after scaling down or up the simulations as indicated to make a smooth transition between measurements and calculations. Integration of these distributions over the full angular range from 0° to 180° give the total capture cross sections, shown in Fig. 7.2, and tabulated in Appendix C.

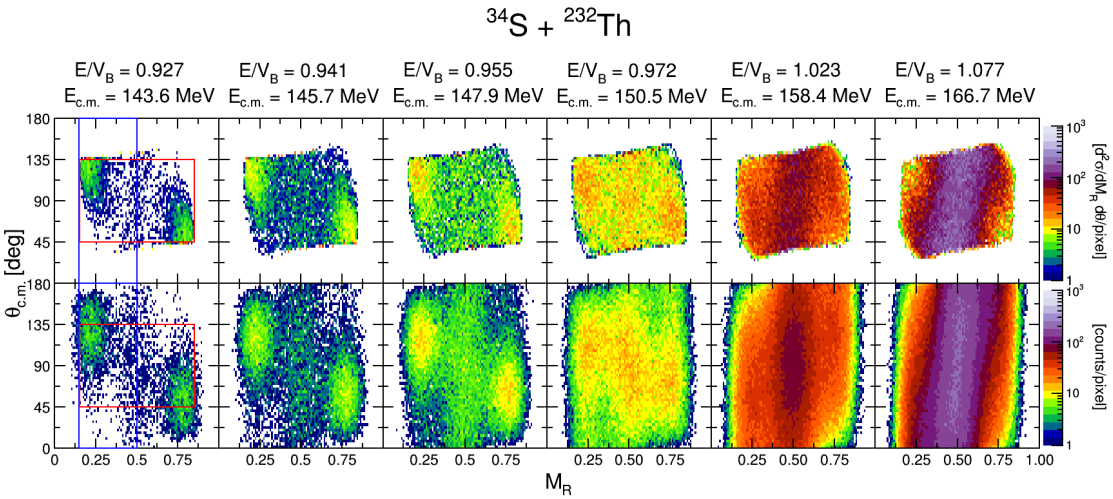

(a) The upper panels show the experimental solid angle normalised MADs and the lower panels are simulated MADs. Blue and red rectangles are gates used to produce the distributions below. Centre-of-mass energies are indicated.

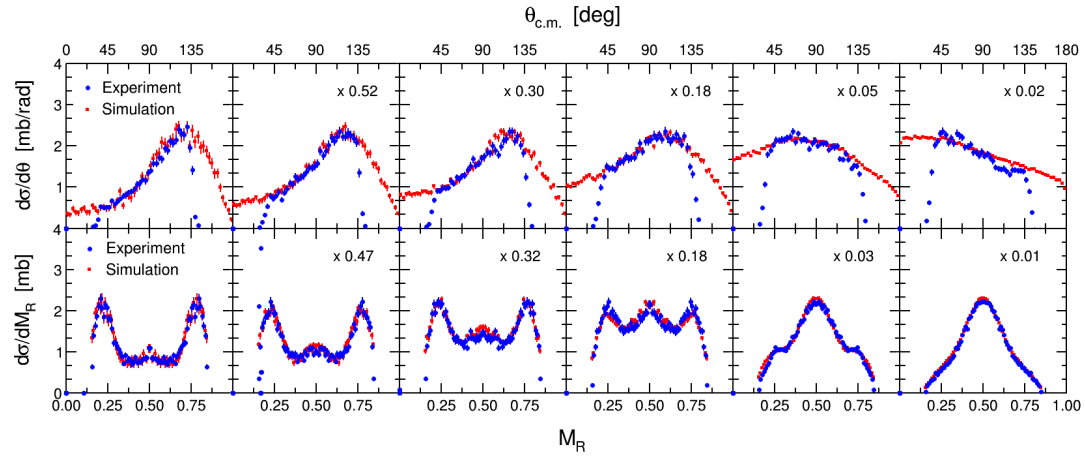

(b) Angular distributions are in the top row of panels and M_R-distributions in the bottom row for the energies indicated in (a). Blue circles are experimental data and red rectangular points are best-fitting simulations.

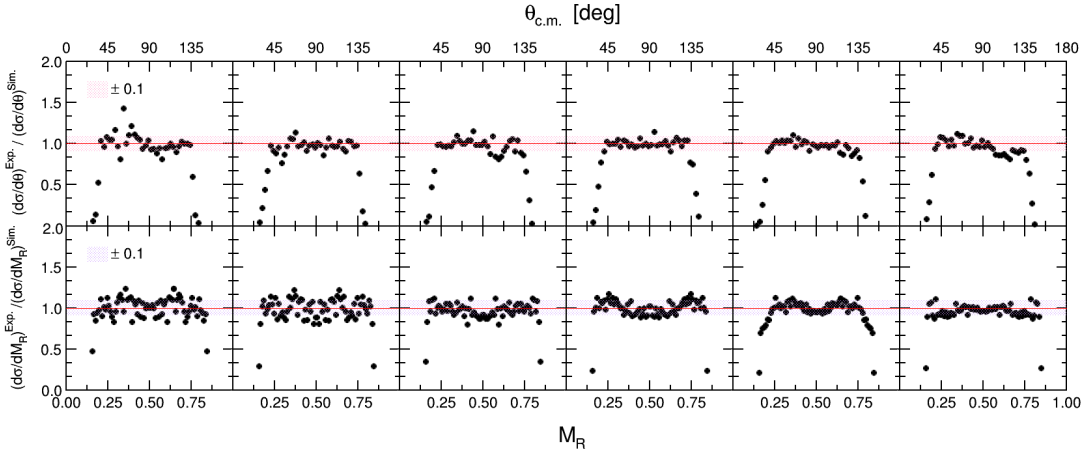

(c) Ratio between experiment to simulation. Perfect agreement (ratio = 1) is indicated by the red line. The shaded band corresponds to a ± 0.1 range.

Figure 6.10: Comparisons between experiment and simulation for ^{34}S + ^{232}Th.

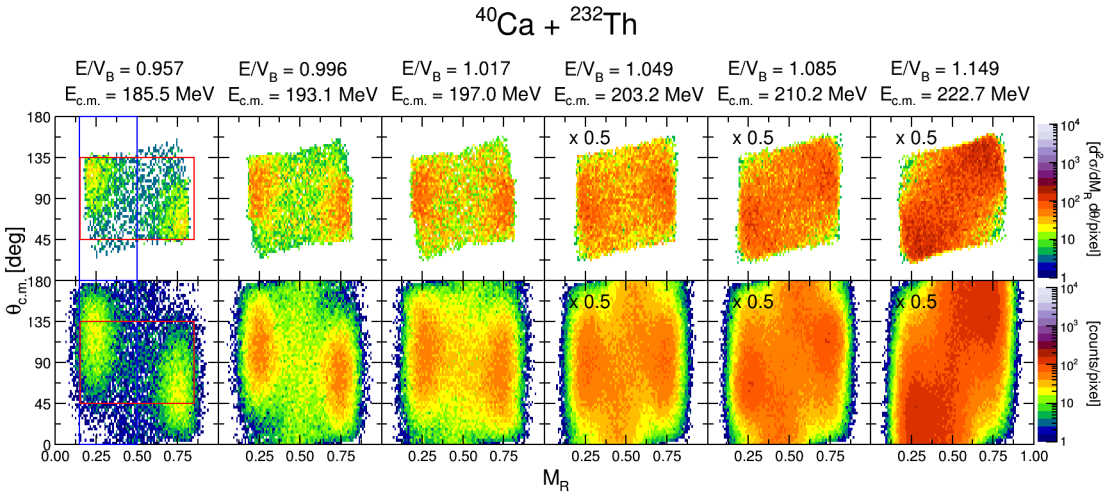

(a) The upper panels show the experimental solid angle normalised MADs and the lower panels are simulated MADs. Blue and red rectangles are gates used to produce the distributions below. Centre-of-mass energies are indicated.

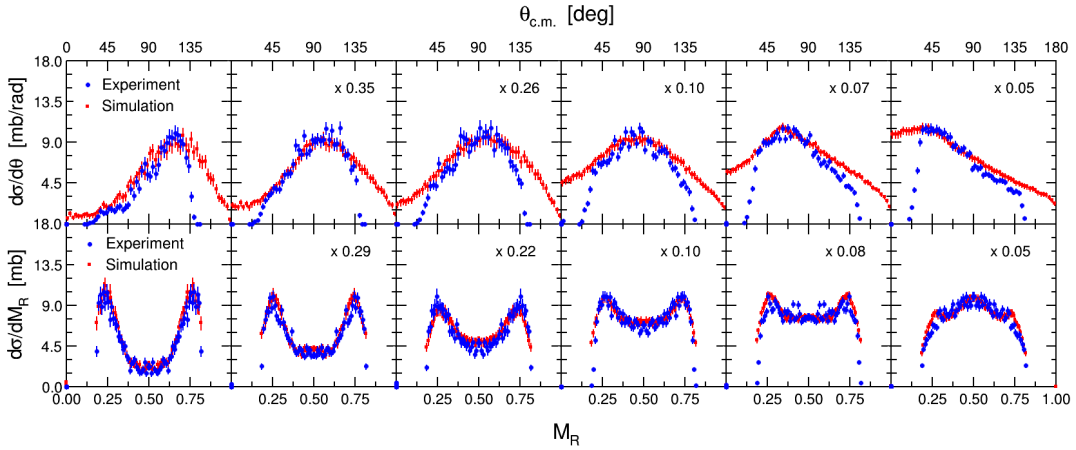

(b) Angular distributions are in the top row of panels and M_R-distributions in the bottom row for the energies indicated in (a). Blue circles are experimental data and red rectangular points are best-fitting simulations.

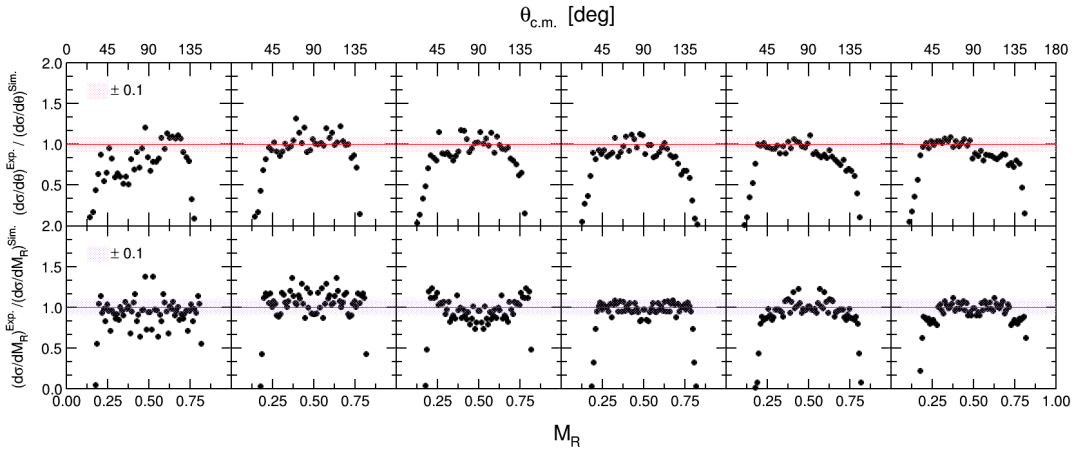

(c) Ratio between experiment to simulation. Perfect agreement (ratio = 1) is indicated by the red line. The shaded band corresponds to a ± 0.1 range.

Figure 6.11: Comparisons between experiment and simulation for ^{40}Ca + ^{232}Th.

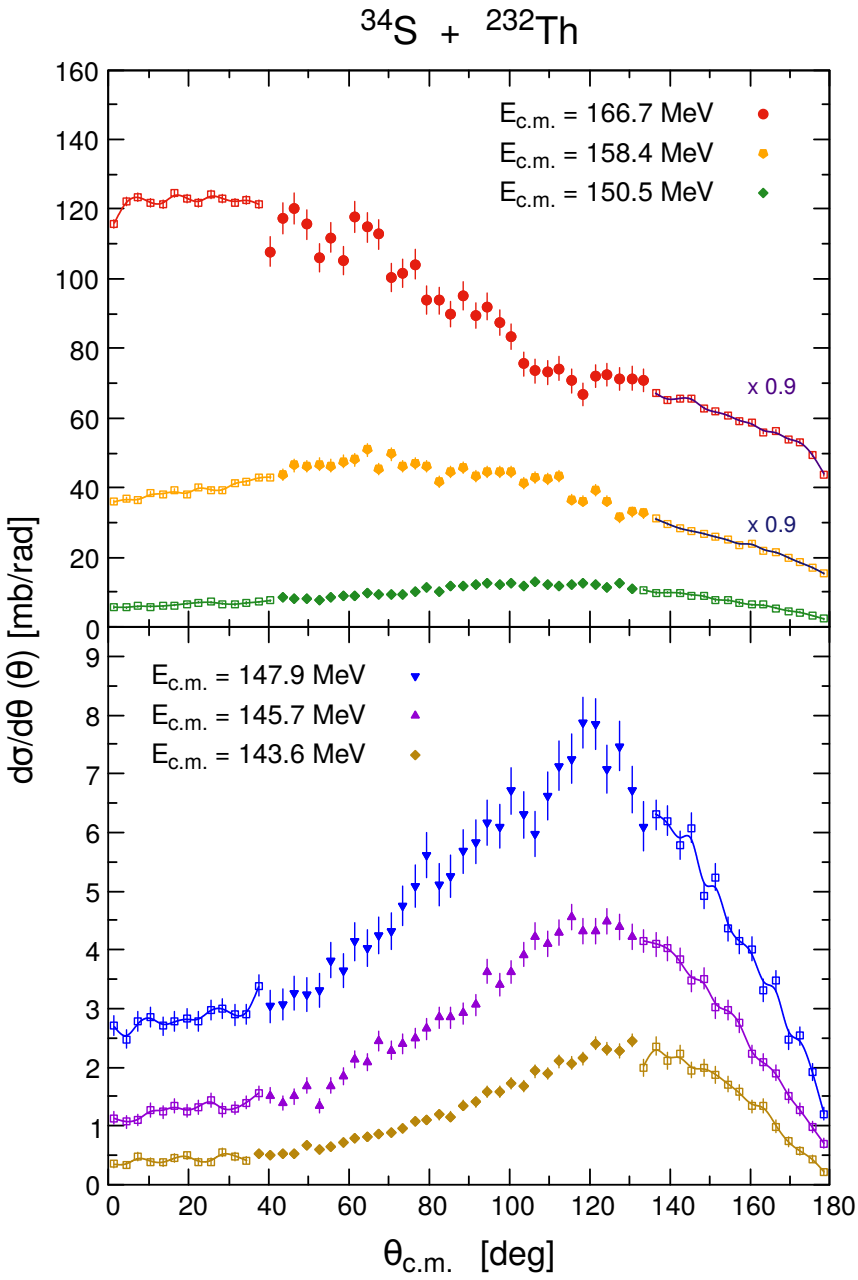

Figure 6.12: Fission fragment angular distributions for ^{34}S + ^{232}Th at ($M_R < 0.5$) for different energies as a function of the scattering angle in the centre-of-mass frame. Filled points are from the experimental data, lines join the hollow points from the QF simulations. To make a smooth transition between the measurements and the simulated data in the angular range $\theta_{c.m.} > 130°$, the simulation was scaled down by the indicated factor. The integration of the angular distribution gives the total capture cross section.

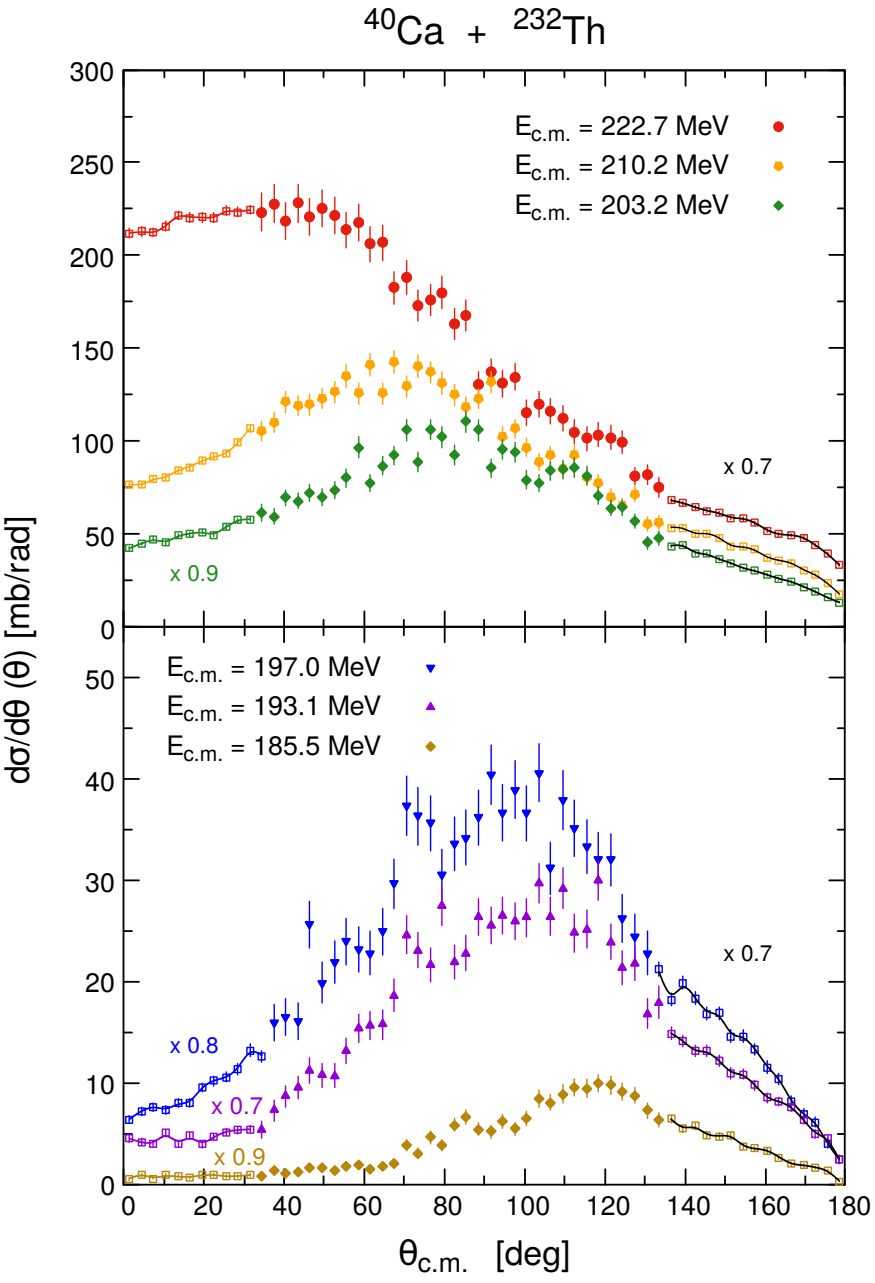

Figure 6.13: Fission fragment angular distributions for ^{40}Ca + ^{232}Th at ($M_R < 0.5$) for different energies as a function of the scattering angle in the centre-of-mass frame. Filled points are from the experimental data, lines join the hollow points from the QF simulations. To make a smooth transition between the measurements and the simulated data in the angular range $\theta_{c.m.} < 40°$ and $\theta_{c.m.} > 130°$, the simulation was scaled down by the indicated factor. The integration of the angular distribution gives the total capture cross section.

6.4.2.3 Verification of simulations

The simulations for ^{40}Ca + ^{232}Th reactions were verified by comparing with measurements for ^{48}Ca + ^{232}Th, which had a wider experimental angular coverage but are expected to have comparable MADs to ^{40}Ca + ^{232}Th. This comparison supports the reliability of QF angular distributions generated using Quasisim.

The closest energy range to compare the two systems is at $\sim$ 15% above the barrier energy. Both systems seem to have similar angular distributions, as shown Fig. 6.14. The light-blue region is the angular range covered by the 2-MWPC configuration with full efficiency; light-grey regions show the extended angular coverage given by the 3rd MWPC with full efficiency; red-filled circles are the measured ^{40}Ca + ^{232}Th reaction, open yellow and brown circles are simulated data; blue-filled rectangles are the measured ^{48}Ca + ^{232}Th reaction.

This comparison focuses on how well the trend of simulated angular distributions at backward angles and forward angles follows the experimental observations. In both ex-

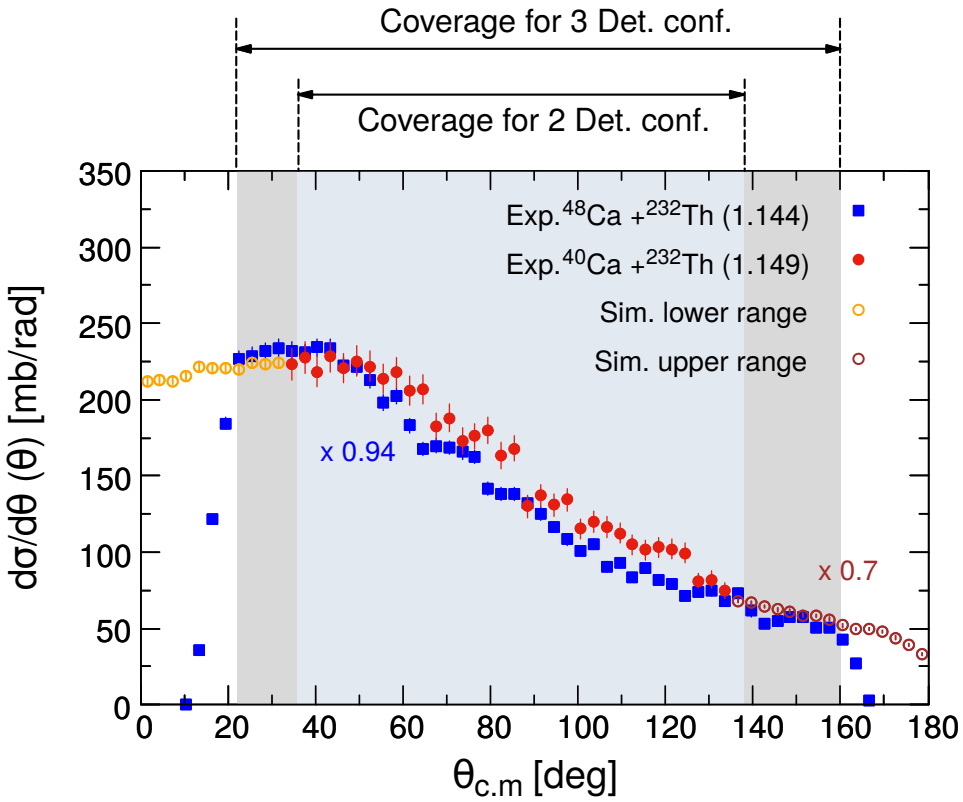

Figure 6.14: The experimental angular distributions for ^{40}Ca + ^{232}Th that (red points) was extrapolated using the simulation (hollow points). The experimental angular distribution for ^{48}Ca + ^{232}Th measured using the 3-MWPC configuration is shown by the blue points. The E/V_B value is given inside the bracket. The light-blue region is the two MWPC angular coverage, the light grey regions indicate the extra angular coverage provided by the small back detector.

tended angular regions, the trend of simulated data follows that of the ^{48}Ca + ^{232}Th measured data; both showing a slightly decreasing trend at more forwards angles, and also a decreasing trend at backward angles.

In the full angular coverage range, the simulated angular distribution agree well with experimental angular distributions for ^{40}Ca + ^{232}Th and ^{48}Ca + ^{232}Th. This indicates that the simulated angular distributions represent the QF angular distributions well.

6.4.3 Determination of ^{48}Ca + ^{232}Th capture cross sections

Fig. 6.15 shows the MADs and angular distributions of the projectile-like fission fragments ($M_R < 0.5$) for ^{40}Ca + ^{232}Th and ^{48}Ca + ^{232}Th reactions. There is a strong similarity between MADs of ^{40}Ca + ^{232}Th and ^{48}Ca + ^{232}Th indicating that two systems are comparable in QF outcomes. This allowed angular distributions for the ^{48}Ca + ^{232}Th system to be extrapolated to 0° and to 180° using the simulations for the ^{40}Ca + ^{232}Th system.

Angular distributions at the very forward and backward angles, $\sim$ 20% of the full angular range, must rely on extrapolation. Except for data at the three highest beam energies, the vast majority of the QF yield is found in the angular range with experimental coverage, as seen in Fig. 6.15b. Thus it is expected that there is no significant contribution to the total capture cross sections from the extrapolated regions.

The five simulation results for ^{40}Ca + ^{232}Th (from the lowest beam energies) were applied directly to the five lowest energies for ^{48}Ca + ^{232}Th. The highest beam energy reaction for ^{40}Ca + ^{232}Th was applied to the three highest beam energies for ^{48}Ca + ^{232}Th. The simulation results for ^{40}Ca + ^{232}Th were rescaled down or up for ^{48}Ca + ^{232}Th to make a smooth transition between measured data and simulated data.

Especially for the three highest energy reactions where a large number of QF fragments are populating at forward angles (close to 0°), the sensitivity of the total cross section to changes in the extrapolation was examined in two ways as shown in Fig. 6.16. One applied a different scale value to the Quasisim calculations, whilst the other changed the trend with angle of the Quasisim calculations. Both examinations were applied at the forward angles since the extrapolated yield here was far larger than at backward angles. Firstly, for $\pm$ 5% variations in scaling of the simulated data, as shown in Fig. 6.16a, there is $\pm$ 1.6% change in the total cross section. Secondly, the different extrapolation trends (falling or rising with decreasing angle) shown in Fig. 6.16b lead to a $\pm$ 2% of change in the total cross section. These variations in the extrapolated angular distributions do not significantly affect the determination of the total cross sections and the experimental capture barrier energies, which is required for the coupled channels calculations.

Fig. 6.17 shows angular distributions for ^{48}Ca + ^{232}Th for all energies. The extrapolation is shown by the small dots joined by lines. Total cross sections for all systems will be presented in the next chapter.

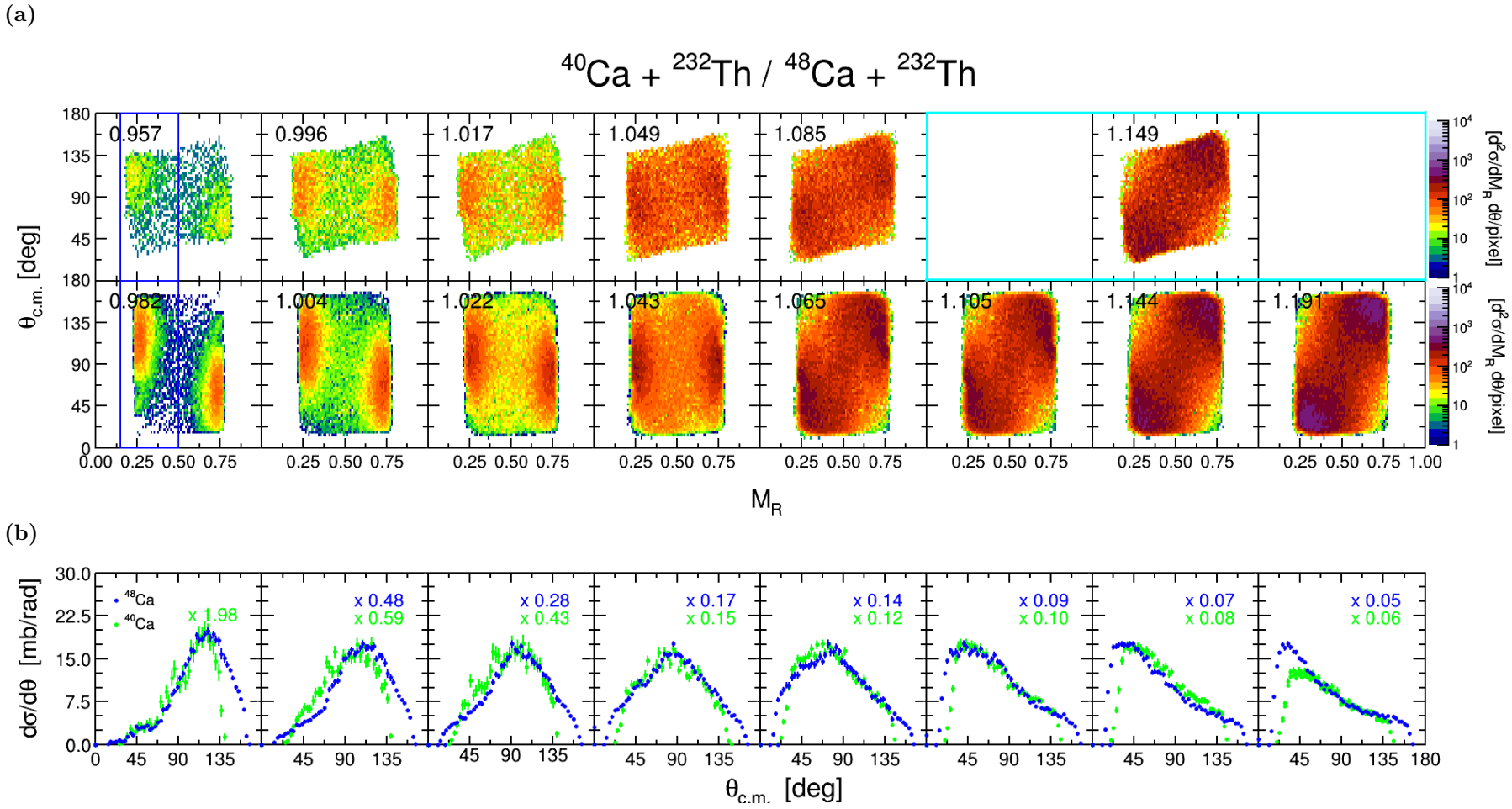

Figure 6.15: The top row of (a) shows normalised experimental MADs for the ^{40}Ca + ^{232}Th reaction and the bottom panels for the ^{48}Ca + ^{232}Th reaction. The ratios of E to V_B are indicated. The MADs are aligned with reactions having the similar E/V_B ratios. (b) Fission angular distributions for $M_R < 0.5$ (blue boxes shown (a)) for ^{48}Ca + ^{232}Th (blue dots) and for ^{40}Ca + ^{232}Th (green dots). In the last three panels, differently scaled angular distribution for ^{40}Ca + ^{232}Th at $E/V_B = 1.149$ are displayed.

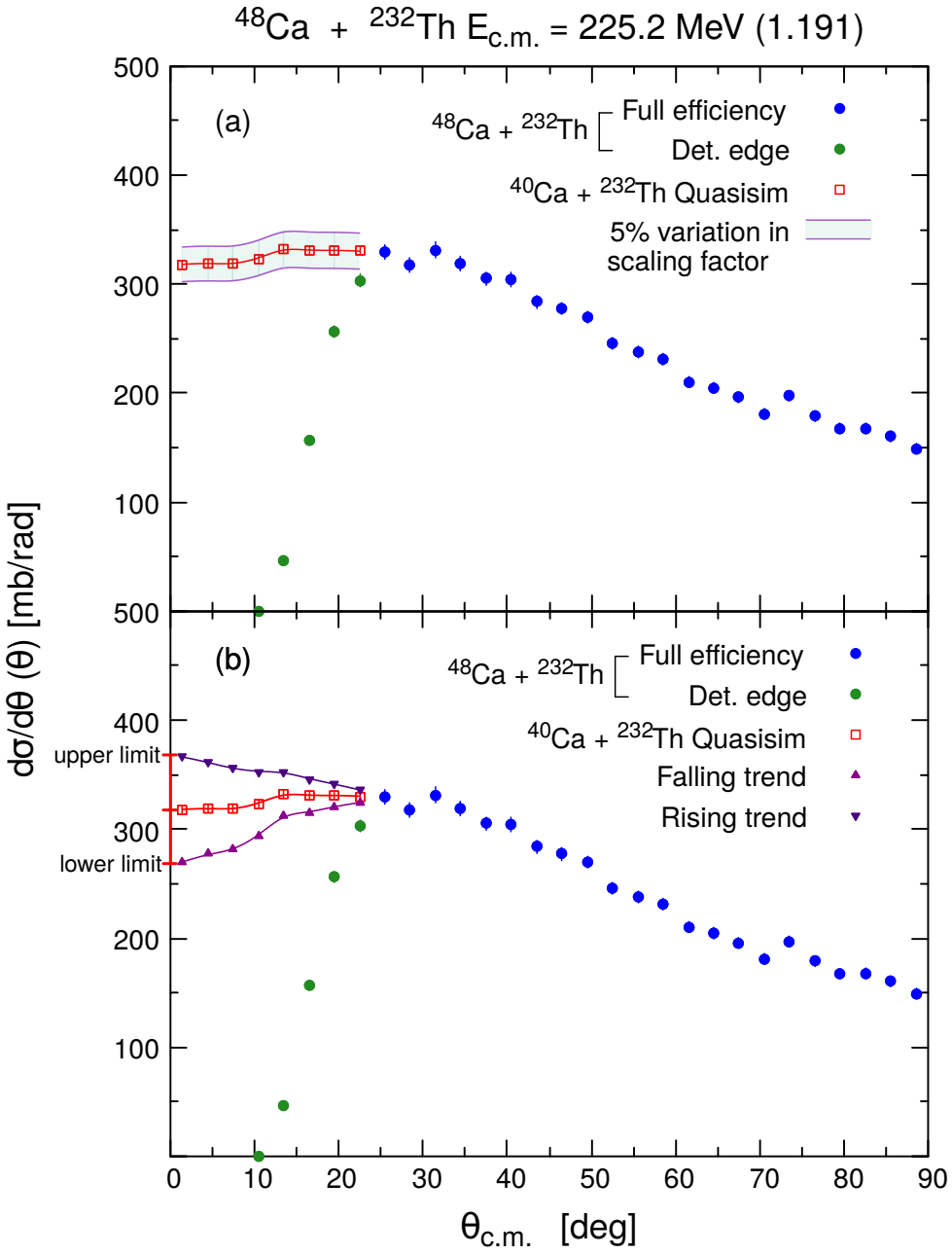

Figure 6.16: (a) Scaling the simulation (hollow points) by ±5% (shaded band) changes the total capture cross section by ± 1.6%. (b) Testing different trends at forward angles. Based on the best smooth transition of ^{40}Ca + ^{232}Th simulated data, the trend of the angular distribution in the angular range not covered in the experiment for ^{48}Ca + ^{232}Th may have a rising or falling trend as the angle goes forward. This results in a ±2% change in the capture cross section. Note that the QF contribution is very small at backward angles and distributions are expected to have a naturally falling trend. See Fig. 6.15b.

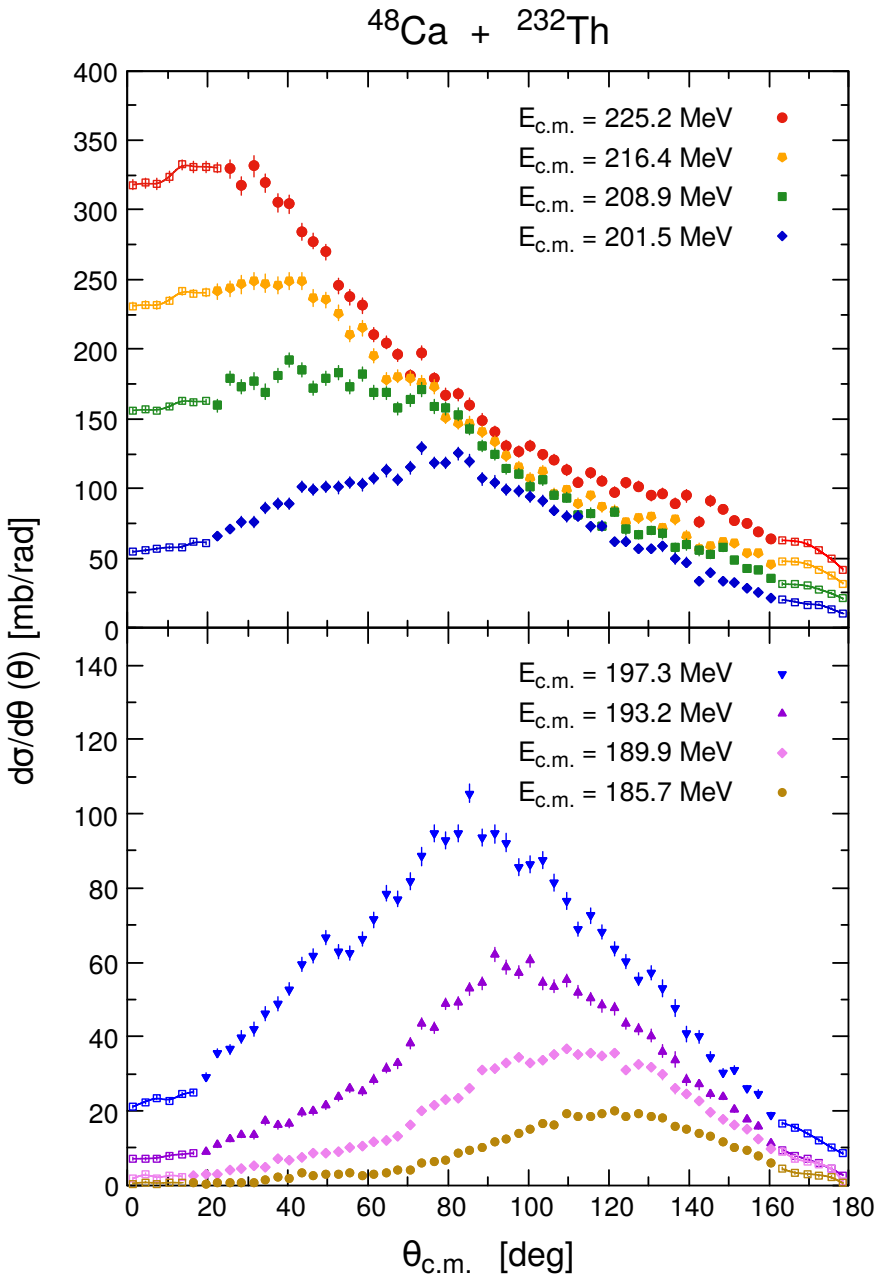

Figure 6.17: Fission fragment angular distributions for ^{48}Ca + ^{232}Th at different energies as a function of the scattering angle in the centre-of-mass frame. Filled points are from the experimental data and lines join the hollow points from the ^{40}Ca + ^{232}Th QF simulations. To make a smooth transition between the measurements and the simulated data, simulated data for ^{40}Ca + ^{232}Th were scaled up or down. The integration of the angular distributions gives the total capture cross section.

Chapter 7

Interpretation and Conclusions

Overview

The first part of this chapter focuses on the calculations of capture cross sections using the coupled channels model. In Section 7.2, comparisons of these calculations with the measured capture cross sections are then made. From this comparison, suppression of the capture cross section is found, which correlates with the yield of transfer-fission (shown in Section 5.3). Suppression factors estimated qualitatively (R) and those of quantitatively (S_{exp}) are compared as a function of the reaction charge product. Lastly, the work presented in this thesis is summarised.

7.1 Coupled channel calculations

Here the coupled channels model (CC) calculations for all the reactions studied in this work are compared with the experimental capture cross sections. The input parameters for the CC calculations using the code CCFULL [6] were similar to those performed to generate the angular momentum distributions required for the experimental capture cross section determination discussed in Section 6.4.2. The main difference between the two sets of CC calculations is the capture barriers that the calculations were constrained to match. The previous calculations were constrained by expectations from a model [81], whilst the calculations in this chapter were constrained by the experimental barrier energies obtained from the experimental capture cross sections, as discussed below. In Section 7.1.2, excitations of collective vibrational or rotational states of the target/projectile nuclei included in the CC calculations are described.

7.1.1 Capture barrier energies

The experimental capture barrier energies for each system were obtained using the classical expression given by Eq. 2.5. Fig. 7.1 shows measured capture cross sections as a function of $1/E_{c.m.}$. The inverse of the x-axis intercept of a linear fit to the experimental data at above barrier energies gives the experiment barrier energy. Table 7.1 shows a comparison of measured barriers and calculations from Eq. 3.6 [81]. Measured barriers are around

1 MeV lower than the calculated values. A larger number of experimental above-barrier cross sections for the $^{34}S + ^{232}Th$ system would have been preferable in order to increase the reliability of the experimental barrier energy. Uncertainties in the barrier energies were evaluated only from statistical uncertainties in the cross sections fitted.

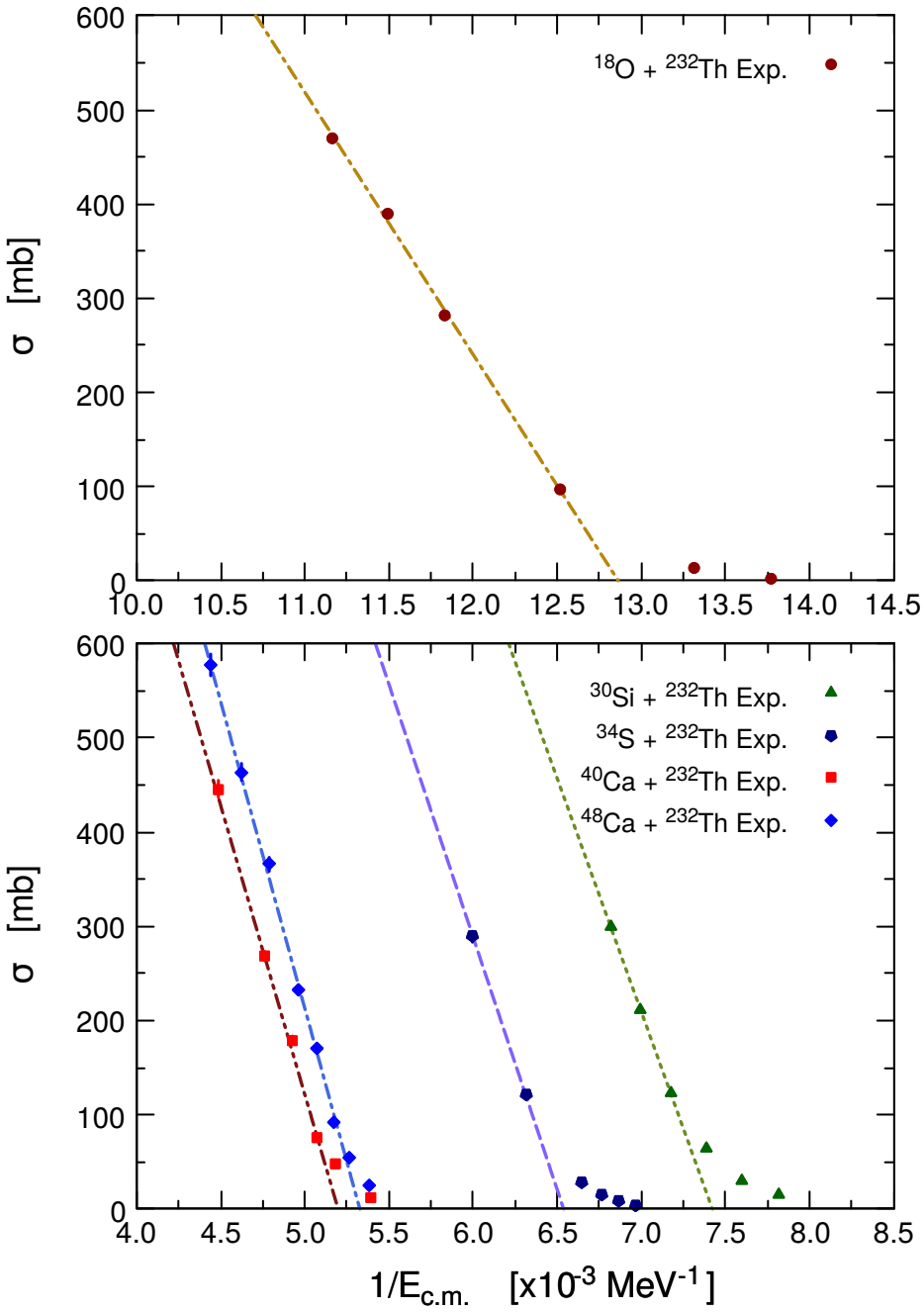

Figure 7.1: Experimental capture cross sections as a function of $1/E_{c.m.}$. The inverse of the x-intercept is the capture barrier from a classical barrier-passing model (Eq. 2.5).

Table 7.1: Comparisons of experimental capture barriers with capture barriers calculated from Ref. [81].

System	Fusion (Capture) Barriers	
	W. J. Świątecki et al. [81]	**Experiment**
^{18}O + ^{232}Th	78.0	77.7 ± 0.1
^{30}Si + ^{232}Th	135.7	134.7 ± 0.1
^{34}S + ^{232}Th	154.8	152.9 ± 0.1
^{40}Ca + ^{232}Th	193.8	192.4 ± 0.1
^{48}Ca + ^{232}Th	189.1	187.9 ± 0.2

7.1.2 Consideration of relevant couplings

The nuclear structure of the reactants was induced in the CC calculations. Depending on which coupling were included, the CC calculated cross sections could vary, in particular, at below-barrier energies. However, as it is the above-barrier energies that are being analysed in this work, "standard" couplings were used in the CC calculations, without considering possible multiple phonon excitations or transfer channels. Couplings and parameters used in this work are given in Table 7.2. The information on energy levels and transition strengths were taken from the Evaluated Nuclear Structure Data File (ENSDF) [92].

The ^{232}Th nucleus is well-known to be a prolate deformed nucleus, having a large quadruple moment ($Q_0 = 9.66$) [93], and is a good rotor[1] ($R_{42} = \frac{E_x(4^+)}{E_x(2^+)} = 3.26$) [92]. The rotational couplings included were the quadrupole (β_2) and hexadecapole (β_4) degrees of freedom, with vibrational coupling to the octupole (3^-) state included [94, 95]. The ^{18}O is assumed to be an inert spherical nucleus. The coupling to the 2^+ state in ^{30}Si ($R_{42} = 2.36$) and ^{34}S ($R_{42} = 2.2$) was included [92], but treated as vibrational. The octupole vibrational state was included for both ^{40}Ca and ^{48}Ca projectiles since the 3^- state has a stronger transition strength compared to the 2^+ state [92].

The coupled channels calculations used a Wood-Saxon nuclear potential, with a deep potential depth V_0 (depending on the Z_1Z_2), a fixed diffuseness of $a_0 = 0.65$ fm, which is a typical value reproducing elastic scattering data [13], and a variable nuclear potential radius parameter r_0, adjusting to reproduce the mean capture barrier energy.

Calculated capture cross sections for all systems using CCFULL were obtained through two steps. Firstly, the capture barrier resulting from CC calculations without adding couplings (which produces a single peaked barrier distribution) was matched the experimental

[1]The ratio of 4^+ to 2^+ excitation energy is a simple way to test the collectivity and nature of excited states of a nucleus. If $R_{42} < 2$, a nucleus can be treated as spherical single-particle. It can be treated as a vibrator if $R_{42} \sim 2$ or a good rotor for $R_{42} \sim 3.33$.

Table 7.2: The ratio of E(2^+) to E(4^+) (R_{42}), the spin and parity (J^π), excitation energy (E_x), type of coupling (rotational or vibrational), multipolarity (λ), and deformation parameters (β_λ) used in the coupled channels calculations for the target and projectile nuclei. The transition strength B(Eλ) are given for Ca projectiles, taken from the ENSDF.

Nucleus		R_{42}	**Coup. states**	J^π	E_x [MeV]	λ	β_λ	**B(Eλ) [W.u]**	**Ref.**
Targ.	^{232}Th	3.26	Rotational			2	0.207		[96]
						4	0.108		[96]
			Vibrational	3^-	0.774	3	0.085		[92, 94, 95]
Proj.	^{18}O	1.79	inert						
	^{30}Si	2.36	Vibrational	2^+	2.235	2	0.315		[93, 92]
	^{34}S	2.20		2^+	2.127	2	0.252		[93, 92]
	^{40}Ca	1.35		2^+	3.904	2	0.123	2.2	[93, 92]
				3^-	3.737	3	0.411	31	[92, 95]
	^{48}Ca	1.18		2^+	3.831	2	0.106	1.71	[93, 92]
				3^-	4.507	3	0.23	5.8	[92, 95]

Table 7.3: Wood-Saxon nuclear potential parameters used for the coupled channels calculations. A fixed diffuseness parameter $a_0 = 0.65$ fm, and large depth (V_0) were used. The radius parameter (r_0) was adjusted to match the experimental barrier energy, given in Table 7.1.

System	**Nuclear potential**		
	V_0 [MeV]	a_0 [fm]	r_0 [fm]
^{18}O + ^{232}Th	225	0.65	1.129
^{30}Si + ^{232}Th	255	0.65	1.124
^{34}S + ^{232}Th	600	0.65	1.062
^{40}Ca + ^{232}Th	600	0.65	1.038
^{48}Ca + ^{232}Th	600	0.65	1.047

capture barrier by adjusting r_0. After adding couplings, r_0 was readjusted to make the weighted average barrier match the experimental capture barrier since the coupling effects result in a barrier distribution ($d^2(\mathrm{E}\sigma)/dE^2$ against E [18]) having multiple peaks.

7.2 Suppression of capture cross sections

Measured cross sections are compared with CC calculations in Fig. 7.2. The left panels show cross sections on a linear scale, and on a log scale in the right panels. None of the measurements agree with the CC calculations using $a_0 = 0.65$. The CC calculations overestimate experiment at all energies above the capture barriers. In order to make the CC calculations agree with the experimental data, the CC calculations for each reaction needed to be multiplied by a factor S ($\sigma_{exp} = S\,\sigma_{CC}$). This scaling value is defined as the suppression factor (S_{exp}), which seems to be independent of beam energy for each reaction.

The suppression factors were determined only for the above-barrier energies used in the fits to determine the average experimental capture barrier (Fig. 7.1). Nevertheless, the scaled CC calculations describe the whole energy range rather well, as seen in the right-hand panels in Fig. 7.2. The uncertainties in the suppression factors were estimated to be in the range $\pm$ 0.02 to $\pm$ 0.03. This range arose from statistical uncertainties in the experimental cross sections, in the experimental mean capture barrier energies V_B, and in the CC calculations. The change resulting in using a different nuclear potential diffuseness for the CC calculations was not included in the uncertainty, since the suppression factors will be compared in Section 7.3 with those determined previously using this diffuseness parameter.

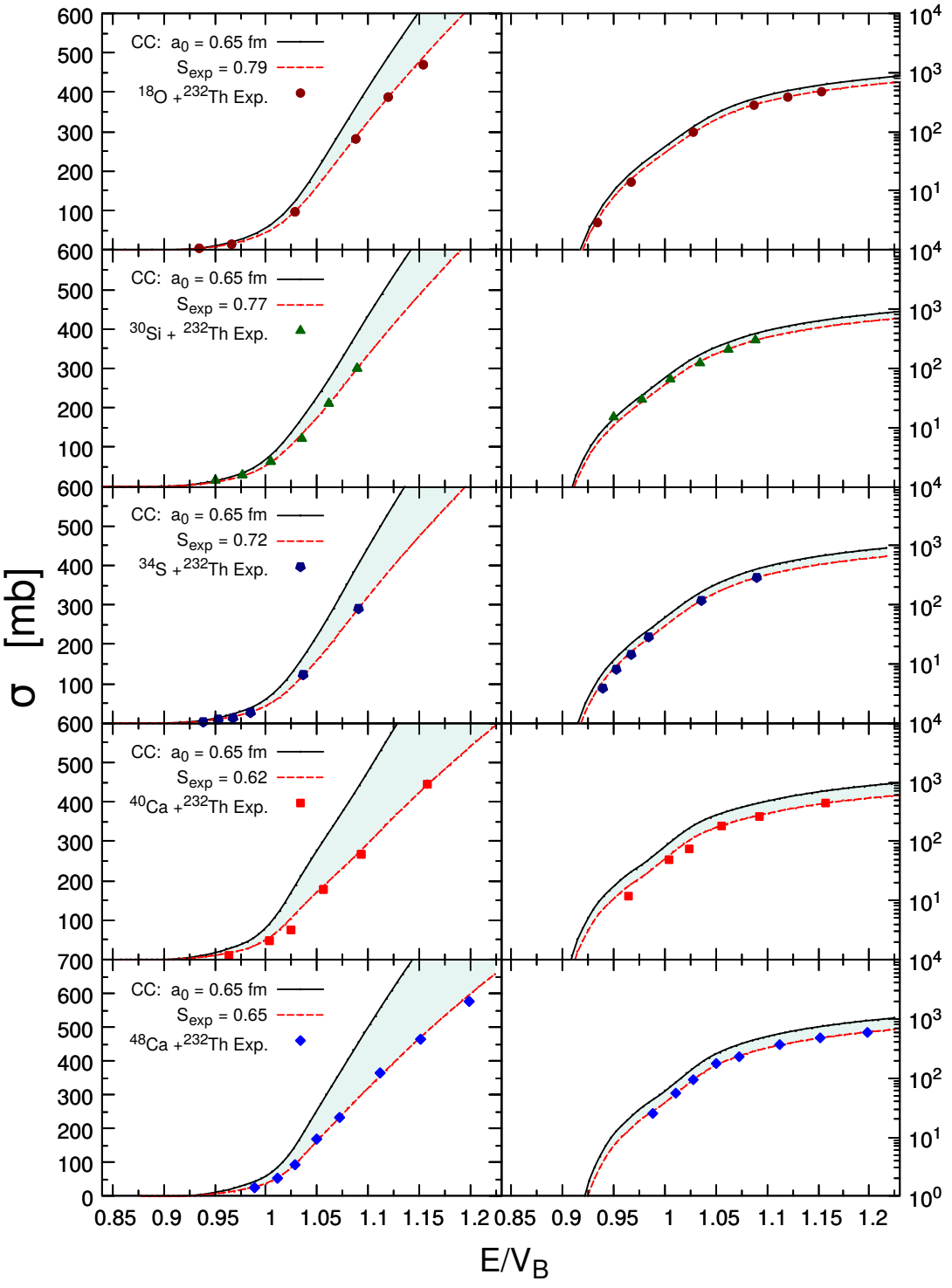

Figure 7.2: Experimental fusion cross-sections (data points) for ^{18}O, ^{30}Si, ^{34}S, ^{40}Ca, and ^{48}Ca + ^{232}Th reactions plotted on a linear scale (left side) and logarithmic scale (right side). All coupled channels (CC) calculations used a nuclear potential with a diffuseness parameter of 0.65 fm. Details of couplings and nuclear potential parameters are given in the Tables 7.2 and 7.3. Measured capture cross sections for all systems are lower than the CC calculations by the indicated suppression factors (S_{exp}).

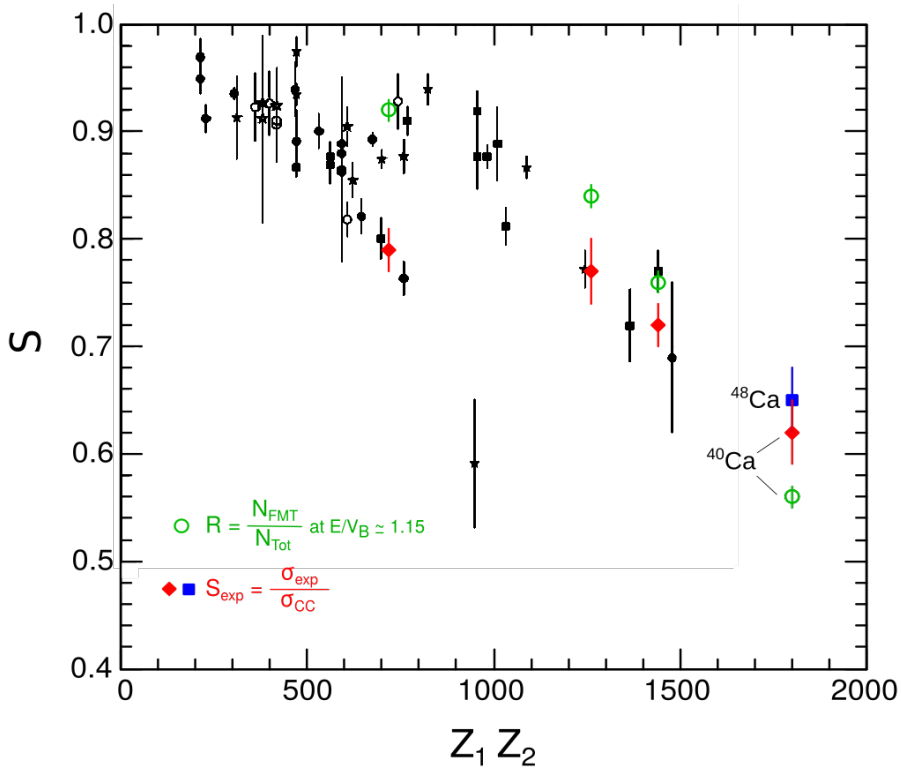

Figure 7.3: Suppression factor (S) as a function of Z_1Z_2. Red and blue solid points (S_{exp}) are ratio of the experimental capture cross section (σ_{exp}) for ^{18}O, ^{30}Si, ^{34}Si and ^{40}Ca and ^{48}Ca + ^{232}Th target at above-barrier energies to those of coupled channels calculations (σ_{CC}) using a standard nuclear potential diffuseness ($a_0 = 0.65$ fm). Green hollow points (R) are ratio of the number of the FMT-fission events (N_{FMT}) to the total fission events (N_{Tot}) at $E/V_B \simeq 1.15$, determined in Section 5.3. The results of the current work were overlaid on the top of the results obtained Ref. [15].

7.3 Correlation of capture suppression and transfer-fission

In Fig 7.3, R (green points) and S_{exp} (red and blue points) are presented together with suppression factors (S) extracted by J. O. Newton et al. [15] for capture cross sections from a wide range of reactions. The present results for S_{exp} sit within those trends very nicely. Now there is the opportunity to test the suggestion in Ref. [15] that deep inelastic scattering (energy dissipation) might be responsible for the increasing suppression with Z_1Z_2, using the new transfer-fission results.

The green points R in Fig. 7.3 show the ratio of FMT-fission (resulting only from capture) divided by total fissions (including 3-body events associated with mass-transfer). The points were evaluated at $E/V_B \simeq 1.15$, from the results shown in Fig. 5.10. The qualitative correlation is good, although this measure shows an even steeper fall with Z_1Z_2. There are good reasons why this should be so.

Let us consider in detail the origin of fission events that are outside the gate in ($v_{par} - v_{CN}$) *vs* v_{perp} applied to select FMT-fission (see Fig. 5.2). We have described these events

by the term transfer-fission. This process, discussed in more detail below, we believe is the main contributor. However, in general, any 3-body outcome following a collision will be outside the FMT gate if one of the masses gives sufficient recoil to the the remaining system so that it is deflected outside the FMT gate. In practice, a nucleus of charge three to four would be have enough Coulomb energy to disturb the 2-body kinematics. Thus we may also use the term 3-body kinematics - which clearly corresponds to the case of fission following a transfer reaction.

To relate the ratio of 2-body fission (FMT-fission) to the sum of 2 and 3-body fission (denoted by R), to the factor S suppressing capture, we need to consider in detail all origins for 3-body events, and determine how they would affect the value of R.

Considering transfer-fission, we can define two categories. The first corresponds to transfer on grazing trajectories that cannot result in fusion. If these have a cross section σ_{Tr}^{Gr}, the 3-body fission cross section will be the product of this cross section, and the average probability of fission P_{fis}^{Gr} for these events: $\sigma_{3\text{-}body} = \sigma_{Tr}^{Gr} P_{fis}^{Gr}$. The fission probability will depends on the thermal (excitation) energy of the heavy transfer partner - it must be higher than the fission barrier ($\sim$ 6 MeV), and an increase by slightly more than the neutron binding energy will give another chance of fission if first-chance fission is survived. By $\sim$ 20 MeV, P_{fis} will be close to unity.

The second category of transfer-induced fission comes from transfer reactions on an incoming trajectory that would have resulted in fusion. If sufficient kinetic energy is dissipated, the trajectory may be changed to one of reflection from the barrier, and similarly may result in eventual fission of the heavy transfer partner. If the cross section is labelled σ_{Tr}^{DIC}, the 3-body fission cross section is $\sigma_{3\text{-}body} = \sigma_{Tr}^{DIC} P_{fis}^{DIC}$, resulting in a total 3-body fission given by:

$$\sigma_{3\text{-}body} = \sigma_{Tr}^{Gr} P_{fis}^{Gr} \; + \; \sigma_{Tr}^{DIC} P_{fis}^{DIC} \tag{7.1}$$

where Gr and DIC stand for grazing and deep inelastic collisions respectively. Tr and fis represent transfer and fission reactions.

Thus the ratio R from the above discussion can be written:

$$R = \frac{\sigma_{2\text{-}body}}{\sigma_{2\text{-}body} \; + \; \sigma_{3\text{-}body}} = \frac{\sigma_{FMT}}{\sigma_{FMT} \; + \; \sigma_{Tr}^{Gr} P_{fis}^{Gr} \; + \; \sigma_{Tr}^{DIC} P_{fis}^{DIC}} \, . \tag{7.2}$$

There is a third possible source of 3-body fission events. This is a mass-asymmetric QF event, following capture, where the fissility and excitation energy of the heavy QF fragment is sufficiently large that it fissions after the primary QF event. It is expected that a relatively narrow range of masses will contribute, as fission barriers around ^{208}Pb are well over 20 MeV [97]. We define the QF cross section in this (so far) arbitrary mass range to be σ_{QF}^{Asym}, and the average probability of fission as P_{fis}^{QF}. The cross section of this class of 3-body fission events is then $\sigma_{QF}^{Asym} P_{fis}^{QF}$. According to Ref. [30], this cross section

should be a small fraction of the total FMT-fission cross section. However, as discussed in Section 5.1.1.2, the fission source velocity spectra measured in this work show evidence of some contribution of such events.

The impact of sequential fission of the heavy QF fragment is different to transfer-induced fission. It reduces the 2-body cross section, whist increasing the 3-body cross section. Thus the final expression for R becomes:

$$R = \frac{\sigma_{FMT} \; - \; \sigma_{QF}^{Asym} \, P_{fis}^{QF}}{\sigma_{FMT} \; + \; \sigma_{Tr}^{Gr} \, P_{fis}^{Gr} \; + \; \sigma_{Tr}^{DIC} \, P_{fis}^{DIC} \; + \; \sigma_{QF}^{Asym} \, P_{fis}^{QF}} \, . \tag{7.3}$$

To fully disentangle all source of 3-body fission, which results from either transfer reactions or sequential fission following mass-asymmetric QF, dedicated triple coincidence measurements will be required. Analysis methods for such data are under development.

Qualitatively estimated suppression factor (R) can be compared with quantitatively estimated values (S), which is a ratio of experimental FMT-fission cross sections to CC calculations and is expressed as:

$$S = \frac{\sigma_{FMT}}{\sigma_{CC}} \tag{7.4}$$

The suggestion of J. O. Newton et al. [15] was that the measured capture cross (σ_{FMT} here) is smaller than σ_{CC} because of deep inelastic transfer cross sections:

$$\sigma_{FMT} = \sigma_{CC} \; - \; \sigma_{Tr}^{DIC} \, , \tag{7.5}$$

rearranging this equation gives a denominator of Eq. 7.4:

$$\sigma_{CC} = \sigma_{FMT} \; + \; \sigma_{Tr}^{DIC} \, . \tag{7.6}$$

Thus S is given by:

$$S = \frac{\sigma_{FMT}}{\sigma_{FMT} \; + \; \sigma_{Tr}^{DIC}} \, . \tag{7.7}$$

There should be a close correspondence between the expressions for S and R only under certain conditions. The terms are identical if (1) $\sigma_{QF}^{Asym} \, P_{fis}^{QF} = 0$, and (2) $\sigma_{Tr}^{Gr} \, P_{fis}^{Gr} = 0$, and (3) $P_{fis}^{DIC} = 1$. In most reactions studied here, $\sigma_{QF}^{Asym} \, P_{fis}^{QF}$ will be small, since the fraction of QF yield with large mass-asymmetries is small, although P_{fis}^{QF} could be approaching unity. At $E/V_B \simeq 1.15$, where the comparison in Fig. 7.3 is made, only for the ^{40}Ca + ^{232}Th reactions could this term be significant. In this case, the expression for S must be modified, since identification of σ_{FMT} with $\sigma_{2\text{-}body}$ is no longer appropriate, and the experimental value of S in these reactions corresponds to:

$$S_{exp} = \frac{\sigma_{2\text{-}body}}{\sigma_{CC}} = \frac{\sigma_{FMT} \; - \; \sigma_{QF}^{Asym} \, P_{fis}^{QF}}{\sigma_{CC}} \, . \tag{7.8}$$

For the lighter projectiles, we can safely take the 3-body QF contribution to be negli-

gible. Then Eq. 7.2 for R is applicable and comparing CC calculations gives the capture suppression factor as:

$$S_{exp} = \frac{\sigma_{2\text{-}body}}{\sigma_{CC}} = \frac{\sigma_{FMT}}{\sigma_{CC}} \,. \tag{7.9}$$

Depending on the charge product of the two colliding nuclei, R can be larger or smaller than S_{exp}. For the lightest projectile, the excitation energies in transfer reactions have been measured by D. C. Rafferty et al. in the ^{16,18}O, ^{19}F + ^{208}Pb reactions at sub-barrier energies [14], corresponding to the grazing condition at above-barrier energies. The fraction of yield at excitation energies above 6 MeV is small, and above 12 MeV even smaller, indicating that P_{fis}^{Gr} will be very small, and P_{fis}^{DIC} also rather small. In this case, clearly R will be greater than S, and this is seen to be the case in Fig. 7.3.

For the intermediate mass projectiles (^{30}Si and ^{34}S) the value of R is much closer to S, suggesting a higher value of P_{fis}. This is consistent with the rapid increase in excitation energies following transfer/DIC observed in reactions on Pb [14]. For ^{40}Ca and ^{48}Ca projectile reactions, R is smaller than S due to the effect of sequential fission events.

The message from the values of R and S_{exp} as a function of Z_1Z_2 determined in this work is clear. The result of Ref. [15] that there is a systematic suppression of capture, increasing with Z_1Z_2 has been confirmed. The strong correlation of the 3-body fission probability with the suppression factor is very good evidence that the origin of the suppression is energy dissipation before reaching the barrier radius, as originally suggested in Ref. [15].

7.4 Perspectives for future work

The coupled channels model is essentially a model for elastic, inelastic and transfer reactions: cross sections for channels that are explicitly included are calculated, but fusion is mimicked by essentially absorbing the flux that passes the barrier. Therefore, the model cannot account for processes that cause loss of kinetic energy into complex excitations (partial thermalisation) prior to reaching the fusion barrier. The measurements in this work show that such processes become increasingly important with increasing Z_1Z_2.

Including (partial or full) thermalisation in a quantum model is a challenge common to all areas of physics. In the case of nuclear reactions, a possible way forward can be to develop a phenomenological model of energy dissipation, based on these and other measurements. This description can then be incorporated in existing coupled channels model. Such a line of work is currently being pursued at the ANU. Microscopic models, such as the Time Dependent Hartee Fock theory, can in principle include effects of dissipation. However, in its current implementation, it is limited to one-body dissipation and further work would be necessary to incorporate energy dissipation realistically.

In terms of future measurements, it will be useful to separate transfer-induced fis-

sion from sequential fission of the heavy quasi-fission fragment (Section 7.3). The latter can be significant for reactions induced by Ca and heavier beams. It is attributed to transfer-fission (and not capture) in the present measurements. Triple-coincidence measurements will enable a more robust determination of capture cross sections and thus of the suppression.

Ultimately, it would be useful to ensure that inelastic, transfer and capture cross sections do indeed exhaust the total reaction cross sections. The latter can be obtained by measuring the angular distribution of elastic scattering.

7.5 Summary

In this work, the reduction of capture cross sections in heavy ion collisions was explored, in particular, focusing on the role energy dissipation plays. Here, transfer-fission events were used as an indicator of energy dissipation in reactions competing with capture. As ^{232}Th and neighbouring nuclei have relatively low fission barriers ($\sim$ 6 MeV), nucleon exchange (transfer reactions) during the collisions can result in excitation energies in the target-like nucleus larger than the fission barrier-height. If this energy is thermalized, it can result in fission of the target-like nucleus, which is a signal that this has happened. Since the probability of multi-nucleon transfer reactions involving significant dissipation of kinetic energy (also known as deep inelastic scattering) is strongly influenced by the density overlap of the colliding nuclei, a systematic study of both transfer-fission and capture reactions as a function of Z_1Z_2 was carried out in this work. The first part of this work focused on the qualitative understanding of the ratio of transfer-fission to fusion-fission, and the second part focused on the quantitative reduction of capture (FMT-fission) cross sections by comparing the measured cross sections with coupled channels calculations.

To extract absolute capture cross sections, it was necessary to extrapolate measured angular distributions to angles close to the beam axis which the CUBE detectors did not cover. Two methods were used for extrapolation, depending on the proportion of quasifission (QF) in the capture reaction products. In this work, the mass-angle correlation seen in the MAD was used as a criterion to identify the contribution of fast QF following capture. Reactions showing a strong correlation were ^{34}S + ^{232}Th, ^{40}Ca + ^{232}Th, and ^{48}Ca + ^{232}Th. For these reactions, fission angular distributions were extrapolated by reproducing the MADs using a simulation of QF. For the light systems (^{18}O + ^{232}Th and ^{30}Si + ^{232}Th), the standard transition state model (TSM) analysis of the fission angular distributions was used to determine cross sections, since there was little correlation of mass with angle, indicating that angular distributions calculated with the TSM formalism should be appropriate.

The ratio of the measured FMT (2-body) fission cross section to the capture cross section predicted by the coupled channels calculations was taken as the suppression factor.

This suppression factor increases with increasing Z_1Z_2. In other words, more transfer-induced fission took place as the charge product increases because of the larger density overlap of the colliding nuclei before contact, thus more energy is dissipated. This result shows that transfer reactions, which lead to energy dissipation, play a significant role in fusion reactions. It provides evidence of energy dissipative process occurring outside the barrier. Therefore, energy dissipation both outside and inside the barrier must be taken into account to develop a realistic model of capture and fusion.

Appendix A: Coulomb trajectory calculation

As introduced in Section 2.4, Quasisim is a Monte Carlo code based on a classical phenomenological approach [30] to simulate quasifission (QF) mass-angle distributions (MADs) [54].

The observed angle of a QF fragment θ_{QF} is determined from the sum of angles associated with the Coulomb trajectories of the projectile and target and the rotation angle (θ_s) of the dinuclear system as it evolves between contact and scission, as shown in Fig. A.1. θ_{QF} is given by:

$$\theta_{QF}(t_s) = \pi - [\Theta_{in} + \Theta_{rot}(t_s) + \Theta_{out}] \tag{A.1}$$

where Θ_{in} and Θ_{out} are the angles associated with the Coulomb trajectories for the incoming and outgoing nuclei. $\theta_{rot}(t_s)$ is the rotation angle of the dinuclear system, given in Section 2.4.2. This appendix focuses on Θ_{in} and Θ_{out}.

The following derivations of angles related to the Coulomb trajectories are based on Elastic Coulomb scattering (Rutherford scattering) given by Krane [88]. Firstly, the Coulomb trajectory of the incoming nucleus (Θ_{in}) is calculated as follows. Here Θ_{in} is defined by the angle between the vectors joining the centres of the two colliding nuclei at infinity and that at a minimum separation distance D_{in} approach, as shown in Fig. A.1. If the impact parameter $b > 0$, the incoming projectile is deflected through a scattering angle θ_{in}. Conservation of angular momentum defines the relationship between the impact parameter b_{in} and scattering angle:

$$b_{in} = \frac{D_{in}}{2} \cot\left(\frac{\theta_{in}}{2}\right) ; \tag{A.2}$$

where b_{in} is calculated from an orbital angular momentum L and a beam energy E_{lab}. It is given by:

$$b_{in} = \frac{L\hbar}{\mu\, v_\infty} \tag{A.3}$$

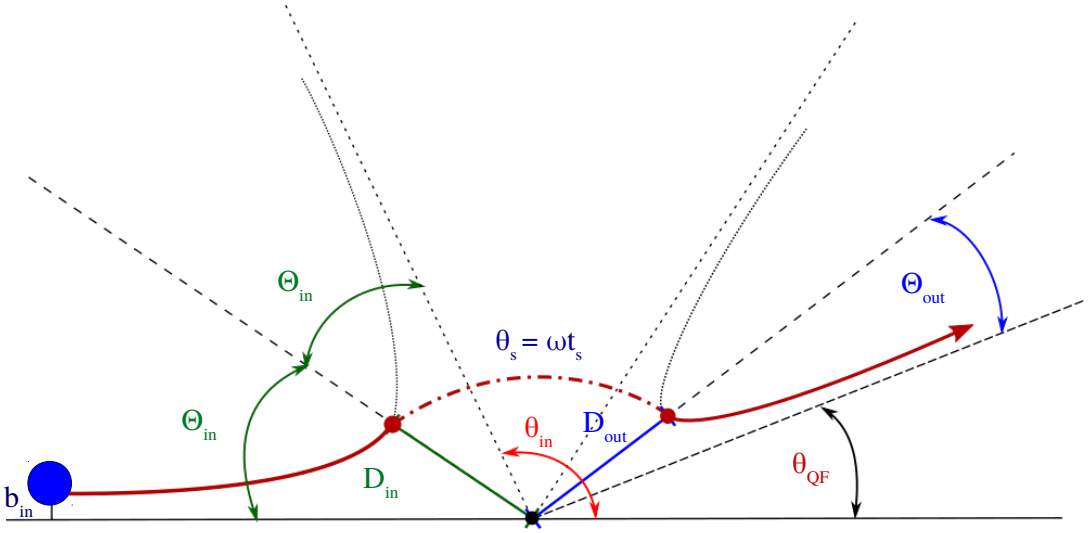

Figure A.1: Schematic illustration of the path during a collision resulting in quasifission (red) associated with the Coulomb trajectories for the incoming and outgoing nuclei and rotation of the system. According to Rutherford scattering, the incoming projectile nucleus is deflected by θ_{in} at the distance D_{in} which is parametrised by the impact parameter b_{in}. D_{out} and b_{out} are parameters associated with the outgoing nucleus that take into account the change in masses while the system is rotating, as described in the text.

where μ is the reduced mass ($\mu = \frac{A1A2}{A_1+A_2}$) and v_∞ the velocity of the incident projectile ($v_\infty = 1.385\sqrt{\frac{E_{lab}(\mathrm{MeV})}{A_{proj}}}$ in cm/ns).

The minimum separation distance D_{in} is determined by:

$$D_{in} = \frac{D_{min}}{2}\left(1 + \sqrt{1 + \left(\frac{2b_{in}}{D_{min}}\right)^2}\right) \tag{A.4}$$

where D_{min} is the distance of closest approach in a head-on collision ($b = 0$). At this point, the initial kinetic energy is converted into Coulomb potential energy and thus D_{min} can be written as:

$$D_{min} = \frac{e^2}{4\pi\varepsilon_0}\frac{Z_1 Z_2}{E_{c.m.}}\,. \tag{A.5}$$

Therefore, by substituting Eq. A.3 and Eq. A.4 into Eq. A.2 gives Θ_{in}. This angle is expressed in terms of the scattering angle:

$$2\Theta_{in} = \pi - \theta_{in} \tag{A.6}$$

and substituting the scattering angle θ_{in} defined from Eq. A.2 into this equation gives:

$$\Theta_{in} = \frac{\pi}{2} - \tan^{-1}\left(\frac{D_{in}}{2b_{in}}\right)\,. \tag{A.7}$$

The outgoing projectile-like nucleus also follows a Coulomb trajectory, and thus Θ_{out} is expressed similar to Eq. A.7 but with the outgoing channels of D_{out} and b_{out}:

$$\Theta_{out} = \frac{\pi}{2} - \tan^{-1}\left(\frac{D_{out}}{2b_{out}}\right) . \tag{A.8}$$

D_{out} and b_{out} must be estimated for the QF fragment which originated from the projectile nucleus, whose mass has changed while the system is undergoing rotation. To do this, the distance of closest approach (D_{out}) is first determined by assuming the composite system has no radial velocity at scission and its kinetic energy is fully damped such that it follows Viola systematics [81]. The total kinetic energy (TKE) in terms of mass ratio M_R, as discussed in Section 4.4.2, is given by:

$$TKE_{Viola}(M_R) = \frac{0.789(1 - M_R)\, Z_{CN}^2}{[M_R^{1/3} + (1 - M_R)^{1/3}]\, A_{CN}^{1/3}} \tag{A.9}$$

where CN denotes the compound nucleus.

This TKE_{Viola} is shared by two fragments according to their M_R proportion using following relations:

$$\begin{aligned} Z_1 = M_R Z_{CN},\ Z_2 = (1 - M_R) Z_{CN} , \\ A_1 = M_R Z_{CN},\ A_2 = (1 - M_R) A_{CN} . \end{aligned} \tag{A.10}$$

A minimum separation distance D_{out} for the outgoing nucleus is obtained from the rearrangement of the Coulomb potential energy (similar to Eq. A.5) and is given by:

$$D_{out} = \frac{e^2}{4\pi\varepsilon_0}\frac{Z_1 Z_2}{E'_{c.m.}} \tag{A.11}$$

$$= \frac{e^2}{4\pi\varepsilon_0}\frac{Z_1 Z_2}{TKE_{Viola}} \tag{A.12}$$

$$= 1.834\, A_{CN}^{1/3}\, (M_R^{1/3} + (1 - M_R^{1/3}) \tag{A.13}$$

where $E'_{c.m.}$ is the kinetic energy of a mass ratio of M_R.

To determine the impact parameter for the outgoing QF channel, it is assumed that 2/7 of the initial orbital angular momentum (L) is converted into intrinsic angular momentum in the two fragments; that is, the dinuclear system carries the $5/7L$ [98]. Therefore, the outgoing impact parameter is expressed as:

$$b_{out} = \frac{5}{7}\frac{b_{in}\mu v_\infty^{in}}{\mu_{out} v_\infty^{out}} \tag{A.14}$$

where μ is the reduced mass $\left(\mu = \frac{A_1 A_2}{A_1 + A_2}\right)$ and v_∞^{out} is the relative velocity of two fission fragments. The μ_{out} and v_∞^{out} in terms of M_R give:

$$\mu_{out} = M_R(1 - M_R)A_{CN} , \tag{A.15}$$

$$v_{\infty}^{out} = v_1 + v_2 \tag{A.16}$$

$$= 1.385\sqrt{\frac{TKE_v(1-M_R)}{A_{CN}M_R}} + 1.385\sqrt{\frac{TKE_vM_R}{A_{CN}(1-M_R)}} \tag{A.17}$$

$$= 1.385\sqrt{\frac{TKE_v}{A_{CN}}}\left(\left(\frac{1-M_R}{M_R}\right)^{1/2} + \left(\frac{M_R}{1-M_R}\right)^{1/2}\right). \tag{A.18}$$

Substituting Eq. A.15 and Eq. A.18 into Eq. A.14 gives the value of b_{out}. Thus, the angle related to the Coulomb trajectory for the outgoing fragment (Θ_{out}) can be evaluated by substituting Eq. A.13 and A.14 into Eq. A.8.

Appendix B: Calculation of moment of inertia

B.1 Time-Dependent Hartree-Fock (TDHF) calculation

Time-Dependent Hartree-Fock (TDHF) [99] is a microscopic model based on mean field theory which employs the Skyrme energy functional for dynamical calculations. The TDHF calculation code used in this work was provided by Dr. Cedric Simenel [91].

The time-dependent moment of inertia can be evaluated from the TDHF calculations. The rigid body of inertia tensor for a system with time-dependent density $\rho(t)$ is given by [58]:

$$\frac{I_{ij}}{m} = \int \rho(r,t)(r^2\delta_{ij} - x_i x_j)dV \tag{B.1}$$

where ρ is the local number density calculated from the TDHF evolution in units of the number of nucleons (n) per fm^3, m is the mass of a nucleon, and $x_{i=x,\,y,\,z}$ refers to the 3-D Cartesian coordinates.

The moment of inertia from the TDHF calculations as a function of time was calculated by finding the rigid moment of inertia at each time step, using the TDHF density. The only component of I_{ij} needed was I_{zz} since we are interested in the moment of inertia about the rotation axis with coordinates at the centre of mass of the system ($x_{c.m.}$, $y_{c.m.}$) which is perpendicular to the xy-plane,

$$\frac{I_{zz}}{m} = \int \tilde{\rho}(r,t)(x^2 + y^2)dV \tag{B.2}$$

Eq. B.2 calculates the moment of inertia I about the z-axis, which has coordinates $(0,0)$ in the xy-plane. This is not what we want, rather $I_{c.m.}$ about the axis through the centre-of-mass. Based on the parallel axis theorem [100] (with both axes perpendicular to the xy-plane), the inertia tensor with respect to the axis passing through the centre of mass can be written as:

$$\frac{I_{c.m.}}{m}(t) = \frac{I_{zz}}{m} - A_{CN}(x^2_{c.m.}(t) + y^2_{c.m.}(t))\,. \tag{B.3}$$

where A_{CN} is the total number of nucleons.

B.2 Geometry-based calculation

B.2.1 Collision of spherical nuclei

The moment of inertia of the dinuclear system of two spherical nuclei undergoing a collision is:

$$I_{sphere} = m_1 x_1^2 + \frac{2}{5} m_1 r_1^2 + m_2 x_2^2 + \frac{2}{5} m_2 r_2^2 \tag{B.4}$$

where x_1 and x_2 are displacements of constituent nuclei that are derived based on Archimedes' principle: the masses of the two constituents of the dinuclear system are balanced at the centre of mass $x_{c.m.}$ shown in Fig. B.1 and are expressed as follows:

$$x_1 = \frac{r_1 + r_2}{1 + \frac{m_1}{m_2}} \tag{B.5}$$

$$x_2 = \frac{r_1 + r_2}{1 + \frac{m_2}{m_1}} \tag{B.6}$$

B.2.2 Collision of a spherical projectile with a deformed target nucleus

In the case of collisions on a deformed target nucleus, the initial shapes of the composite (dinuclear) system are different for tip or side collisions. The tip collision forms an elongated shape whereas the side collisions lead to a more compact shape. Since the forces acting on the dinuclear systems are different due to their different shapes, the dinuclear system evolves differently, giving a different range of rotational angles. Because of this, the moments of inertia for tip and side collisions are estimated separately.

Firstly, distances from the centre of the nucleus to the centre of mass point for the tip collision are determined based on the radii of the deformed target nucleus. For the tip collision, they are expressed as:

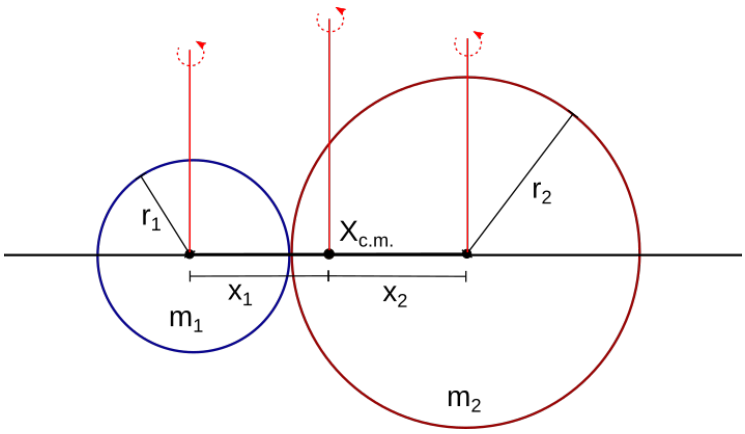

Figure B.1: Schematic view of the dinuclear system of the collision between two spherical nuclei having a mass of m_1 and m_2, respectively.

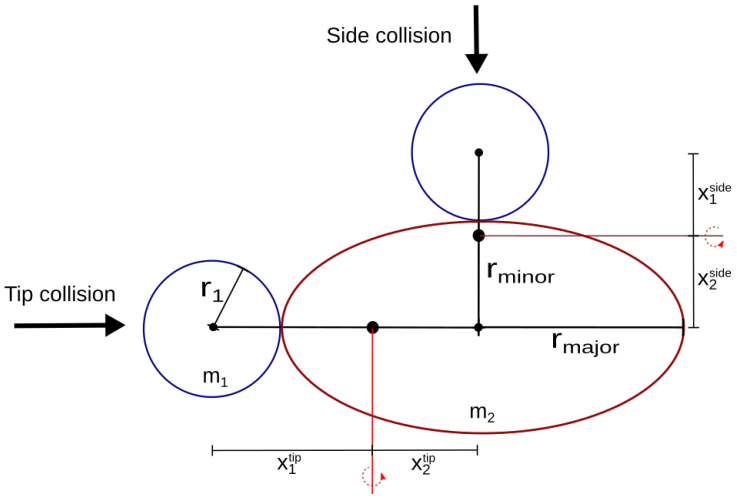

Figure B.2: Schematic view of the collision of a spherical projectile with a deformed target.

$$x_1^{tip} = \frac{r_1 + r_{major}}{1 + \frac{m_1}{m_2}} \tag{B.7}$$

$$x_2^{tip} = \frac{r_1 + r_{major}}{1 + \frac{m_2}{m_1}} \tag{B.8}$$

where replacing r_{major} to r_{minor} gives x_1^{side} and x_2^{side} for the side collision.

The moments of inertia for the tip collision and the side collision are:

$$I_{tip} = m_1(x_1^{tip})^2 + \frac{2}{5}m_1 r_1^2 + m_2(x_2^{tip})^2 + \frac{1}{5}m_2(r_{minor}^2 + r_{major}^2) \tag{B.9}$$

$$I_{side} = m_1(x_1^{side})^2 + \frac{2}{5}m_1 r_1^2 + m_2(x_2^{side})^2 + \frac{2}{5}m_2(r_{minor}^2) \tag{B.10}$$

where the last of the both equations is the moment of inertia tensor of a spheroid with z-axis along the axis of symmetry.

The radii of the deformed nuclei are estimated from the deformation parameter. The radius of the most common equilibrium shapes of nuclei are defined as [88]

$$R(\theta, \phi) = R_{av}[1 + \beta Y_{20}(\theta, \phi)] \tag{B.11}$$

where $R_{av} = r_0 A^{1/3}$, β is the quadrupole deformation parameter and Y_{20} is the spherical harmonics, given by:

$$Y_{20} = \frac{1}{4}\sqrt{\frac{5}{\pi}}(3\cos^2\theta - 1) \tag{B.12}$$

When $\theta = 90°$, this gives r_{minor} and when $\theta = 0°$, this gives r_{major}.

Appendix C: Capture cross sections

The total capture cross sections (σ_{cap}) were obtained by integrating the experimental differential cross section with the extrapolated distributions calculated with the TSM formalism for the light systems (Section 6.4.1), and QF simulations for the heavy systems (Section 6.4.2). The total capture cross sections for all systems are listed in the following tables. These cross sections have be renormalised for the 2% cross sections due to the efficiency of the MWPC.

Uncertainties arise mainly from extrapolation to the angular range not covered experimentally. Using the TSM formalism, it is the uncertainty in K_0 that largely determines the cross section uncertainty. For the Quasisim extrapolation, uncertainties come from the estimated uncertainty in extrapolation, as described in Section 6.4.2.

Table C.1: The capture cross sections for the ^{18}O + ^{232}Th reaction.

$E_{\mathbf{c.m.}}$ [MeV]	$\sigma_{\mathbf{cap}}$ [mb]	$\delta\sigma_{\mathbf{cap}}$ [mb]
72.6	2.95	0.04
75.1	14.28	0.11
79.9	97.15	0.47
84.5	281.3	1.0
87.0	389.2	1.4
89.6	470.4	1.7

Table C.2: The capture cross sections for the ^{30}Si + ^{232}Th reaction.

$E_{\mathbf{c.m.}}$ [MeV]	$\boldsymbol{\sigma}_{\mathbf{cap}}$ [mb]	$\boldsymbol{\delta\sigma}_{\mathbf{cap}}$ [mb]
128.0	14.73	0.18
131.6	30.14	0.26
135.7	64.18	0.54
139.4	122.4	1.0
143.0	211.3	1.7
146.6	299.1	2.5

Table C.3: The capture cross sections for the ^{34}S + ^{232}Th reaction.

$E_{\mathbf{c.m.}}$ [MeV]	$\boldsymbol{\sigma}_{\mathbf{cap}}$ [mb]	$\boldsymbol{\delta\sigma}_{\mathbf{cap}}$ [mb]
143.6	3.79	0.08
145.7	8.11	0.16
147.9	14.52	0.29
150.5	28.16	0.56
158.4	120.8	2.4
166.7	289.4	5.8

Table C.4: The capture cross sections for the ^{40}Ca + ^{232}Th reaction.

$E_{\mathbf{c.m.}}$ [MeV]	$\boldsymbol{\sigma}_{\mathbf{cap}}$ [mb]	$\boldsymbol{\delta\sigma}_{\mathbf{cap}}$ [mb]
185.5	11.9	0.2
193.1	46.6	0.9
197.0	73.2	1.5
203.2	182.7	3.7
210.2	272.6	5.5
222.7	455.9	9.1

Table C.5: The capture cross sections for the ^{48}Ca + ^{232}Th reaction.

$E_{\mathbf{c.m.}}$ [MeV]	$\sigma_{\mathbf{cap}}$ [mb]	$\delta\sigma_{\mathbf{cap}}$ [mb]
185.7	24.9	0.5
189.9	53.9	1.1
193.2	91.8	1.8
197.3	171.1	3.4
201.5	232.3	4.6
208.9	366.0	7.3
216.4	463.9	9.3
225.5	577	12

Appendix D: 'dacube' code structure

'dacube' is a package of scripts that are required to analyse the fission data. These include conversion scripts to make the proper structure of ROOT files, plotting tools such as plotting the standard style of MAD, a script for multiple figures, and the main source code. The source code (src) includes scripts relevant to binary event reconstruction and differential cross section calculations. The following diagrams show the full structure of the source code and guide how individual scripts are related, and how the experimental information is processed through the code.

A basic knowledge of the C/C++ programming language and the use of the ROOT-based program 'dacube' are required for the data analysis of fission measurements. The author made this map for 'dacube' users, to help them understand the complex structure of the code.

Dacube - Part 2. Compositions

dacube is a script-based analysis program for the ANU CUBE spectrometer for two-body fission studies.
Detail information for running the code and general information are given in 'dacube CUBE analysis package documentation'.

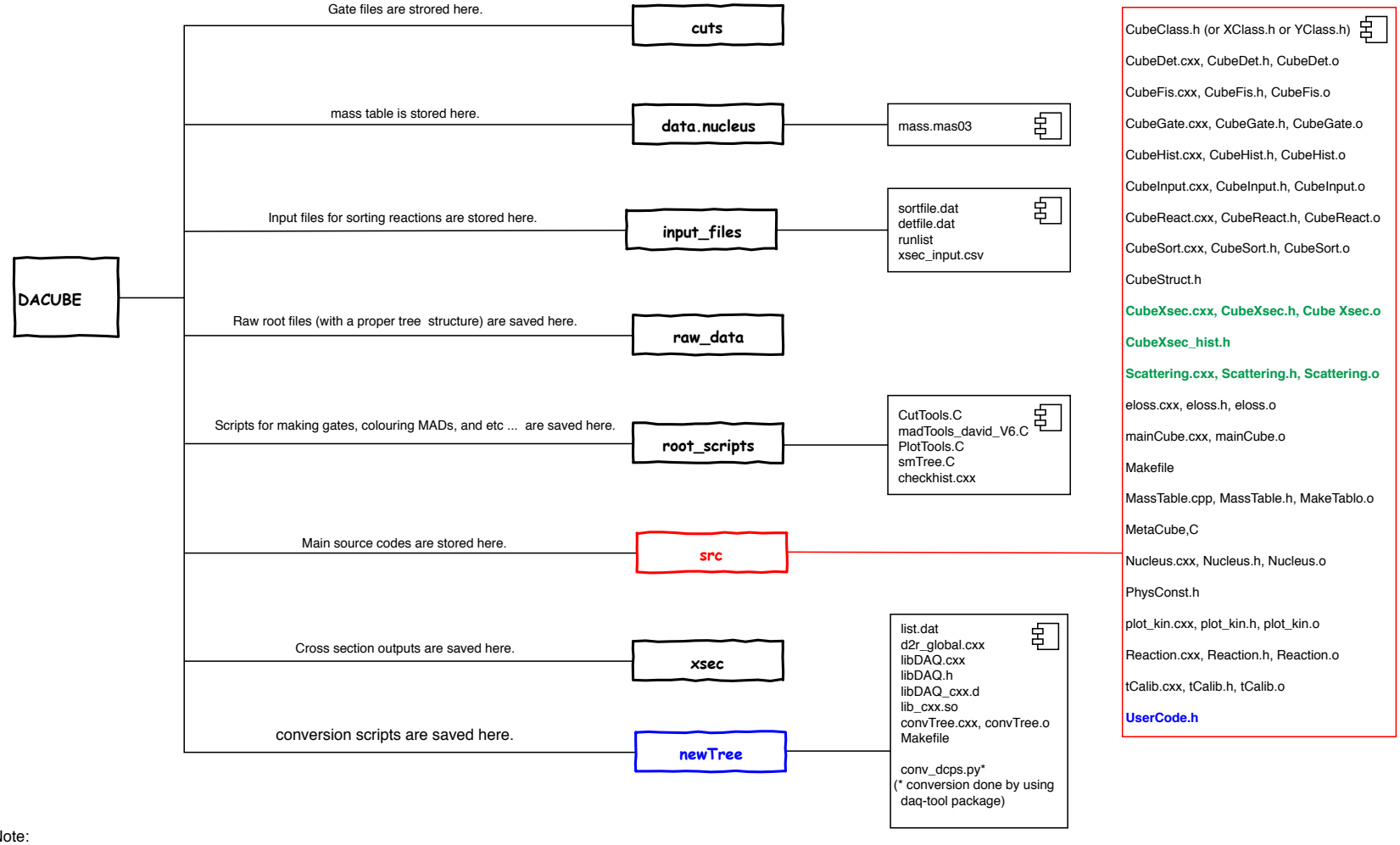

Note:
Source code version is src_2/3det_v4.1, released Feb. 2018.
UserCode.h is a script where we add a gate information
scripts labeled with green colour are scripts related to the cross section calculations.

Dacube - Part 3. Sorting

CubeSort.cxx is the heart of the dacube code to sort CUBE data. The root tree structure, data processing, etc ..., are all done in here with the exception of energy loss calculations. Dependencies: CubeClass.h, eloos.C, eloss.h Root libraries, and GNU math library

Any new branches, such as the 3rd detector components must be added here first.

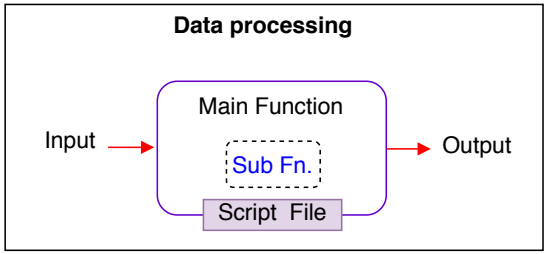

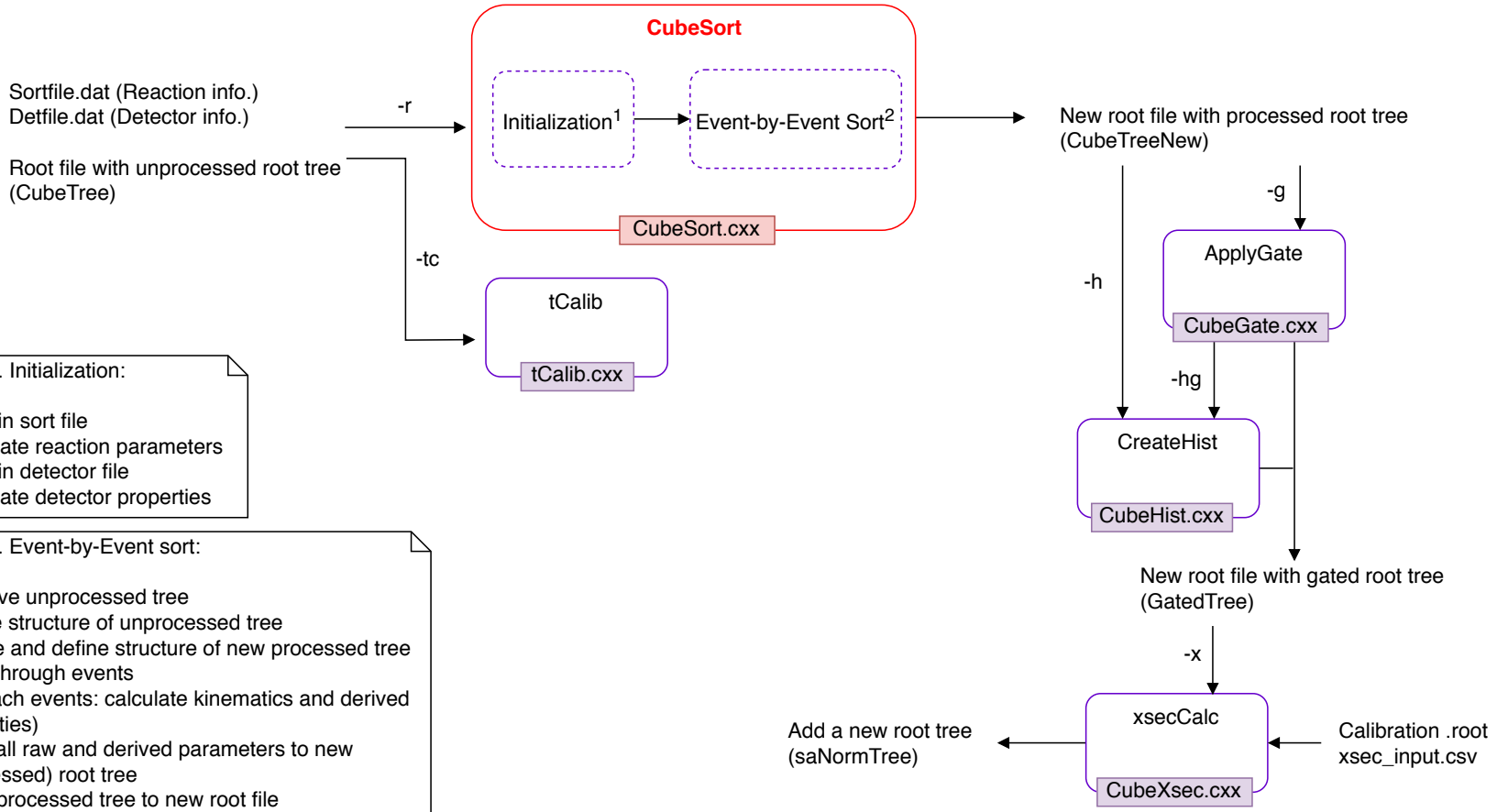

Note1. Initialization:

Read in sort file
Calculate reaction parameters
Read in detector file
Calculate detector properties

Note2. Event-by-Event sort:

Retrieve unprocessed tree
Define structure of unprocessed tree
Create and define structure of new processed tree
Loop through events
(for each events: calculate kinematics and derived quantities)
Save all raw and derived parameters to new (processed) root tree
Write processed tree to new root file

Dacube - Part 3.1 CubeSort: Initialization

The first step of sorting data is reading all input files. Store reaction parameters and detector geometry. Open unprocessed root file and Get Cube Tree.

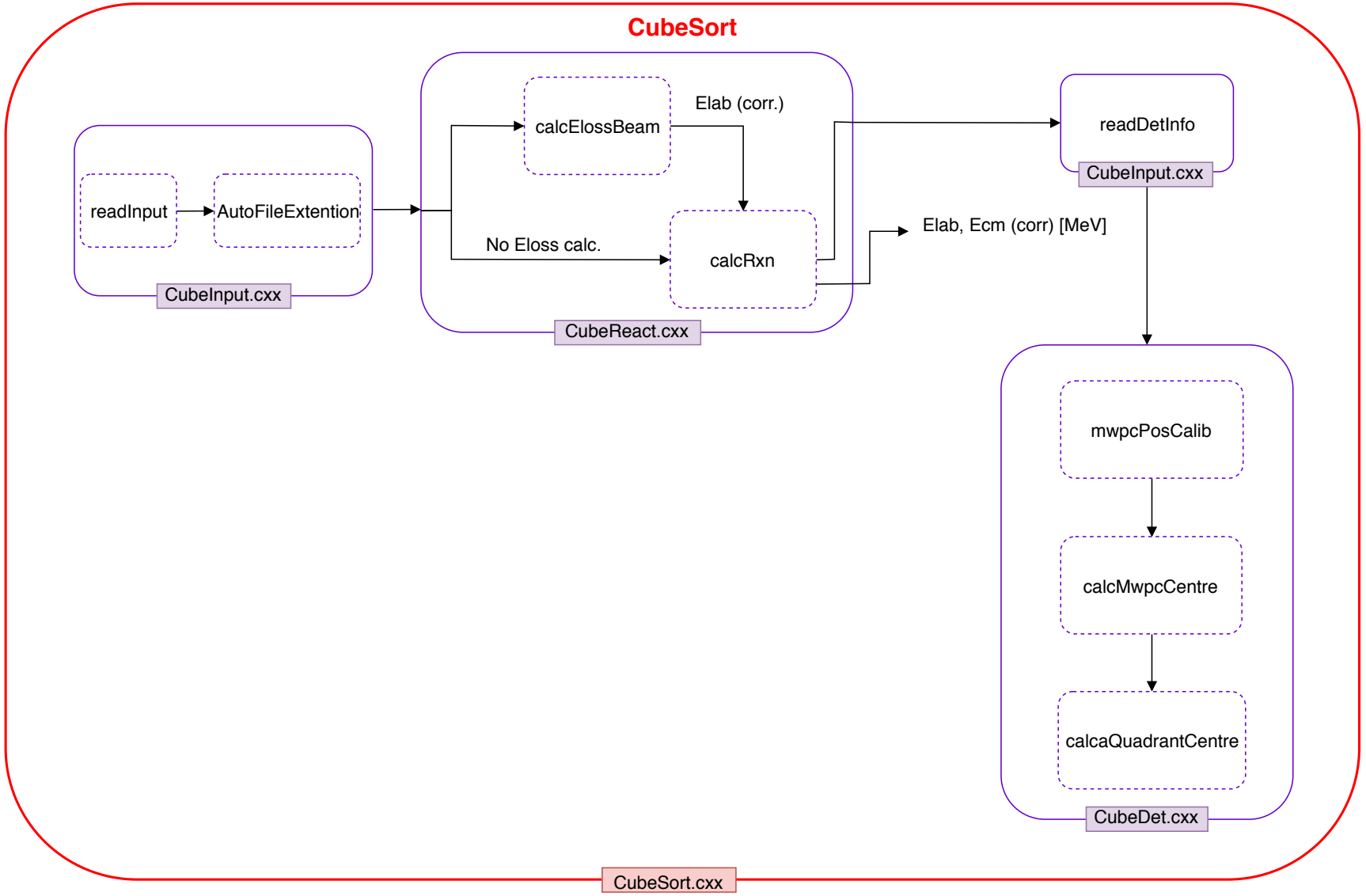

Dacube - Part 3.2 CubeSort: Event-by-Event Sort

Reactions are reconstructed event-by-event through CubeClass loop. Kinematics are reconstruced based on the assumption that coincident events are two-body fission.

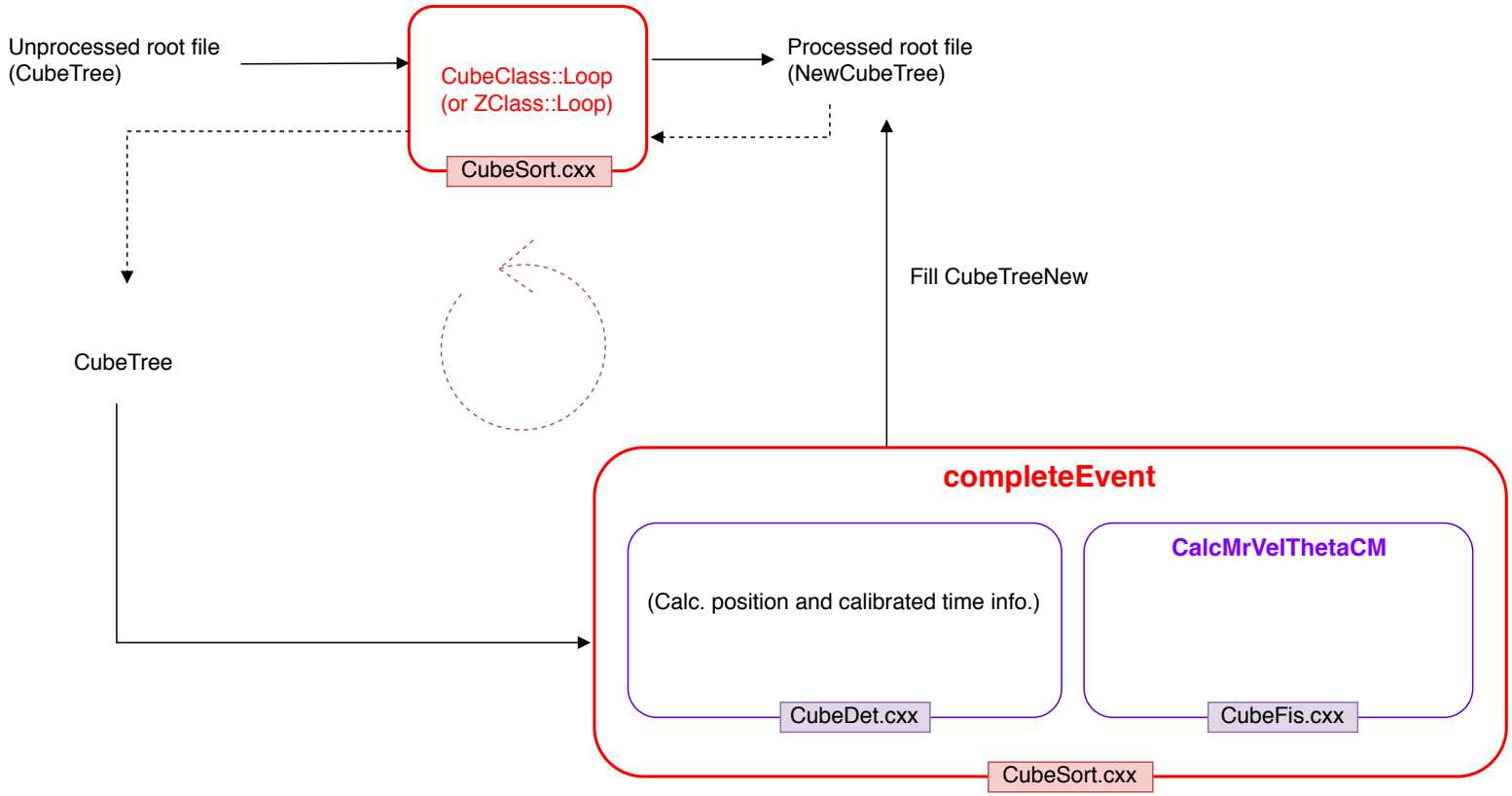

Note:
CubeClass is for 2 detector configuraiton.
ZClass is a for 3 detector configuration.

Transformation & Calibration:

Detector coord. --> Cartesian coord.
Cartesian coord --> Spherical coord.
Time calib.

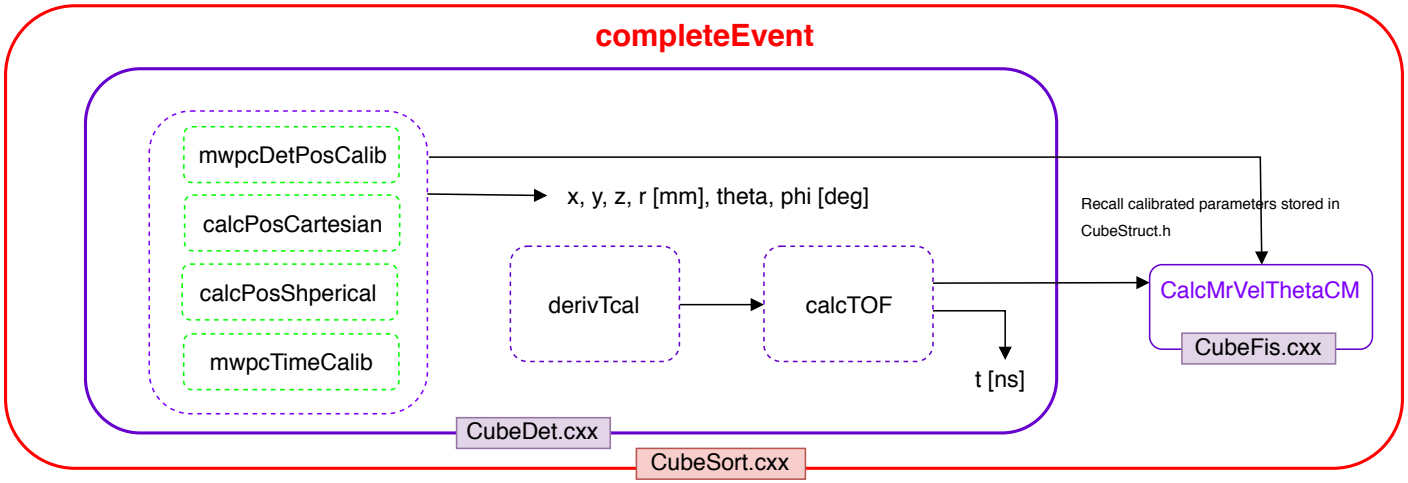

Kinematic Calculation Logic: AC beam (beam type=1)

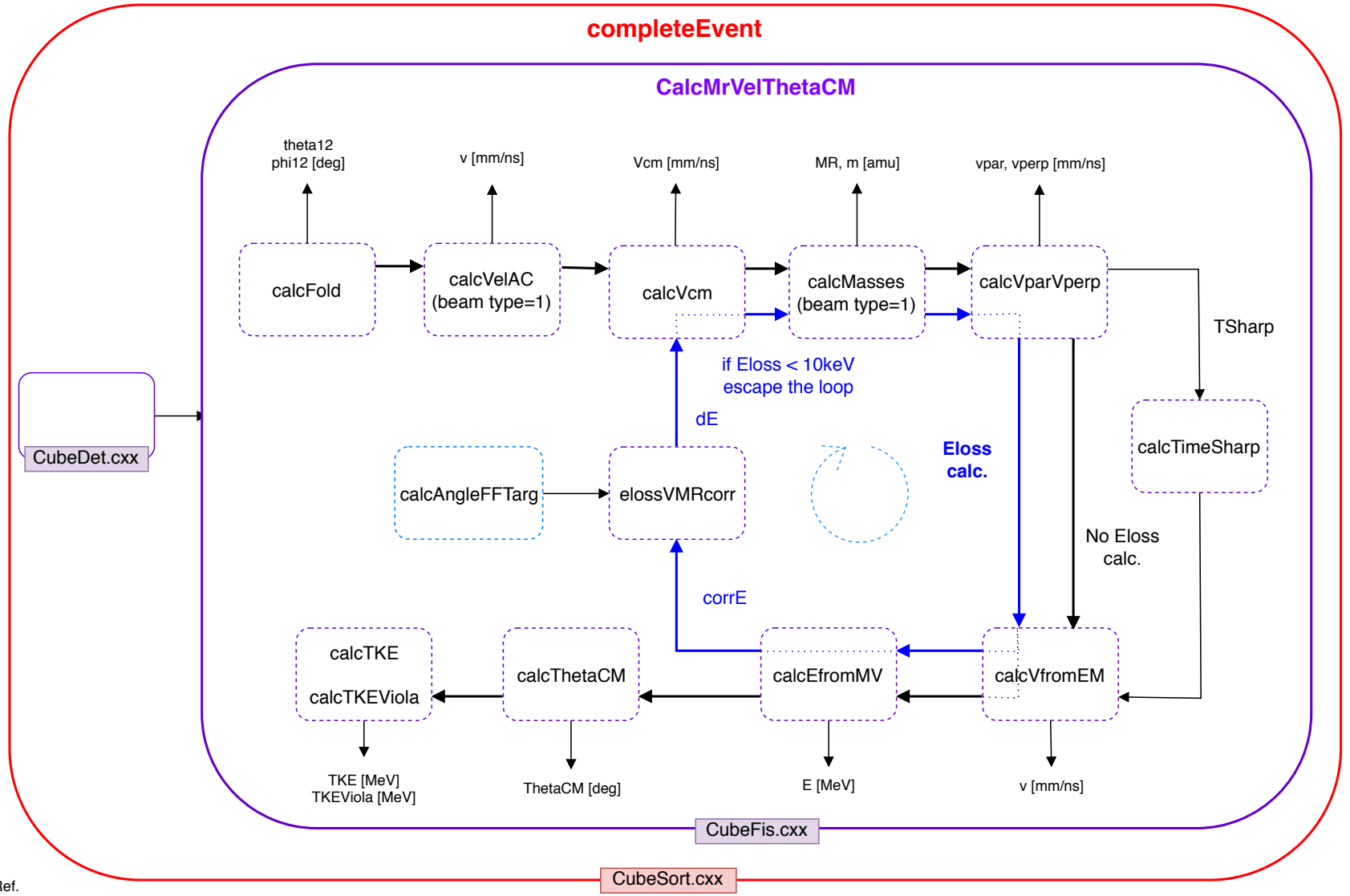

Ref.
[23] Kinematic coincidence method: Phys. Rev. C 53 1290 (1996)
[78] Viola system: Phys. Rev. C 31, 1550 (1985)

Kinematic Calculation Logic: Time Difference Method (beam type >1, Ap >2)

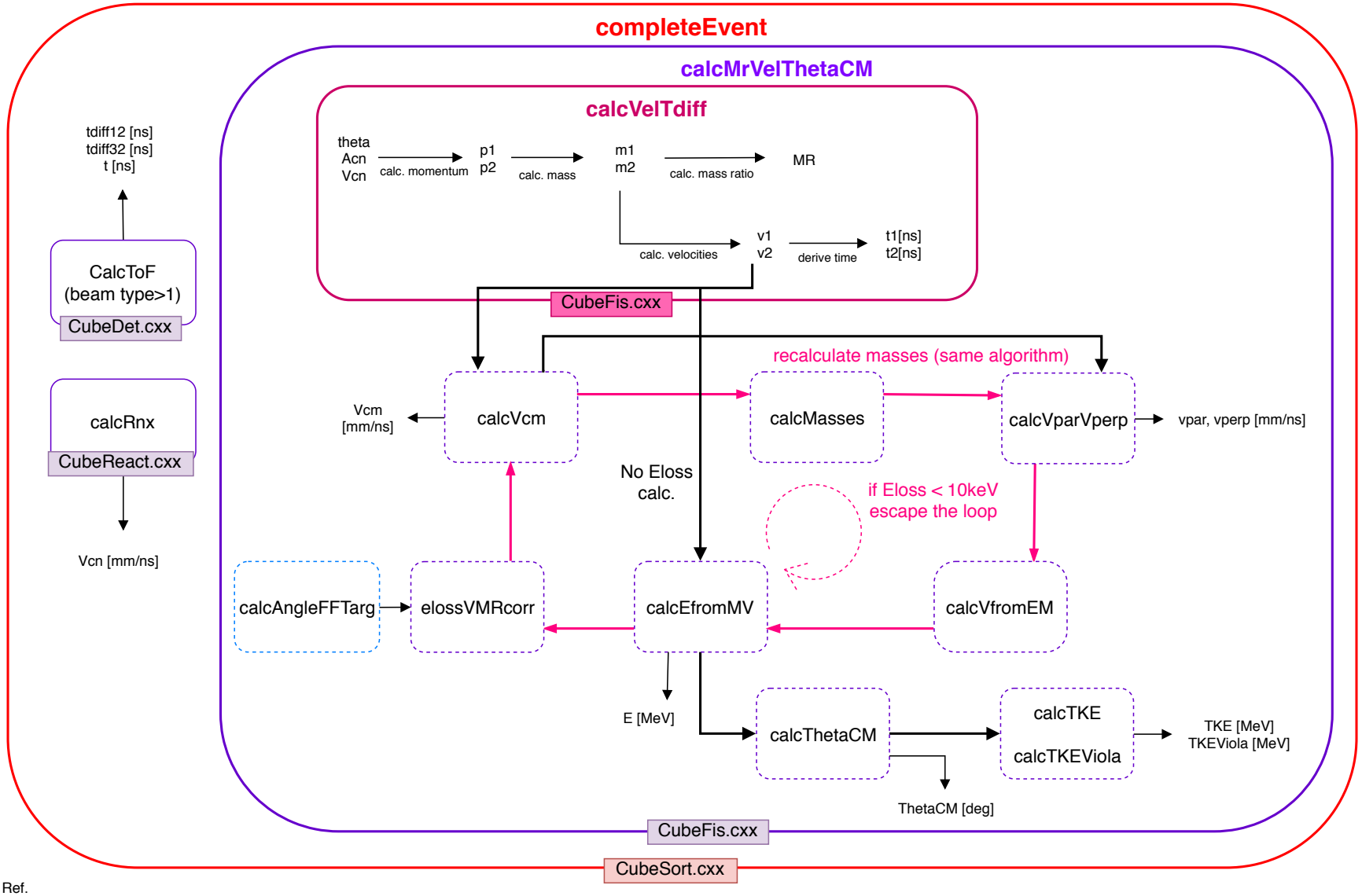

Ref.
[79] Time difference method: Phys. Rev. C 77 034610 (2008)

Kinematic Calculation Logic: Time Difference Method (beam type >1, Ap <=2)

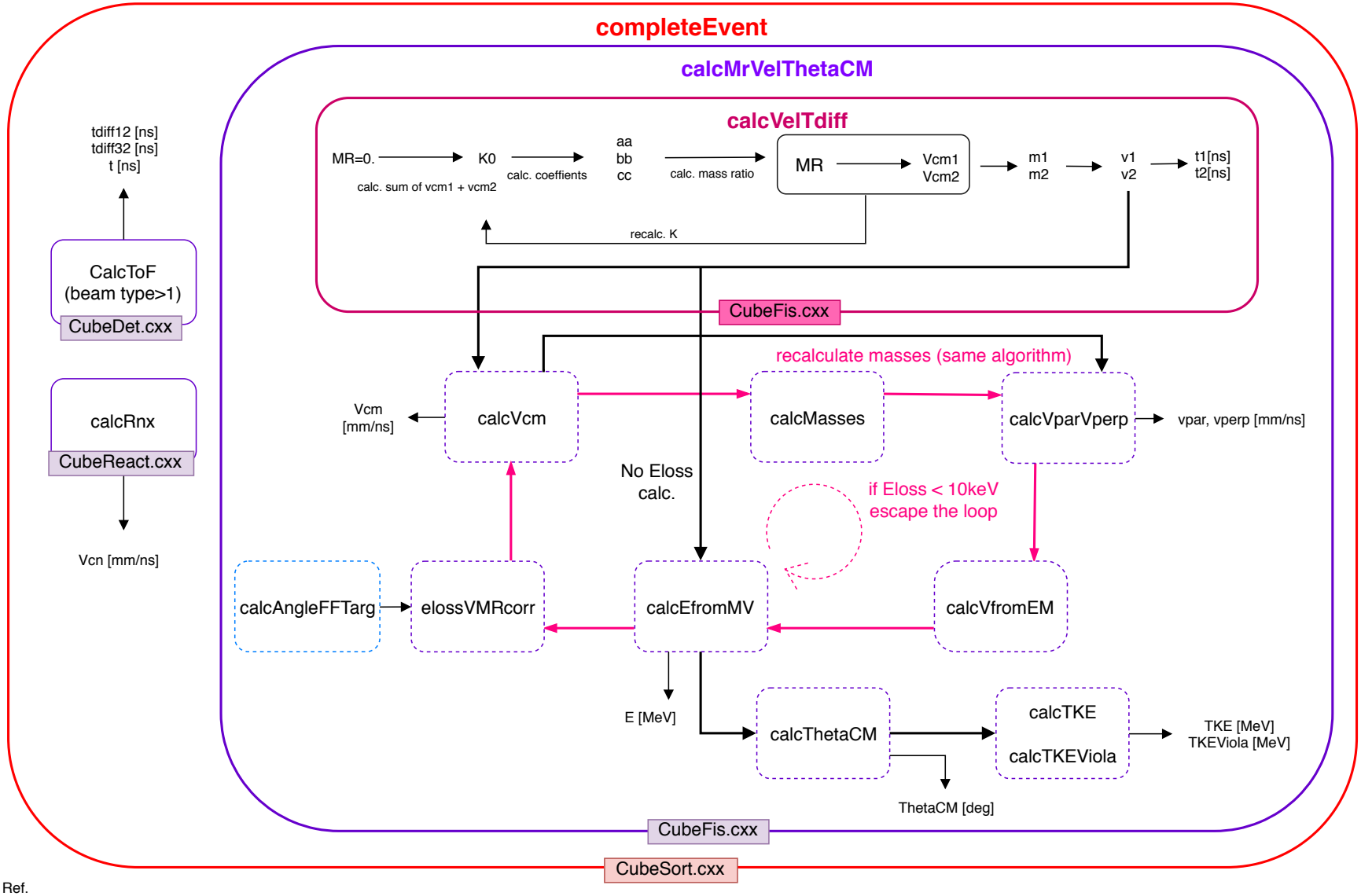

Ref.
[82] Simod Giraud (July 2015), 'Light particle induced fission, test of a new time-difference method'

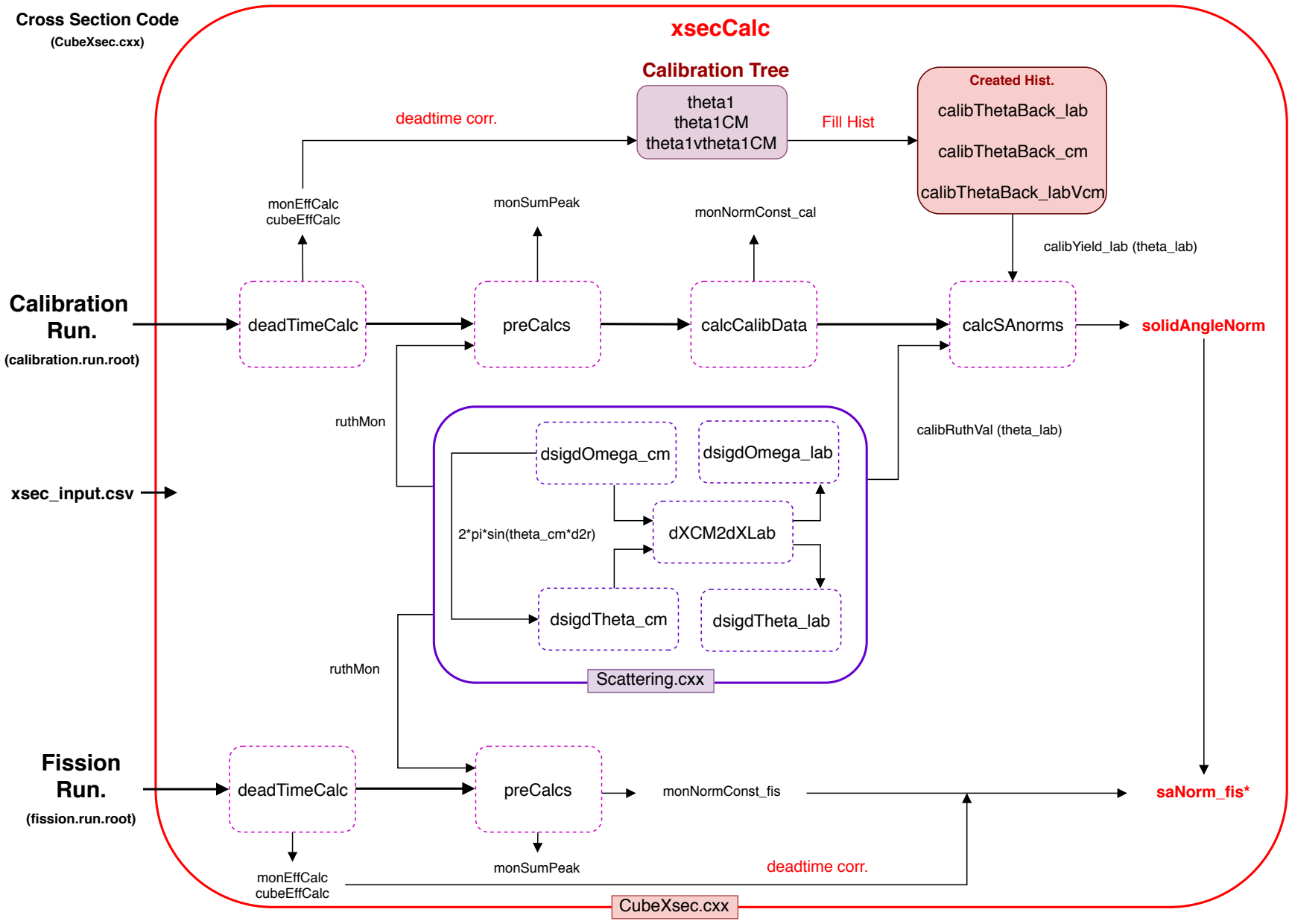
Cross Section Code
(CubeXsec.cxx)
xsecCalc
Calibration Tree
theta1
theta1CM
theta1vtheta1CM
deadtime corr.
Fill Hist
Created Hist.
calibThetaBack_lab
calibThetaBack_cm
calibThetaBack_labVcm
monEffCalc
cubeEffCalc
monSumPeak
monNormConst_cal
calibYield_lab (theta_lab)
Calibration Run.
(calibration.run.root)
deadTimeCalc
preCalcs
calcCalibData
calcSAnorms
solidAngleNorm
ruthMon
calibRuthVal (theta_lab)
xsec_input.csv
dsigdOmega_cm
dsigdOmega_lab
2*pi*sin(theta_cm*d2r)
dXCM2dXLab
dsigdTheta_cm
dsigdTheta_lab
Scattering.cxx
ruthMon
Fission Run.
(fission.run.root)
deadTimeCalc
preCalcs
monNormConst_fis
saNorm_fis*
monEffCalc
cubeEffCalc
monSumPeak
deadtime corr.
CubeXsec.cxx

Bibliography

[1] A. Sobiczewski, F. Gareev, and B. Kalinkin, "Closed shells for Z > 82 and N > 126 in a diffuse potential well," *Phys. Lett.*, vol. 22, no. 4, pp. 500 – 502, 1966.

[2] W. D. Myers and W. J. Swiatecki, "Nuclear masses and deformations," *Nucl. Phys.*, vol. 81, no. 1, pp. 1 – 60, 1966.

[3] L. Ö hrström and J. Reedijk, "Names and symbols of the elements with atomic numbers 113, 115, 117 and 118 (IUPAC Recommendations 2016)," *Pure and Applied Chemistry*, vol. 88, no. 12, pp. 1225–1229, 2016.

[4] S. Hofmann and G. Münzenberg, "The discovery of the heaviest elements," *Rev. Mod. Phys.*, vol. 72, pp. 733–767, Jul 2000.

[5] N. Bohr, "Neutron Capture and Nuclear Constitution," *Nature*, vol. 137, pp. 344–348, Feb 1936.

[6] K. Hagino and N. Takigawa, "Subbarrier fusion reactions and many-particle quantum tunneling," *Progress of Theoretical Physics*, vol. 128, no. 6, pp. 1061–1106, 2012.

[7] D. Hinde, M. Dasgupta, A. Diaz-Torres, and M. Evers, "Quantum coherence and decoherence in low energy nuclear collisions: from superposition to irreversibility," *Nuclear Physics A*, vol. 834, no. 1, pp. 117c – 122c, 2010. The 10th International Conference on Nucleus-Nucleus Collisions (NN2009).

[8] I. J. Thompson, "Coupled reaction channels calculations in nuclear physics," *Computer Physics Reports*, vol. 7, no. 4, pp. 167–212, 1988.

[9] T. TAMURA, "Analyses of the Scattering of Nuclear Particles by Collective Nuclei in Terms of the Coupled-Channel Calculation," *Rev. Mod. Phys.*, vol. 37, pp. 679–708, Oct 1965.

[10] S. Szilner, L. Corradi, G. Pollarolo, S. Beghini, B. R. Behera, E. Fioretto, A. Gadea, F. Haas, A. Latina, G. Montagnoli, F. Scarlassara, A. M. Stefanini, M. Trotta, A. M. Vinodkumar, and Y. Wu, "Multinucleon transfer processes in ^{40}Ca +^{208} Pb," *Phys. Rev. C*, vol. 71, p. 044610, Apr 2005.

[11] F. L. H. Wolfs, W. Henning, K. E. Rehm, and J. P. Schiffer, "Strength of deep-inelastic scattering for ^{58}Ni +^{124} Sn at sub-barrier energies," *Phys. Lett.*, vol. B196, pp. 113–116, 1987.

[12] J. G. Keller, B. B. Back, B. G. Glagola, D. Henderson, S. B. Kaufman, S. J. Sanders, R. H. Siemssen, F. Videbaek, B. D. Wilkins, and A. Worsham, "Distribution of reaction strength in ^{32}S +^{182} W collisions," *Phys. Rev. C*, vol. 36, pp. 1364–1374, Oct 1987.

[13] M. Evers, M. Dasgupta, D. J. Hinde, D. H. Luong, R. Rafiei, R. du Rietz, and C. Simenel, "Cluster transfer in the reaction ^{16}O +^{208} Pb at energies well below the fusion barrier: A possible doorway to energy dissipation," *Phys. Rev. C*, vol. 84, p. 054614, Nov 2011.

[14] D. C. Rafferty, M. Dasgupta, D. J. Hinde, C. Simenel, E. C. Simpson, E. Williams, I. P. Carter, K. J. Cook, D. H. Luong, S. D. McNeil, K. Ramachandran, K. Vo-Phuoc, and A. Wakhle, "Multinucleon transfer in ^{16,18}O, ^{19}F + ^{208}Pb reactions at energies near the fusion barrier," *Phys. Rev. C*, vol. 94, p. 024607, Aug 2016.

[15] J. O. Newton, R. D. Butt, M. Dasgupta, D. J. Hinde, I. I. Gontchar, C. R. Morton, and K. Hagino, "Systematic failure of the Woods-Saxon nuclear potential to describe both fusion and elastic scattering: Possible need for a new dynamical approach to fusion," *Phys. Rev. C*, vol. 70, p. 024605, Aug 2004.

[16] R. G. Stokstad, Y. Eisen, S. Kaplanis, D. Pelte, U. Smilansky, and I. Tserruya, "Effect of Nuclear Deformation on Heavy-Ion Fusion," *Phys. Rev. Lett.*, vol. 41, pp. 465–469, Aug 1978.

[17] J. R. Leigh, M. Dasgupta, D. J. Hinde, J. C. Mein, C. R. Morton, R. C. Lemmon, J. P. Lestone, J. O. Newton, H. Timmers, J. X. Wei, and N. Rowley, "Barrier distributions from the fusion of oxygen ions with ^{144,148,154}Sm and ^{186}W," *Phys. Rev. C*, vol. 52, pp. 3151–3166, Dec 1995.

[18] M. Dasgupta, , D. J. Hinde, N. Rowley, and A. M. Stefanini, "MEASURING BARRIERS TO FUSION," *Annu. Rev. Nucl. Part. Sci.*, vol. 48, no. 1, pp. 401–461, 1998.

[19] M. Dasgupta, D. J. Hinde, A. Diaz-Torres, B. Bouriquet, C. I. Low, G. J. Milburn, and J. O. Newton, "Beyond the Coherent Coupled Channels Description of Nuclear Fusion," *Phys. Rev. Lett.*, vol. 99, p. 192701, Nov 2007.

[20] C. L. Jiang, K. E. Rehm, R. V. F. Janssens, H. Esbensen, I. Ahmad, B. B. Back, P. Collon, C. N. Davids, J. P. Greene, D. J. Henderson, G. Mukherjee, R. C. Pardo,

M. Paul, T. O. Pennington, D. Seweryniak, S. Sinha, and Z. Zhou, "Influence of Nuclear Structure on Sub-Barrier Hindrance in Ni + Ni fusion," *Phys. Rev. Lett.*, vol. 93, p. 012701, Jun 2004.

[21] J. Newton, R. Butt, M. Dasgupta, D. Hinde, I. Gontchar, C. Morton, and K. Hagino, "Systematics of precise nuclear fusion cross sections: the need for a new dynamical treatment of fusion?," *Phys. Lett. B*, vol. 586, no. 3, pp. 219 – 224, 2004.

[22] C. R. Morton, A. C. Berriman, M. Dasgupta, D. J. Hinde, J. O. Newton, K. Hagino, and I. J. Thompson, "Coupled-channels analysis of the ^{16}O+^{208}Pb fusion barrier distribution," *Phys. Rev. C*, vol. 60, p. 044608, Aug 1999.

[23] L. Corradi, "The evolution from quasi-elastic to deep inelastic processes and its connection to fusion," *Journal of Physics: Conference Series*, vol. 282, p. 012005, feb 2011.

[24] G. Pollarolo, "Role of transfer reactions in heavy-ion collisions at the Coulomb barrier," *EPJ Web of Conferences*, vol. 17, pp. 08002–, 10 2011.

[25] A. Winther, "GRAZING. A Fortran program for estimating reactions in collision between Heavy Nuclei." http:/www.to.infn.it/~nanni/grazing.

[26] D. J. Hinde, M. Dasgupta, J. R. Leigh, J. C. Mein, C. R. Morton, J. O. Newton, and H. Timmers, "Conclusive evidence for the influence of nuclear orientation on quasifission," *Phys. Rev. C*, vol. 53, pp. 1290–1300, Mar 1996.

[27] H. Britt, *Fission properties of the Actinides.* Actinides in Perspective, Perganibm Oxfird, 1982.

[28] M.-L. Yoneama, E. Jacobs, J. Arruda-Neto, B. Bhandari, D. D. Frenne, S. PommÃľ, K. Persyn, and K. Govaert, "Study of the 232th fission barrier by electron-induced fission," *Nuclear Physics A*, vol. 604, no. 3, pp. 263 – 285, 1996.

[29] B. B. Back, "Complete fusion and quasifission in reactions between heavy ions," *Phys. Rev. C*, vol. 31, pp. 2104–2112, Jun 1985.

[30] J. Tōke, R. Bock, G. Dai, A. Gobbi, S. Gralla, K. Hildenbrand, J. Kuzminski, W. Müller, A. Olmi, H. Stelzer, B. Back, and S. Bjørnholm, "Quasi-fission − the mass-drift mode in heavy-ion reactions," *Nucl. Phys. A*, vol. 440, no. 2, pp. 327 – 365, 1985.

[31] W. Q. Shen, J. Albinski, A. Gobbi, S. Gralla, K. D. Hildenbrand, N. Herrmann, J. Kuzminski, W. F. J. Müller, H. Stelzer, J. Tke, B. B. Back, S. Bjrnholm, and S. P. Srensen, "Fission and quasifission in u-induced reactions," *Phys. Rev. C*, vol. 36, pp. 115–142, Jul 1987.

[32] J. Blocki, H. Feldmeier, and W. Swiatecki, "Dynamical hindrance to compound-nucleus formation in heavy-ion reactions," *Nucl. Phys. A*, vol. 459, no. 1, pp. 145 – 172, 1986.

[33] W. J. Swiatecki, "The Dynamics of Nuclear Coalescence or Reseparation," *Phys, Scr.*, vol. 24, no. 1B, p. 113, 1981.

[34] R. D. Woods and D. S. Saxon, "Diffuse Surface Optical Model for Nucleon-Nuclei Scattering," *Phys. Rev.*, vol. 95, pp. 577–578, Jul 1954.

[35] R. Brogila and A. Winther, *Heavy Ion Reactions*, vol. Vol. 1: Elastic and Inelastic Reactions. The Benjamin/Cummings Publishing Company, InC., 1981.

[36] I. Gontchar, D. Hinde, M. Dasgupta, and J. Newton, "Surface diffuseness of nuclear potential from heavy-ion fusion reactions," *Nucl. Phys. A*, vol. 722, pp. C479 – C483, 2003.

[37] M. Dasgupta, D. J. Hinde, J. O. Newton, and K. Hagino, "The Nuclear Potential in Heavy-Ion Fusion," *Progress of Theoretical Physics Supplement*, vol. 154, pp. 209–216, 2004.

[38] L. C. Vaz, J. M. Alexander, and G. Satchler, "Fusion barriers, empirical and theoretical: Evidence for dynamic deformation in subbarrier fusion," *Physics Reports*, vol. 69, no. 5, pp. 373 – 399, 1981.

[39] D. D. Gregorio, J. F. Niello, A. Pacheco, D. Abriola, S. Gil, A. Macchiavelli, J. Testoni, P. Pascholati, V. Vanin, R. Neto, N. Filho, M. Coimbra, P. Gomes, and R. Stokstad, "Fusion of ^{16}O+^{144}Sm at sub-barrier energies," *Phys. Lett. B*, vol. 176, no. 3, pp. 322 – 326, 1986.

[40] D. Brink and D. Brink, *Semi-Classical Methods for Nucleus-Nucleus Scattering.* Cambridge Monographs on Mathematical Physics, Cambridge University Press, 1985.

[41] K. Hagino and A. B. Balantekin, "WKB approximation for multichannel barrier penetrability," *Phys. Rev. A*, vol. 70, p. 032106, Sep 2004.

[42] R. Broglia, C. Dasso, S. Landowne, and G. Pollarolo, "Estimate of enhancements in sub-barrier heavy-ion fusion cross sections due to coupling to inelastic and transfer reaction channels," *Phys. Lett. B*, vol. 133, no. 1, pp. 34 – 38, 1983.

[43] R. G. Stokstad and E. E. Gross, "Analysis of the sub-barrier fusion of ^{16}O+^{148,150,152,154}Sm," *Phys. Rev. C*, vol. 23, pp. 281–294, Jan 1981.

[44] R. G. Stokstad, Y. Eisen, S. Kaplanis, D. Pelte, U. Smilansky, and I. Tserruya, "Fusion of ^{16}O + ^{148,150,152,154}Sm at sub-barrier energies," *Phys. Rev. C*, vol. 21, pp. 2427–2435, Jun 1980.

[45] G. Montagnoli and A. M. Stefanini, "Recent experimental results in sub- and near-barrier heavy-ion fusion reactions," *The European Physical Journal A*, vol. 53, p. 169, Aug 2017.

[46] M. Dasgupta, D. J. Hinde, S. L. Sheehy, and B. Bouriquet, "Suppression of fusion by breakup: Resolving the discrepancy between the reactions of ^{9}Be with ^{208}Pb and ^{209}Bi," *Phys. Rev. C*, vol. 81, p. 024608, Feb 2010.

[47] B. Wang, W.-J. Zhao, A. Diaz-Torres, E.-G. Zhao, and S.-G. Zhou, "Systematic study of suppression of complete fusion in reactions involving weakly bound nuclei at energies above the coulomb barrier," *Phys. Rev. C*, vol. 93, p. 014615, Jan 2016.

[48] A. M. Stefanini, D. Ackermann, L. Corradi, D. R. Napoli, C. Petrache, P. Spolaore, P. Bednarczyk, H. Q. Zhang, S. Beghini, G. Montagnoli, L. Mueller, F. Scarlassara, G. F. Segato, F. Soramel, and N. Rowley, "Influence of Complex Surface Vibrations on the Fusion of ^{58}Ni + ^{60}Ni," *Phys. Rev. Lett.*, vol. 74, pp. 864–867, Feb 1995.

[49] E. Williams, D. Hinde, M. Dasgupta, Carter, K. I.P., Cook, D. Jeung, D. Luong, S. McNeil, C. Palshetkar, D. Rafferty, C. Ramachandran, K.and Simenel, E. Simpson, and A. Wakhle, "Exploring dissipative processes at high angular momentum in ^{58}Ni + ^{60}Ni reactions," *EPJ Web of Conferences*, vol. 117, p. 08021, 2016.

[50] R. Vandebosch and J. R. Huizenga, *Nuclear Fission.* Cambridge Monographs on Mathematical Physics, Academic Press, 1973.

[51] H. Rossner, J. R. Huizenga, and W. U. Schröder, "Fission fragment angular distributions," *Phys. Rev. C*, vol. 33, pp. 560–575, Feb 1986.

[52] C. R. Morton, D. J. Hinde, J. R. Leigh, J. P. Lestone, M. Dasgupta, J. C. Mein, J. O. Newton, and H. Timmers, "Resolution of the anomalous fission fragment anisotropies for the ^{16}O+^{208}Pb reaction," *Phys. Rev. C*, vol. 52, pp. 243–251, Jul 1995.

[53] C. Morton, D. Hinde, A. Berriman, R. Butt, M. Dasgupta, A. Godley, and J. Newton, "Memory of entrance-channel deformation for fast-fission," *Phys. Lett. B*, vol. 481, no. 2, pp. 160 – 164, 2000.

[54] R. du Rietz, D. J. Hinde, M. Dasgupta, R. G. Thomas, L. R. Gasques, M. Evers, N. Lobanov, and A. Wakhle, "Predominant Time Scales in Fission Processes in Reactions of S, Ti and Ni with W: Zeptosecond versus Attosecond," *Phys. Rev. Lett.*, vol. 106, p. 052701, Feb 2011.

[55] R. du Rietz, E. Williams, D. J. Hinde, M. Dasgupta, M. Evers, C. J. Lin, D. H. Luong, C. Simenel, and A. Wakhle, "Mapping quasifission characteristics and timescales in heavy element formation reactions," *Phys. Rev. C*, vol. 88, p. 054618, Nov 2013.

[56] M. Dasgupta, A. Navin, Y. Agarwal, C. Baba, H. Jain, M. Jhingan, and A. Roy, "Fusion of ^{28}Si+^{68}Zn, ^{32}S+^{64}Ni, ^{37}Cl+^{59}Co and ^{45}Sc+^{51}V," *Nucl. Phys. A*, vol. 539, no. 2, pp. 351 – 369, 1992.

[57] "Wolfram mathword: Moment of Inertia." http://mathworld.wolfram.com/MomentofInertia.html.

[58] A. S. Umar, V. E. Oberacker, and C. Simenel, "Shape evolution and collective dynamics of quasifission in the time-dependent hartree-fock approach," *Phys. Rev. C*, vol. 92, p. 024621, Aug 2015.

[59] E. Prasad, A. Wakhle, D. J. Hinde, E. Williams, M. Dasgupta, M. Evers, D. H. Luong, G. Mohanto, C. Simenel, and K. Vo-Phuoc, "Exploring quasifission characteristics for ^{34}S +^{232} Th forming ^{266}Sg," *Phys. Rev. C*, vol. 93, p. 024607, Feb 2016.

[60] Y. Aritomo, K. Hagino, K. Nishio, and S. Chiba, "Dynamical approach to heavy-ion induced fission using actinide target nuclei at energies around the Coulomb barrier," *Phys. Rev. C*, vol. 85, p. 044614, Apr 2012.

[61] A. Wakhle, C. Simenel, D. J. Hinde, M. Dasgupta, M. Evers, D. H. Luong, R. du Rietz, and E. Williams, "Interplay between Quantum Shells and Orientation in Quasifission," *Phys. Rev. Lett.*, vol. 113, p. 182502, Oct 2014.

[62] D. J. Hinde, M. Dasgupta, J. R. Leigh, J. P. Lestone, J. C. Mein, C. R. Morton, J. O. Newton, and H. Timmers, "Fusion-Fission versus Quasifission: Effect of Nuclear Orientation," *Phys. Rev. Lett.*, vol. 74, pp. 1295–1298, Feb 1995.

[63] D. J. Hinde, D. Y. Jeung, E. Prasad, A. Wakhle, M. Dasgupta, M. Evers, D. H. Luong, R. du Rietz, C. Simenel, E. C. Simpson, and E. Williams, "Sub-barrier quasifission in heavy element formation reactions with deformed actinide target nuclei," *Phys. Rev. C*, vol. 97, p. 024616, Feb 2018.

[64] D. Bromley, "The development of electrostatic accelerators," *Nuclear Instruments and Methods*, vol. 122, pp. 1 – 34, 1974.

[65] T. Ophel, J. Harrison, J. Newton, R. Spear, E. Titterton, and D. Weisser, "The 14UD pelletron accelerator at the Australian National University," *Nuclear Instruments and Methods*, vol. 122, pp. 227 – 234, 1974.

[66] N. R. Lobanov and D. C. Weisser, "Three-stub quarter wave superconducting resonator design," *Phys. Rev. ST Accel. Beams*, vol. 9, p. 112002, Nov 2006.

[67] "National Electrostattics Corp.; Soucre of Negative Ions by Cesium Souttering." http://www.pelletron.com/products/snics/.

[68] R. Middleton, "A survey of negative ion sources for tandem accelerators," *Nuclear Instruments and Methods*, vol. 122, pp. 35 – 43, 1974.

[69] K. Brand, "Improvement of the reflected beam sputter source," *Nuclear Instruments and Methods*, vol. 154, no. 3, pp. 595 – 596, 1978.

[70] R. Middleton, *The Negative Ion Cookbook*. Brookhaven National Laboratory Tandem Van de Graaff Accelerator, 1989.

[71] V. Nikolaev and I. Dmitriev, "On the equilibrium charge distribution in heavy element ion beams," *Physics Letters A*, vol. 28, no. 4, pp. 277 – 278, 1968.

[72] J. Yntema, "Heavy ion stripping in tandem accelerator terminals," *Nuclear Instruments and Methods*, vol. 122, pp. 45 – 52, 1974.

[73] R. Spear, D. Kean, M. Esat, A. Joye, and M. Fewell, "Energy calibration of the ANU 14UD Pelletron accelerator," *Nuclear Instruments and Methods*, vol. 147, no. 3, pp. 455 – 459, 1977.

[74] N. R. Lobanov, "Superconducting resonator used as a phase and energy detector for linac setup," *Phys. Rev. Accel. Beams*, vol. 19, p. 072801, Jul 2016.

[75] D. C. W. Nikolai R. Lobanov, "Lead-Tin Plating Split Loop Resonators," in *Proc. 11th International Conference on RF Superconductivity (SRF2003)*, Sept 2003.

[76] A. Stuchbery and D. Weisser, "Beam optics design for the ANU linear booster accelerator," *Nuclear Instruments and Methods in Physics Research Section A: Accelerators, Spectrometers, Detectors and Associated Equipment*, vol. 382, no. 1, pp. 172 – 175, 1996. Proc. of the 7th International Conference on Heavy Ion Accelerator Technology.

[77] P. L. Nikolai R. Lobanov and D. Tsifakis, "Tuning the linac with superconducting respnator used as a phase detector," in *Proc. 17th International Conference on RF Superconductivity (SRF2015)*, pp. 602 – 606, Sept 2015.

[78] W. Leo, *Techniques for Nuclear and Particle Physics Experiments*. Springer-Verlag, 1994.

[79] G. F. Knoll, *Radiation detection and measurement*. John Wiley & Sons, 2010.

[80] R. Brun and F. Rademakers, "ROOT: An object oriented data analysis framework," *Nuclear Instruments and Methods in Physics Research Section A: Accelerators, Spectrometers, Detectors and Associated Equipment*, vol. 389, no. 1, pp. 81 – 86, 1997. New Computing Techniques in Physics Research V.

[81] W. J. Świątecki, K. Siwek-Wilczyńska, and J. Wilczyński, "Fusion by diffusion. II. Synthesis of transfermium elements in cold fusion reactions," *Phys. Rev. C*, vol. 71, p. 014602, Jan 2005.

[82] R. G. Thomas, D. J. Hinde, D. Duniec, F. Zenke, M. Dasgupta, M. L. Brown, M. Evers, L. R. Gasques, M. D. Rodriguez, and A. Diaz-Torres, "Entrance channel dependence of quasifission in reactions forming ^{220}Th," *Phys. Rev. C*, vol. 77, p. 034610, Mar 2008.

[83] G. Arfken, H. Weber, and F. Harris, *Mathematical Methods for Physicists: A Comprehensive Guide*. YBP Print DDA, Elsevier, 2013.

[84] M. A. Finlayson, *Technical Information Manual*. CAEN, Nov 2016.

[85] S. Giraud, "Light particle induced fission, test of a new time-dfference method," Master's thesis, Australian National University, July 2015.

[86] J. F. Ziegler, U. Littmark, and J. P. Biersack, *The stopping and range of ions in solids / J.F. Ziegler, J.P. Biersack, U. Littmark*. Pergamon New York, 1985.

[87] V. E. Viola, K. Kwiatkowski, and M. Walker, "Systematics of fission fragment total kinetic energy release," *Phys. Rev. C*, vol. 31, pp. 1550–1552, Apr 1985.

[88] K. S. Krane, *Inroductory Nuclear Physics*. John Wiley and Sons Ltd., 1987.

[89] C. R. Morton, *Fusion Barrier Distributions and Fission Fragment Anisotropies in Heavy-Ion Fusion Reactions*. PhD thesis, The Australian National University, 1995.

[90] E. Prasad, D. J. Hinde, E. Williams, M. Dasgupta, I. P. Carter, K. J. Cook, D. Y. Jeung, D. H. Luong, C. S. Palshetkar, D. C. Rafferty, K. Ramachandran, C. Simenel, and A. Wakhle, "Fusion and quasifission studies for the ^{40}Ca +^{186} W,^{192} Os reactions," *Phys. Rev. C*, vol. 96, p. 034608, Sep 2017.

[91] C. Simenel, "Nuclear quantum many-body dynamics," *The European Physical Journal A*, vol. 48, p. 152, Nov 2012.

[92] "Evaluated nuclear strucutre data file (ENSDF)," *Nuclear Data for Science and Technology*.

[93] S. Raman, C. Nestor, and P. Tikkane, "TRANSITION PROBABILITY FROM THE GROUND TO THE FIRST-EXCITED 2^+ STATE OF EVEN-EVEN NUCLIDES," *Atomic Data and Nuclear Data Tables*, vol. 78, no. 1, pp. 1 – 128, 2001.

[94] T. Elze and J. Huizenga, "COLLECTIVE STATES OF ^{232}Th, ^{238}U, ANU ^{242}Pu.," *Nucl. Phys. A*, vol. 187, pp. 545 – 566, 1 1972.

[95] T. Kibedi and R. Spear, "REDUCED ELECTRIC-OCTUPOLE TRANSITION PROBABILITIES, B(E3;$0^+_1 \rightarrow 3^-_1$) - AN UPDATED," *Atomic Data and Nuclear Data Tables*, vol. 80, no. 1, pp. 35 – 82, 2002.

[96] P. Moller, J. Nix, W. Myers, and W. Swiatecki, "Nuclear Ground-State Masses and Deformations," *Atomic Data and Nuclear Data Tables*, vol. 59, no. 2, pp. 185 – 381, 1995.

[97] P. Möller, A. J. Sierk, T. Ichikawa, A. Iwamoto, R. Bengtsson, H. Uhrenholt, and S. Åberg, "Heavy-element fission barriers," *Phys. Rev. C*, vol. 79, p. 064304, Jun 2009.

[98] F. Plasil, "ANGULAR MOMENTUM EFFECTS IN FUSION-FISSION AND FUSION-EVAPORATION REACTIONS," *Journal de Physique Colloques*, vol. 41, no. C10, pp. C10–183–C10–199, 1980.

[99] C. Golabek and C. Simenel, "Collision dynamics of two ^{238}U atomic nuclei," *Phys. Rev. Lett.*, vol. 103, p. 042701, Jul 2009.

[100] C. Clapham, J. Nicholson, and J. Nicholson, *The Concise Oxford Dictionary of Mathematics*. Oxford Paperback Reference, OUP Oxford, 2014.